frontiers | Research Topics

Insights in Nuclear Medicine 2022

Edited by
Giorgio Treglia

Published in
Frontiers in Medicine

ISSN 1664-8714
ISBN 978-2-8325-3202-7
DOI 10.3389/978-2-8325-3202-7

About Frontiers

Frontiers is more than just an open access publisher of scholarly articles: it is a pioneering approach to the world of academia, radically improving the way scholarly research is managed. The grand vision of Frontiers is a world where all people have an equal opportunity to seek, share and generate knowledge. Frontiers provides immediate and permanent online open access to all its publications, but this alone is not enough to realize our grand goals.

Frontiers journal series

The Frontiers journal series is a multi-tier and interdisciplinary set of open-access, online journals, promising a paradigm shift from the current review, selection and dissemination processes in academic publishing. All Frontiers journals are driven by researchers for researchers; therefore, they constitute a service to the scholarly community. At the same time, the *Frontiers journal series* operates on a revolutionary invention, the tiered publishing system, initially addressing specific communities of scholars, and gradually climbing up to broader public understanding, thus serving the interests of the lay society, too.

Dedication to quality

Each Frontiers article is a landmark of the highest quality, thanks to genuinely collaborative interactions between authors and review editors, who include some of the world's best academicians. Research must be certified by peers before entering a stream of knowledge that may eventually reach the public - and shape society; therefore, Frontiers only applies the most rigorous and unbiased reviews. Frontiers revolutionizes research publishing by freely delivering the most outstanding research, evaluated with no bias from both the academic and social point of view. By applying the most advanced information technologies, Frontiers is catapulting scholarly publishing into a new generation.

What are Frontiers Research Topics?

Frontiers Research Topics are very popular trademarks of the *Frontiers journals series*: they are collections of at least ten articles, all centered on a particular subject. With their unique mix of varied contributions from Original Research to Review Articles, Frontiers Research Topics unify the most influential researchers, the latest key findings and historical advances in a hot research area.

Find out more on how to host your own Frontiers Research Topic or contribute to one as an author by contacting the Frontiers editorial office: frontiersin.org/about/contact

Insights in nuclear medicine: 2022

Topic editor
Giorgio Treglia — Ente Ospedaliero Cantonale (EOC), Switzerland

Citation
Treglia, G., ed. (2023). *Insights in nuclear medicine: 2022*.
Lausanne: Frontiers Media SA. doi: 10.3389/978-2-8325-3202-7

Table of contents

frontiers | Frontiers in Medicine

TYPE Editorial
PUBLISHED 26 July 2023
DOI 10.3389/fmed.2023.1259644

OPEN ACCESS

EDITED AND REVIEWED BY
Egesta Lopci,
University of Milan, Italy

*CORRESPONDENCE
Giorgio Treglia
giorgio.treglia@eoc.ch

RECEIVED 16 July 2023
ACCEPTED 18 July 2023
PUBLISHED 26 July 2023

CITATION
Treglia G (2023) Editorial: Insights in nuclear medicine: 2022. *Front. Med.* 10:1259644. doi: 10.3389/fmed.2023.1259644

Editorial: Insights in nuclear medicine: 2022

Giorgio Treglia[1,2,3]*

[1]Division of Nuclear Medicine, Imaging Institute of Southern Switzerland, Ente Ospedaliero Cantonale, Bellinzona, Switzerland, [2]Faculty of Biomedical Sciences, Università della Svizzera italiana, Lugano, Switzerland, [3]Faculty of Biology and Medicine, University of Lausanne, Lausanne, Switzerland

KEYWORDS

PET, SPECT, oncology, neurology, cardiology, internal medicine, nuclear medicine, imaging

Editorial on the Research Topic
Insights in nuclear medicine: 2022

This Research Topic includes 10 articles related to applications of nuclear medicine techniques in different fields of medicine.

Fluorine-18 fluorodeoxyglucose ([^{18}F]FDG) is the most common radiopharmaceutical used for positron emission tomography (PET) and it allows to evaluate the glucose metabolism for oncological and non-oncological indications.

Morland et al. performed a study to construct a PET model to improve lymph node assessment in patients with non-small cell lung carcinoma (NSCLC). A total of 162 NSCLC patients from two centers were included. A model combining visual assessment of lymph node status and tumor maximal standardized uptake values (SUVmax) was selected. The authors demonstrated that primary tumor SUVmax improves lymph node status prediction and could allow a better selection of NSCLC patients who are candidates for minimally invasive approaches (Morland et al.).

Beyond [^{18}F]FDG, other PET radiopharmaceuticals evaluating different metabolic pathways can be used for oncological indications as radiolabelled choline which is useful to assess the cell membrane turnover.

The study of Ghidaglia et al. assessed the influence of key histological characteristics on [^{18}F]FDG PET and [^{18}F]fluorocholine PET positivity in 62 patients with hepatocellular carcinoma (HCC). The authors clearly demonstrated that, among different key histological characteristics, [^{18}F]FDG PET and [^{18}F]fluorocholine PET positivity appear driven by both the grade and microvascular invasion components in HCC (Ghidaglia et al.).

Another article included in this collection was focused on [^{18}F]fluorocholine PET/computed tomography (PET/CT) but for a non-oncological indication. Imperiale et al. investigated the value of presurgical [^{18}F]fluorocholine PET/CT in detecting additional hyperfunctioning parathyroids despite a positive [^{99m}Tc]Tc-sestamibi parathyroid scintigraphy in 64 patients with primary hyperparathyroidism (pHPT). [^{18}F]fluorocholine PET/CT resulted more accurate and useful than [^{99m}Tc]Tc-sestamibi scintigraphy in pHPT patients with positive scintigraphic results. Positive parathyroid scintigraphy could be not satisfactory before neck surgery particularly in patients with multiglandular disease. Based on these findings, [^{18}F]fluorocholine PET/CT outperforms [^{99m}Tc]Tc-sestamibi scintigraphy in detecting hyperfunctioning parathyroid glands and its role in the diagnostic algorithm of pHPT patients should be highlighted.

Another example of non-oncological application of PET imaging is reported by a review article included in this collection which summarizes the potential role and recommendations of [^{18}F]FDG PET/CT in bacteremia or bloodstream infections. [^{18}F]FDG PET/CT should be considered in suspected complex bloodstream infections, in patients at high risk of metastatic spread, and in bloodstream infection in patients hospitalized in intensive care units. As a matter of fact, in these patients [^{18}F]FDG PET/CT has an impact on the management, treatment strategy, and outcome, mainly by directing the diagnostic process ameliorating the detection of infectious foci or by modifying treatment regimens, resulting in reduced relapse and mortality rates. Interestingly, a negative [^{18}F]FDG PET/CT has a positive prognostic value and may obviate the need for further workup in patients with bloodstream infections (Hess).

Overall, nuclear medicine imaging techniques are now widely accepted and increasingly used for diagnosis and treatment monitoring of several inflammatory and infectious diseases. An expert opinion article included in this collection written by Glaudemans and Gheysens discuss the current available guidelines on nuclear medicine imaging in infectious and inflammatory diseases, the current limitations of these imaging techniques, and future perspectives of nuclear medicine research for differentiating infection, inflammation and malignancy (Glaudemans and Gheysens).

Among the different PET tracers, radiolabelled fibroblast activation protein inhibitor (FAPI) is emerging both for oncological and non-oncological indications. A case series included in this collection suggested that FAPI PET may be useful for differentiating aseptic loosening from periprosthetic joint infection showing clear advantages over routine examinations (Wang et al.).

Somatostatin receptor PET using radiolabelled somatostatin analogs is currently used for the diagnosis of neuroendocrine tumors (NETs) due to their overexpression of somatostatin receptors. A pilot study from Weissinger et al. explored whether split renal function could be evaluated using imaging data from somatostatin receptor PET/CT performed in 25 patients with NETs prior to peptide receptor radionuclide therapy (PRRT). The authors demonstrated that static somatostatin receptor PET/CT performed at about 30 mins after radiopharmaceutical injection may be used to estimate both split renal function and absolute renal function using the accumulation index (renal parenchyma volume/SUVmean) (Weissinger et al.).

In a preclinical study included in this collection Ding et al. aimed to improve the accuracy of glomerular filtration rate measurement by using Gallium-68 Ethylenediaminetetraacetic acid ([^{68}Ga]Ga-EDTA) PET and evaluating its performance in healthy mice and murine models of renal dysfunction. Dynamic [^{68}Ga]Ga-EDTA PET provided a reliable and precise means of evaluating renal function in two murine models of renal injury, supporting the possible clinical application of this imaging technique in the near future (Ding et al.).

Beyond PET, nuclear medicine imaging includes also planar scintigraphy and single-photon emission computed tomography (SPECT) techniques which can be used in oncological and non-oncological fields.

The study of Boccalini et al. investigated the effects of manual and semi-automatic methods for assessing semi-quantitative indices in myocardial innervation imaging using iodine-123 metaiodobenzylguanidine ([^{123}I]MIBG) scintigraphy in 35 patients with idiopathic Parkinson's disease. The semi-automatic method evaluated by the authors improved the agreement among raters in classifying scintigraphic images as normal or abnormal. These findings have important implications for semi-quantitative assessment of [^{123}I]MIBG scintigraphy in clinical routine.

Nuclear medicine does not include only imaging techniques but also therapeutic applications.

Peptide receptor radionuclide therapy (PRRT) is an effective and well-tolerated treatment option for patients with NETs that prolongs progression-free survival. In their retrospective study Trautwein et al. analyzed prognostic risk factors in 62 patients with NETs treated with PRRT. The authors found that PET-based molecular tumor volume at somatostatin receptor PET and chromogranin A in combination were significant prognostic factors for long-term overall survival. Furthermore, an interim somatostatin receptor PET/CT after two cycles of PRRT had the potential in identifying non-responders who may benefit from a change in therapy at an early stage (Trautwein et al.).

In conclusion, the articles included in this Research Topic clearly highlight the bright future of nuclear medicine and radiopharmaceutical sciences.

Author contributions

GT drafted the manuscript and revised the final version. The author contributed to the article and approved the submitted version.

Conflict of interest

The author declares that the research was conducted in the absence of any commercial or financial relationships that could be construed as a potential conflict of interest.

Publisher's note

frontiers | Frontiers in Medicine

TYPE Case Report
PUBLISHED 24 November 2022
DOI 10.3389/fmed.2022.1014463

OPEN ACCESS

EDITED BY
Giorgio Treglia,
Ente Ospedaliero Cantonale (EOC), Switzerland

REVIEWED BY
Francesco Dondi,
Università degli Studi di Brescia, Italy
Edel Noriega-Álvarez,
Hospital General Universitario de Ciudad Real, Spain

*CORRESPONDENCE
Guoqiang Zhang
gqzhang301orth@163.com
Jiying Chen
chenjiying_301@163.com
Jiahe Tian
www9299sss@163.com

†These authors have contributed equally to this work and share first authorship
‡These authors have contributed equally to this work

SPECIALTY SECTION
This article was submitted to Nuclear Medicine, a section of the journal Frontiers in Medicine

RECEIVED 08 August 2022
ACCEPTED 23 August 2022
PUBLISHED 24 November 2022

CITATION
Wang Y, Wang R, Geng L, Li Q, Qi E, Shi Y, Wang Y, Zheng Q, Zhang G, Chen J and Tian J (2022) Different uptake patterns of ^{68}Ga-FAPI in aseptic loosening and periprosthetic joint infection of hip arthroplasty: A case series and literature review. *Front. Med.* 9:1014463. doi: 10.3389/fmed.2022.1014463

Different uptake patterns of ^{68}Ga-FAPI in aseptic loosening and periprosthetic joint infection of hip arthroplasty: A case series and literature review

Yiqun Wang[1,2†], Ruimin Wang[1†], Lei Geng[3,4†], Qingxiao Li[1], Erpeng Qi[5], Yuanyuan Shi[2], Yanmei Wang[6], Qingyuan Zheng[3,4], Guoqiang Zhang[3,4*‡], Jiying Chen[3,4*‡] and Jiahe Tian[1*‡]

[1]Department of Nuclear Medicine, The First Medical Centre, Chinese PLA General Hospital, Beijing, China, [2]Beijing Key Laboratory of Sports Injuries, Department of Sports Medicine, Institute of Sports Medicine of Peking University, Peking University Third Hospital, Beijing, China, [3]Department of Orthopedics Surgery, The First Medical Center, Chinese PLA General Hospital, Beijing, China, [4]Department of Orthopedics Surgery, The Fourth Medical Centre, Chinese PLA General Hospital, Beijing, China, [5]Department of Interventional Ultrasound, The First Medical Centre, Chinese PLA General Hospital, Beijing, China, [6]General Electric (GE) Healthcare China, Shanghai, China

Background: The diagnosis of a periprosthetic joint infection (PJI) is always a difficult point in research on the surgery of joints. The current diagnostic criteria include a comprehensive analysis of multiple tests; however, there are no effective visual examinations yet that can differentiate between aseptic loosening and the PJI.

Case presentation: This case report describes four patients with symptomatic total hip arthroplasty (THA), two cases of loosening and two cases of infection. Although the four cases were correctly diagnosed by the tissue culture, preoperative tests and pathological examination could not effectively distinguish an infection from a non-infection. Based on a preclinical study and theoretical feasibility, gallium-68 (^{68}Ga)-labeled fibroblast activation protein inhibitor positron emission tomography/computed tomography (^{68}Ga-FAPI PET/CT) was performed. Through ^{68}Ga-FAPI PET/CT scanning, not only were the causes diagnosed correctly but the lesions were also located.

Conclusion: When the lesion is located between the bone and the prosthesis, ^{68}Ga-FAPI PET/CT could differentiate aseptic loosening from periprosthetic joint infection (PJI). ^{68}Ga-FAPI PET/CT has clear advantages over routine examinations and has a prospective application in detecting PJI.

KEYWORDS

^{68}Ga-FAPI, PET/CT, hip, arthroplasty, image analysis, case report

Introduction

Periprosthetic joint infection (PJI) is one of the most devastating complications in total joint arthroplasty. The incidence of PJI varies from 1 to 15% and places a heavy burden on patients and their families and the health system (1, 2).

Prompt and correct diagnosis is the premise of any effective treatment. Neither the Musculoskeletal Infection Society (MSIS) criteria proposed in 2011 (3) nor the

International Consensus Group (International Consensus Meeting (ICM)) criteria developed in 2018 (4) are effective in the diagnosis of PJI, and the diagnosis does not rely on a single test. However, it should be noted that nuclear medicine-related examinations are rarely included in any of the diagnostic criteria.

Gallium-68 (^{68}Ga)-labeled fibroblast activation protein inhibitor ^{68}Ga-FAPI) is one of the radionuclides that is currently of great interest (5, 6).

Fibroblast activation protein (FAP) is mainly secreted by activated fibroblasts and plays an important role in inflammation, infection, and immunity (7). A literature review reported that a fibrous membrane is produced by the loosening of prosthesis (8) and that all typical signs of infection, such as granulomas and fibrosis, have fibroblast expression. Therefore, theoretically, ^{68}Ga-FAPI has the potential for aseptic loosening and PJI imaging. In our previous animal studies (9, 10), ^{68}Ga-FAPI, compared with 18F-fluorodeoxyglucose (^{18}F-FDG), has clear advantages, including no uptake of muscles and the intestine, showing a wide range of lesions and a higher sensitivity to disease detection. Although the performance characteristics of the loosening model and the infection model are totally different, the maximum standardized uptake value (SUVmax) alone cannot effectively distinguish between the models of loosening and infection, so speculating the e performance characteristics of ^{68}Ga-FAPI in clinical cases is crucial.

In this study, four typical cases, including aseptic loosening of the acetabular cup, PJI of the acetabular cup, aseptic loosening of the femoral stem, and PJI of the femoral stem and acetabular cup, are presented. Using the ^{68}Ga-FAPI PET/CT [gallium-68 (^{68}Ga)-labeled fibroblast activation protein inhibitor positron emission tomography/computed tomography] not only confirmed the final diagnosis but also helped determine the location and extent of the lesions.

Case series

This case series report was approved by the Institutional Review Board of the Chinese People's Liberation Army General Hospital and followed CARE (Case Report) guidelines (Supplementary Figure). Cases were identified in our department between January and February 2021. Written, informed consent forms and permission to use patient data for scientific purposes were obtained at the time of patient's examination. The final diagnosis was based on the ICM criteria in 2018.

Case 1: Aseptic loosening of the acetabular cup

A 60-year-old female patient complained of left hip pain for ∼2 years. She had cemented total hip arthroplasty (THA) for 9 years. Her serological and synovial tests were normal (Table 1). X-ray and ^{68}Ga-FAPI PET/CT were performed (Figure 1). The x-ray results showed osteolysis around the acetabular cup, and PET/CT scan images showed moderate uptake around the periacetabular cup and the proximal femoral stem. This case was diagnosed as an aseptic loosening, and the acetabular cup was easily removed during the operation. Pathology and tissue culture were all negative.

Case 2: PJI of the acetabular cup

A 60-year-old male patient presented to our orthopedic center due to failure of THA. He had a cementless THA 9 months ago. However, because of the wrong implant size, the patient began to complain of pain in the left hip immediately after surgery. There were no visible abnormalities on the preoperative examinations. The x-ray results showed a slightly smaller prosthesis, and ^{68}Ga-FAPI PET/CT showed high-intensity uptake along the entire acetabular cup, which was totally different from the first case. This uptake pattern was believed to be indicative of PJI. Given the preoperative diagnosis and patient's history, one-stage reconstruction was chosen. However, the pathology revealed more than 20 neutrophils in 10 high-power fields on the frozen section slides, and the tissue culture revealed a mixed infection of *Acinetobacter baumannii* and *Staphylococcus epidermidis*. Therefore, the final diagnosis of this patient was PJI.

Case 3: Aseptic loosening of the femoral stem

A 76-year-old male patient complained of left hip pain for 3 years. He had a THA 20 years ago, and serological results were normal, except for interleukin 6 (IL-6) (Table 1). No clear finding was discovered on x-ray. ^{68}Ga-FAPI PET/CT showed moderate uptake along the entire femoral stem (Figure 1). This case was diagnosed as aseptic loosening; meanwhile, the pathology results were positive, and the tissue culture was negative.

Case 4: PJI of the femoral stem and the acetabular cup

A 68-year-old male patient was admitted to our orthopedic center due to persistent right hip pain for ∼3 years. He underwent primary THA 13 years ago, and after 3 years, the patient underwent revision surgery for aseptic loosening. The patient was diagnosed with an iliac fossa abscess 1 year ago, and a blood culture revealed the presence of *Klebsiella pneumoniae*.

TABLE 1 Results of examinations.

Test	WBC (10^9/L)	CRP (mg/dl)	D-dimer (μg/ml)	ESR (mm/h)	IL-6 (pg/ml)	Synovial WBC	Synovial PMN (%)	Pathology	SUVmax
Case 1	5.88	0.05	3.6	16	2.55	0.112	55	–	6.6
Case 2	9	0.515	4	25	1.5	/	/	+	13.31
Case 3	5.65	0.05	0.5	13	8.6	/	/	+	8.55
Case 4	5.63	1.967	0.9	28	13.3	7	72	+	20.08

Normal range of examinations: WBC < 10, CRP < 1, D-dimer < 0.86, ESR < 30, IL-6 < 1.5, Synovial WBC < 3, Synovial PMN% < 80.
WBC, white blood cells; CRP, C-reactive protein; ESR, erythrocyte sedimentation rate; IL-6, interleukin 6; PMN%: polymorphonuclear leukocytes; SUVmax, maximum standard unit value.

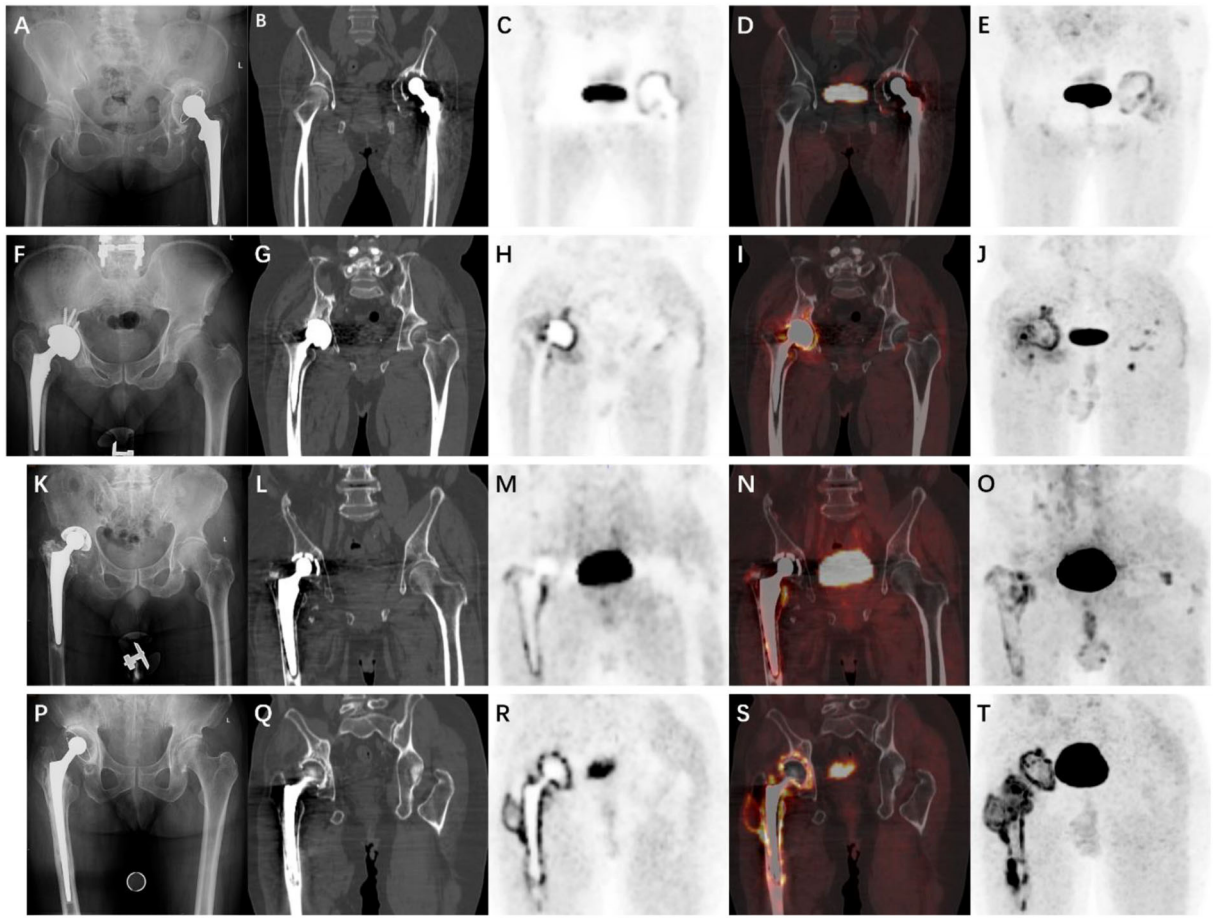

FIGURE 1
X-ray and ^{68}Ga-FAPI PET/CT [gallium-68 (^{68}Ga)-labeled fibroblast activation protein inhibitor positron emission tomography/computed tomography] images of each patient. **(A–E)** Case 1. **(F–J)** Case 2. **(K–O)** Case 3. **(P–T)** Case 4. First column: X-rays. Second column: Computed tomography (CT) images. Third column: Positron emission tomography (PET) images. Fourth column: Fusion images. Fifth column: Maximum intensity projection (MIP).

Recently, the patient's hip joint symptoms worsened, and serological results showed elevated C-reactive protein (CRP) and IL-6 and synovial white blood cell (WBC) counts were also elevated (Table 1). X-ray, triple-phase bone scintigraphy, and ^{68}Ga-FAPI PET/CT were also performed. The x-ray results were inconclusive, and PET/CT showed intense uptake around the entire acetabular cup and the femoral stem (Figure 1). For triple-phase bone scintigraphy, although the uptake in the late phase was not strong, the three phases were all positive (Figure 2), which was indicative of infection. Intraoperative

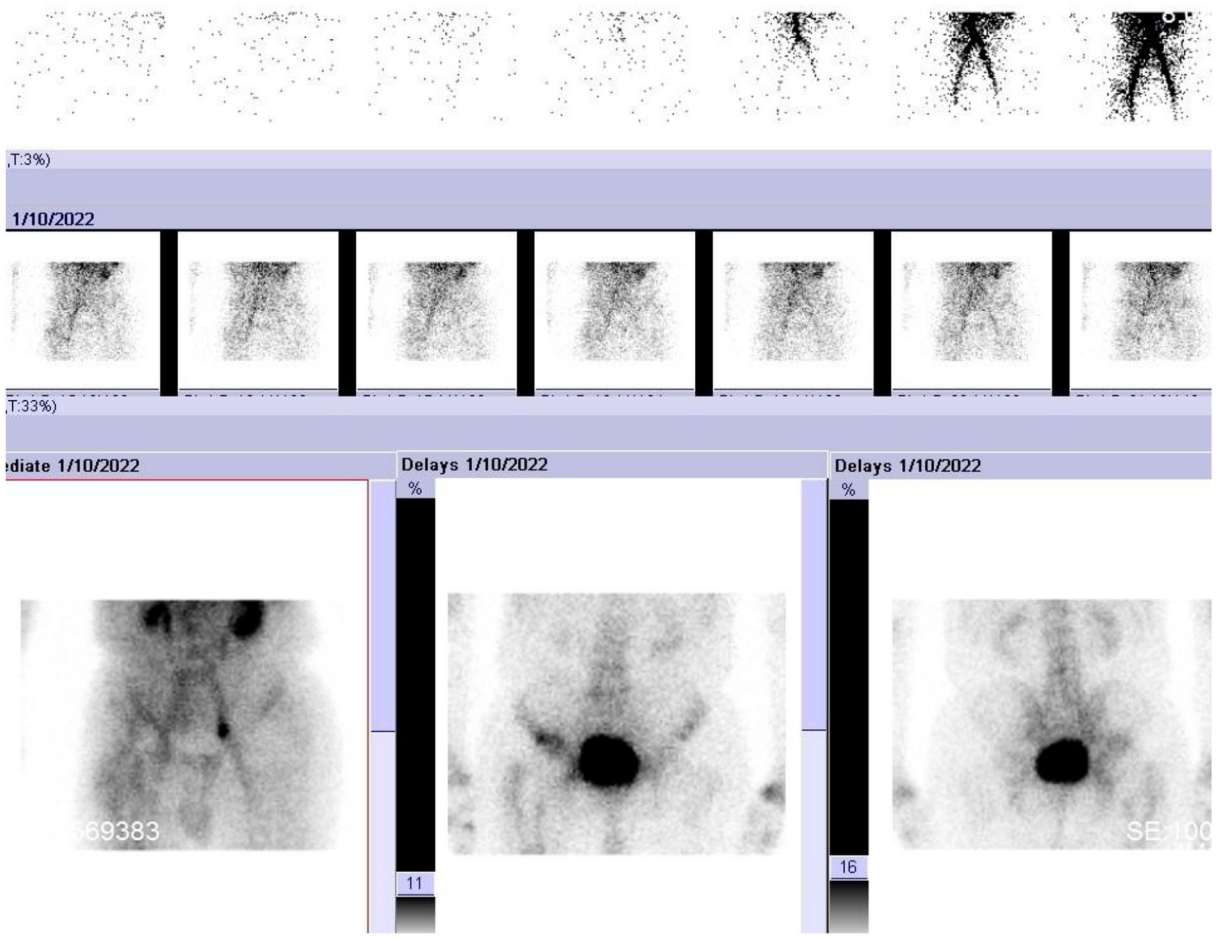

FIGURE 2
Triple-phase bone scanning of Case 4.

pathology showed 5–10 neutrophils in 10 high-power fields, and a two-stage reconstruction was chosen. The pathogen was identified as *Klebsiella pneumoniae* by intraoperative tissue culture.

Discussion

In 2011, the Musculoskeletal Infection Society (MSIS) proposed the diagnostic criteria for PJI (3). Since then, the American Academy of Orthopedic Surgeons (AAOS), the Infectious Diseases Society of America (IDSA), the European Bone and Joint Society (EBJIS), and the International Consensus Meeting on Periprosthetic Joint Infection have also developed their criteria for PJI. Currently, the diagnosis of PJI is becoming increasingly mature and standard, and it no longer depends on a single test, but many researchers are also looking forward to finding a more accurate and even perfect examination. What are the advantages and disadvantages of commonly used tests in clinical practice?

Erythrocyte sedimentation rate (ESR) and C-reactive protein (CRP) are the most commonly used serological tests, which are economical and quick to obtain results. However, their specificity is not ideal, as underlying inflammatory joint diseases can also lead to elevated outcomes. In addition, their thresholds are different in different reports. Another point to note is that serological tests depend on the host's response to pathogens. For low-toxic, latent bacterial infection, serological tests may increase the probability of false negatives, and for patients with other diseases, such as pneumonia, erysipelas, cellulitis, and tumors, serological tests are likely to increase the possibility of false positives.

The synovial fluid analysis mainly consisted of WBC count, leukocyte esterase (LE)%, and polymorphonuclear leukocyte (PMN)%. WBC count and PMN% are considered to be highly sensitive and specific for PJI diagnosis; however, no clear

thresholds are given in either MSIS or in IDSA diagnostic criteria, and the threshold varies greatly among different reports (11). The reasons attributed to the difference in the threshold values are thought to be as follows: (1) joint hematoma or postoperative inflammatory reaction will lead to a change in the threshold; (2) many studies exclude inflammatory joint disease, leading to unreliable results; and (3) metal-on-metal hip arthroplasty may lead to false positives. LE was originally used to detect urinary tract infections (UTIs) and was proposed for the diagnosis of PJI in ∼2010. However, in the LE study, many cases were excluded due to excessive blood and debris in the articular fluid or vague results, which in turn also led to unreliable results (11).

The advantage of histopathology is that it is not affected by preoperative antibiotics. Using intraoperative freezing can help obtain the results in the operating room and guide treatment. However, its accuracy depends on the experience of pathologists, and some bacteria may not cause sustained neutrophil infiltration. In addition, although the most commonly used criterion is a mean of five or more polymorphonuclear leukocytes (PMN%) seen in five high-power fields, the standards reported are not uniform (12). In addition, some scholars proposed the classification according to the periprosthetic interface membrane, including wear particle-induced type, infectious type, combined type, and indeterminate type. This classification is not as widely used as the previous one, but it suggested that the presence of infection was not merely neutrophil infiltration and that neutrophil infiltration is not necessarily an infection (8).

Tissue culture is a useful test, but obtaining only a single specimen reduces the sensitivity of the test and makes it difficult to interpret contamination. The current standard is to take five specimens during the operation, and two positive cultures of the same organism are defined as PJI. If only one is positive, then other tests need to be combined (3, 4). However, when the infection is located between the bone and the prosthesis or in the biofilm, this method becomes inadequate. Therefore, some scholars use sonication of the removed prostheses to diagnose infection. This method uses colony-forming units per milliliter (CFU/ml) for diagnosis. Although most of the results calculated from the receiver operating characteristic (ROC) curve were satisfactory, the threshold of CFU/ml reported varied from 1 to 200 (13). Moreover, the process of sonication requires many steps, and the standards of different institutions are not uniform, which increase the uncertainty and unreliability of the results. In addition, sonication also requires tissue culture, and the choice of culture medium and culture days can also influence the results.

Through the analysis of the commonly used tests, we found that, regardless of the serological test, synovial analysis, or tissue culture, they all have an insurmountable defect, namely, the inability to locate infections, and in clinical practice, the determination of the infection boundary is usually dependent on experience. At present, there are many reports describing approximately 1.5-stage or partial two-stage reconstruction (14, 15), in which the infected part is exchanged and the normal part is not treated. Although these methods could reduce the trauma of the operation and the burden of medical treatment, there is no suitable test that can be used as the basis for these treatments.

From triple-phase bone scintigraphy, which has been used for the longest time, to the radiolabelled leukocytes, known as the "gold standard" imaging technique for PJI, and to ^{18}F-FDG, which is the most widely used radionuclide in the clinic, scholars have never stopped their attempts to make an imaging diagnosis of PJI, and the results of the same tests are inconsistent, and each examination has limitations that cannot be overcome. For example, the limitations of single-photon emission computerized tomography (SPECT/CT) include high radiation dose, long examination time, and unsatisfactory resolution, while in our previous report, the imaging of the blood vessels, the intestines, and the muscles of ^{18}F-FDG has a certain influence on diagnosis, and ^{18}F-FDG cannot reflect the situation of soft tissue remodeling, as some cases had nonspecific uptake for years after surgery. PET/CT itself has certain advantages, but a more specific radionuclide is needed. Based on our previous animal experiments and theoretical feasibility, ^{68}Ga-FAPI was selected in this study (9, 10, 16).

Regarding the classification proposed by Reinartz et al. (17), based on the ^{18}F-FDG uptake pattern, our previous report noted a deficiency in this classification, namely, the absence of an infection between the bone and the prosthesis. In this report, ^{68}Ga-FAPI showed a completely different uptake pattern in aseptic loosening and PJI. For aseptic loosening, the uptake pattern is mainly characterized by low-intensity linear uptake between the bone and the prosthesis, while the uptake pattern of PJI is characterized by high-intensity diffuse uptake. Through the literature review, this is the first report that demonstrated the different manifestations of loosening and infection on PET/CT of the acetabular cup and the femoral stem.

Meanwhile, this report has several limitations. First, only four cases are presented here, and a large number of cohort studies are warranted to verify this diagnostic criterion based on the uptake pattern. Second, all the patients had a gap of at least 6 months between THA and PET/CT scans, and whether the early period after THA influences ^{68}Ga-FAPI results is also worth researching.

Conclusions

In this study, we reported four symptomatic patients with THA. Compared with routine tests, ^{68}Ga-FAPI PET/CT not only diagnosed correctly but also determined the location and extent

of the lesion. This advantage is of great implication for 1.5-stage or partial two-stage reconstruction. Although related studies are warranted, ^{68}Ga-FAPI has shown an important application value in PJI diagnosis.

Data availability statement

The original contributions presented in the study are included in the article/Supplementary material, further inquiries can be directed to the corresponding author/s.

Ethics statement

The studies involving human participants were reviewed and approved by institutional review board of Chinese People's Liberation Army General Hospital. The patients/participants provided their written informed consent to participate in this study. Written informed consent was obtained from the individual(s) for the publication of any potentially identifiable images or data included in this article.

Author contributions

YiW, RW, and LG wrote the original draft. YS, YaW, and QZ collected and interpreted the data. QL and EQ designed the project. GZ, JC, and JT reviewed and edited the draft. All authors contributed to the article and approved the submitted version.

Conflict of interest

The authors declare that the research was conducted in the absence of any commercial or financial relationships that could be construed as a potential conflict of interest.

Publisher's note

All claims expressed in this article are solely those of the authors and do not necessarily represent those of their affiliated organizations, or those of the publisher, the editors and the reviewers. Any product that may be evaluated in this article, or claim that may be made by its manufacturer, is not guaranteed or endorsed by the publisher.

Supplementary material

The Supplementary Material for this article can be found online at: https://www.frontiersin.org/articles/10.3389/fmed.2022.1014463/full#supplementary-material

References

1. Li R, Song L, Quan Q, Liu MW, Chai W, Lu Q, et al. Detecting periprosthetic joint infection by using mass spectrometry. *J Bone Joint Surg Am Vol.* (2021) 103:1917–26. doi: 10.2106/JBJS.20.01944

2. Qu PF, Li R, Xu C, Chai W, Li H, Fu J, et al. A clinical pilot study to evaluate CD64 expression on blood monocytes as an indicator of periprosthetic joint infection. *J Bone Joint Surg Am Vol.* (2020) 102:e99. doi: 10.2106/JBJS.20.00057

3. Parvizi J, Zmistowski B, Berbari EF, Bauer TW, Springer BD, Della Valle CJ, et al. New definition for periprosthetic joint infection: from the Workgroup of the Musculoskeletal Infection Society. *Clin Orthop Relat Res.* (2011) 469:2992–4. doi: 10.1007/s11999-011-2102-9

4. Parvizi J, Tan TL, Goswami K, Higuera C, Della Valle C, Chen AF et al. The 2018 definition of periprosthetic hip and knee infection: an evidence-based and validated criteria. *J Arthroplast*. (2018) 33:1309–14. doi: 10.1016/j.arth.2018.02.078

5. Lan L, Zhang S, Xu T, Liu H, Wang W, Feng Y, et al. Prospective comparison of (68)Ga-FAPI vs. (18)F-FDG PET/CT for tumor staging in biliary tract cancers. *Radiology*. (2022) 17:213118. doi: 10.1148/radiol.213118

6. Jacobson FL, Van den Abbeele AD. Importance of (68)Ga-FAPI PET/CT for detection of cancer. *Radiology.* (2022) 303:200–1. doi: 10.1148/radiol.212884

7. Buechler MB, Fu W, Turley SJ. Fibroblast-macrophage reciprocal interactions in health, fibrosis, and cancer. *Immunity.* (2021) 54:903–15. doi: 10.1016/j.immuni.2021.04.021

8. Morawietz L, Classen RA, Schröder JH, Dynybil C, Perka C, Skwara A, et al. Proposal for a histopathological consensus classification of the periprosthetic interface membrane. *J Clin Pathol.* (2006) 59:591–7. doi: 10.1136/jcp.2005.027458

9. Wang Y, Li Y, Han L, Wang J, Zhang C, Qi E, et al. (18)F-FDG and (68) Ga-FAPI PET/CT for the evaluation of periprosthetic joint infection and aseptic loosening in rabbit models. *BMC Musculoskeletal Disord.* (2022) 23:592. doi: 10.1186/s12891-022-05537-w

10. Wang Y, Liu H, Yao S, Guan Z, Li Q, Qi E, et al. Using 18F-flurodeoxyglucose and 68Ga-fibroblast activation protein inhibitor PET/CT to evaluate a new periprosthetic joint infection model of rabbit due to Staphylococcus aureus. *Nucl Med Commun.* (2022) 43:232–41. doi: 10.1097/MNM.0000000000001495

11. Osmon DR, Berbari EF, Berendt AR, Lew D, Zimmerli W, Steckelberg JM, et al. Diagnosis and management of prosthetic joint infection: clinical practice guidelines by the infectious diseases society of America. *Clin Infect Dis Off Pub Infect Dis Soc Am.* (2013) 56:e1–e25. doi: 10.1093/cid/cis966

12. Bori G, Soriano A, García S, Gallart X, Mallofre C, Mensa J. Neutrophils in frozen section and type of microorganism isolated at the time of resection arthroplasty for the treatment of infection. *Arch Orthop Trauma Surg.* (2009) 129:591–5. doi: 10.1007/s00402-008-0679-6

13. Tande AJ, Patel R. Prosthetic joint infection. *Clin Microbiol Rev.* (2014) 27:302–45. doi: 10.1128/CMR.00111-13

14. Fukui K, Kaneuji A, Ueda S, Matsumoto T. Should well-fixed uncemented femoral components be revised in infected hip arthroplasty? Report of five trial cases. *J Orthopaed.* (2016) 13:437–42. doi: 10.1016/j.jor.2015.09.006

15. Hernandez NM, Buchanan MW, Seyler TM, Wellman SS, Seidelman J, Jiranek WA. 1.5-stage exchange arthroplasty for total knee arthroplasty periprosthetic joint infections. *J Aarthroplasty.* (2021) 36:1114–9. doi: 10.1016/j.arth.2020.09.048

16. Dondi F, Albano D, Treglia G, Bertagna F. Emerging role of FAPI PET imaging for the assessment of benign bone and joint diseases. *J Clin Med.* (2022) 11:4514. doi: 10.3390/jcm11154514

17. Reinartz P, Mumme T, Hermanns B, Cremerius U, Wirtz DC, Schaefer WM, et al. Radionuclide imaging of the painful hip arthroplasty: positron-emission tomography versus triple-phase bone scanning. *J Bone Joint Surg Br Vol.* (2005) 87:465–70. doi: 10.1302/0301-620X.87B4.14954

frontiers | Frontiers in Medicine

TYPE Brief Research Report
PUBLISHED 02 December 2022
DOI 10.3389/fmed.2022.1073720

OPEN ACCESS

EDITED BY
Giorgio Treglia,
Ente Ospedaliero Cantonale (EOC), Switzerland

REVIEWED BY
Alberto Miceli,
Università di Genova, Italy
Agostino Chiaravalloti,
University of Rome Tor Vergata, Italy

*CORRESPONDENCE
Valentina Garibotto
valentina.garibotto@hcuge.ch

†These authors have contributed equally to this work

SPECIALTY SECTION
This article was submitted to Nuclear Medicine, a section of the journal Frontiers in Medicine

RECEIVED 18 October 2022
ACCEPTED 17 November 2022
PUBLISHED 02 December 2022

CITATION
Boccalini C, Carli G, Vanoli EG, Cocco A, Albanese A, Garibotto V and Perani D (2022) Manual and semi-automated approaches to MIBG myocardial scintigraphy in patients with Parkinson's disease. *Front. Med.* 9:1073720. doi: 10.3389/fmed.2022.1073720

Manual and semi-automated approaches to MIBG myocardial scintigraphy in patients with Parkinson's disease

Cecilia Boccalini[1,2,3†], Giulia Carli[2,4†], Emilia Giovanna Vanoli[5], Antoniangela Cocco[6], Alberto Albanese[6,7], Valentina Garibotto[3,8,9*] and Daniela Perani[1,2,5]

[1]School of Psychology, Vita-Salute San Raffaele University, Milan, Italy, [2]*In vivo* Human Molecular and Structural Neuroimaging Unit, Division of Neuroscience, Scientific Institute for Research, Hospitalization and Healthcare (IRCCS) San Raffaele Scientific Institute, Milan, Italy, [3]Laboratory of Neuroimaging and Innovative Molecular Tracers (NIMTlab), Geneva University Neurocenter and Faculty of Medicine, University of Geneva, Geneva, Switzerland, [4]Department of Nuclear Medicine and Molecular Imaging, University of Groningen, University Medical Center Groningen, Groningen, Netherlands, [5]Nuclear Medicine Unit, San Raffaele Hospital, Milan, Italy, [6]Department of Neurology, Scientific Institute for Research, Hospitalization and Healthcare (IRCCS) Humanitas Research Hospital, Milan, Italy, [7]Department of Neuroscience, Catholic University, Milan, Italy, [8]Division of Nuclear Medicine and Molecular Imaging, Geneva University Hospitals, Geneva, Switzerland, [9]Center for Biomedical Imaging, Geneva, Switzerland

Objective: This study investigates the effects of manual and semi-automatic methods for assessing MIBG semi-quantitative indices in a clinical setting.

Materials and methods: We included ^{123}I-MIBG scans obtained in 35 patients with idiopathic Parkinson's Disease. Early and late heart-to-mediastinum (H/M) ratios were calculated from ^{123}I-MIBG images using regions of interest (ROIs) placed over the heart and the mediastinum. The ROIs were derived using two approaches: (i) manually drawn and (ii) semi-automatic fixed-size ROIs using anatomical landmarks. Expert, moderate-expert, and not expert raters applied the ROIs procedures and interpreted the ^{123}I-MIBG images. We evaluated the inter and intra-rater agreements in assessing ^{123}I-MIBG H/M ratios.

Results: A moderate agreement in the raters' classification of pathological and non-pathological scores emerged regarding early and late H/M ratio values (κ = 0.45 and 0.69 respectively), applying the manual method, while the early and late H/M ratios obtained with the semi-automatic method reached a good agreement among observers (κ = 0.78). Cohen-Kappa values revealed that the semi-automatic method improved the agreement between expert and inexpert raters: the agreement improved from a minimum of 0.29 (fair, for early H/M) and 0.69 (substantial, in late H/M) with the manual method, to 0.90 (perfect, in early H/M) and 0.87 (perfect, in late H/M) with the semi-automatic method.

Conclusion: The use of the semi-automatic method improves the agreement among raters in classifying' H/M ratios as pathological or non-pathological, namely for inexpert readers. These results have important implications for semi-quantitative assessment of ^{123}I-MIBG images in clinical routine.

KEYWORDS

Parkinson's disease, MIBG scintigraphy, H/M ratios, manual-drawing approach, semi-automatic fixed-size ROIs

Introduction

Parkinson's disease (PD) and parkinsonisms are a spectrum of multisystem neurodegenerative diseases characterised by early involvement of the autonomic and enteric nervous systems (1). PD-related neuropathology (α-synuclein aggregates) is not restricted to the central nervous system but affects several organs and tissues (2, 3). The denervation of the autonomic nervous system can be assessed by ^{123}I-metaiodobenzylguanidine (MIBG) scintigraphy (4), which can be clinically helpful as a supportive diagnostic tool (5). ^{123}I-MIBG, a norepinephrine analogue (6), is taken up into the presynaptic cardiac sympathetic nerves by the norepinephrine uptake-1 transporter, and the amount of ^{123}I-MIBG retention over several hours after administration reflects neuronal integrity (7). Thus, ^{123}I-MIBG cardiac scintigraphy measures the postganglionic presynaptic cardiac sympathetic nerve endings of the noradrenergic nervous system. It was developed for the assessment of heart diseases (8). Subsequently, cardiac ^{123}I-MIBG scintigraphy was clinically applied in the PD spectrum, showing a reduced cardiac uptake in the vast majority of patients (9), representing a sensitive test for this clinical condition. Therefore, positive results at ^{123}I-MIBG scintigraphy are considered a supportive biomarker for PD detection (5) and differential diagnosis (10). ^{123}I-MIBG scintigraphy can accurately distinguish Lewy Bodies (LB) related disorders [i.e., PD, Dementia with LB (DLB)] and non-LB related disorders (e.g., Alzheimer's disease and progressive supranuclear palsy) (10).

The most used quantitative measurements of ^{123}I-MIBG uptake are the heart-to-mediastinum (H/M) ratios calculated from early (15 min) and late (3–4 h) ^{123}I-MIBG static planar images. The method used to obtain these parameters is mainly based on manually drawing cardiac regions of interest (ROIs). However, the position and size of the cardiac ROI, as well as the level of experience in drawing the ROIs on the planar ^{123}I-MIBG images, might affect the final H/M ratio measures.

The effects of different methods to assess ^{123}I-MIBG parameters for clinical interpretation should be carefully considered (11, 12). Therefore, this study aimed to compare two different methods assessing the H/M ratios in a series of PD patients, (i) the typical manual-drawing method and (ii) the fixed-size ROIs approach following Veltman's guidelines for the standardisation of ^{123}I-MIBG parameters. Veltman et al. (13) demonstrated good reproducibility of fixed-size mediastinal and cardiac ROIs in assessing H/M ratios in patients with heart failure; here, we wanted to extend these findings in PD. ^{123}I-MIBG images of 35 PD patients were analysed by highly expert, moderate-expert, and inexpert raters. We evaluated the influences of cardiac ROI size and position and the impact of raters' experience on assessing the H/M ratios.

Methods

Participants

The study included 35 patients fulfilling the PD clinical diagnostic criteria (5). All participants gave their written informed consent to the experimental procedure, as approved by the Ethical Committees of Scientific Institute for Research, Hospitalization and Healthcare (IRCCS) San Raffaele Hospital. The protocol conformed to the ethical standards of the Declaration of Helsinki for the protection of human subjects.

^{123}I-metaiodobenzylguanidine scintigraphy data acquisition

^{123}I-MIBG myocardial scintigraphy was performed at the Nuclear Medicine Unit, San Raffaele Hospital, using (NM/CT 670, Milwaukee, WI, United States) manufactured by GE Healthcare medical systems, according to the standard procedure (13). All patients have suspended medication and stopped eating any food that could influence ^{123}I-MIBG myocardial uptake (14). A total of 111 MBq of ^{123}I-MIBG was injected intravenously. ^{123}I-MIBG planar images were obtained with a gamma camera in two temporal windows: 15 min after the injection (early-image) and 4 h after the injection (delayed-image). Static planar imaging was obtained with 256 × 256 matrix. Only planar images in thoracic anterior view were used for quantitative evaluation. All camera heads were equipped with low-energy high-resolution collimators and all images

were acquired with a 15% energy window centred at the 159 keV photopeak of ^{123}I. The image acquisition time was approximately 5 min. All planar images were analysed using Xeleris (Discovery NM/CT 670, GE Healthcare, Milwaukee, WI, United States) and PMOD software (PMOD Technologies Ltd.), for manual and semi-automatic methods respectively.

^{123}I-metaiodobenzylguanidine scintigraphy planar image analyses

Early and late H/M ratios were calculated from ^{123}I-MIBG planar images using ROIs placed over the heart and the upper mediastinum. The ROIs were derived using two different approaches: manually drawn ROIs and semi-automatic fixed-size ROIs. In the first approach, a rectangular mediastinal ROI has been used with unspecified size. The cardiac ROI was a polygonal manually drawn ROI including the myocardium and the left ventricular cavity (**Figure 1A**). The manual method was performed on a Xeleris workstation, following the recommendations described in the proposal for standardisation by Flotats et al. (14).

For the semi-automatic method, we followed the guidelines of Veltman et al. (13) (**Figure 1B**). An "anatomical landmark square" was formed by the lung apexes (upper square border), the upper cardiac border (lower square border), and the medial contours of the lungs (medial square borders) to place fixed-size mediastinum and oval cardiac ROIs. Precisely, a fixed-size rectangular mediastinal ROI (13 × 20 pixel) and an oval cardiac ROI (60 × 70 pixel) were placed on ^{123}I-MIBG planar images. The mediastinal ROI was placed in the half of the "anatomical landmark square" formed by lungs apexes, the upper cardiac border, and the medial contours of the lung. The cardiac oval ROI was placed in the lower-right quadrant, over the myocardium, including the left ventricular cavity. The use of fixed-size ROI, which the operators only need to move according to the anatomical landmark square, gives partial automation to the method. This semiautomatic method was processed using the PMOD software.

Three raters (expert, moderately-expert, and not expert) analysed the ^{123}I-MIBG images using both procedures. Of note, the inexpert rater followed a brief training (2 h) for the manual drawing analysis. The other raters were experienced in the analysis of ^{123}I-MIBG myocardial scintigraphy, with mean more than 5 and 10 years of experience, respectively. Anonymised data were analysed in a random order to avoid bias by order effects.

Statistical analyses

The intra- and inter-rater agreements were tested to assess the reproducibility of the measured H/M ratios.

The inter-rater agreements

The intraclass correlation coefficients (ICC) were used to assess agreement among independent raters, considering the H/M ratios as a continuous variable. ICC values < 0.5, between

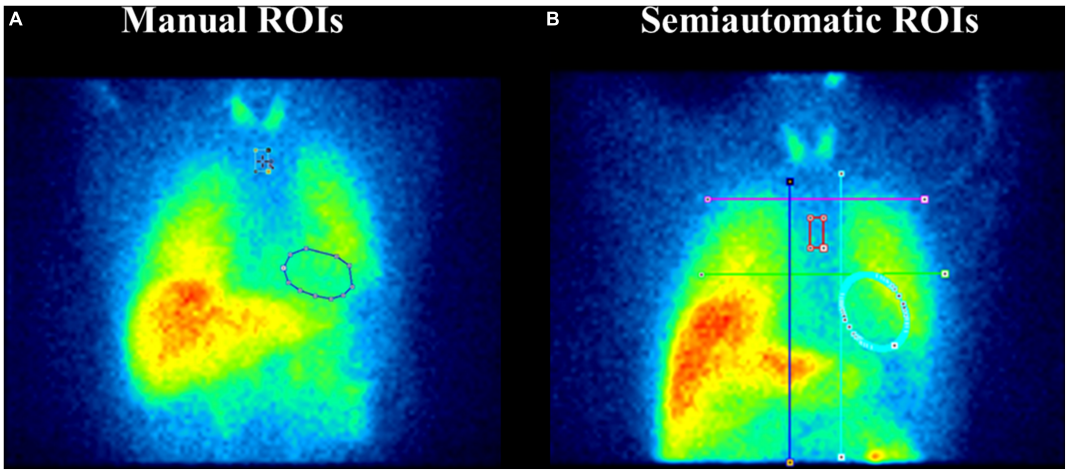

FIGURE 1
Manual and fixed-size regions of interest (ROIs) on planar ^{123}I-metaiodobenzylguanidine (MIBG) images. Panel **(A)** depicts the manual ROIs method. A rectangular mediastinal ROI is used with unspecified size and located on planar MIBG images below the thyroid. The manual-drawn cardiac ROI is polygonal and includes the myocardium and the left ventricular cavity. Panel **(B)** represents the semi-automatic ROIs method. An "anatomical landmark square" is formed by the lung apexes (upper square border), the upper cardiac border (lower square border), and the medial contours of the lungs (medial square borders) to place fixed-size mediastinum and oval cardiac ROIs. Precisely, a fixed-size rectangular mediastinal ROI (13 × 20 pixel) and an oval cardiac ROI are placed on MIBG planar images. The mediastinal ROI is placed in the half of the "anatomical landmark square" formed by lungs apexes, the upper cardiac border, and the medial contours of the lung. The cardiac oval ROI (60 × 70 pixel) is placed in the lower-right quadrant, over the myocardium, including the left ventricular cavity.

0.5 and 0.75, between 0.75 and 0.9, and greater than 0.90 are indicative of poor, moderate, good, and excellent reliability, respectively (15).

We applied previously published cut-off for pathological scans (<1.9 early ratios and <1.7 late ratios) to classify the H/M ratios into mutually exclusive categories (pathological and not) (16). Following this categorisation, we calculated the Fleiss' kappa, κ to measure the inter-rater agreement between the raters (17, 18). The following classification was suggested for assessing the strength of agreement: $\kappa < 0.20$ poor, 0.21–0.40 fair, 0.41–0.60 moderate, 0.61–0.80 good, and 0.81–1.00 very good (19). Last, Cohen's Kappa was also used to measure the agreement between two raters after classifying the H/M ratios as pathological or not. Cohen's Kappa values 0.01–0.20, 0.21–0.40, 0.41–0.60, 0.61–0.80, and 0.81–1.00 were considered slight, fair, moderate, substantial, and perfect agreement, respectively (20). A Chi-square test was run to test differences in the proportion of patients classified as pathological or not by different raters.

The intra-rater agreements

The correlations between the H/M ratios obtained with the two methods by each rater were analysed by the Spearman correlation coefficients. The significance level was $p < 0.001$.

All statistical analyses were performed using the SPSS software package, version 26.0 (SPSS, Chicago, IL, United States).

Results

A total of 35 PD patients [63.66 ± 9.74 years of age, 27 (77%) men] were included in the study. Table 1 reported the number of PD patients that fell into the category of "pathological sympathetic innervation," according to the cut-off value of early and late H/M ratios, obtained with manual approach and semi-automatic approach for the three raters.

The inter-rater agreements results

The raters showed excellent reliability measured by ICC in both methods (i.e., manual and semi-automatic) (Table 1). Of note, the agreement among raters tends to be higher in the semi-automatic procedure (ICC = 0.95 and ICC = 0.97, early and delayed H/M ratio, respectively) compared to the manual one (ICC = 0.94 and ICC = 0.95, early and delayed H/M ratio, respectively) (Table 1).

Fleiss' kappa showed a moderate agreement in the raters' classification of normal and pathological scores regarding early H/M ratio values ($\kappa = 0.45$, $p < 0.0005$) by using the manual method. Instead, the agreement was good when the early H/M ratio was obtained with the semi-automatic method ($\kappa = 0.78$). Similarly, the late H/M ratios showed increased raters compliance moving from manual ($\kappa = 0.69$) to semi-automatic approaches ($\kappa = 0.78$). Of note, with the semi-automatic method, fewer PD patients fell under the category "non-pathological" for

TABLE 1 Inter and intra-rater indices on ^{123}I-metaiodobenzylguanidine (MIBG) parameters.

	Early H/M ratio		Delayed H/M ratio	
	Manual method	**Semi-automatic method**	**Manual method**	**Semi-automatic method**
Inter-raters analysis				
Continue values				
Expert (1)	1.49 ± 0.27	1.59 ± 0.27	1.41 ± 0.37	1.51 ± 0.35
Moderate- expert (2)	1.54 ± 0.28	1.53 ± 0.26	1.46 ± 0.35	1.44 ± 0.33
Inexpert (3)	1.65 ± 0.32	1.62 ± 0.28	1.56 ± 0.40	1.51 ± 0.36
ICC (95% CI)	0.94 (0.80–0.97)	0.95 (0.90–0.97)	0.95 (0.89–0.97)	0.97 (0.95–0.98)
Categorical values (*n* pathological/35)				
Expert (1)	32	28	24	20
Moderate-expert (2)	31	31	24	26
Inexpert (3)	26	28	20	23
Fleiss Kappa (95% CI)	0.45 (0.44–0.46)	0.78 (0.78–0.79)	0.69 (0.69–0.71)	0.78 (0.78–0.79)
Cohen Kappa 1–2	0.63	0.76	0.66	0.68
Cohen Kappa 1–3	0.29	0.90	0.69	0.87
Cohen Kappa 2–3	0.54	0.68	0.75	0.79
Intra-rater analysis				
Spearman coefficient 1	$p = 0.92$, $p = 0.000$		$p = 0.92$, $p = 0.000$	
Spearman coefficient 2	$p = 0.86$, $p = 0.000$		$p = 0.93$, $p = 0.000$	
Spearman coefficient 3	$p = 0.91$, $p = 0.000$		$p = 0.91$, $p = 0.000$	

the inexpert and the moderate-expert raters (Table 1), with a more significant agreement among raters (Table 1). Specifically, the chi-square test found significant differences between the proportion of subjects classified as pathological or not by expert versus inexpert raters and moderate expert versus inexpert raters ($p < 0.05$) only with the manual method. The differences were not significant between raters when they applied the semi-automatic method ($p > 0.05$).

Cohen Kappa values revealed that applying a semi-automatic method instead of the manual one leads to an improvement in agreement, especially between expert and inexpert raters; the agreement moved from 0.29 (fair, in early H/M ratios) and 0.69 (substantial, in late H/M ratios) to 0.90 (perfect, in early H/M ratios) and 0.87 (perfect, late H/M ratios).

The intra-rater agreements results

The Spearman correlation analysis showed a robust intra-rater agreement in the assessment of early and delayed H/M values (Spearman Coefficient > 0.80, $p < 0.001$).

Discussion

This study investigated the effects of different methods assessing ^{123}I-MIBG parameters on the clinical interpretation of ^{123}I-MIBG images. To do this, we evaluated the reproducibility of delayed and early H/M ratios using two types of approach: (i) manual-drawing method and (ii) fixed-size ROIs approach following literature guidelines proposed for heart failure (13). Our results indicate that the use of fixed-size ROIs located following an "anatomical landmark square" (semi-automatic approach) improves the agreement among raters in classifying' H/M ratios as PD pathological or non-pathological. Of note, the semi-automatic procedure produced a perfect agreement between experienced and inexperienced observers (Table 1).

The use of a rectangular mediastinal ROI with unspecified size and manually drawn cardiac ROI is commonly used (21). However, fixed-size ROIs are recommended in the proposal to standardise ^{123}I-MIBG parameters, but they were validated in patients with heart failure and without comparing the semi-automatic method with the standard visual one (13). Our results support and extend these findings in PD. The raters showed good inter and intra-rater agreements in early and late H/M ratios (continue values) applying manual-drawn and semiautomatic methods. This finding suggests that both methods for the calculation of the H/M ratios benefit from excellent reproducibility. However, the semi-automatic procedure showed a higher percentage of raters' consistency, assessing both early and late H/M ratios (Table 1).

The classification of the H/M ratios into pathological or not according to clinical cut-off (16) further highlighted the differences in the approaches. The agreement among raters in classifying patients into pathological or not, according to H/M ratios measures (categorical values) was higher in the semi-automatic procedure than in the manual one (Table 1). This variation might be explained by the fact that the expert and inexpert raters showed low agreement, especially in assessing early H/M ratio values using the manual method (Cohen Kappa 0.29). Instead, in the semi-automatic procedure, the consistency between the raters became perfect (Cohen Kappa 0.90). This improvement suggests that the semi-automatic procedure improves the interpretation of planar ^{123}I-MIBG images in clinical settings.

This study has some limitations, particularly the small sample size and the lack of a control group. The data used in the present study have been acquired in the context of a protocol aiming to profile the dementia risk in PD with imaging biomarkers, where the acquisition of healthy controls was not planned. Moreover, we are aware that the superimposition of non-cardiac structures in the heart ROI might affect the ^{123}I-MIBG planar measures. This bias is intrinsic to the planar image technique because of the lack of three-dimensional information. A volumetric single photon emission computed tomography (SPECT) acquisition protocol would help to overcome this limitation, because of three-dimensional information. ^{123}I-MIBG-SPECT imaging can minimise the superimposition of the anatomic structures seen in two-dimensional planar images (e.g., lungs overlapping the heart) (22). We used the planar procedure in our study to obtain the ^{123}I-MIBG images because the quantification of global cardiac innervation using volumetric SPECT is less established than planar ^{123}I-MIBG imaging (23). This bias would equally affect the H/M ratios obtained with manual and semi-automatic ROI placement, most likely not impacting our study's main result.

Data availability statement

The raw data supporting the conclusions of this article will be made available by the authors, without undue reservation.

Ethics statement

The studies involving human participants were reviewed and approved by the Ethical Committees of IRCCS San Raffaele Hospital. The patients/participants provided their written informed consent to participate in this study.

Author contributions

CB and GC contributed to the conception and study design, statistical analysis, interpretation of results, and drafted the

manuscript. EV contributed to the conception and study design and revised the manuscript. AC and AA provided clinical data and revised the manuscript. DP contributed to the study design, interpretation of results, and revision of the manuscript. VG contributed to the interpretation of results and revision of the manuscript. All authors read and approved the final manuscript.

Funding

This study was supported by the CARIPLO Project "Evaluation of autonomic, genetic, imaging, and biochemical markers for Parkinson related dementia: Longitudinal assessment of a PD cohort" 2016–2020 (grant agreement no. 2014-0832) (DP). Open access funding was provided by the University of Geneva.

Conflict of interest

The authors declare that the research was conducted in the absence of any commercial or financial relationships that could be construed as a potential conflict of interest.

Publisher's note

References

1. Obeso JA, Stamelou M, Goetz CG, Poewe W, Lang AE, Weintraub D, et al. Past, present, and future of Parkinson's disease: a special essay on the 200th Anniversary of the Shaking Palsy. *Mov Disord.* (2017). 32:1264–310. doi: 10.1002/mds.27115

2. Borghammer P. How does parkinson's disease begin? Perspectives on neuroanatomical pathways, prions, and histology. *Mov Disord.* (2018) 33:48–57. doi: 10.1002/mds.27138

3. Orimo S, Ghebremedhin E, Gelpi E. Peripheral and central autonomic nervous system: does the sympathetic or parasympathetic nervous system bear the brunt of the pathology during the course of sporadic PD? *Cell Tissue Res.* (2018) 373:267–86. doi: 10.1007/s00441-018-2851-9

4. Knudsen K, Borghammer P. Imaging the Autonomic Nervous System in Parkinson's Disease. *Curr Neurol Neurosci Rep.* (2018) 18:79. doi: 10.1007/s11910-018-0889-4

5. Postuma RB, Berg D, Stern M, Poewe W, Olanow CW, Oertel W, et al. MDS clinical diagnostic criteria for Parkinson's disease. *Mov Disord.* (2015) 30:1591–601. doi: 10.1002/mds.26424

6. Wieland DM, Brown LE, Les Rogers W, Worthington KC, Wu JL, Clinthorne NH, et al. Myocardial imaging with a radioiodinated norepinephrine storage analog. *J Nucl Med.* (1981) 22:22–31.

7. Sisson JC, Wieland DM. Radiolabeled meta-iodobenzylguanidine: pharmacology and clinical studies. *Am J Physiol Imaging.* (1986) 1:96–103.

8. Carrió I. Cardiac neurotransmission imaging. *J Nucl Med.* (2001) 42:1062–76.

9. Orimo S, Suzuki M, Inaba A, Mizusawa H. 123I-MIBG myocardial scintigraphy for differentiating Parkinson's disease from other neurodegenerative parkinsonism: a systematic review and meta-analysis. *Parkinsonism Relat Disord.* (2012) 18:494–500. doi: 10.1016/j.parkreldis.2012.01.009

10. King AE, Mintz J, Royall DR. Meta-analysis of 123I-MIBG cardiac scintigraphy for the diagnosis of Lewy body–related disorders. *Mov Disord.* (2011) 26:1218–24. doi: 10.1002/mds.23659

11. Nuvoli S, Spanu A, Fravolini ML, Bianconi F, Cascianelli S, Madeddu G, et al. [123I] Metaiodobenzylguanidine (MIBG) cardiac scintigraphy and automated classification techniques in parkinsonian disorders. *Mol Imaging Biol.* (2019) 22:703–10. doi: 10.1007/s11307-019-01406-6

12. Roberts G, Kane JPM, Lloyd JJ, Petrides GS, Howe K, O'Brien JT, et al. A comparison of visual and semiquantitative analysis methods for planar cardiac 123I-MIBG scintigraphy in dementia with Lewy bodies. *Nucl Med Commun.* (2019) 40:734–43. doi: 10.1097/MNM.0000000000001024

13. Veltman CE, Boogers MJ, Meinardi JE, Al Younis I, Dibbets-Schneider P, Van derWall EE, et al. Reproducibility of planar 123I-meta-iodobenzylguanidine (MIBG) myocardial scintigraphy in patients with heart failure. *Eur J Nucl Med Mol Imaging.* (2012) 39:1599–608. doi: 10.1007/s00259-012-2180-2

14. Flotats A, Carrió I, Agostini D, Le Guludec D, Marcassa C, Schaffers M, et al. Proposal for standardisation of 123 I-metaiodobenzylguanidine (MIBG) cardiac sympathetic imaging by the EANM Cardiovascular Committee and the European Council of Nuclear Cardiology. *Eur J Nucl Med Mol Imaging.* (2010) 37:1802–12. doi: 10.1007/s00259-010-1491-4

15. Koo TK, Li MY. A guideline of selecting and reporting intraclass correlation coefficients for reliability research. *J Chiropr Med.* (2016) 15:155–63. doi: 10.1016/j.jcm.2016.02.012

16. Nagamachi S, Wakamatsu H, Kiyohara S, Fujita S, Futami S, Tamura S, et al. Usefulness of rCBF analysis in diagnosing Parkinson's disease: supplemental role with MIBG myocardial scintigraphy. *Ann Nucl Med.* (2008) 22:557–64. doi: 10.1007/s12149-008-0156-x

17. Fleiss JL. Measuring nominal scale agreement among many raters. *Psychol Bull.* (1971) 76:378. doi: 10.1037/h0031619

18. Fleiss JL, Levin B, Paik MC. *Statistical Methods for Rates and Proportions*. Hoboken, NJ: John wiley and sons (2013).

19. Landis JR, Koch GG. The measurement of observer agreement for categorical data. *Biometrics.* (1977) 33:159–74. doi: 10.2307/2529310

20. McHugh ML. Interrater reliability: the kappa statistic. *Biochem Med.* (2012) 22:276–82. doi: 10.11613/BM.2012.031

21. van der Veen L, Scholte A, Stokkel M. Mathematical methods to determine quantitative parameters of myocardial 123I-MIBG studies: a review of the literature. *Nucl Med Commun.* (2010) 31:617–28. doi: 10.1097/MNM.0b013e328337a99b

22. Oh J-K, Choi E-K, Song I-U, Kim J-S, Chung Y-A. Comparison of I-123 MIBG planar imaging and SPECT for the detection of decreased heart uptake in Parkinson disease. *J Neural Trans.* (2015) 122:1421–7. doi: 10.1007/s00702-015-1409-1

23. van der Veen BJ, Al Younis I, de Roos A, Stokkel MPM. Assessment of global cardiac I-123 MIBG uptake and washout using volumetric quantification of SPECT acquisitions. *J Nucl Cardiol.* (2012) 19:752–62. doi: 10.1007/s12350-012-9539-4

frontiers | Frontiers in Medicine

TYPE Original Research
PUBLISHED 19 January 2023
DOI 10.3389/fmed.2023.1087957

OPEN ACCESS

EDITED BY
Giorgio Treglia,
Ente Ospedaliero Cantonale (EOC), Switzerland

REVIEWED BY
Hui Tan,
Fudan University, China
Freddy E. Escorcia,
National Institutes of Health (NIH), United States

*CORRESPONDENCE
Florent L. Besson
✉ florent.besson@aphp.fr

SPECIALTY SECTION
This article was submitted to Nuclear Medicine, a section of the journal Frontiers in Medicine

RECEIVED 02 November 2022
ACCEPTED 02 January 2023
PUBLISHED 19 January 2023

CITATION
Ghidaglia J, Laurent V, Sebagh M, Pascale A, Durand E, Golse N and Besson FL (2023) Influence of key histological characteristics on 18F-fluorodeoxyglucose /18F-choline positron emission tomography positivity in hepatocellular carcinoma: A machine learning study.
Front. Med. 10:1087957.
doi: 10.3389/fmed.2023.1087957

Influence of key histological characteristics on 18F-fluorodeoxyglucose /18F-choline positron emission tomography positivity in hepatocellular carcinoma: A machine learning study

Jérôme Ghidaglia[1], Vincent Laurent[2], Mylène Sebagh[3,4,5], Alina Pascale[4,6], Emmanuel Durand[1,5,7], Nicolas Golse[4,5,6] and Florent L. Besson[1,5,7]*

[1]Department of Biophysics and Nuclear Medicine-Molecular Imaging, Hôpitaux Universitaires Paris-Saclay, Assistance Publique-Hôpitaux de Paris, Le Kremlin-Bicêtre, France, [2]Université Paris-Saclay, Centre Borelli, Gif-sur-Yvette, France, [3]Department of Pathology, Hôpitaux Universitaires Paris-Saclay, Assistance Publique-Hôpitaux de Paris, Le Kremlin-Bicêtre, France, [4]Universite Paris-Saclay, Inserm, Physiopathogènése et Traitement des Maladies du Foie, UMR-S 1193, Villejuif, Île-de-France, France, [5]Université Paris-Saclay, School of Medicine, Le Kremlin-Bicêtre, France, [6]Centre Hépato Biliaire, Hepatobiliary and Liver Transplant Unit, Hôpitaux Universitaires Paris-Saclay, Assistance Publique-Hôpitaux de Paris, Villejuif, France, [7]Université Paris-Saclay, Commissariat à l'énergie atomique et aux énergies alternatives (CEA), Centre National de la Recherche Scientifique (CNRS), Inserm, BioMaps, Le Kremlin-Bicêtre, France

Purpose: To determine the characteristics influence of key histological on 18F-fluorodeoxyglucose (18F-FDG) and 18F-choline positron emission tomography (PET) positivity in hepatocellular carcinoma (HCC).

Materials and methods: The 18F-FDG/18F-choline PET imaging findings of 103 histologically proven HCCs (from 62 patients, of which 47 underwent hepatectomy and 15 received liver transplantation) were retrospectively examined to assess the following key histological parameters: Grade, capsule, microvascular invasion (mVI), macrovascular invasion (MVI), and necrosis. Using a ratio of 70/30 for training and testing sets, respectively, a penalized classification model (Elastic Net) was trained using 100 repeated cross-validation procedures (10-fold cross-validation for hyperparameter optimization). The contribution of each histological parameter to the PET positivity was determined using the Shapley Additive Explanations method. Receiver operating characteristic curves with and without dimensionality reduction were finally estimated and compared.

Results: Among the five key histological characteristics of HCC (Grade, capsule, mVI, MVI, and necrosis), mVI and tumor Grade (I–III) showed the highest relevance and robustness in explaining HCC uptake of 18F-FDG and 18F-choline. MVI and necrosis status both showed high instability in outcome predictions. Tumor capsule had a minimal influence on the model predictions. On retaining only mVI and Grades I–III for the final analysis, the area under the receiver operating characteristic (ROC) curve values were maintained (0.68 vs. 0.63, 0.65 vs. 0.64, and 0.65 vs. 0.64 for 18F-FDG, 18F-choline, and their combination, respectively).

Conclusion: 18F-FDG/18F-choline PET positivity appears driven by both the Grade and mVI components in HCC. Consideration of the tumor microenvironment will likely be necessary to improve our understanding of multitracer PET positivity.

KEYWORDS

hepatocellular carcinoma, PET/CT, 18F-FDG, 18F-choline, machine learning

Introduction

Hepatocellular carcinoma (HCC) is a leading cause of cancer death worldwide, and thus represents a major health challenge (1). While conventional imaging remains essential for the management of HCC (2–5), positron emission tomography (PET) imaging has been increasingly used in this field (6, 7). In particular, 18F-fluorodeoxyglucose (18F-FDG) and 18F-choline PET radiotracers, which, respectively target the carbohydrate and fatty acid metabolic pathways, have shown their complementarity in clinical practice for the initial staging and treatment management of HCC (8–11). At present, combined use of 18F-FDG and 18F-choline is still not standard practice, partially because their biological significance in HCC remains largely unknown. Seminal papers have suggested that there is an inverse PET behavior in terms of their uptake in HCC, according to their grade of differentiation; namely, poorly-differentiated tumors tend to be 18F-FDG-avid, whereas well-differentiated tumors tend to be choline-avid (12, 13). Although attractive, these historical findings have been recently challenged by the results of our recent dedicated literature synthesis based on 99 HCCs reported over the past 16 years (14). To date, little is known about the true influence of key histological characteristics of HCC on 18F-FDG/18F-choline PET uptake.

Following our systematic review (14), we conducted the present original study to determine the influence of key histological characteristics on 18F-FDG and 18F-choline PET positivity in HCC.

Materials and methods

The present study was conducted in compliance with the tenets of the declaration of Helsinki. According to the rules of our institution, all patients were systematically informed of data collection and research purposes. All included patients were specifically informed and did not object to this study, which was approved by our University Ethical Committee (IRB no. CEPS-440).

Database characteristics

A total of 103 consecutive histologically proven HCCs (62 patients, of whom 47 were treated by hepatectomy and 15 by liver transplantation) with available baseline 18F-FDG and 18F-choline PET data were retrospectively reviewed. For all patients, the whole surgical sample was available, and the following histological characteristics were reported for each HCC tumor: degree of differentiation [Grade I, II, or III of the WHO classification (15)]; presence or absence of a capsule; microvascular invasion (mVI): microscopic neoplastic emboli discovered on histology; macrovascular invasion (MVI): macroscopic emboli visible with the naked eye during management of the macroscopic part and/or visible through imaging; and presence or absence of necrosis. The 18F-FDG and 18F-choline PET data were acquired before surgery on the same hybrid PET/computed tomography (CT) device (Biograph mCT FlowMotion, Siemens Healthineers, Erlangen, Germany), and were reconstructed using the same 3D iterative algorithm (3D time-of-flight–ordered subset expectation maximization method, two iterations and 21 subsets with time-of-flight and point spread function modeling, and with random, dead time, scatter, decay, and attenuation corrections; matrix size = 400 × 400), with postfiltering (Gaussian filter: 3.0 mm).

18F-FDG and 18F-choline image analyses

All HCC PET data were reviewed by two nuclear imaging physicians (JG and FLB, with 4 and 12 years of expertise in hybrid PET imaging, respectively) on the same professional workstation (syngo.via, Siemens Healthineers, Munich, Germany). For both 18F-FDG and 18F-choline, any focal radiotracer uptake compared to the surrounding liver background was considered positive, whereas iso or hypometabolic lesions were both considered negative. Any disagreements between the two readers were resolved by consensus. Additionally, for each HCC tumor, the peak standardized uptake values normalized by the lean body mass (SUL_{peak}) were semi-automatically extracted. The choice of SULpeak was motivated by technical considerations of robustness and reliability (16, 17).

Statistical analyses

All categorical data are expressed as numbers and percentages, while continuous data are expressed as medians and interquartile ranges. A machine learning structured procedure was performed lesion-wise to decipher the influence of all HCC histological features on 18F-FDG and 18F-choline dual-tracer PET uptake behaviors, and to select the most relevant ones. This procedure was as follows:

(1) Univariate correlation analyses (Spearman's non-parametric rank correlations) were performed to identify monotonic relationships between binarized histological characteristics (Grade, capsule, necrosis, mVI, and MVI) and dual-radiotracer visual PET uptake behaviors (positive for 18F-FDG, 18F-choline, or both). To note, because Grade II–an intermediate with potential overlaps between very well-differentiated (Grade I) and poorly differentiated (Grade III) tumors–was under represented, and to avoid any linear relationship between the variables during the label encoding process,

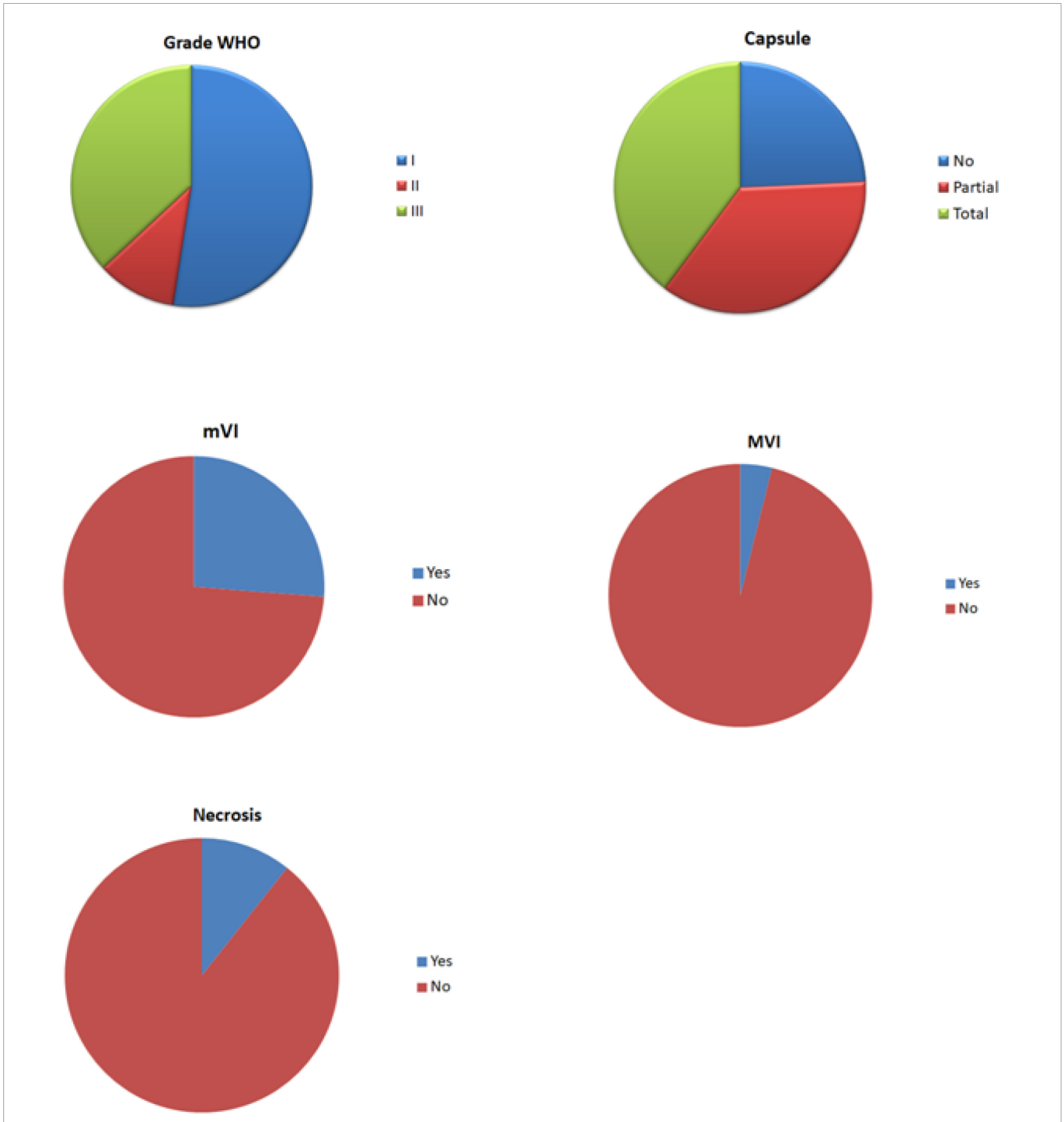

FIGURE 1
Pie chart of the histological characteristics of hepatocellular carcinomas (HCCs).

only the Grades I and III were encoded, while capturing the entire information of the dataset.

(2) For each of the 18F-FDG, 18F-choline, and dual-PET tracer behaviors, a general linear regression classifier (L1 + L2 regularization, ElasticNet) was used to assess the impact of HCC histological components on PET tracer positivity. The overall dataset was split into training and test sets at a 70–30% ratio. To prevent potential overfitting and measure model stability, the learning procedures were 10-fold cross-validated for hyperparameter optimization (the lesions of a patient belong to the same sample), and the final models were repeated 100 times. For the three PET behaviors, the contribution of each histological component to the model's prediction (PET positivity uptake) was deciphered using the Shapley Additive Explanations (SHAP) method, and the performances of the models were assessed by estimating the corresponding receiver operating characteristic (ROC) curves.

(3) Finally, a feature selection process was performed by fine-tuning the regularization path of the regression models (grid search: α ranged from 0.1 to 100, and the L1/L2 ratio ranged from 0 to 1), and the ultimate penalization coefficients were chosen based on

model's stability, simplicity, and overall performance. ROC curves of the dimensionality-reduced models (including the most relevant histological features) were estimated and compared to the non-dimensionality-reduced models.

All statistical analyses were performed using Python (version 3.8.8; Python Software Foundation)[1] and Scikit-Learn library (version 1.1)[2]. For all analyses, statistical significance was set at $p < 0.05$.

Results

Database characteristics

The characteristics of all included patients, together with histological characteristics of their HCCs, are shown in Figure 1 and Table 1. Briefly, the 62 included patients had a mean age of 66 years (range: 56–76 years), and 55 (89%) were male. Liver disease was explicitly reported for 55 patients (89%), and 47 were treated by surgery (76%) and 15 by liver transplantation (24%). Each patient had a mean of 1.5 (range: 1–2) HCCs, and the mean delay between the two PET/CT examinations was 5.5 (range: 4–7) days. At the lesion level (n = 103), a total of 54, 11, and 38 tumors were classified as Grade I (52%), II (11%), and III (37%), respectively. The presence of a capsule was reported in 78 cases (76%), and vascular invasion was reported for 31 tumors.

18F-FDG and 18F-choline image analyses

The visual analyses of the PET imaging data are summarized in Table 2, upper panel. Briefly, 56% of the HCC tumors negative for 18F-FDG were Grade I tumors, whereas 55% of HCC tumors positive for 18F-FDG were Grade III tumors. On the other hand, 62% of the HCC tumors positive for 18F-choline were Grade I tumors, and up to 36% of them were Grade III. On total, 35 HCC tumors (34% of the whole dataset, 20 Grade I and 15 Grade III) were positive for both the two radiotracers. Concerning the capsule status, its presence was observed in 73% of the 18F-FDG PET positive HCC cases and 77% of the 18F-FDG PET negative HCC cases, while 78% of the 18F-choline PET positive and 74% of the 18F-choline PET negative HCC cases showed evidence of capsule. For vascular invasion, macro vascular invasion was reported in 9% of the 18F-FDG PET positive HCC cases and 1% of the 18F-FDG PET negative HCC cases, and in 7 and 2% of HCC cases for 18F-choline PET positive and 18F-choline PET negative cases, respectively. Finally, mVI was reported in 42% of the 18F-FDG PET positive HCC cases versus 19% for the 18F-FDG PET negative HCC cases, and 38% of the 18F-choline PET positive HCC cases versus 17% for the 18F-choline PET negative HCC cases. HCCs with the various dual-tracer PET behaviors are shown in Figure 2. As illustrated in Figure 3, the intensity of 18F-FDG and 18F-choline PET uptakes assessed using SUL_{peak} showed higher radiotracer concentration in cases of mVI (18F-choline only) and between the Grade I–II and II–III (for 18F-FDG only). There were no other between-group differences.

TABLE 1 Dataset characteristics.

Patient characteristics (n = 62)	
Sex (M/F)	55/7
Age in years	66 (56–76)
Treatment procedure	
• Surgery	n = 47
• Liver transplantation	n = 15
Liver disease	
• No evident liver disease	n = 7
• Viral infection (HCV, HBV)	n = 22
• Non-alcoholic steatohepatitis (NASH)/ethylism (OH)	n = 20
• Other	n = 14
AFP	6.25 (3–10.5)
Number of lesions per patient	1.5 (1–2)
BCLC classification	
• A	n = 44
• B	n = 10
• C	n = 0
• D	n = 2
• Unclassified	n = 6
Delay between 18F-FDG and 18F-choline imaging (days)	5.5 (4–7)
Patient's blood glucose (mmol/L)	5.5 (4–7)
Weight (kg)	77.5 (70–85)
Injected dose 18F-FDG (MBq)	271.5 (241–302)
Delay between injection and PET (FDG) (min)	60 (60–60)
Injected dose of 18F-choline (MBq)	161.5 (136–187)
Delay between injection and PET (choline) (min)	25 (20–30)
Lesion characteristics (n = 103)	
Grade WHO	
• I	n = 54
• II	n = 11
• III	n = 38
Capsule	
• No	n = 25
• Partial	n = 37
• Total	n = 41
Vascular invasion	
• Macro	n = 4
• Micro	n = 27
Necrosis	
• Yes	n = 11
• No	n = 92

Contribution of key histological characteristics on 18F-FDG and 18F-choline PET positivity

A correlation heatmap showing the relationships between the histological characteristics of the 103 HCCs and their PET behaviors is provided in Figure 4. The three PET uptake behaviors

1 http://www.python.org

2 https://scikit-learn.org

TABLE 2 Positron emission tomography (PET) results.

HCC (n = 103)	Visual analysis			
	18F-FDG		18F-choline	
	Positive	Negative	Positive	Negative
Grade WHO				
• I	15/33 (45%)	39/70 (56%)	28/45 (62%)	26/58 (45%)
• II	0/33 (0%)	11/70 (16%)	1/45 (2%)	10/58 (17%)
• III	18/33 (55%)	20/70 (29%)	16/45 (36%)	22/58 (38%)
Capsule				
• No	9/33 (27%)	16/70 (23%)	10/45 (22%)	15/58 (26%)
• Partial	13/33 (39%)	24/70 (34%)	18/45 (40%)	19/58 (33%)
• Total	11/33 (33%)	30/70 (43%)	17/45 (38%)	24/58 (41%)
Vascular invasion				
• Macro	3/33 (9%)	1/70 (1%)	3/45 (7%)	1/58 (2%)
• Micro	14/33 (42%)	13/70 (19%)	17/45 (38%)	10/58 (17%)

HCC (n = 103)	Semi-quantitative analysis	
	18F-FDG	18F-choline
Grade WHO		
• I	3.0 (2–4)	6.5 (4–9)
• II	4.25 (1–7.5)	5.5 (3–8)
• III	3.0 (2–4)	6.5 (4–9)
Capsule		
• No	3.0 (2–4)	6.0 (4–8)
• Partial	4.0 (2–6)	6.5 (4–9)
• Total	3.0 (1–5)	6.5 (4–9)
Vascular invasion		
• Macro	4.75 (1.5–8)	7.25 (3.5–11)
• Micro	4.0 (2–6)	6.5 (4–9)

For the upper panel of the table, the ratios represent the number of tumors verifying the histological characteristic of interest normalized by the positron emission tomography (PET) status. The related percentages are also provided.

were significantly correlated with mVI (18F-FDG positivity: Spearman's ρ = 0.25, p = 0.01; 18F-choline positivity: ρ = 0.23, p = 0.02; 18F-FDG/18F-choline positivity: ρ = 0.27, p = 0.006). A significant correlation between 18F-FDG PET positivity and tumor differentiation (Grade III) was also observed (ρ = 0.25, p = 0.01). No other histological–PET correlations were significant. Considering all the histological characteristics (Grade, capsule, necrosis, mVI, and MVI), the regression classifier provided area under the ROC curve (AUC) values of 0.63, 0.64, and 0.64 for 18F-FDG, 18F-choline, and 18F-FDG/18F-choline PET positivity, respectively [**Figure 5A** (G)]. As shown in **Figure 5B** (G), Grade I–III and mVI histological parameters contributed most to explaining PET positivity in all three cases (18F-FDG, 18F-choline, and dual-tracer positivity), whereas capsule, necrosis, and MVI parameters were non-relevant. **Figure 6A** (H) shows the impact of the regularization paths on coefficient scattering. Based on their stability, which emphasizes their interpretability [**Figure 5B** (G)], the mVI and Grades I–III were retained in the final analysis. By fixing the regularization parameter to 0.5, AUC values of the dimensionality-reduced models were maintained [**Figure 6B** (H)].

Discussion

In this study, which included data from 103 histologically proven HCCs, a structured machine learning procedure was used to ascertain the influence of the main histological characteristics of HCC on 18F-FDG and 18F-choline PET uptake. Among the five key histological characteristics (Grade, capsule, mVI, MVI, and necrosis), mVI and tumor Grade (I–III) showed the highest relevance and robustness in explaining HCC uptake of 18F-FDG and 18F-choline. MVI and necrosis status both showed high instability in outcome predictions, which highlights their non-relevance in model building. Tumor capsule had a very weak influence on model predictions.

This is the first study to specifically examine the influence of several key histological characteristics of HCC on 18F-FDG/18F-choline PET positivity, and our results complement previous findings on PET imaging of HCC. First, our recent systematic review, which included 99 HCCs from six studies, revealed there to be a very large overlap of 18F-FDG/18F-choline PET findings between well- and less-differentiated histological subtypes (14). While Grade III was significantly correlated with 18F-FDG PET visual positivity in the

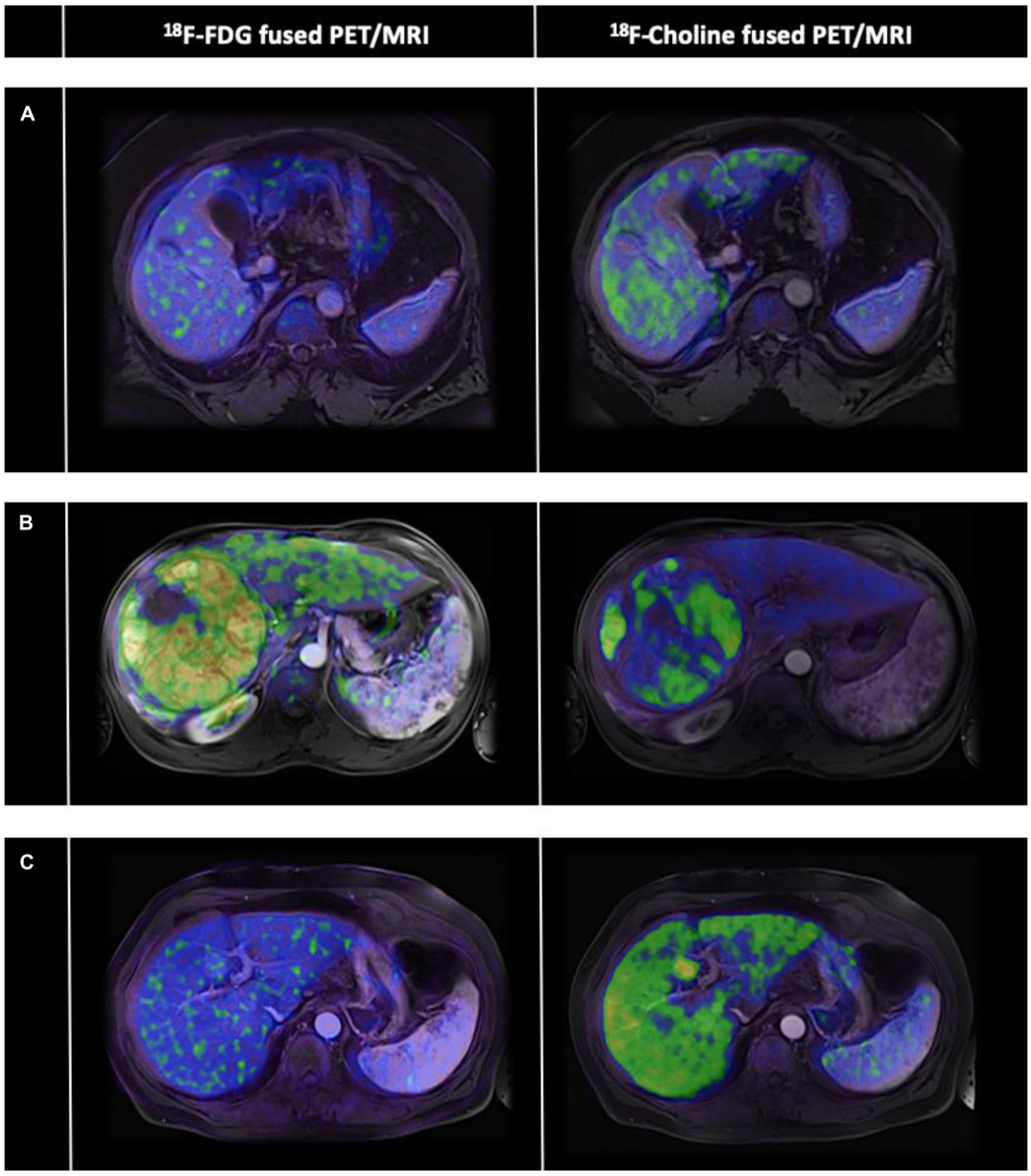

FIGURE 2
Case-mix of hepatocellular carcinoma (HCC) with various dual-tracer positron emission tomography (PET) profiles. The PET part of the non-contrast-enhanced PET/computed tomography (CT) data 18F fluorodeoxyglucose (18F-FDG on the left panel and 18F-choline on the right panel) of three HCCs **(A–C)** were retrospectively fused to their available contrast-enhanced MRI data (axial T1-weighted MRI pulse sequences with arterial phase contrast enhancement). **(A)** Dual-PET radiotracers negative uptake (HCC Grade III, with mVI). **(B)** Dual-PET radiotracers positive uptake (HCC Grade I, with mVI). **(C)** Negative 18F-FDG uptake but positive 18F-choline uptake (HCC Grade I-II, without mVI).

present study, no difference in SUL_{peak} was observed between Grade I and III for this radiotracer. Second, we found significant correlations of both 18F-FDG and 18F-choline positivity with microvascular invasion (mVI). To note, HCCs can be broadly classified as proliferative or non-proliferative tumors according to their level of differentiation, genetic and epigenetic features, and immunological characteristics (18). Based on this emerging molecular classification, the proliferative class includes poorly differentiated tumors with a high degree of vascular invasion, while the non-proliferative class corresponds to well-to-moderately differentiated tumors with less vascular invasion. Furthermore, a significant relationship between 18F-FDG uptake and mVI has been reported previously (19–21). Our rigorous feature selection process, which was performed without *a priori*, showed that among the common key histological features, Grade and mVI were the most relevant parameters in explaining the 18F-FDG and 18F-choline PET positivity in HCCs. In accordance with findings of seminal studies (12, 13), our results suggest that 18F-FDG/18F-choline dual-tracer PET positivity is driven by the Grade (poorly differentiated for 18F-FDG and well-differentiated for 18F choline), but also microvascular invasion, rather than the Grade alone. Moreover, we found that these key histological characteristics of HCC only moderately predicted PET positivity (AUCs of 68, 65, and 65% for 18F-FDG, 18F-choline, and 18F-FDG/18F-choline, respectively, vs. an AUC of 50% in the random model). As in any tumor, HCC cells are surrounded by a complex cellular microenvironment with close interactions (21, 22). In such an ecosystem, immune cell infiltrate appears to be critical for tumor growth and adaptability (23, 24), and could even be a defining

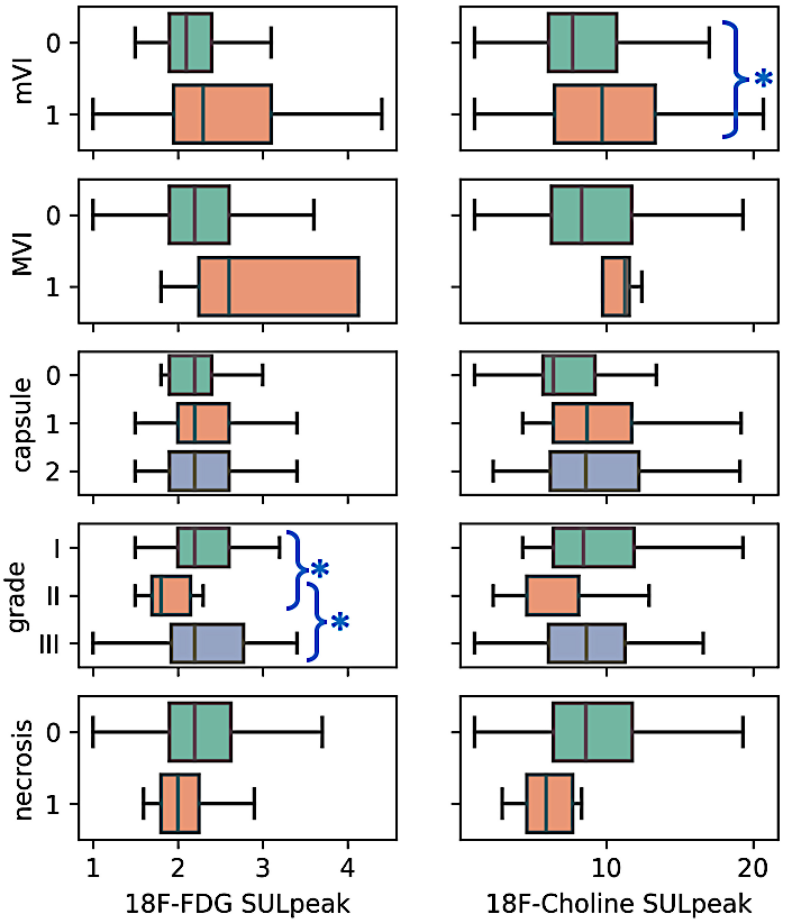

FIGURE 3
Boxplot of the semi quantitative positron emission tomography (PET) data according to histological characteristics. Among the five histological characteristics, higher 18F- choline uptake was observed in the case of mVI positive tumors ($p < 0.05$, non-parametric mann-whitney U test, blue asterisk). Also, 18F-FDG uptake between the Grades I–II and II–III was significant ($p < 0.05$, non-parametric kruskal wallis ANOVA with *post-hoc* tests, blue asterisk). For the remaining macrovascular invasion (MVI), capsule (no, partial, total), and necrosis (absence, presence) characteristics, no difference in radiotracers uptake was observed between the tumor subgroups ($p > 0.05$).

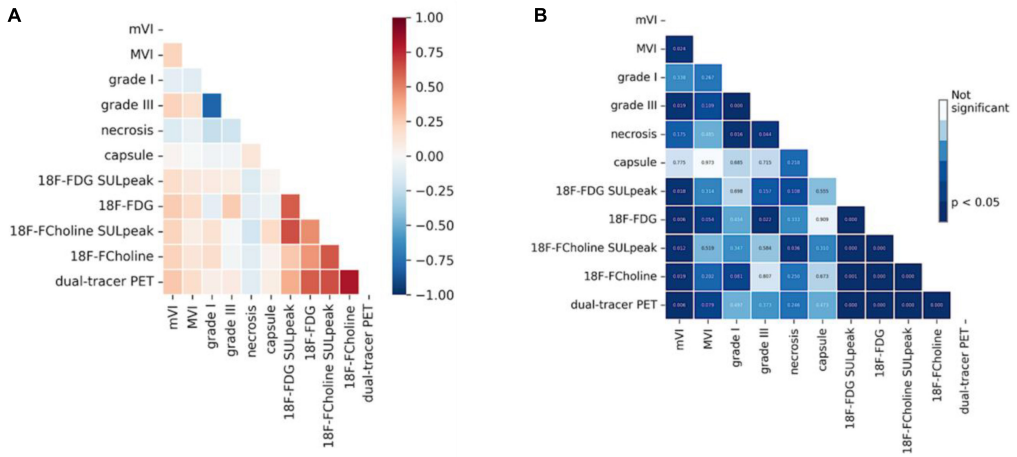

FIGURE 4
Heatmap of the correlations between histological and positron emission tomography (PET) metrics (Spearman's rank correlation). **(A)** Spearman *ρ*coefficients between histological characteristics of hepatocellular carcinoma (HCC) and PET uptake positivity. **(B)** Corresponding *p*-values Here, only the mVI and Grade III were significantly correlated to the PET metrics.

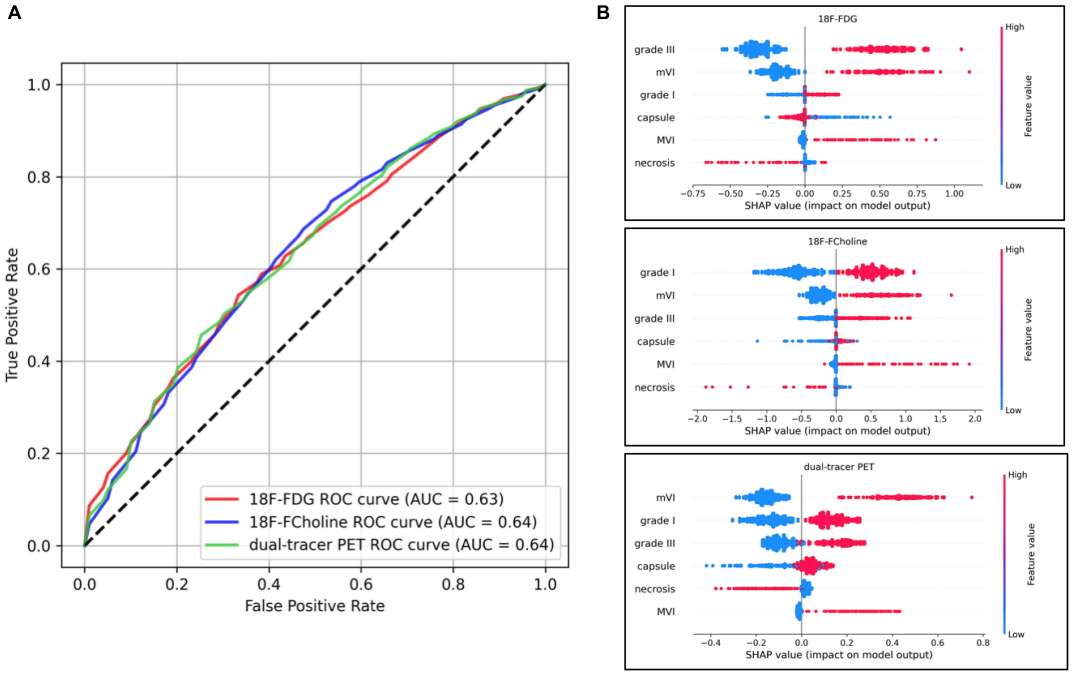

FIGURE 5
Model performances including all histological parameters, and Shapley Additive Explanations (SHAP) plot analyses. **(A)** Receiver operating characteristic (ROC) curves of the three models' performances. The ROC curve illustrates the capacity of classifiers to discriminate positive and negative cases at different thresholds (e.g., for the 18F-fluorodeoxyglucose (18F-FDG) model and a desired 60% positive rate, the algorithm will yield 40% false alarms). The random model is represented by identity (dotted line) and the perfect model (with no randomness) is $y = 1$ on $[0,\ 1]$. **(B)** Impact on positron emission tomography (PET) positivity is shown with SHAP values on the x-axis, and values of histological characteristics are shown in color (blue and red for low and high values, respectively).

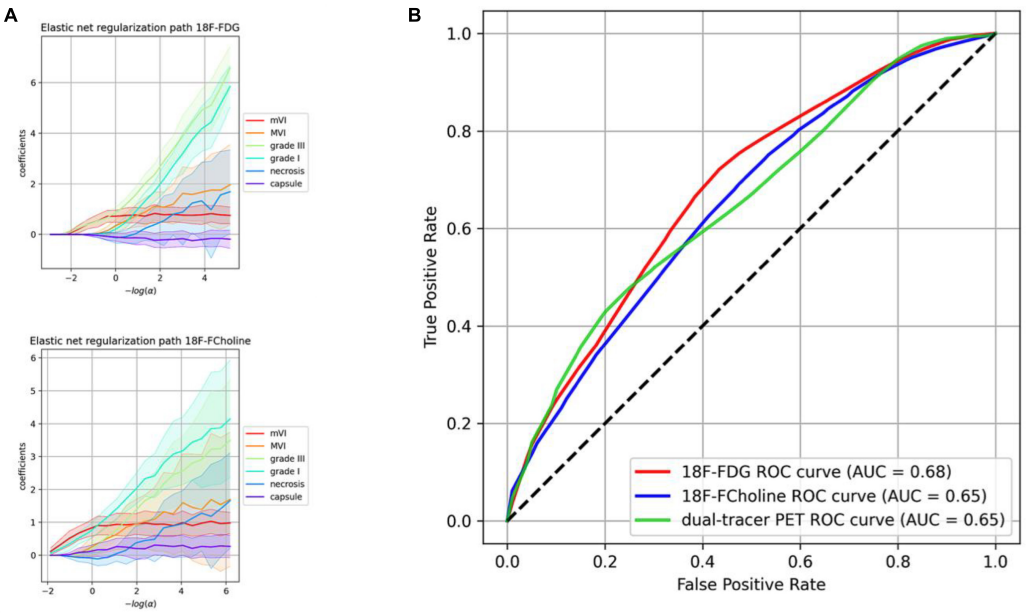

FIGURE 6
Regularization paths and model performances including the most relevant histological parameters finally retained. **(A)** Regularization paths for 18F-fluorodeoxyglucose (18F-FDG) and 18F-choline. The more the penalization decreases (right side), the more the coefficients are scattered. **(B)** Receiver operating characteristic (ROC) curves of the dimensionality-reduced models' performance. The ROC curve illustrates the capacity of classifiers to discriminate positive and negative cases at different thresholds (e.g., for the 18F-FDG model and a desired 60% positive rate, the algorithm will yield 38% of false alarms). The random model is represented by identity (dotted line), and the perfect model (with no randomness) is $y = 1$ on $[0,\ 1]$.

feature of an emerging subclasses of tumor phenotypes (18, 23). To note, high immune activity has been observed in both non-proliferative and proliferative HCCs (18). Thus, in all these tumors, the 18F-FDG and 18F-choline PET signatures are also likely to be partially associated with increased immune activity (24, 25). Based on these considerations, and given the fact that all grade

II tumors exhibited low avidity both for 18F-FDG and 18F-choline in our study, new molecular radioprobes would be of particular interest to improve the clinical relevance of PET imaging in the management of HCC. PET radiotracers targeting the immune microenvironment of tumor cells (26) or HCC neovasculature (27, 28) appear promising in this field.

Our study has several limitations that should be noted. First, this was a retrospective monocentric study. However, the dataset included more than 100 HCCs, for which complete histological and dual-radiotracer PET lesion data were available. Second, we applied a general linear classifier to predict PET positivity of HCCs. Moreover, we tested other machine learning procedures (gradient boosting, SVC), but these models did not converge due to the intrinsic properties of this real-life dataset. Third, we did not consider the influence of tumor microenvironment, and only focused on the most widely used histological characteristics of HCC tumor cells. Based on our results and the emerging concepts of immune-mediated phenotypes in HCC, further studies are warranted to improve our understanding of the factors underlying multitracer PET positivity in this field.

To conclude, among five widely used histological parameters, we found that Grade and microvascular invasion were the most relevant parameters in explaining both 18F-FDG and 18F-choline PET positivity in HCC. Consideration of the tumor microenvironment in future work could improve our understanding of multitracer PET positivity.

Data availability statement

The original contributions presented in this study are included in this article/supplementary material, further inquiries can be directed to the corresponding author.

Ethics statement

The studies involving human participants were reviewed and approved by IRB no. CEPS-440. The patients/participants provided their written informed consent to participate in this study.

Author contributions

All authors contributed to design and acquisition analysis, revising for intellectual content, final approval, agreed to be accountable for all aspects of this work (accuracy and integrity of any part of the work), and approved the submitted version.

Conflict of interest

The authors declare that the research was conducted in the absence of any commercial or financial relationships that could be construed as a potential conflict of interest.

Publisher's note

All claims expressed in this article are solely those of the authors and do not necessarily represent those of their affiliated organizations, or those of the publisher, the editors and the reviewers. Any product that may be evaluated in this article, or claim that may be made by its manufacturer, is not guaranteed or endorsed by the publisher.

References

1. Sung H, Ferlay J, Siegel RL, Laversanne M, Soerjomataram I, Jemal A, et al. Global cancer statistics 2020: GLOBOCAN estimates of incidence and mortality worldwide for 36 cancers in 185 countries. *CA Cancer J Clin.* (2021) 71:209–49. doi: 10.3322/caac.21660

2. Chernyak V, Fowler KJ, Kamaya A, Kielar AZ, Elsayes KM, Bashir MR, et al. Liver imaging reporting and data system (LI-RADS) Version 2018: imaging of hepatocellular carcinoma in at-risk patients. *Radiology.* (2018) 289:816–30. doi: 10.1148/radiol.2018181494

3. van der Pol C, Lim C, Sirlin C, McGrath T, Salameh J, Bashir M, et al. Accuracy of the liver imaging reporting and data system in computed tomography and magnetic resonance image analysis of hepatocellular carcinoma or overall malignancy—a systematic review. *Gastroenterology.* (2019) 156:976–86. doi: 10.1053/j.gastro.2018.11.020

4. Llovet J, Lencioni R. mRECIST for HCC: performance and novel refinements. *J Hepatol.* (2020) 72:288–306. doi: 10.1016/j.jhep.2019.09.026

5. Llovet J, Villanueva A, Marrero J, Schwartz M, Meyer T, Galle P, et al. Trial design and endpoints in hepatocellular carcinoma: AASLD consensus conference. *Hepatology.* (2021) 73:158–91.

6. Bertagna F, Bertoli M, Bosio G, Biasiotto G, Sadeghi R, Giubbini R, et al. Diagnostic role of radiolabelled choline PET or PET/CT in hepatocellular carcinoma: a systematic review and meta-analysis. *Hepatol Int.* (2014) 8:493–500. doi: 10.1007/s12072-014-9566-0

7. Signore G, Nicod-Lalonde M, Prior J, Bertagna F, Muoio B, Giovanella L, et al. Detection rate of radiolabelled choline PET or PET/CT in hepatocellular carcinoma: an updated systematic review and meta-analysis. *Clin Transl Imaging.* (2019) 7:237–53. doi: 10.1007/s40336-019-00332-5

8. Castilla-Lièvre M, Franco D, Gervais P, Kuhnast B, Agostini H, Marthey L, et al. Diagnostic value of combining ^{11}C-choline and ^{18}F-FDG PET/CT in hepatocellular carcinoma. *Eur J Nucl Med Mol Imaging.* (2016) 43:852–9. doi: 10.1007/s00259-015-3241-0

9. Wu H, Wang Q, Li B, Li H, Zhou W, Wang Q. F-18 FDG in conjunction with 11C-choline PET/CT in the diagnosis of hepatocellular carcinoma. *Clin Nucl Med.* (2011) 36:1092–7. doi: 10.1097/RLU.0b013e3182335df4

10. Talbot J, Gutman F, Fartoux L, Grange J, Ganne N, Kerrou K, et al. PET/CT in patients with hepatocellular carcinoma using [(18)F]fluorocholine: preliminary comparison with [(18)F]FDG PET/CT. *Eur J Nucl Med Mol Imaging.* (2006) 33:1285–9.doi: 10.1007/s00259-006-0164-9

11. Chalaye J, Costentin CE, Luciani A, Amaddeo G, Ganne-Carri N, Baranes L, et al. Positron emission tomography/computed tomography with 18F-fluorocholine improve tumor staging and treatment allocation in patients with hepatocellular carcinoma. *J Hepatol.* (2018) 69:336–44. doi: 10.1016/j.jhep.2018.02.018

12. Yamamoto Y, Nishiyama Y, Kameyama R, Okano K, Kashiwagi H, Deguchi A, et al. Detection of hepatocellular carcinoma using 11C-choline PET: comparison with 18F-FDG PET. *J Nucl Med Off Publ Soc Nucl Med.* (2008) 49:1245–8.

13. Talbot J, Fartoux L, Balogova S, Nataf V, Kerrou K, Gutman F, et al. Detection of hepatocellular carcinoma with PET/CT: a prospective comparison of 18F-fluorocholine and 18F-FDG in patients with cirrhosis or chronic liver disease. *J Nucl Med Off Publ Soc Nucl Med.* (2010) 51:1699–706.

14. Ghidaglia J, Golse N, Pascale A, Sebagh M, Besson FL. 18F-FDG /18F-choline dual-tracer PET behavior and tumor differentiation in hepatocellular carcinoma. A systematic review. *Front Med.* (2022) 9:924824. doi: 10.3389/fmed.2022.924824

15. Bosman F, World Health Organization [WHO], International Agency for Research on Cancer. editors. *WHO classification of tumours of the digestive system.* 4th ed. Lyon: International Agency for Research on Cancer (2010).

16. Vanderhoek M, Perlman S, Jeraj R. Impact of different standardized uptake value measures on pet-based quantification of treatment response. *J Nucl Med.* (2013) 54:1188–94. doi: 10.2967/jnumed.112.113332

17. Sher A, Lacoeuille F, Fosse P, Vervueren L, Cahouet-Vannier A, Dabli D, et al. For avid glucose tumors, the SUV peak is the most reliable parameter for [18F]FDG-PET/CT quantification, regardless of acquisition time. *EJNMMI Res.* (2016) 6:21. doi: 10.1186/s13550-016-0177-8

18. Llovet JM, Kelley RK, Villanueva A, Singal AG, Pikarsky E, Roayaie S, et al. Hepatocellular carcinoma. *Nat Rev Dis Primer.* (2021) 7:6.

19. Kornberg A, Freesmeyer M, Bärthel E, Jandt K, Katenkamp K, Steenbeck J, et al. 18F-FDG-uptake of hepatocellular carcinoma on PET predicts microvascular tumor invasion in liver transplant patients. *Am J Transplant Off J Am Soc Transplant Am Soc Transpl Surg.* (2009) 9:592–600.

20. Mul S, Chalaye J, Legou F, Tenenhaus A, Calderaro J, Pregliasco AG, et al. Hepatobiliary MR contrast agent uptake as a predictive biomarker of aggressive features on pathology and reduced recurrence-free survival in resectable hepatocellular carcinoma: comparison with dual-tracer 18F-FDG and 18F-FCH PET/CT. *Eur Radiol.* (2020) 30:5348–57. doi: 10.1007/s00330-020-06923-5

21. Sabaté-Llobera A, Mestres-Mart J, Reynés-Llompart G, Llad L, Mils K, Serrano T, et al. 2-[18F]FDG PET/CT as a predictor of microvascular invasion and high histological grade in patients with hepatocellular carcinoma. *Cancers.* (2021) 13:2554. doi: 10.3390/cancers13112554

22. Kurebayashi Y, Matsuda K, Ueno A, Tsujikawa H, Yamazaki K, Masugi Y, et al. Immunovascular classification of HCC reflects reciprocal interaction between immune and angiogenic tumor microenvironments. *Hepatol Baltim Md.* (2022) 75:1139–53.

23. Zou J, Luo C, Xin H, Xue T, Xie X, Chen R, et al. The role of tumor-infiltrating B cells in the tumor microenvironment of hepatocellular carcinoma and its prognostic value: a bioinformatics analysis. *J Gastrointest Oncol.* (2022) 13:1959–66.

24. Hu C, Xuan Y, Zhang X, Liu Y, Yang S, Yang K, et al. Immune cell metabolism and metabolic reprogramming. *Mol Biol Rep.* (2022) 49:9783–95.

25. Sanchez-Lopez E, Zhong Z, Stubelius A, Sweeney S, Booshehri L, Antonucci L, et al. Choline uptake and metabolism modulate macrophage IL-1β and IL-18 production. *Cell Metab.* (2019) 29:1350–1362.e7. doi: 10.1016/j.cmet.2019.03.011

26. Wang H, Zhu W, Ren S, Kong Y, Huang Q, Zhao J, et al. 68Ga-FAPI-04 versus 18F-FDG PET/CT in the detection of hepatocellular carcinoma. *Front Oncol.* (2021) 11:693640. doi: 10.3389/fonc.2021.693640

27. Kunikowska J, Cieślak B, Gierej B, Patkowski W, Kraj L, Kotulski M, et al. [68 Ga]ga-prostate-specific membrane antigen PET/CT: a novel method for imaging patients with hepatocellular carcinoma. *Eur J Nucl Med Mol Imaging.* (2021) 48:883–92.

28. Hirmas N, Leyh C, Sraieb M, Barbato F, Schaarschmidt BM, Umutlu L, et al. 68Ga-PSMA-11 PET/CT improves tumor detection and impacts management in patients with hepatocellular carcinoma. *J Nucl Med Off Publ Soc Nucl Med.* (2021) 62:1235–41. doi: 10.2967/jnumed.120.257915

frontiers | Frontiers in Medicine

TYPE Perspective
PUBLISHED 27 February 2023
DOI 10.3389/fmed.2023.1149925

OPEN ACCESS

EDITED BY
Giorgio Treglia,
Ente Ospedaliero Cantonale (EOC), Switzerland

REVIEWED BY
Florent L. Besson,
Assistance Publique Hopitaux De Paris, France

*CORRESPONDENCE
Andor W. J. M. Glaudemans
✉ a.w.j.m.glaudemans@umcg.nl

SPECIALTY SECTION
This article was submitted to Nuclear Medicine, a section of the journal Frontiers in Medicine

RECEIVED 06 February 2023
ACCEPTED 09 February 2023
PUBLISHED 27 February 2023

CITATION
Glaudemans AWJM and Gheysens O (2023) Expert opinions in nuclear medicine: Finding the "holy grail" in infection imaging. *Front. Med.* 10:1149925. doi: 10.3389/fmed.2023.1149925

Expert opinions in nuclear medicine: Finding the "holy grail" in infection imaging

Andor W. J. M. Glaudemans[1]*and Olivier Gheysens[2]

[1]Department of Nuclear Medicine and Molecular Imaging, University of Groningen, University Medical Center Groningen, Groningen, Netherlands, [2]Department of Nuclear Medicine, Cliniques Universitaires Saint-Luc and Institute of Clinical and Experimental Research (IREC), Université Catholique de Louvain, Brussels, Belgium

Nuclear medicine imaging techniques are now widely accepted and increasingly used for diagnosing and treatment monitoring of infectious and inflammatory diseases. The latter has been exemplified by numerous recent clinical guidelines in which PET imaging is now part of the diagnostic flowcharts. In this perspective paper we discuss the current available guidelines, the current limitations, and we provide the future aims of research to achieve the holy grail in nuclear medicine: the differentiation between infection, inflammation and malignancy.

KEYWORDS

molecular imaging, infection, inflammation, PET-CT, LAFOV PET, specific radiotracers

1. Introduction

Infectious diseases are extremely common worldwide and their incidence increases. Everyone is prone to infectious diseases, but some people more than others, including those with suppressed or compromised immune systems, young children, adults over 60 years, and those with foreign body material. Infection can be considered as the new cancer, or even worse since infectious diseases are often transmissible and drug resistant. Antimicrobial resistance has emerged as one of the leading health threats of the 21st century which requires a global and coordinated action plan to address (1).

Inflammatory diseases are not transmissible, but inflammation is part of the body's complex biological response to external stimuli. When overacting, healthy tissues can be caught up in this reaction leading to systemic inflammation or auto-immune diseases. Furthermore, inflammation is also thought to be a key player for the development of malignancies and cardiovascular disorders.

Infectious and inflammatory diseases affect millions of people worldwide, resulting in significant morbidity and mortality and huge socio-economic burden. While still developing new drugs to treat "old" infectious diseases like HIV or tuberculosis, "new" infectious diseases are emerging and will continue to emerge, as has recently been witnessed by the COVID-19 pandemic. This illustrates in a nutshell the importance of infection and inflammation. Moreover, we have to recognize these diseases at an early stage, and diagnose them correctly in order to start as soon as possible the correct treatment and to evaluate early on treatment efficacy, all aiming at avoiding further sufferance, disability, transmission and resistance.

Diagnosis and treatment evaluation of infection and inflammation usually rely on clinical findings, laboratory parameters, and histological and/or microbiological results. The problem, however, is that clinical constitutional symptoms and laboratory parameters are often nonspecific, and that histology may not always be feasible or often requires an invasive procedure

that may lead to sampling errors or complications. In addition, such assessment does not reflect the whole disease burden and activity.

Functional imaging plays a pivotal role in the diagnosis and treatment follow-up in patients with infectious or inflammatory diseases. Morphological imaging methods, such as ultrasound, computed tomography (CT) and magnetic resonance imaging (MRI) are commonly used, but focus on morphological changes and tissue distortions, which often occur at a later disease stage. In contrast, functional imaging methods, such as positron emission tomography (PET) are able to detect functional changes already at an earlier stage, and are able to evaluate treatment response after a few days or weeks. The combination of PET and CT (PET/CT) makes it possible to image functional and anatomical changes in one single imaging session.

2. Evidence

The most commonly used radiopharmaceutical (tracer) for this functional imaging of infectious and inflammatory diseases is [^{18}F] fluorodeoxyglucose (FDG). The past decade, plenty of evidence has become available for the use of [^{18}F]FDG-PET/CT in a broad range of infectious and inflammatory indications. The Inflammation & Infection Committee of the European Association of Nuclear Medicine (EANM), consisting of experts in the field, has dedicatedly worked on processing this evidence into workable diagnostic flowcharts, guidelines, and procedural recommendations for the optimum use of these nuclear medicine imaging techniques in close collaboration with and involvement of the clinical societies. This has resulted in widely adopted guidelines and recommendations for infective endocarditis (2, 3), vasculitis and polymyalgia rheumatica (4), vascular graft infections (5, 6), peripheral bone infection (7), prosthetic joint infection (8), and spondylodiscitis (9). Furthermore, [^{18}F]FDG-PET/CT can be considered as an invaluable imaging tool in, e.g., patients with fever of unknown origin, both in adults and in children (10, 11), patients with bacteremia at high-risk (12), fungal infections (13, 14) and infected renal or liver cysts (15, 16).

3. Limitations

Although [^{18}F]FDG-PET/CT has been proven a good method for several indications as shown above with acceptable diagnostic accuracy in most infectious and inflammatory diseases, it also presents several limitations. The most important one is linked to the lack of specificity of [^{18}F]FDG uptake. Both infectious and inflammatory conditions demonstrate increased [^{18}F]FDG uptake, making it very challenging to differentiate between infection and inflammation. In addition to immune cells, cancer cells also show enhanced [^{18}F]-FDG uptake, thereby further challenging the diagnostic process. Another well-known limitation of [^{18}F]FDG is the physiologic uptake throughout the body, but especially in the brain, the intestines and the urinary tract, hereby limiting the possibility to detect infection or inflammation in those organs/tissues. Thirdly, diagnosing an infection shortly after therapeutic interventions (surgery or radiation therapy) may cause difficulties, since cells involved in the wound healing process and granulation tissue also cause an increased tracer uptake. Reactive uptake due to foreign body material may occur in, e.g., vascular grafts, orthopedic implants, or prosthetic heart valves. Finally, several drugs are known to influence [^{18}F]FDG uptake. Metformin increases intestinal glucose uptake, insulin (but also exercise-induced insulin secretion) results in elevated [^{18}F]FDG uptake in physiological tissues (e.g., muscles), antibiotics (>7 days) are associated with a lower chance of revealing an infection focus, and corticosteroids (>10 days) reduce the sensitivity for diagnosing inflammation (e.g., vasculitis) (17).

4. Future

As illustrated above, [^{18}F]FDG-PET/CT is an excellent tool when searching for infection or inflammation, but its non-specificity is a major drawback. Consequently, we keep searching for new radiopharmaceuticals and to obtain as much information as possible to prevent, diagnose and ideally cure these diseases. The research community continues to develop better imaging techniques and equipment, and more specific radiopharmaceuticals. We remain steadfast in our determination to achieve diagnostically accurate imaging of infection and inflammation enabling to discriminate with high precision between infection, inflammation and malignancy. We keep on looking for this "holy grail" in nuclear medicine by focusing on two major research areas to achieve this goal.

4.1. Toward more specific tracers

Advances in disease understanding and translational medicine have taken us to the next level of practicing medicine. Personalized medicine has come within our grasp and has the potential to provide optimized treatment based on individual patient characteristics. Oncology is leading this new way of practicing with multiple examples of clinical translation of molecular disease characteristics into personalized treatment strategies that are becoming the standard of care. In analogy to cancer, nuclear medicine techniques offer the unique opportunity to target cell subpopulations and molecules that are involved in infectious and inflammatory lesions, to select patients who will most likely benefit from a particular treatment and for early therapy follow-up. Nuclear medicine provides the opportunity to highlight the cell types and subtypes that are involved in the process, the presence of a pathogen (bacteria of fungus), or the involvement of cytokines and chemokines. Several developments are ongoing in this area, e.g., the use of radiolabeled lymphocytes and macrophages (18, 19). [^{68}Ga]/[^{18}F] labeled fibroblast activation protein inhibitor (FAPI), developed for oncological indications, is nowadays more and more used in inflammatory diseases for detecting active fibroblasts. Furthermore, pilot studies using specific tracers for detecting bacterial infections (20, 21) look promising. One can envision that it could become possible in the near future to tell the clinician not only that there is an infection, but also reveal the bacterial type (Gram positive or Gram negative) causing the infection, hereby guiding antibiotic treatment in an early phase.

4.2. Toward a higher sensitivity

The first commercial introduction of PET was in 1978, but it took another 15 years until PET really became a clinically used imaging

system. The real changes occurred in the 21st century, first by introducing hybrid PET/CT camera systems, followed in 2018 by the introduction of the first digital PET/CT systems leading to important improvements in spatial resolution and signal-to-noise ratios. Despite all these advances, an average whole-body PET/CT acquisition takes around 20 min.

Another hybrid imaging technique, PET/MRI, has been introduced a couple of years ago, but did not change the nuclear medicine community as expected. At this moment, it remains more or less a research tool, with specific advantages for specific indications, but its high costs, complexity, and long scanning time remain important limitations. In the field of infection and inflammation, however, PET/MRI could be beneficial in particular cases, such as cardiac sarcoidosis and amyloidosis, inflammatory bowel diseases, diabetic foot infections and osteomyelitis, and especially in children with infection because of the significant lower radiation exposure (22).

More recently, the next game-changing technology is the large axial field of view (LAFOV) PET/CT camera, with a substantial increase in sensitivity, hereby allowing for faster scanning and/or an important reduction in injected activity, hence radiation burden (23, 24). The first LAFOV PET/CT cameras have now been installed in larger nuclear medicine departments.

For infection and inflammation imaging, these LAFOV PET/CT scanners have four major advantages:

1. LAFOV systems enable ultrafast whole-body scanning within 2–3 min compared to the standard 15–20 min acquisition on conventional PET/CT systems This is particularly beneficial for critically ill patients, patients admitted to the Intensive Care Unit, patients who suffer from pain/discomfort, or children who can now be scanned without the need for sedation (25).
2. The increased sensitivity may enable us to detect infections or inflammatory processes that were not detectable using conventional PET/CT scanners due to low metabolic activity of the disease process (chronic low-grade infections, infections with low bacterial load) or due to limited sensitivity (biofilms on prosthetic material, inflammation of cranial vessels, e.g., temporal and maxillary arteries).
3. The higher sensitivity makes it possible to scan at later time points, even after 4 or 5 half-lives of the radionuclide. This may be beneficial for some indications to have a better discrimination between perfusion/blood pool activity and inflammation, e.g., in large vessel vasculitis or cardiac sarcoidosis.
4. It is now possible to perform dynamic imaging with all the major organs in the same field of view. Since [^{18}F]FDG uptake in infectious and inflammatory processes is a dynamic process, dynamic imaging may show differences in glucose metabolism kinetics between infection and inflammation, thereby hopefully allowing to differentiate between both.

While we are working on these new specific radiopharmaceuticals and evaluating all the developments in software and hardware, we still have some other issues to solve in the next years. One of them is the challenge to image the immune system, since all the cells involved in infection, inflammation and tumorigenesis are highly interconnected. Targeting one particular cell subpopulation to reach higher specificity is therefore challenging. This may be solved perhaps in the combination of radiopharmaceuticals ("cocktails") to enhance the characterization of these complex biological processes.

Another issue may be the infrastructure of nuclear medicine departments. Having the choice of various radiopharmaceuticals to image disease processes in day-to-day practice is a great molecular weapon to personalize the patient's management. However, this requires investments in local infrastructure and distribution facilities.

5. Conclusion

Nuclear medicine imaging techniques are now widely accepted and increasingly used for diagnosing and treatment monitoring of infectious and inflammatory diseases. The latter has been exemplified by numerous recent clinical guidelines in which PET imaging is now part of the diagnostic flowcharts. And the future looks bright with huge developments in both camera systems (LAFOV PET/CT) and in specific infection and inflammation tracers. In the next years, we should make use of these developments and facilitate a smooth translation in clinical practice to finally be able to differentiate between tumor and infection, between infection and inflammation, and to evaluate therapy in an early phase, aiming at a better personalized care. The race to find the holy grail of nuclear imaging in infections continues and, step by step, gets closer to the finish. However, this requires a continuing and close collaboration with clinicians and well-designed prospective studies.

Data availability statement

The original contributions presented in the study are included in the article/supplementary material, further inquiries can be directed to the corresponding author.

Author contributions

AG and OG contributed to the conception and design of this manuscript. AG wrote the first draft of the manuscript. All authors contributed to the article and approved the submitted version.

Conflict of interest

The authors declare that the research was conducted in the absence of any commercial or financial relationships that could be construed as a potential conflict of interest.

Publisher's note

References

1. WHO. *Antimicrobial Resistance*. Available at: https://www.who.int/news-room/fact-sheets/detail/antimicrobial-resistance

2. Habib, G, Lancellotti, P, Antunes, MJ, Bongiorni, MG, Casalta, JP, del Zotti, F, et al. ESC guidelines for the management of endocarditis: the Task Force for the management of infective endocarditis of the European Society of Cardiology (ESC). Endorsed by: European Association for Cardio-Thoracic Surgery (EACTS), the European Association of Nuclear Medicine (EANM). *Eur Heart J*. (2015) 36:3075–128. doi: 10.1093/eurheartj/ehv319

3. Slart, RHJA, Glaudemans, AWJM, Gheysens, O, Lubberink, M, Kero, T, Dweck, MR, et al. Procedural recommendations of cardiac PET/CT imaging: standardization in inflammatory-, infective-, infiltrative-, and innervation (4Is)-related cardiovascular diseases: a joint collaboration of the EACVI and the EANM. *Eur J Nucl Med Mol Imaging*. (2021) 48:1016–39. doi: 10.1007/s00259-020-05066-5

4. Slart, RHJA, Glaudemans, AWJM, Chareonthaitawee, P, Treglia, G, Besson, FL, Bley, TA, et al. FDG-PET/CT(A) imaging in large vessel vasculitis and polymyalgia rheumatica: joint procedural recommendation of the EANM, SNMMI, and the PET Interest Group (PIG), and endorsed by the ASNC. *Eur J Nucl Med Mol Imaging*. (2018) 45:1250–69. doi: 10.1007/s00259-018-3973-8

5. Chakfé, N, Diener, H, Lejay, A, Assadian, O, Berard, X, Caillon, J, et al. European Society for Vascular Surgery (ESVS) 2020 clinical practice guidelines on the management of vascular graft and endograft infections. *Eur J Vasc Endovasc Surg*. (2020) 59:339–84. doi: 10.1016/j.ejvs.2019.10.016

6. Lauri, C, Signore, A, Glaudemans, AWJM, Treglia, G, Gheysens, O, Slart, RHJA, et al. Evidence-based guideline of the European Association of Nuclear Medicine (EANM) on imaging infection in vascular grafts. *Eur J Nucl Med Mol Imaging*. (2022) 49:3430–51. doi: 10.1007/s00259-022-05769-x

7. Glaudemans, AWJM, Jutte, PC, Cataldo, MA, Cassar-Pullicino, V, Gheysens, O, Borens, O, et al. Consensus document for the diagnosis of peripheral bone infection in adults: a joint paper by the EANM, EBJIS, and ESR (with ESCMID endorsement). *Eur J Nucl Med Mol Imaging*. (2019) 46:957–70. doi: 10.1007/s00259-019-4262-x

8. Signore, A, Sconfienza, LM, Borens, O, Glaudemans, AWJM, Cassar-Pullicino, V, Trampuz, A, et al. Consensus document for the diagnosis of prosthetic joint infections: a joint paper by the EANM, EBJIS, and ESR (with ESCMID endorsement). *Eur J Nucl Med Mol Imaging*. (2019) 46:971–88. doi: 10.1007/s00259-019-4263-9

9. Lazzeri, E, Bozzao, A, Cataldo, MA, Petrosillo, N, Manfrè, L, Trampuz, A, et al. Joint EANM/ESNR and ESCMID-endorsed consensus document for the diagnosis of spine infection (spondylodiscitis) in adults. *Eur J Nucl Med Mol Imaging*. (2019) 46:2464–87. doi: 10.1007/s00259-019-04393-6

10. van Rijsewijk, ND, IJpma, FF, Wouthuyzen-Bakker, M, and Glaudemans, AW. Molecular imaging of fever of unknown origin: an update. *Semin Nucl Med*. (2023) 53:4–17. doi: 10.1053/j.semnuclmed.2022.07.002

11. Pijl, JP, Kwee, TC, Legger, GE, Peters, HJH, Armbrust, W, Schölvinck, EH, et al. Role of FDG-Pet/CT in children with fever of unknown origin. *Eur J Nucl Med Mol Imaging*. (2020) 47:1596–604. doi: 10.1007/s00259-020-04707-z

12. Pijl, JP, Glaudemans, AWJM, Slart, RHJA, Yakar, D, Wouthuyzen-Bakker, M, and Kwee, TC. FDG-PET/CT for detecting an infection focus in patients with bloodstream infection: factors affecting diagnostic yield. *Clin Nucl Med*. (2019) 44:99–106. doi: 10.1097/RLU.0000000000002381

13. Ankrah, AO, Span, LF, Klein, HC, de Jong, PA, Dierckx, RAJO, Kwee, TC, et al. Role of FDG PET/CT in monitoring treatment response in patients with invasive fungal infections. *Eur J Nucl Med Mol Imging*. (2019) 46:174–83. doi: 10.1007/s00259-018-4192-z

14. Ankrah, AO, Lawal, IO, Dierckx, RAJO, Sathekge, MM, and Glaudemans, AWJM. Imaging of invasive fungal infections – The role of PET/CT. *Semin Nucl Med*. (2023) 53:57–69. doi: 10.1053/j.semnuclmed.2022.07.003

15. Neuville, MF, Lovinfosse, O, Jadoul, A, Thys, M, Seidel, L, Hustinx, R, et al. The use of a visual 4-point scoring scale improves the yield of ^{18}F-FDG-PET-Ct imaging in the diagnosis of renal and hepatic cyst infection in patients with autosomal dominant polycystic kidney disease. *Eur J Nucl Med Mol Imaging*. (2021) 48:254–9. doi: 10.1007/s00259-020-04903-x

16. Pijl, JP, Kwee, TC, Slart, RHJA, and Glaudemans, AWJM. FDG-PET/CT for diagnosis of cyst infection in autosomal dominant polycystic kidney disease. *Clin Transl Imaging*. (2018) 6:61–7. doi: 10.1007/s40336-017-0261-8

17. Pijl, JP, Nienhuis, PH, Kwee, TC, Glaudemans, AWJM, Slart, RHJA, and Gormsen, LC. Limitations and pitfalls of FDG-PET/CT in infection and inflammation. *Semin Nucl Med*. (2021) 51:633–45. doi: 10.1053/j.semnuclmed.2021.06.008

18. van der Veen, EL, Antunes, IF, Maarsingh, P, Hessels-Scheper, J, Zijlma, R, Boersma, HH, et al. Clinical-grade N-(4-[^{18}F]fluorobenzoyl)-interleukin-2 for PET imaging of activated T-cells in humans. *EJNMMI Radiopharm Chem*. (2019) 4:15. doi: 10.1186/s41181-019-0062-7

19. Verweij, NJF, Yaqub, M, Bruijnen, STG, Pieplenbosch, S, Ter Wee, MM, Jansen, G, et al. First in man study of [^{18}F]fluoro-PEG-folate PET: a novel macrophage imaging technique to visualize rheumatoid arthritis. *Sci Rep*. (2020) 10:1047. doi: 10.1038/s41598-020-57841-x

20. Krekorian, M, Cortenbach, KRG, Boswinkel, M, Kip, A, Franssen, GM, Veltien, A, et al. In vivo PET imaging of monocytes labeled with [^{89}Zr]Zr-PLGA-NH_2 nanoparticles in tumor and *Staphylococcus aureus* infection models. *Cancers*. (2021) 13:5069. doi: 10.3390/cancers13205069

21. Yao, S, Xing, H, Zhu, W, Wu, Z, Zhang, Y, Ma, Y, et al. Infection imaging with (18) F-FDS and first-in-human evaluation. *Nucl Med Biol*. (2016) 43:206–14. doi: 10.1016/j.nucmedbio.2015.11.008

22. Sollini, M, Berchiolli, R, Kirienko, M, Rossi, A, Glaudemans, AWJM, Slart, RHJA, et al. PET/MRI in infection and inflammation. *Semin Nucl Med*. (2018) 48:225–41. doi: 10.1053/j.semnuclmed.2018.02.003

23. Slart, RHJA, Tsoumpas, C, Glaudemans, AWJM, Noordzij, W, Willemsen, ATM, Borra, RJH, et al. Long axial field of view PET scanners: a road map to implementation and new possibilities. *Eur J Nucl Med Mol Imaging*. (2021) 48:4326–245.

24. Van Sluis, J, Borra, R, Tsoumpas, C, van Snick, JH, Roya, M, Ten Hove, D, et al. Extending the clinical capabilities of short- and long-lived positron-emitting radionuclides through high sensitivity PET/CT. *Cancer Imaging*. (2022) 22:69. doi: 10.1186/s40644-022-00507-w

25. Van Rijsewijk, ND, van Leer, B, Ivashchenko, OV, Schölvinck, EH, van den Heuvel, F, et al. Ultra-low dose infection imaging of a newborn without sedation using long axial field-of-view PET/CT. *Eur J Nucl Med Mol Imaging*. (2022), online ahead of print.) 50:622–3. doi: 10.1007/s00259-022-05979-3

frontiers | Frontiers in Medicine

TYPE Original Research
PUBLISHED 27 March 2023
DOI 10.3389/fmed.2023.1143473

OPEN ACCESS

EDITED BY
Giorgio Treglia,
Ente Ospedaliero Cantonale (EOC), Switzerland

REVIEWED BY
Fang Xie,
Fudan University, China
Haojun Chen,
First Affiliated Hospital of Xiamen University, China
Xiaowei Ma,
Second Xiangya Hospital, Central South University, China

*CORRESPONDENCE
Wei Cao
✉ caowei@hust.edu.cn
Dawei Jiang
✉ daweijiang@hust.edu.cn

SPECIALTY SECTION
This article was submitted to Nuclear Medicine, a section of the journal Frontiers in Medicine

RECEIVED 13 January 2023
ACCEPTED 28 February 2023
PUBLISHED 27 March 2023

CITATION
Ding Y, Liu Y, Zhang L, Deng Y, Chen H, Lan X, Jiang D and Cao W (2023) Quantitative assessment of renal functions using ^{68}Ga-EDTA dynamic PET imaging in renal injury in mice of different origins. *Front. Med.* 10:1143473. doi: 10.3389/fmed.2023.1143473

Quantitative assessment of renal functions using ^{68}Ga-EDTA dynamic PET imaging in renal injury in mice of different origins

Ying Ding[1,2,3], Yu Liu[1,2,3], Li Zhang[1,2,3], Yinqian Deng[1,2,3], Huanyu Chen[1,2,3], Xiaoli Lan[1,2,3], Dawei Jiang[1,2,3]* and Wei Cao[1,2,3]*

[1]Department of Nuclear Medicine, Union Hospital, Tongji Medical College, Huazhong University of Science and Technology, Wuhan, China, [2]Hubei Key Laboratory of Molecular Imaging, Wuhan, China, [3]Key Laboratory of Biological Targeted Therapy, The Ministry of Education, Wuhan, China

Background: Early detection of kidney diseases can be challenging as conventional methods such as blood tests or imaging techniques (computed tomography (CT), magnetic resonance imaging (MRI), or ultrasonography) may be insufficient to assess renal function. A single-photon emission CT (SPECT) renal scan provides a means of measuring glomerular filtration rates (GFRs), but its diagnostic accuracy is limited due to its planar imaging modality and semi-quantification property. In this study, we aimed to improve the accuracy of GFR measurement by preparing a positron emission tonometry (PET) tracer ^{68}Ga-Ethylenediaminetetraacetic acid (^{68}Ga-EDTA) and comprehensively evaluating its performance in healthy mice and murine models of renal dysfunction.

Methods: Dynamic PET scans were performed in healthy C57BL/6 mice and in models of renal injury, including acute kidney injury (AKI) and unilateral ureter obstruction (UUO) using ^{68}Ga-EDTA. In a 30-min dynamic scan, PET images and time-activity curves (TACs) were acquired. Renal function and GFR values were measured using renograms and validated through serum renal function parameters, biodistribution results, and pathological staining.

Results: ^{68}Ga-EDTA dynamic PET imaging quantitatively captured the tracer elimination process. The calculated GFR values were 0.25 ± 0.02 ml/min in healthy mice, 0.01 ± 0.00 ml/min in AKI mice, and 0.25 ± 0.04, 0.29 ± 0.03 and 0.24 ± 0.01 ml/min in UUO mice, respectively. Furthermore, ^{68}Ga-EDTA dynamic PET imaging and GFR_{PET} were able to differentiate mild renal impairment before serum parameters indicated any changes.

Conclusions: Our findings demonstrate that ^{68}Ga-EDTA dynamic PET provides a reliable and precise means of evaluating renal function in two murine models of renal injury. These results hold promise for the widespread clinical application of ^{68}Ga-EDTA dynamic PET in the near future.

KEYWORDS

nuclear medicine, glomerular filtration rate, PET imaging, kidney injury, ^{68}Ga-EDTA

1. Introduction

The assessment of renal function is crucial in determining patient treatment and management in clinical practice. The most commonly used clinical measurements include serum creatinine (Cr), urea nitrogen (BUN), and cystatin C (Cys-C) to rapidly and cost-effectively reflect renal function (1). As the glomerular filtration rate (GFR) decreases, these biomarkers increase, particularly when GFR falls below 60 ml/min (1.73 m^2) (2). However, due to the wide range and frequent fluctuations of these serum markers, it can be difficult to detect increased serum levels and respond to renal injury in a timely manner. Measured GFR (mGFR) provides a quantitative evaluation of renal filtration capacity, but the gold standard for measuring GFR, which involves testing plasma and urinary clearance rates of inulin, is not widely used due to its high cost and its time-consuming and repetitive natures (3). Imaging-based techniques to measure renal function have been developed and may replace traditional methods, which include iohexol-enhanced computed tomography (CT) (4) and gadolinium-enhanced magnetic resonance renography (MRR) (5, 6), as well as nuclear medicine renal imaging. These techniques can directly reflect changes in renal anatomy and visualize the passage of contrast agents through the kidney. However, the use of milligram-scale CT or magnetic resonance (MR) contrast agents can cause tubular reabsorption (7), and large doses may increase the risk of allergy or nephrotoxicity (8).

Nuclear imaging techniques, such as single-photon emission CT (SPECT) and positron emission tomography (PET), provide dynamic renal imaging by using traces of radioactive probes that are specifically filtered or reabsorbed by the kidney to visualize excretion and measure GFR. The most commonly used nuclear imaging method to assess renal function in clinical practice is the ^{99m}Tc-diethylenetriaminepentaacetic acid (^{99m}Tc-DTPA) renal scan, which plays a crucial role in the assessment of unilateral renal function, renovascular hypertension, hydronephrosis, and renal transplantation. However, GFR values obtained from ^{99m}Tc-DTPA SPECT imaging can often be unreliable, especially in patients with renal abnormalities and excessive body weight or in pediatric patients. This is due to the limitations of SPECT imaging, including non-individualized renal depth correction and semi-quantitative capabilities, which may result in biased GFR values (9–11). Furthermore, SPECT planar imaging provides limited information, especially in patients with space-occupying lesions in the kidney, leading to inaccurate and redundant examinations and increased costs.

Positron emission tonometry presents a possible solution to assess GFR in a non-invasive manner. The superior three-dimensional (3D) capabilities of PET detectors improve quantitative and localization accuracy compared to the limitations of SPECT planar imaging. This allows for the direct measurement of GFR by integrating information related to the spatial position of the kidney and the excretion kinetics of the tracer. Additionally, the high sensitivity of PET imaging enables the use of a lower administration activity compared to SPECT, reducing the risk of toxic effects and radiation exposure to ensure patient safety (12). This feature makes PET a particularly advantageous option for pediatric patients and those with severely impaired renal function, where an accurate assessment of GFR is crucial in making informed clinical treatment decisions.

Ethylenediaminetetraacetic acid (EDTA) is a well-known chelating agent and has a history of use in radiochemistry research. It has a robust capacity to form stable complexes with most metal ions and is known to be entirely filtered by the renal glomerulus (13, 14). ^{51}Cr-EDTA has properties similar to inulin, and its blood clearance rate is extensively used to estimate GFR in Europe. However, due to the limited availability of Cr-51, this method is gradually being phased out. Compared to DTPA, EDTA has significantly less binding to plasma proteins, leading to rapid and specific glomerular filtration (15). Ga-68, with its short half-life (68 min) and high decay energy, obtained from a ^{68}Ge-^{68}Ga generator, is an excellent choice for renal PET imaging. These properties make ^{68}Ga-EDTA a promising candidate to meet the requirements of an ideal renal tracer. Our previous studies have confirmed that the renal excretion curve of ^{68}Ga-EDTA aligns well with a one-compartment elimination pharmacokinetic model curve (16). Dynamic imaging data from ^{68}Ga-EDTA PET/CT can be used to directly calculate total GFR and split renal GFR in mice. In this study, we aimed to comprehensively evaluate the potential application of ^{68}Ga-EDTA in the quantification of GFR in healthy animals as well as in mice with renal dysfunction, such as rhabdomyolysis-induced acute kidney injury (AKI) and unilateral ureter obstruction (UUO), and to provide a user-friendly GFR measurement procedure.

2. Materials and methods

2.1. Materials

All chemicals were purchased from Aladdin Biochemical Technology Co., Ltd. (China) as reagent grade and used as received without further purification unless otherwise stated.

2.2. Radiolabeling and quality control

Ga-68 was eluted from a ^{68}Ge/^{68}Ga-generator (ITG, Germany) with the eluent of 0.05 M HCl. ^{68}Ga-EDTA was prepared by mixing 10 μl of EDTA (0.5 M, pH = 8.0) and 37 MBq of $^{68}GaCl_3$ (17, 18), and pH was adjusted to ~5 by adding the NaOAc buffer (0.02 M, pH = 6.8). Radiochemical purity (RCP) of ^{68}Ga-EDTA was performed using instant thin-layer chromatography (TLC) silica gel plates (Agilent Technologies, Inc., CA, USA), developed with 0.2 M sodium acetate (pH = 4.5), and analyzed by a TLC scanner (Zhongcheng Tech. Co., Ltd., Hefei, China). Radiolabeling efficiency was determined by the γ-counter (2470 Automatic Gamma Counter, WIZARD, PerkinElmer, Norwalk CT, USA) ($n = 3$). The stability of ^{68}Ga-EDTA *in vitro* was examined in phosphate buffer solution (PBS) and fetal bovine serum (FBS). ^{68}Ga-EDTA was mixed with PBS and 10% FBS in a ratio of 1:2 and incubated in a water bath at 37°C. The mixture supernatant was developed using ITLC-SG and analyzed by TLC and the γ-counter at 30, 60, and 120 min.

2.3. Animal studies

Animal experiments were performed on male C57BL/6 mice (8 weeks, 19–22 g, Hubei Biont Biotechnology Co., Ltd., China). All animal protocols were reviewed and approved by the Institutional Animal Care and Use Committee of Tongji Medical College of Huazhong University of Science and Technology.

2.3.1. Establishment of the AKI model

All mice were deprived of water for 24 h before the establishment of AKI. Glycerol (50% v/v in 0.9% saline) was injected into the hind limb of each mouse (8 ml/kg, *i.m.*) after water deprivation. PET imaging and biodistribution studies were performed 24 h after injection.

2.3.2. Establishment of the UUO model

All mice were anesthetized with 2% isoflurane (RWD Life Science Co., Ltd., Shenzhen, China). A vertical incision was made in the abdominal wall of the mouse, exposing the left ureter and the lower pole of the kidney. The ureter was ligated in two points using a 4.0 silk and cut in half. The wound was sewn up using a 4.0 silk. Operations were performed in a sterile environment to avoid animal infection. Scanning experiments were performed on postoperative days 1, 8, and 22.

2.4. Small animal dynamic PET/CT renal imaging

^{68}Ga-EDTA dynamic PET was performed on Trans PET Discoverist 180 (RAYCAN Technology Co., Ltd., Suzhou, China). Mice were anesthetized with 2% isoflurane and then placed on a scanner bed with their tail vein catheterized. Along with the 30-min dynamic PET scan, simultaneous intravenous injection of ^{68}Ga-EDTA (2.80 ± 0.24 MBq/50 μl) was performed. Based on our previous study, tracer injection was accomplished within the initial 10 s to obtain an eligible blood perfusion curve in the kidneys. CT scanning was performed directly after PET scanning and reconstructed with an image matrix size of 512*512*512. The dynamic image was reconstructed using the 3-D ordered subset expectation maximization algorithm with point spread function modeling (OSEM-3D-PSF) reconstruction algorithm. The 30-min list-mode files were divided into 28 frames (10 s*6, 30 s*6, 60 s*6, and 120 s*10). For each frame, we implemented an OSEM-3D-PSF with two iterations and 12 subsets. The image matrix size for OSEM-3D-PSF is 320 × 320 × 200 with isotropic voxel sizes of 0.5 mm × 0.5 mm × 0.5 mm.

2.5. Renogram analysis

The reconstructed PET/CT data were processed and analyzed using Siemens Inveon Research Workplace software version 4.2 for volume-of-interest (VOI) analysis. CT images and PET/CT fusion images were used to guide the VOIs due to the partial volume effect. We manually delineated the VOIs of the heart, bilateral kidneys, and bladder. The Inveon Research Workspace was used to automatically calculate the radioactivity within the VOIs of each frame. We located standardized VOIs of the heart's left ventricle near the cardiac apex with a volume of 27 voxels (3*3 *3) to reduce the influence of cardiac muscles. The VOIs of the kidneys were delineated by the CT images, especially for animals with a renal disease. We defined elliptical VOIs in the bilateral kidneys that are appressed to the lower pole of the kidney and semiautomatically adjusted them according to the radioactive distribution in the kidney. We defined VOIs of the bladder by their signal intensity on CT images. Time-activity curves (TACs) were generated using the radioactivity in each frame in VOIs plotted against the time point of each frame. The renogram was defined as TAC of each kidney. In addition, for further quantitative assessment, four novel indicators were used. Time-to-peak (T_{max}), peak value, and time to half-maximum ($T_{1/2}$) were obtained by analyzing the renogram (19). Blood perfusion parameter (BP) was denoted as the slope of the renogram from 0 min to T_{max}, and renal elimination parameter (EP) was denoted as the slope of the renogram from T_{max} to 30 min.

2.6. GFR calculation

The area under the curve (AUC) method was used to calculate the mouse GFR (20–23). Our previous study demonstrated the reliability of this method compared with others and showed good consistency with the blood clearance of ^{68}Ga-EDTA (16). Briefly, we hypothesized that ^{68}Ga-EDTA was excreted by the kidney at a stable rate, and this radiopharmaceutical was only filtered through glomerulus irreversibility; the GFR of each mouse can be calculated as:

$$\mathrm{GFR} = \frac{\mathrm{Activity}_{\mathrm{bladder}}(30\ \mathrm{min})}{\int_{0\ \mathrm{min}}^{30\ \mathrm{min}} \mathrm{Activity}_{\mathrm{plasma}}\mathrm{dt}} \quad (1)$$

The radioactivity in plasma was corrected with the blood radioactivity concentration and hematocrit (Hct), as mentioned in the following formula (24, 25):

$$\mathrm{Activity}_{\mathrm{plasma}}(t) = \mathrm{Activity}_{\mathrm{blood}}(t) \times \frac{1}{(1 - Hct)} \quad (2)$$

Referring to Gate's method, we defined the split GFR of each kidney as the ratio of $\mathrm{AUC}_{\mathrm{splitkidney}}$ to $\mathrm{AUC}_{\mathrm{bilateralkidneys}}$ from 1 to 2 min multiplied by the total GFR, and the formula is:

$$\text{Split GFR} = \frac{\text{AUC of split kidney}_{1-2\ \mathrm{min}}}{\text{AUC of bilateral kidneys}_{\ 1-2\ \mathrm{min}}} \times \mathrm{GFR} \quad (3)$$

2.7. Biodistribution study

The blood, brain, heart, lung, liver, spleen, kidneys, stomach, small intestine, large intestine, muscle, bone, and whole tail were taken 30 min after the tracer injection. Samples were washed three times with PBS, dried, and weighed. The radioactivity of each

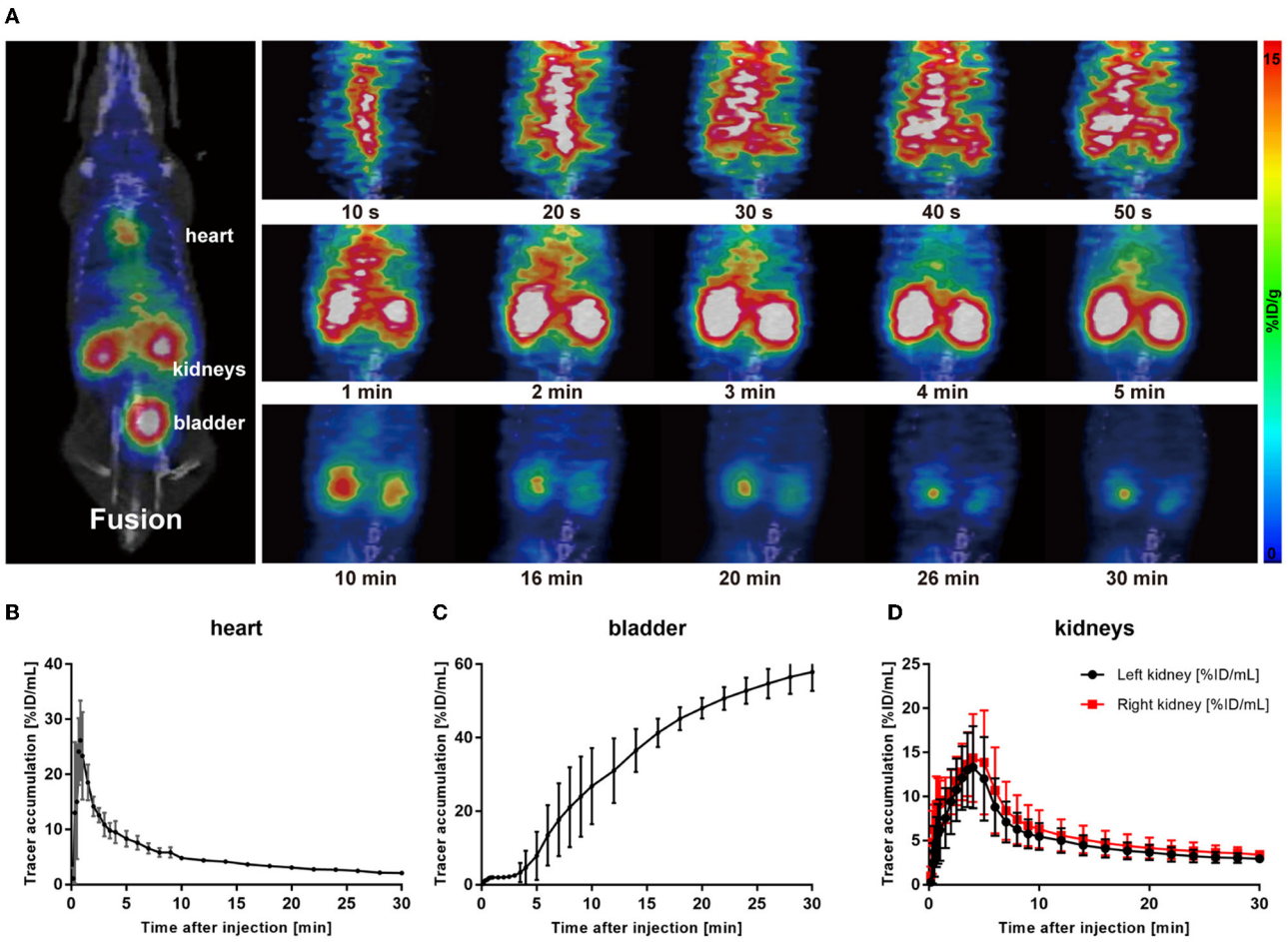

FIGURE 1
^{68}Ga-EDTA dynamic positron emission tonometry (PET)/computed tomography (CT) imaging of healthy mice. **(A)** Coronal fusion images of ^{68}Ga-EDTA dynamic PET/CT scanning in healthy mice after intravenous injection of ^{68}Ga-EDTA. **(B)** The heart time-activity curve (TAC) of healthy mice was obtained *via* PET imaging. **(C)** The bladder TAC of healthy mice was obtained *via* PET imaging. **(D)** The renograms of healthy mice were obtained *via* PET imaging.

sample was determined using a γ-counter. The results of tissues' uptake were decay-corrected.

2.8. Biological toxicity tests and histopathology

Blood and tissue samples were collected from mice 24-h post-injection. The blood samples were collected for routine blood tests, Cr, BUN, serum alanine aminotransferase (ALT), and aspartate aminotransferase (AST). Tissues were collected after blood collection and fixed with 4% paraformaldehyde at room temperature for 24 h for hematoxylin and eosin (H&E) and periodic acid-Schiff (PAS) staining.

2.9. Statistical analysis

GraphPad Prism software (Version 7.0, GraphPad Software, Inc., USA) and Origin 2021 software (OriginLab, Northampton, UK) were used to produce figures and compute statistical analyses. The quantitative data are presented as the mean ± standard deviation (SD). A one-way analysis of variance (ANOVA) test was performed to compare the difference between the healthy mice and the renal dysfunctional mice. The results were statistically significant when the p-value was <0.05.

3. Results

3.1. Radiochemistry

A facile radiolabeling method was developed by mixing ^{68}Ga (eluted with 0.1 M HCl) and EDTA (0.5 M, pH 8.0) for 10 min in a sodium acetate buffer (0.2 M, pH ~6.8). The labeling efficiency of ^{68}Ga-EDTA was over 99%. The stability of ^{68}Ga-EDTA was evaluated in PBS and FBS for 2 h and showed no significant decomposition (~95%), as shown in Supplementary Figure S1. These results indicate that ^{68}Ga-EDTA is a stable complex suitable for further investigation.

TABLE 1 Renogram information.

		Normal	AKI	UUO-1d	UUO-8d	UUO-22d
Peak value (%ID/mL)		14.78 ± 3.89	4.82 ± 0.56*	13.58 ± 6.20	12.00 ± 2.25	11.62 ± 0.69
T_{max} (min)		3.81 ± 0.96	3.13 ± 1.30	4.38 ± 3.84	2.17 ± 0.29	2.50 ± 0.87
$T_{1/2}$ (min)		7.63 ± 1.51	Not reached	14.00 ± 4.00	10.00 ± 6.93	7.67 ± 2.52
BP	R	3.57 ± 0.76	2.45 ± 1.41*	3.78 ± 1.48	5.52 ± 0.36	5.11 ± 2.00
(%ID/mL·min)	L	3.95 ± 0.73	1.39 ± 0.53*	1.54 ± 0.86*	0.77 ± 0.10*	0.55 ± 0.01*
EP	R	−0.48 ± 0.19	−0.05 ± 0.01	−0.39 ± 0.27	−0.31 ± 0.06	−0.32 ± 0.03
(%ID/mL·min)	L	−0.43 ± 0.14	−0.04 ± 0.01	0.42 ± 0.32	0.17 ± 0.12	0.04 ± 0.01

All parameters were compared with those of healthy mice individually using the one-way analysis of variance (ANOVA) test. *$p < 0.05$.

TABLE 2 ^{68}Ga-EDTA dynamic positron emission tonometry- (PET-) derived glomerular filtration rate (GFR).

		Normal	AKI	UUO-1d	UUO-8d	UUO-22d
Total GFR (mL/min)		0.25 ± 0.02	0.01 ± 0.00***	0.25 ± 0.04	0.29 ± 0.03	0.24 ± 0.01
AUC_{1-2min} (%)	R	0.55	0.57	0.68	0.80	0.78
	L	0.44	0.43	0.32	0.20	0.22
Split GFR (mL/min)	R	0.14	0.007	0.17	0.24	0.19
	L	0.11	0.005	0.08	0.06	0.05

All parameters were compared with those of healthy mice individually using the one-way ANOVA test. ***$p < 0.001$.

3.2. ^{68}Ga-EDTA dynamic PET/CT imaging of healthy mice

To demonstrate the performance of ^{68}Ga-EDTA eliminated in healthy mice, a 30-min dynamic PET scan was performed (Figure 1A). ^{68}Ga-EDTA was injected as a bolus through a tail vein catheter; this tracer circulated within the blood promptly within the first 10 s after injection and reached the bilateral kidneys as early as 40 s p.i., and the contour of the kidneys can be immediately observed. Up to 50 s p.i., ^{68}Ga-EDTA basically flowed out from the heart, and the kidneys were delineated ever more clearly. The renal cortex and pelvis can be distinguished from 1 to 6 min. At ∼5 min, a small amount of tracers started to appear in the bladder. This rapid renal elimination of ^{68}Ga-EDTA confirmed that the tracer was primarily filtered by the renal glomerulus, revealing negligible potential renal tubular reabsorption and secretion. No other obvious tracer retention can be seen in images during scanning, indicating that extra-renal elimination of ^{68}Ga-EDTA can be largely excluded. Biodistribution experiments were carried out at 30 min p.i. (Table 3 and Figure 6). Remaining ^{68}Ga-EDTA in the blood and organs were low. In the end of observation (30 min), the tracer had mainly accumulated in the bladder, and the blood concentration was lower than 0.3%ID/ml. Rapid renal excretion and low organ accumulation indicate the high biocompatibility of ^{68}Ga-EDTA. In the toxicity test, the routine blood test, renal function, and liver function parameters showed that ^{68}Ga-EDTA had no effects on renal function, hematopoietic function, or hepatic function (Supplementary Table S1). Pathological analysis of the tissue sections did not show any negative effects of ^{68}Ga-EDTA on the major organs (Supplementary Figure S3).

Radioactivity counts gained from four volumes of interest (VOIs) were plotted against time and then used to form a TAC of ^{68}Ga-EDTA (Figures 1B–D). Renogram specially refers to TAC of the split kidney (Figure 1D). The renal function was quantified by parameters mentioned in the method, including the peak value, T_{max}, $T_{1/2}$, BP, and EP (Table 1). Kidneys of healthy C57BL/6 mice have a rich supply of blood and powerful filtration capacity. Once the tracer entered the kidneys, it perfused with circulation and achieved dynamic balance during rapid distribution within the initial 60 s. During this process, the tracer was continuously filtered by the renal glomerulus. When the filtration was greater than the perfusion, the renogram started to present a downward trend. The excretion curve of ^{68}Ga-EDTA was fitted using a two-exponential decay (Supplementary Figure S2) with a $T_{1/2-Fast}$ of 1.93 ± 0.59 min and a $T_{1/2-Slow}$ of 17.54 ± 7.92 min. The tracer in the kidneys raised to the peak (T_{max}) at 3.81 ± 0.96 min with an average peak value of 14.78 ± 3.89%ID/ml. The blood perfusion in healthy kidneys was defined as BP with a ratio of 3.57 ±0.76%ID/ml·min for the right kidney and 3.95 ± 0.73%ID/ml·min for the left kidney. After arriving at the peak, the tracer started rapid diffusion followed by elimination. The kidneys excreted half of the tracer ($T_{1/2}$) at 7.63 ± 1.51 min. The average elimination speed of healthy mice was denoted as EP with a ratio of −0.48 ± 0.19%ID/ml·min for the right kidney and −0.43 ± 0.14%ID/ml·min for the left kidney. The GFR of healthy C57BL/6 mice calculated by ^{68}Ga-EDTA dynamic PET imaging is 0.25 ± 0.02 ml/min (Table 2), and the split GFR for the right and left kidney is 0.14 and 0.11 ml/min, respectively.

3.3. ^{68}Ga-EDTA dynamic PET/CT imaging of AKI mice

Acute kidney injury is a serious but common clinical syndrome which is induced by drug toxicity, renal parenchymal disease, or renovascular disease (26). Glycerol-induced AKI is

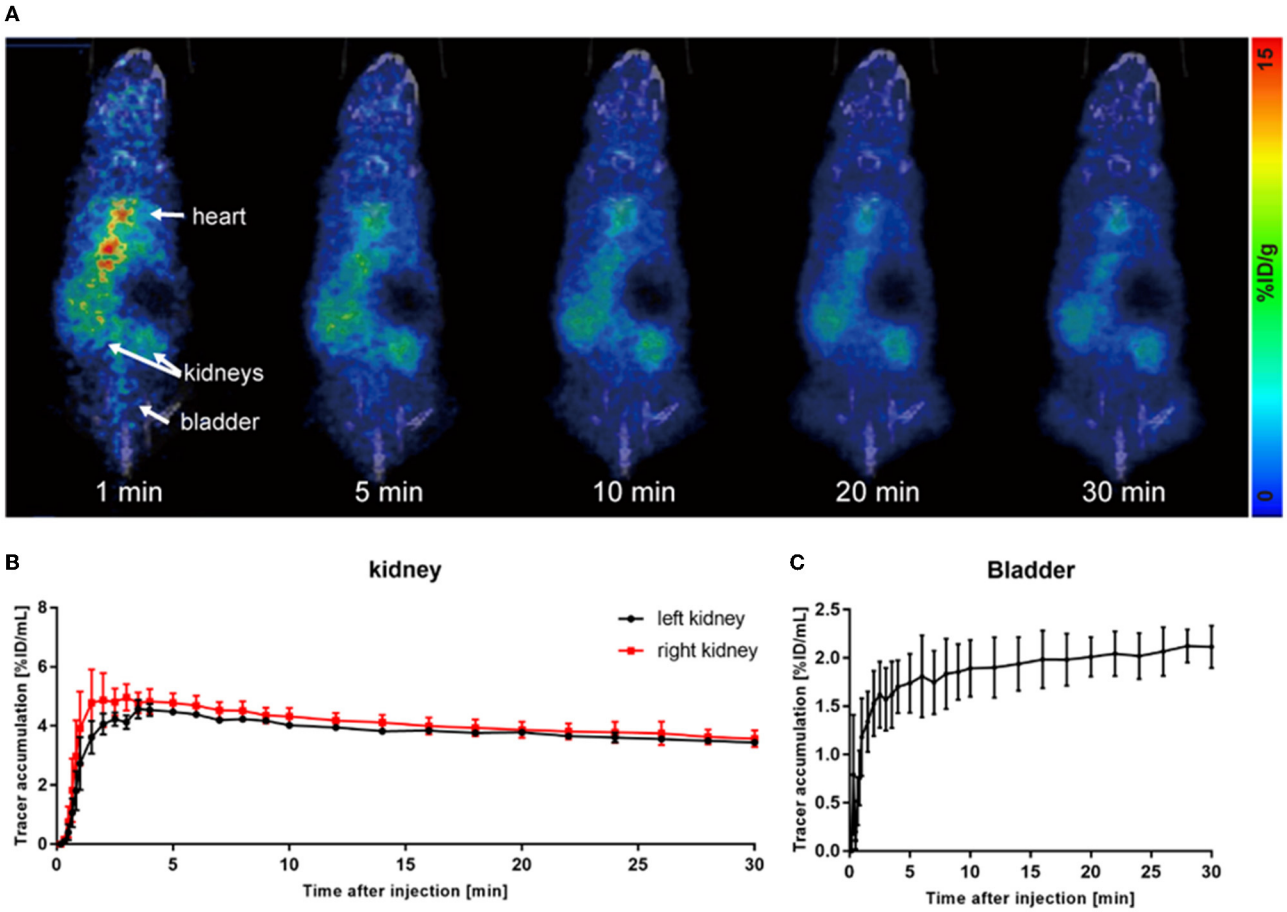

FIGURE 2
^{68}Ga-EDTA dynamic PET/CT imaging of acute kidney injury (AKI) mice. **(A)** Coronal fusion images of ^{68}Ga-EDTA dynamic PET/CT scanning in AKI mice. **(B)** The renograms of AKI mice were obtained *via* PET imaging. **(C)** The bladder TAC of AKI mice was obtained *via* PET imaging.

one of the most widely used models of acute renal dysfunction. The high dose of glycerol injected in the muscle induces rhabdomyolysis and results in a decrease in renal blood perfusion and renal tubular necrosis. In this study, we used the glycerol-AKI model to assess whether ^{68}Ga-EDTA PET scanning was suitable for the diagnosis of renal dysfunction. Within 24 h of glycerol injection, nephron necrosis was obviously observed in renal tissue sections, the renal tubular lumen became swollen, and renal tubular epithelial cells started desquamation and necrosis (Figure 5).

As shown in Figure 2A, most of the tracers circulated in the blood pool after injection, and only a small amount of tracers entered the kidneys. Eventually, almost no tracer was observed to be excreted into the bladder (Figure 2C). Due to the damage to the excretory capacity, the tracer still remained at a relatively high level in the heart until the end of observation. Renograms of AKI kidneys showed a low and flat curve (Figure 2B).

The quantitative analysis of the AKI renograms (Figures 4G, H) demonstrated that the kidneys of rhabdomyolysis-induced AKI had a reduced blood supply and impaired excretory function. ^{68}Ga-EDTA reached the peak at 3.13 ± 1.30 min (T_{max}) in kidneys of AKI, with an average peak value of 4.82 ± 0.56%ID/ml, and the average BP for the right kidney was 2.45 ± 1.41 and 1.39 ± 0.53%ID/ml·min for the left. The EP was −0.05 ± 0.01 and −0.04 ± 0.01%ID/ml·min for the right and left kidneys, respectively. All the indicators were lower than healthy ($p < 0.05$). No discernible downward trend appeared in the renograms over the observation period, and less than half of the tracer was excreted.

The average GFR value of AKI mice was 0.01 ± 0.00 ml/min, which was significantly lower than that of healthy mice (Figure 4C). The split GFR for right and left kidneys was 0.007 and 0.005 ml/min, respectively. For a more intuitive contrast, we assessed Cr and BUN in mice, both of which were significantly higher than in healthy mice (Figures 4A, B). Radioactivity biodistribution experiments were performed to verify the accuracy of dynamic PET scanning (Table 3 and Figures 6B, C). At 30 min p.i., the radioactivity in the blood exceeds 2.8%ID/g, which is 10 times higher than normal. In addition, all organs had a higher accumulation of radioactivity than healthy organs, which is consistent with the results from the PET images.

TABLE 3 Biodistribution of ^{68}Ga-EDTA in five groups.

Tissue	Control (%ID/g)	AKI (%ID/g)	UUO-1d (%ID/g)	UUO-8d (%ID/g)	UUO-22d (%ID/g)
Blood	0.266 ± 0.023	2.812 ± 2.463	1.338 ± 0.411	1.770 ± 0.631	1.223 ± 0.568
Brain	0.014 ± 0.005	0.107 ± 0.064	0.133 ± 0.086	0.152 ± 0.041	0.068 ± 0.046
Heart	0.056 ± 0.014	0.476 ± 0.519	0.328 ± 0.098	0.353 ± 0.124	0.237 ± 0.174
Lung	0.131 ± 0.039	1.479 ± 1.231	0.881 ± 0.318	1.232 ± 0.416	0.789 ± 0.496
Liver	0.205 ± 0.110	1.284 ± 0.267	1.034 ± 0.200	1.434 ± 0.919	0.708 ± 0.325
Spleen	0.708 ± 0.040	2.822 ± 1.438	3.465 ± 1.172	2.808 ± 1.735	1.252 ± 0.529
Kidneys	1.072 ± 0.230	7.416 ± 3.968	20.422 ± 5.582	8.088 ± 1.933	3.043 ± 0.804
Stomach	0.115 ± 0.096	0.755 ± 0.918	0.467 ± 0.099	0.521 ± 0.145	0.318 ± 0.211
Small intestine	0.052 ± 0.020	0.301 ± 0.268	0.206 ± 0.063	0.288 ± 0.046	0.137 ± 0.089
Large intestine	0.060 ± 0.024	0.500 ± 0.475	0.485 ± 0.409	0.474 ± 0.200	0.159 ± 0.090
Muscle	0.031 ± 0.010	0.431 ± 0.347	0.524 ± 0.396	0.462 ± 0.174	0.238 ± 0.152
Bone	0.163 ± 0.088	0.957 ± 0.804	0.919 ± 0.601	0.747 ± 0.380	0.325 ± 0.228

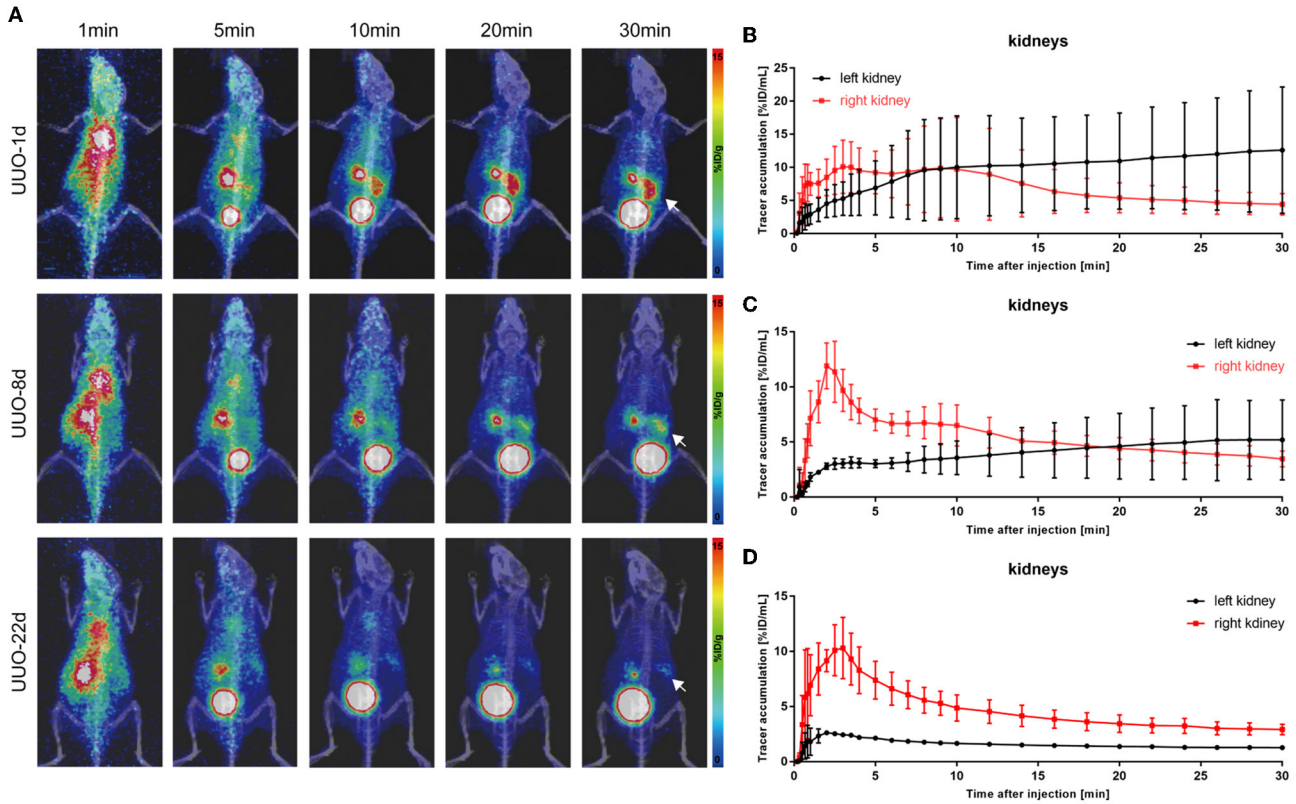

FIGURE 3
^{68}Ga-EDTA dynamic PET/CT imaging of unilateral ureter obstruction (UUO) in mice and the vital renograms. **(A)** Coronal fusion images of ^{68}Ga-EDTA dynamic PET/CT scanning on UUO mice on days 1, 8, and 22 after UUO (white arrows, the left ureter was ligated). **(B)** The renograms of UUO-1d mice were obtained *via* PET imaging. **(C)** The renograms of UUO-8d mice were obtained *via* PET imaging. **(D)** The renograms of UUO-22d mice were obtained *via* PET imaging.

3.4. ^{68}Ga-EDTA dynamic PET/CT imaging of UUO mice

Unilateral ureter obstruction is a typical model of chronic renal tubulointerstitial fibrosis. This model was established by extensive ligation of one of the ureters, and the destruction of the renal parenchyma in the obstructed kidney continued over time, posing a challenge for the sustainable dynamic observation of renal function. PET scanning was performed on UUO mice on post-operative days 1, 8, and 22. As shown in Figure 3, ^{68}Ga-EDTA

10.3389/fmed.2023.1143473

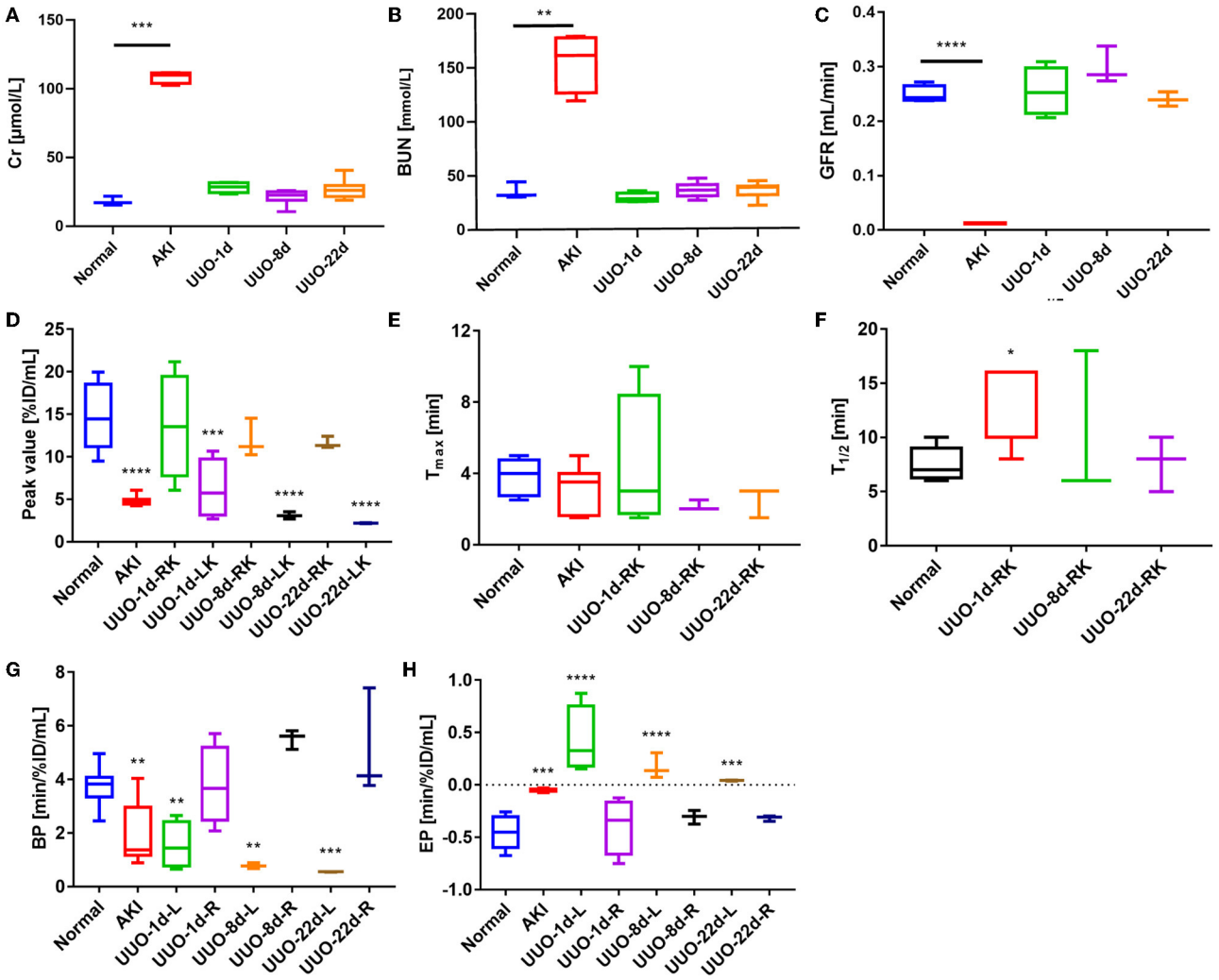

FIGURE 4
Renal function of healthy mice and mice with renal dysfunction, as represented by glomerular filtration rate (GFR), creatinine (Cr), urea nitrogen (BUN), and other figure parameters. **(A)** The Cr values of healthy mice and mice with renal dysfunction. **(B)** BUN values of healthy mice and mice with renal dysfunction. **(C)** The GFR values of healthy mice and mice with renal dysfunction. **(D)** The renogram peak value of healthy mice, AKI mice, and the split kidneys in UUO mice. *The peak value of the obstructed kidney (left kidney) in UUO mice was 4 min p.i. **(E)** The renogram T_{max} value of healthy mice, AKI mice, and the right kidney in UUO mice. **(F)** The renogram $T_{1/2}$ value of healthy mice, AKI mice, and the right kidney in UUO mice. **(G)** The renogram BP of healthy mice, AKI mice, and the split kidneys in UUO mice. **(H)** The renogram EP of healthy mice, AKI mice, and the split kidneys in UUO mice. *$p < 0.05$, **$p < 0.01$, ***$p < 0.001$, ****$p < 0.0001$.

dynamic PET images on different days showed functional changes in the split kidneys. The performance of the bilateral kidneys in ^{68}Ga-EDTA dynamic PET scanning is completely different after ureteral ligation. ^{68}Ga-EDTA can be excreted through the counter-lateral kidney and flows normally into the bladder, but it can also be found stuck in the obstructed side. Furthermore, we found the radioactivity contour of the obstructed kidney gradually fading away.

The renograms of UUO mice (Figures 3B–D) and the quantified information (Figures 4D–H) guided us with further analysis (Figures 3B–D). The renogram of the obstructed kidney at 1 day after the operation was a continuously rising curve that reflected hydronephrosis, but this curve gradually decreased over time. To calculate the BP and EP for the obstructed kidney, we set the T_{max} as 4 min. The blood perfusion (BP) of the obstructed kidney was 1.54 ± 0.87%ID/ml·min on day 1, 0.77 ± 0.10%ID/ml·min on day 8, and 0.54 ± 0.01%ID/ml·min on day 22, which decreases over time (Figure 4G). Correspondingly, the elimination (EP) of the obstructed kidney was presented in full contrast to healthy, which is 0.42 ± 0.32%ID/ml·min on day 1, 0.17 ± 0.12%ID/ml·min on day 8, and 0.04 ± 0.01%ID/ml·min on day 22. The contralateral healthy kidney, as the only remaining excretory organ, maintains a highly stable filtration capacity (Figure 4H). The BP of the contralateral kidney was 3.78 ± 1.48%ID/ml·min on post-operative day 1, increasing to 5.52 ± 0.36%ID/ml·min on day 8 and 5.11 ± 2.00%ID/ml·min on day 22, which are equal to the healthy kidney or relatively higher. The elimination (EP) of the contralateral kidney remained stable over the course of the study, which was −0.39 ± 0.27%ID/ml·min on day 1, −0.31 ± 0.06%ID/ml·min on day 8, and −0.32 ±

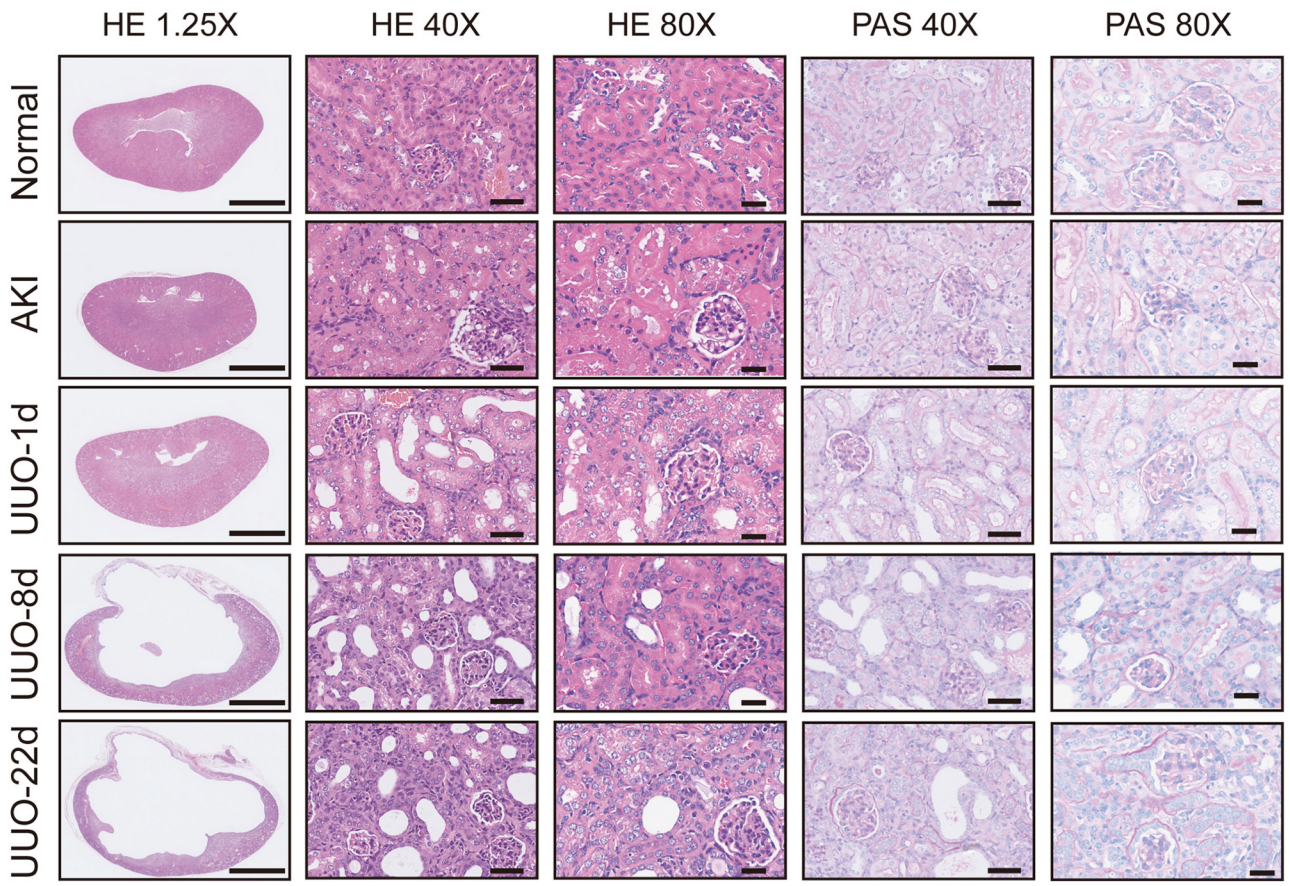

FIGURE 5
Pathological sections of healthy kidneys and kidneys with renal dysfunction. Scale bar for 1.25×: 2.5 mm, 40×: 50 μm, 80×: 25 μm.

0.03%ID/ml·min on day 22. In general, the image-quantified parameters of the contralateral kidney, such as T_{max}, $T_{1/2}$, BP, and EP, were basically the same as those of healthy mice with no statistical difference (Table 1). To our surprise, our calculated GFR values of UUO mice showed no statistical difference from those of healthy mice. The values of Cr and BUN also reflected this circumstance (Figures 4A, B). The average GFR value of UUO mice changed from 0.25 ± 0.04 ml/min on day 1 to 0.29 ± 0.03 ml/min on day 8 and then to 0.24 ± 0.01 ml/min on day 22. However, the GFR_{PET} showed better sensitivity in the evaluation of split renal function. Significant differences were found between the GFR values of the bilateral kidneys in UUO mice (Table 2). The GFR value of the compensatory kidneys in UUO mice was higher than that of the unilateral healthy kidney and reflects the physiologic adjustment of the mice.

Hematoxylin and eosin and PAS section staining of the kidney revealed the pathological changes that occurred in the obstructed kidney, such as the presence of dilated cortical kidney tubules and medullar atrophy as well as the hydronephrosis and renal cortical compression (Figure 5). These changes are confirmed by PET images and the results of radioactivity biodistribution as well (Figure 6C).

3.5. Comprehensive evaluation of renal function

We used ^{68}Ga-EDTA dynamic PET imaging and renograms to comprehensively evaluate mouse renal function. Figure 7 shows the advantage of PET renal scanning for measuring split renal function, and the bubble plot provides a comprehensive and integrated analysis of the split renal function and the overall condition of the examinees, as we accept that renal function should not be solely based on the GFR value. The bubble plot indicates that normal glomerular filtration requires an adequate blood supply and rapid efflux of the tracer through the urinary tract. Glycerol-induced AKI kidneys had a lower BP than healthy ones, and the obstructed renal tubules resulted in very weak excretion, which helps us classify AKI kidneys as renal failure. EP was positive for obstructed kidneys in UUO mice due to the obstruction in the urine outflow. Thus, we were able to identify the obstruction in the urinary tract. The contralateral kidney may have compensatory filtration, resulting in a higher BP and GFR than healthy ones. Therefore, we suggest that the evaluation of a particular renal function should involve multiple factors rather than GFR alone.

4. Discussion

In light of the obvious superiority of PET in image quality and quantification accuracy over SPECT, it was anticipated that more organ and tissue function evaluations will shift to the PET modality. Accurate quantification of renal function in terms of GFR, one of the territories where SPECT imaging used to dominate, has been challenged by its outdated two-dimensional (2D) images and loss of information during reconstruction. Several studies (16, 24, 25, 27–29) have reported the application of PET/CT in the evaluation of renal function and have demonstrated the advantages of PET/CT in the assessment of renal function, especially for those patients with complex urinary problems (14). Many tracers for renal PET imaging were proposed (10, 29). Our previous study demonstrated that ^{68}Ga-EDTA might be an appropriate choice for the assessment of renal function, and the one-compartment pharmacokinetic method can be used for efficient quantification of GFR (16, 18). In this study, we comprehensively evaluated the performance of ^{68}Ga-EDTA as a renal glomerular filtration tracer using healthy C57BL/6 mice. We further expand on the application of ^{68}Ga-EDTA dynamic PET/CT scanning in animals with renal dysfunction, including AKI and UUO, especially investigating the dynamic functional changes in the course of renal dysfunction. We demonstrated the application potential and translational value of ^{68}Ga-EDTA dynamic PET/CT scanning in the quantification of GFR.

Special needs were required for the measurement of renal function. The tracer for assessing GFR must be completely filtrated through the renal glomeruli and have no renal tubular reabsorption or secretion. Our study demonstrated the metabolism process of ^{68}Ga-EDTA *in vivo* and *in vitro*. ^{68}Ga-EDTA remained stable for 2 h. This complex can only be rapidly removed from the circulation *via* the kidneys but not cleaved. ^{68}Ga-EDTA also has an extremely low binding to blood plasma protein (15), which makes it an excellent probe for the assessment of renal GFR. The washout curves of ^{68}Ga-EDTA in the heart and kidneys of healthy mice fit well to the two-exponential decay model, but the washout curves from the injured kidneys in mice with renal dysfunction were not suitable for this model. A one-compartment pharmacokinetic model was stable enough for the vast majority of kidney elimination processes (30), and filtration efficiency can be calculated using the AUC method through PET imaging-derived data. In our study, the ^{68}Ga-EDTA-derived GFR of healthy mice was 0.25 ± 0.02 ml/min, and the split GFR for right and left kidneys was 0.14 and 0.11 ml/min, respectively. This GFR value was highly consistent with our previous study and other studies (16, 31). In addition, the upgrade of the operation process increases the reproducibility and generalizability of the method.

Next, we validated the application of ^{68}Ga-EDTA dynamic PET/CT scanning in mice with renal dysfunction and demonstrated that this method is preferable for assessing renal injury, especially at early stages. Consistent with physiological changes (such as decreased blood perfusion or sluggish excretion), PET imaging detected kidney filtration alterations and was more sensitive than Cr examinations. Glycerol-induced AKI, a representative model of heme protein-related renal injury, is characterized by oliguria, anuria, and a rapid decrease in renal excretory function. ^{68}Ga-EDTA dynamic PET/CT images timely reflected the physiological change in the kidney, including the decrease of blood perfusion and urination. UUO is another typical renal fibrosis injury model. UUO initiates marked fibrosis and leads to the loss of nephrons. However, due to the powerful compensation by the contralateral kidney, whole renal excretion and GFR remains normal (32). However, a decline in renal plasma flow as well as renal excretion can be observed in the duration of obstruction on ^{68}Ga-EDTA dynamic PET/CT images. ^{68}Ga-EDTA-derived GFR and the enriched functional categories from renograms, including peak value, T_{max}, BP, and EP, reflected the known functional characteristics of unilateral renal as well, which demonstrated the superiority of

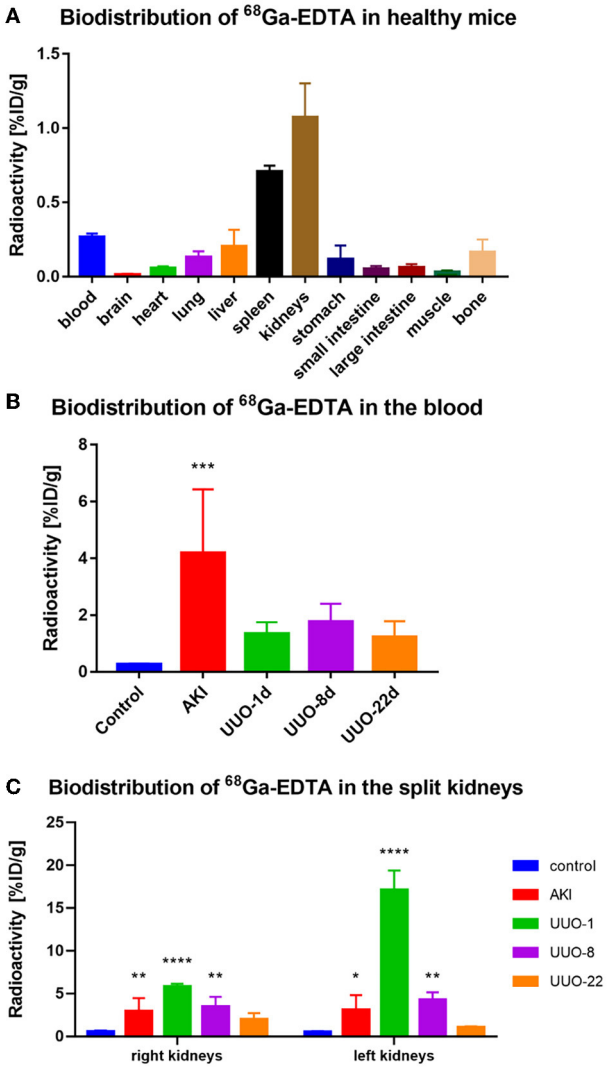

FIGURE 6
The biodistribution of ^{68}Ga-EDTA *in vivo*. **(A)** The biodistribution of ^{68}Ga-EDTA in healthy mice 30-min post-injection. **(B)** The biodistribution of ^{68}Ga-EDTA in the blood in healthy mice and other mice with renal dysfunction 30 min post-injection. **(C)** The biodistribution of ^{68}Ga-EDTA in split kidneys among the different groups. *$p < 0.05$, **$p < 0.01$, ***$p < 0.001$, ****$p < 0.0001$.

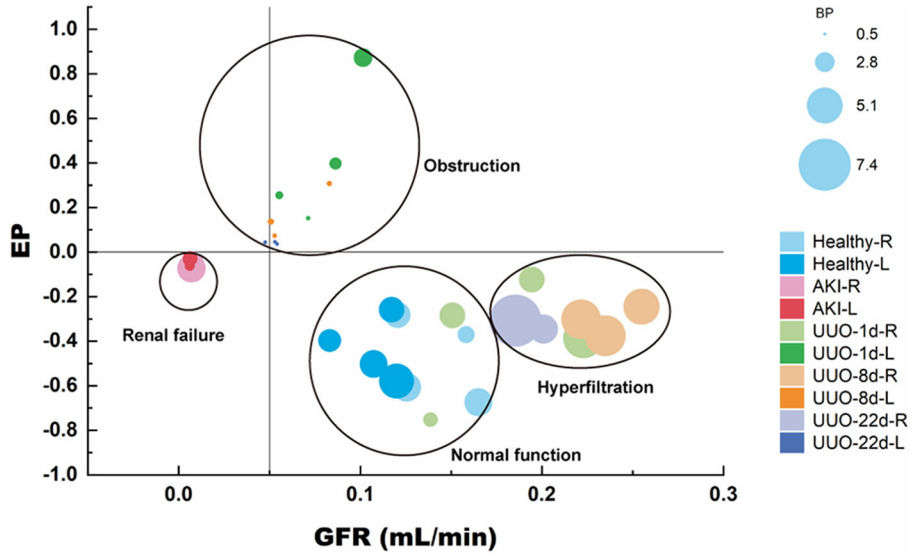

FIGURE 7
Renal function evaluation on synthetic data as reflected/estimated by GFR_{PET}.

PET renal scanning in the measurement of split renal function. Furthermore, the bubble plot (Figure 7) comprehensively and simultaneously analyzed the split renal function as well as the overall situation of the examinees. We are however conscious that renal function should not be solely focused on the GFR value.

^{99m}Tc-diethylenetriaminepentaacetic acid dynamic SPECT renal scanning is well-known for its unique advantages in assessing split kidney GFR and high sensitivity in detecting alterations in renal function. However, this method is far from meeting the needs of clinicians at present. Our study demonstrated the clear predominance of PET imaging in the visual assessment of organ function, especially renal excretion. The notable advantages of ^{68}Ga-EDTA dynamic PET/CT over SPECT/CT lie in the significantly improved accuracy in providing both 3D renal information and GFR calculation. As a 2D imaging modality, SPECT is unable to collect renal depth information and leaves out a significant portion of radioactivity from 3D space, resulting in a less accurate measurement of GFR and misleading results for patients with severely injured kidneys or hyperfiltration (11). PET imaging allows researchers and clinicians to obtain quantitative renal excretory information (10, 25), which can be directly used for GFR measurement to understand glomerular filtration in a real-time and 3D fashion. Our previous report (16) and results from this study validated the feasibility of the AUC method for GFR calculation. We therefore consider that ^{68}Ga-EDTA can be used as a novel renal glomerular filtration tracer, and ^{68}Ga-EDTA dynamic renal PET can enable early and precise evaluation of renal function, which we suggest will overcome the shortcomings of SPECT imaging and transform the future landscape of the diagnosis of renal function.

Finally, some limitations should be noted. Our calculated GFR of the obstructed kidney in UUO mice (~0.05 ml/min) is overestimated owing to the existence of blood perfusion. Despite the known overestimation, our method demonstrated high feasibility and wide compatibility for mice with deformed kidneys and therefore may find better application in real-world practice. Further research is needed to establish a GFR calculation method to rule out the influence of the bladder and urine. Lee et al. (24) and Kirsting et al. (25) used the two-compartment pharmacokinetic modeling to measure murine and human GFR. The main point of this approach lies in the more accurate location of the extravascular functional renal cortex (EVRC), as well as the more precise quantification of the imaging data. However, for PET imaging of mice, the limited resolution of micro-PET made it difficult to precisely outline the EVRC, even with the help of semi-automated delineation. A higher resolution PET detector should be useful to improve detection efficiency.

5. Conclusions

This study comprehensively evaluated the performance of ^{68}Ga-EDTA dynamic PET in the assessment of renal function. ^{68}Ga-EDTA dynamic PET imaging helps clinicians and researchers visualize physiological changes in renal injury models, presents a clear predominance in precise split GFR measurements, and contributes to early warning of renal injury. ^{68}Ga-EDTA dynamic PET is a meaningful method for evaluating renal function and is expected to have clinical applications in the coming years.

Data availability statement

The original contributions presented in the study are included in the article/Supplementary material, further inquiries can be directed to the corresponding authors.

Ethics statement

The animal study was reviewed and approved by the Institutional Animal Care and Use Committee of Tongji Medical College of Huazhong University of Science and Technology.

Author contributions

YDi planned the study, acquired and complied the data, carried out the statistical analysis, and wrote the manuscript. YL, LZ, YDe, and HC acquired the data and processed the images. XL planned this study and reviewed this manuscript. DJ and WC proposed the original idea, planned the study, acquired and complied the data, and wrote and reviewed the manuscript. All authors contributed to the article and approved the submitted version.

Funding

This study was financially supported by the National Key Research and Development Program of China (No. 2017YFC0113302), National Natural Science Foundation of China (82102121 and 22277031), and the open foundation of the Hubei Key Laboratory of Molecular Imaging (2020fzyx023).

Acknowledgments

The authors thank Dr. Qingguo Xie of the School of Life Science and Technology, Huazhong University of Science and Technology, for his kind help in the acquisition of images using the Trans PET Discoverist 180.

Conflict of interest

The authors declare that the research was conducted in the absence of any commercial or financial relationships that could be construed as a potential conflict of interest.

Publisher's note

Supplementary material

The Supplementary Material for this article can be found online at: https://www.frontiersin.org/articles/10.3389/fmed.2023.1143473/full#supplementary-material

References

1. Levey AS, Eckardt KU, Tsukamoto Y, Levin A, Coresh J, Rossert J, et al. Definition and classification of chronic kidney disease: a position statement from Kidney Disease: Improving Global Outcomes (KDIGO). *Kidney Int.* (2005) 67:2089–100. doi: 10.1111/j.1523-1755.2005.00365.x

2. Spanaus KS, Kollerits B, Ritz E, Hersberger M, Kronenberg F, von Eckardstein A. Serum creatinine, cystatin C, and beta-trace protein in diagnostic staging and predicting progression of primary nondiabetic chronic kidney disease. *Clin Chem.* (2010) 56:740–9. doi: 10.1373/clinchem.2009.138826

3. Levey AS, Coresh J, Tighiouart H, Greene T, Inker LA. Measured and estimated glomerular filtration rate: current status and future directions. *Nat Rev Nephrol.* (2020) 16:51–64. doi: 10.1038/s41581-019-0191-y

4. Yuan X, Tang W, Shi W, Yu L, Zhang J, Yuan Q, et al. Determination of glomerular filtration rate (GFR) from fractional renal accumulation of iodinated contrast material: a convenient and rapid single-kidney CT-GFR technique. *Eur Radiol.* (2018) 28:2763–71. doi: 10.1007/s00330-017-5289-7

5. Ebrahimi B, Textor SC, Lerman LO. Renal relevant radiology: renal functional magnetic resonance imaging. *Clin J Am Soc Nephrol.* (2014) 9:395–405. doi: 10.2215/CJN.02900313

6. Cheung CM, Shurrab AE, Buckley DL, Hegarty J, Middleton RJ, Mamtora H, et al. MR-derived renal morphology and renal function in patients with atherosclerotic renovascular disease. *Kidney Int.* (2006) 69:715–22. doi: 10.1038/sj.ki.5000118

7. Stevens LA, Levey AS. Measured GFR as a confirmatory test for estimated GFR. *J Am Soc Nephrol.* (2009) 20:2305–13. doi: 10.1681/ASN.2009020171

8. Rudnick MR, Leonberg-Yoo AK, Litt HI, Cohen RM, Hilton S, Reese PP. The controversy of contrast-induced nephropathy with intravenous contrast: what is the risk? *Am J Kidney Dis.* (2020) 75:105–13. doi: 10.1053/j.ajkd.2019.05.022

9. Ma YC, Zuo L, Zhang CL, Wang M, Wang RF, Wang HY. Comparison of 99mTc-DTPA renal dynamic imaging with modified MDRD equation for glomerular filtration rate estimation in Chinese patients in different stages of chronic kidney disease. *Nephrol Dial Transplant.* (2007) 22:417–23. doi: 10.1093/ndt/gfl603

10. Werner RA, Chen X, Lapa C, Koshino K, Rowe SP, Pomper MG, et al. The next era of renal radionuclide imaging: novel PET radiotracers. *Eur J Nuclear Med Mol Imaging.* (2019) 46:1773–86. doi: 10.1007/s00259-019-04359-8

11. Kang YK, Park S, Suh MS, Byun SS, Chae DW, Lee WW. Quantitative single-photon emission computed tomography/computed tomography for glomerular filtration rate measurement. *Nuclear Med Mol Imaging.* (2017) 51:338–46. doi: 10.1007/s13139-017-0491-8

12. James ML, Gambhir SS. A molecular imaging primer: modalities, imaging agents, and applications. *Physiol Rev.* (2012) 92:897–965. doi: 10.1152/physrev.00049.2010

13. Aronson AL, Ahrens FA. The mechanism of renal transport and excretion of ethylenediaminetetraacetate with interspecies comparisons. *Toxicol Appl Pharmacol.* (1971) 18:1–9. doi: 10.1016/0041-008X(71)90309-7

14. Hofman MS, Hicks RJ. Gallium-68 EDTA PET/CT for renal imaging. *Semin Nucl Med.* (2016) 46:448–61. doi: 10.1053/j.semnuclmed.2016.04.002

15. Gündel D, Pohle U, Prell E, Odparlik A, Thews O. Assessing glomerular filtration in small animals using [(68)Ga]DTPA and [(68)Ga]EDTA with PET imaging. *Mol Imag Biol.* (2018) 20:457–64. doi: 10.1007/s11307-017-1135-1

16. Ding Y, Zhang D, Wang M, Zhang L, Liu Y, Deng Y, et al. Glomerular filtration rate calculation based on (68)Ga-EDTA dynamic renal PET. *Am J Nuclear Med Mol Imaging*. (2022) 12:54–62.

17. Breeman WA, de Jong M, de Blois E, Bernard BF, Konijnenberg M, Krenning EP. Radiolabelling DOTA-peptides with 68Ga. *Eur J Nuclear Med Mol Imaging*. (2005) 32:478–85. doi: 10.1007/s00259-004-1702-y

18. Jiang D, Ge Z, Im HJ, England CG, Ni D, Hou J, et al. DNA origami nanostructures can exhibit preferential renal uptake and alleviate acute kidney injury. *Nat Biomed Eng*. (2018) 2:865–77. doi: 10.1038/s41551-018-0317-8

19. Murase K, Kitamura A, Tachibana A, Kusakabe Y, Matsuura R, Miyazaki S. Quantitative assessment of early experimental diabetes in rats using dynamic contrast-enhanced computed tomography. *Eur J Radiol*. (2010) 74:280–6. doi: 10.1016/j.ejrad.2009.03.006

20. Wesolowski MJ, Conrad GR, Šámal M, Watson G, Wanasundara SN, Babyn P, et al. A simple method for determining split renal function from dynamic (99m)Tc-MAG3 scintigraphic data. *Eur J Nuclear Med Mol Imaging*. (2016) 43:550–8. doi: 10.1007/s00259-015-3216-1

21. Hackstein N, Wiegand C, Langheinrich AC, Rau WS. Measurement of glomerular filtration rate by low-dose iopromide plasma clearance. *Acta Radiol*. (2003) 44:162–5. doi: 10.1034/j.1600-0455.2003.00037.x

22. Gonzalez Melo M, Fontana AO, Viertl D, Allenbach G, Prior JO, Rotman S, et al. A knock-in rat model unravels acute and chronic renal toxicity in glutaric aciduria type I. *Mol Genet Metab*. (2021) 134:287–300. doi: 10.1016/j.ymgme.2021.10.003

23. Majd M, Bar-Sever Z, Santos AI, De Palma D. The SNMMI and EANM procedural guidelines for diuresis renography in infants and children. *J Nuclear Med*. (2018) 59:1636–40. doi: 10.2967/jnumed.118.215921

24. Lee HS, Kang YK, Lee H, Han JH, Moon BS, Byun SS, et al. Compartmental-modelling-based measurement of murine glomerular filtration rate using (18)F-fluoride PET/CT. *Scie Rep*. (2019) 9:11269. doi: 10.1038/s41598-019-47728-x

25. Kersting D, Sraieb M, Seifert R, Costa PF, Kazek S, Kessler L, et al. First experiences with dynamic renal [(68)Ga]Ga-DOTA PET/CT: a comparison to renal scintigraphy and compartmental modelling to non-invasively estimate the glomerular filtration rate. *Eur J Nuclear Med Mol Imaging*. (2022) 49:3373–86. doi: 10.1007/s00259-022-05781-1

26. Petejova N, Martinek A. Acute kidney injury due to rhabdomyolysis and renal replacement therapy: a critical review. *Crit Care*. (2014) 18:224. doi: 10.1186/cc13897

27. Werner RA, Wakabayashi H, Chen X, Hirano M, Shinaji T, Lapa C, et al. Functional renal imaging with 2-deoxy-2-(18)F-fluorosorbitol PET in rat models of renal disorders. *J Nuclear Med*. (2018) 59:828–32. doi: 10.2967/jnumed.117.203828

28. Hofman M, Binns D, Johnston V, Siva S, Thompson M, Eu P, et al. 68Ga-EDTA PET/CT imaging and plasma clearance for glomerular filtration rate quantification: comparison to conventional 51Cr-EDTA. *J Nuclear Med*. (2015) 56:405–9. doi: 10.2967/jnumed.114.147843

29. Shi S, Zhang L, Wu Z, Zhang A, Hong H, Choi SR, et al. [(68)Ga]Ga-HBED-CC-DiAsp: a new renal function imaging agent. *Nuclear Med Biol*. (2020) 82–83:17–24. doi: 10.1016/j.nucmedbio.2019.12.005

30. Galeotti L, Ceccherini F, Fucile C, Marini V, Di Paolo A, Maximova N, et al. Evaluation of pharmacokinetics and pharmacodynamics of deferasirox in pediatric patients. *Pharmaceutics*. (2021) 13:1238. doi: 10.3390/pharmaceutics13081238

31. Qi Z, Whitt I, Mehta A, Jin J, Zhao M, Harris RC, et al. Serial determination of glomerular filtration rate in conscious mice using FITC-inulin clearance. *Am J Physiol Renal Physiol*. (2004) 286:F590–6. doi: 10.1152/ajprenal.00324.2003

32. Cochrane AL, Kett MM, Samuel CS, Campanale NV, Anderson WP, Hume DA, et al. Renal structural and functional repair in a mouse model of reversal of ureteral obstruction. *J Am Soc Nephrol*. (2005) 16:3623–30. doi: 10.1681/ASN.2004090771

frontiers | Frontiers in Medicine

TYPE Mini Review
PUBLISHED 29 March 2023
DOI 10.3389/fmed.2023.1157692

OPEN ACCESS

EDITED BY
Giorgio Treglia,
Ente Ospedaliero Cantonale (EOC),
Switzerland

REVIEWED BY
Domenico Albano,
University of Brescia,
Italy
Ilse Kouijzer,
Radboud University Medical Centre,
Netherlands

*CORRESPONDENCE
Søren Hess
soren.hess@rsyd.dk

SPECIALTY SECTION
This article was submitted to Nuclear Medicine, a section of the journal Frontiers in Medicine

RECEIVED 02 February 2023
ACCEPTED 28 February 2023
PUBLISHED 29 March 2023

CITATION
Hess S (2023) [18F]FDG-PET/CT in patients with bacteremia: Clinical impact on patient management and outcome.
Front. Med. 10:1157692.
doi: 10.3389/fmed.2023.1157692

[18F]FDG-PET/CT in patients with bacteremia: Clinical impact on patient management and outcome

Søren Hess [1,2,3]*

[1]Department of Radiology and Nuclear Medicine, Esbjerg Hospital – University Hospital of Southern Denmark, Esbjerg, Denmark, [2]Department of Regional Health Research, Faculty of Health Sciences, University of Southern Denmark, Odense, Denmark, [3]IRIS – Imaging Research Initiative Southwest, Esbjerg, Denmark

Bacteremia is the presence of viable bacteria in the bloodstream, a complicated and potentially dangerous systemic medical condition that may range from asymptomatic and clinically relatively indolent cases to more severe bloodstream infection (BSI) and ultimately life-threatening septic shock with fatal outcome. BSI is classified as simple (bacteremia only) or complex (BSI with metastatic spread), and the morbidity is higher in the latter, probably due to insufficient eradication. Treatment of simple BSI is usually short-term antibiotic courses, whereas complex BSI with metastatic foci requires more advanced treatment including long-term antibiotics or invasive drainage to gain infection control. Thus, identifying metastatic infection has an important clinical impact but remains a challenge; only half of the patients progress to complex BSI, and many patients present without relevant signs or symptoms, so imaging is pivotal. This review summarizes the potential role and recommendations of [18F]FDG-PET/CT in BSI, based on the relatively sparse and heterogeneous literature. [18F]FDG-PET/CT should be considered in suspected complex BSI, in patients at high risk of metastatic spread, and in BSI in ICU patients. [18F]FDG-PET/CT has an impact on patient management, treatment strategy, and patient outcome, mainly by directing the diagnostic process toward more specific diagnostics or by modifying treatment regimens resulting in reduced relapse rates and reduced mortality. Finally, a negative scan may obviate the need for further workup.

KEYWORDS

[18F]FDG-PET/CT, infection, bacteremia, blood stream infection (BSI), PET

Introduction

Bacteremia or bloodstream infections (BSI) are common and difficult clinical entities with potentially serious consequences including death. Some reports state that BSI occurs in 5–10% of hospitalized patients with overall mortality higher than 15% (1, 2).

In fever of unknown origin, the key issue is usually to establish the focal point of the fever. In BSI, another and perhaps clinically more important issue is to distinguish between simple bacteremia (BSI only) and complex (or metastatic) bacteremia (BSI with solid or metastatic foci). A significant proportion of patients progress from simple bacteremia to complex bacteremia; studies on *Staphylococcus aureus* report metastatic infection in 16–73% of patients (3, 4). Complex bacteremia requires a different treatment strategy, i.e., escalation (added/

combined drug regimens), elongation (prolonged treatment for 4–6 weeks depending on the location of foci), and/or surgical interventions (prosthesis removal or drainage of deep tissue abscesses). Correspondingly, insufficient eradication leads to relapse in approximately 15% and an increase in mortality, but in one-third of cases, the metastatic foci remain asymptomatic (5). Thus, a great deal of work is going into differentiating patients at risk of complex BSI — if they are identified, guidelines usually suggest prolonged treatment to prevent or reduce the risk of fulminant bacterial spread. Risk factors for developing complex BSI include community acquisition, prolonged or persistent symptoms/findings, and prosthetic implants (3). However, 35–50% of all patients at high risk of complex BSI never progress to spread, and as such, as many as 50% of patients are over-treated to prevent spread (4).

Bacteremia is divided into gram-positive and gram-negative bacteremia; gram-positive bacteremia is more common than gram-negative ones. This may be attributable to the increased use of prosthetic devices, intravenous catheters, invasive procedures, and the widespread use of antibiotic prophylaxis with fluoroquinolones that all predispose to gram-positive growth (6).

In gram-positive bacteremia, there are some characteristic associations between species and sites of focal infections, e.g., pneumococci and pneumonia, whereas *S. aureus* infection sites are often more occult, and therefore more commonly encountered as the culprit species in BSI of unknown origin. Gram-negative bacteremia is often caused by *Escherichia coli* and other *Enterobacteriaceae*. It is usually associated with gastrointestinal or urinary tract infections, whereas gram-negative species have much less ability to adhere to prosthetic material than gram-positive ones (6, 7). These pointers should be kept in mind when assessing imaging, but most species can give rise to BSI anywhere, so one must keep an open mind.

Further division is based on where the patient most likely contracted the infectious microorganism: community-acquired BSI (CA-BSI) is usually defined as outpatients or patients with confirmed BSI <48 h post-admission, whereas nosocomial BSI (N-BSI) is usually defined as confirmed BSI >48 h post-admission. In CA-BSI, gram-negative is more prevalent, whereas gram-positive is more prevalent in N-BSI (1, 8).

Some specific scenarios

Staphylococcus aureus is probably the most commonly encountered BSI by the nuclear medicine physician in referrals to [^{18}F]FDG-PET/CT. First, the incidence of *S. aureus* BSI is generally increasing due to an aging population with heart valve prostheses and joint prostheses that are common predilection sites. Second, *S. aureus* has an inherent ability for metastatic spread and progression to complex BSI that require more advanced treatment to reduce the risk of recurrence, prolonged disease, or mortality that may reach 20–40% (9, 10). *Staphylococcus aureus* BSI comprises 20% of N-BSI, and metastatic spread is a dreaded complication (9). Most common are infectious endocarditis, osteomyelitis and joint infections (including prosthetics), and deep tissue abscesses — all trigger treatment modification (i.e., escalation or elongation of antibiotic regimens or surgical interventions) (11). A special entity is *S. aureus*-associated pneumonia, which accounts for 8% of all BSI, 30% of N-BSI, and 68% of all BSI in the intensive care unit (ICU). Overall, BSI is established in 5–15% of community-acquired pneumonia and 24–36% of ventilator-associated pneumonia, whereas the rate of BSI is approximately 60% in both community-acquired *S. aureus* pneumonia and nosocomial *S. aureus* pneumonia in the ICU. In the former, BSI usually occurs early in the course, whereas in the latter case, pneumonia may be ventilator-associated or secondary to influenza, and therefore, BSI may appear rather late (11). Thus, it is clinically relevant to differentiate between bacteremia secondary to *S. aureus* pneumonia and pneumonia secondary to *S. aureus* BSI, so even with well-known pneumonia in ICU patients, an [^{18}F]FDG-PET/CT late in the course may contribute to localizing metastatic foci including the lungs.

Regarding the ICU, the incidence of BSI is at least double that of the general hospital population and mortality is at least 3-fold and described as the leading cause of death in the ICU. Patients are evaluated for foci with the aim of source control, e.g., drainage, but despite extensive workup, foci often remain occult. [^{18}F]FDG-PET/CT is difficult in the ICU setting due to multiple interfering factors leading to reduced scan quality, e.g., multiple intravenous drugs (some dissolved in glucose), generally difficult blood glucose control, and frequently poor kidney and/or liver function (2, 12). The practical setup is also challenging. At our institution, we usually inject FDG in the ICU, and patients are only in the PET center for the scan, but even then, [^{18}F]FDG-PET/CT takes significantly longer than a CT, which puts a strain on ICU resources. Finally, ICU patients are usually hooked up to monitors, ventilators, injection pumps, etc., which may hamper imaging or even the possibility to pass through the scanner. [^{18}F]FDG-PET/CT scans in ICU patients need planning and close cooperation between the specialties.

Febrile neutropenia is a dreaded complication in oncology and hematology, but only 30–50% is due to infection, and BSI is only present in 25–30%. In many cases of febrile neutropenia, fever is caused by chemotherapy or tumor fever, and there is no effect from antibiotics. On the other hand, in approximately 50% of febrile neutropenia patients with BSI, the bacteremia is complex with focal spread, and prolonged treatment is warranted just as in non-oncologic BSI (13).

Aim

This review explores the potential impact of [^{18}F]FDG-PET/CT on subsequent treatment strategies in both simple and complex BSI. A positive PET/CT scan may direct the diagnostic process toward more specific diagnostics. A more direct impact on management is the modification of treatment, for instance, as a guide for invasive treatment, e.g., abscess drainage. It may also cause escalation or elongation of therapy based on positive findings or even de-escalation following negative scans. Sometimes a negative scan may also prompt a switch from intravenous to oral regimens in limited disease. Thus, [^{18}F]FDG-PET/CT may directly influence patient prognosis through its impact on treatment modifications if better focal control reduces morbidity, relapse rates, and mortality (Table 1).

Impact on patient management

Several studies have looked at the overall impact of [^{18}F]FDG-PET/CT on treatment modifications. Brøndserud et al. (14)

TABLE 1 Overview of studies evaluating [^{18}F]FDG-PET/CT in bloodstream infections.

Study	Population	*N*	Study design	Major findings
Studies evaluating the impact of [^{18}F]FDG-PET/CT on treatment				
Brøndserud et al. (14)	BSI with Gram-positive cocci or SA	157	Retrospective	Change in therapy in 15%
van Leerdam et al. (15)	High risk SA-BSI	132	Retrospective	Change in therapy in 17%
Tsai et al. (16)	BSI with mixed species	102	Retrospective	Change in management in 45%
Pijl et al. (2)	BSI in ICU-patients	30	Retrospective	Change in management in 47%
Kluge et al. (12)	BSI in ICU-patients	18	Retrospective	Change in management in 33%
Studies evaluating the impact of [^{18}F]FDG-PET/CT on patient outcome				
Vos et al. (5)	BSI at risk of metastatic spread	115	Prospective	PET increased detection of metastatic foci, reduced relapse rate, and reduced mortality
Berrevoets et al. (4)	High risk BSI with negative PET and echocardiography vs. simple BSI	76	Retrospective	Comparable relapse rates and mortality in simple BSI vs. high risk BSI
Yildiz et al. (17)	High risk BSI with or without PET	102	Retrospective	PET resulted in reduced mortality compared to controls
Studies evaluating the impact of [^{18}F]FDG-PET/CT on management and patient outcome				
Ghanem-Zoubi et al. (18)	SA-BSI with/without PET	149 × 2	Prospective	PET resulted in longer courses of antibiotics and better mortality compared to controls
Berrevoets et al. (3)	High risk BSI	99	Retrospective	PET changed treatment in 73% and reduced mortality
Kouijzer et al. (19)	Complicated BSI with negative PET and echocardiography	106	Retrospective	Switch from intravenous to oral antibiotics is safe and reduce duration of hospital stay

BSI, bloodstream infections; SA, *Staphylococcus aureus*; SA-BSI, *Staphylococcus aureus* bloodstream infections; PET, [^{18}F]FDG-PET/CT.

performed a retrospective study of consecutive patients with confirmed BSI with *S. aureus* and gram-positive cocci other than pneumococci (as they usually present themselves fairly easily). All patients underwent an [^{18}F]FDG-PET/CT scan in the search for infectious foci, and besides the overall diagnostic yield of [^{18}F]FDG-PET/CT, they also evaluated any relevant clinical impact defined as cases where PET results identified foci as the first modality or when findings led to treatment modifications. They found metastatic foci in 56% and high clinical impact in 47% of the 157 included patients, including changes in therapy in 15%. When patients experience long disease courses, some fear a potential negative impact from antibiotic treatment on [^{18}F]FDG-PET/CT efficacy, but in this study, the duration of antibiotic treatment neither influence the clinical impact nor the time interval from confirmed BSI to [^{18}F]FDG-PET/CT.

Patients are often subjected to a wide range of futile examinations prior to PET. Reducing these by performing [^{18}F]FDG-PET/CT earlier would benefit the individual patient and health economics. In this study, patients underwent a median of four futile investigations prior to PET (with a range of 0–12), albeit the study was not specifically designed to evaluate this particular issue.

The most recent study by van Leerdam et al. (15) found similar results with regard to additional foci and change in treatment in a retrospective cohort of patients with *S. aureus* BSI suspected to be complex and therefore pre-planned antibiotic treatment of >6 weeks. They included 132 patients who underwent [^{18}F]FDG-PET/CT and found additional metastatic foci in 52%. The original treatment plan changed in 17%, primarily due to the confirmation or rejection of an infected vascular graft or thrombus. The treatment regimen was shortened in two cases where suspected vascular thrombus infection and arthritis were ruled out. Antibiotic treatment was switched from an intravenous to an oral regimen in three cases with ruled-out infected thrombus but confirmed pulmonary metastatic foci. In 13 cases, intravenous treatment was extended (and in four of these additional rifampicin was also added) due to confirmed infection in vascular or joint prostheses, endocarditis, osteomyelitis, and/or soft tissue abscess. Thus, [^{18}F]FDG-PET/CT could individualize and refine the treatment of *S. aureus* BSI planned for generic long-term antibiotic regimens.

In another retrospective, single-center study, Tsai et al. (16) included 102 patients BSI who underwent [^{18}F]FDG-PET/CT within 1 week of diagnosis. In total, 73% of the scans were positive; the most common organs/tissues were vertebral osteomyelitis/spondylodiscitis (21%) and lung (21%). They found a 3-fold higher impact on management compared with the previous study, i.e., 45% (40 PET+/6 PET−), but in most cases, the modified management comprised referral for subsequent imaging. A low number of PET-negative patients were referred for subsequent imaging, which is an important point; a negative [^{18}F]FDG-PET/CT may reduce the need for further imaging, as also suggested by the aforementioned results from Brøndserud et al.

To avoid over-utilization of PET scans, it is important to stratify which patients to refer for [^{18}F]FDG-PET/CT. Tsai et al. found increased CRP associated with positive scans, but the best cutoff of 54 mg/ml yielded a sensitivity of only 79% with a specificity of 65%.

Pijl et al. (2) included a retrospective, consecutive cohort comprising all ICU patients with proven gram-positive BSI or gram-negative BSI and an [^{18}F]FDG-PET/CT. They included 30 patients with a median CRP of 114 mg/L. *S. aureus* was the predominant cause (37%) and mortality was 30%. Many patients underwent examinations prior to PET, e.g., X-ray (100%), ultrasonography (93%), CT (71%), and MRI (17%). As a special feature, PET scans were quality assessed based on background, motion artifacts, suppression of physiologic

uptake, and overall readability; 70% was deemed adequate and 30% was of poor quality.

In the 21 PET-positive scans, the most common findings were pneumonia or arthritis. Overall, [^{18}F]FDG-PET/CT led directly to a change of management in 14 out of 30 patients (47%). On regression analysis, only PET quality was associated with positive findings (reduced image quality led to fewer PET positives), whereas CRP, duration of antibiotics, duration of admittance to ICU, or mechanical ventilation did not impact diagnostic yield. This is in keeping with some of the findings mentioned previously.

This study also points to the potential of employing PET earlier in the course to limit futile tests.

Finally, [^{18}F]FDG-PET/CT impacted test probability. Overall pretest probability for infection was 73%, whereas the post-test probability was 95% (in PET+) and 22% (in PET−), respectively.

These results were corroborated by an older study by Kluge et al. (12). They retrospectively included 18 ICU patients with severe septicemia without known focus. In total, 12 had BSI, and all were extensively worked up prior to [^{18}F]FDG-PET/CT. The median time from ICU admission to [^{18}F]FDG-PET/CT was 11 days, and 17 out of 18 patients received antibiotics at the time of PET.

The PET results led to therapeutic changes in six patients (33%), i.e., surgery in two, pacemaker removal in two, and initiation or prolonged antibiotics in two cases.

Impact on patient outcome

Another approach is the impact on patient outcomes. This was the focus of one of the first large studies on [^{18}F]FDG-PET/CT in bacteremia by Vos et al., probably the first prospective one (5). It was a case–control study of patients with gram-positive BSI, with risk factors of metastatic spread and with or without a PET scan. Case patients received PET-directed treatment: no foci prompted 14-day treatment, whereas foci prompted prolonged treatment for 6–12 weeks depending on the location of the foci. They compared 115 cases with 230 controls.

Overall, they found metastatic foci in 68% of cases vs. 36% of controls, especially endovascular, spinal, and pulmonary lesions. These foci not only require prolonged antibiotic regimen or invasive intervention, but they also only rarely have localizing symptoms. Overall, the relapse rate was 2.6% in cases versus 7.4% in controls — this was not statistically significant, although the study was designed to detect a 10% decrease, in a subgroup of *S. aureus*-related relapses, the difference reached statistical significance. All-cause 6 months mortality was lower in cases (19%) than in controls (32%).

The two groups were comparable according to baseline characteristics, but two factors stood out: treatment delay was more prevalent in controls (45% vs. 27%), although it did not influence mortality when added as a covariate. The second potential confounder was a higher prevalence of prolonged BSI in the intervention group, which could skew patients toward a higher relapse rate, but they did not obtain continuous blood cultures routinely in the controls, so the true effect of this is equivocal.

Berrevoets et al. (20) looked at the value of a negative [^{18}F]FDG-PET/CT in a retrospective case–control setting. They compared patients with *S. aureus* BSI and risk factors for complex BSI but negative echocardiography and negative [^{18}F]FDG-PET/CT (36 cases) vs. patients with simple BSI (40 controls).

As mentioned earlier, the same prolonged treatment is recommended for manifest complex BSI and patients with risk factors for developing complex BSI. Moreover, as also mentioned previously, 35–50% of patients with risk factors never develop complex BSI and are over-treated.

In this study, they investigated the safety of a similar 2-week treatment regimen in simple BSI vs. selected groups of BSI with a high risk for complicating spread. They found comparable relapse rates and mortality (both infection-specific and all-cause of 19% vs. 15%). These results suggest that it is safe to withhold preventive measures (prolonged antibiotic regimen) in high-risk patients with negative [^{18}F]FDG-PET/CT scans.

Yildiz et al. (17) compared high-risk patients infected with *S. aureus* in a retrospective case–control setup, i.e., 48 cases undergoing [^{18}F]FDG-PET/CT versus 54 controls without scans. Overall, mortality was 31%, which was reduced significantly from 44% in controls to 17% in cases, and the reduced mortality remained at 30 days, 90 days, and 1 year. This is in accordance with the most prevalent findings being spondylodiscitis, bone or joint prosthesis infections, vascular graft infections, and abscesses; findings that all require more aggressive treatment such as surgery, removal of prostheses, or prolonged antibiotic regimen to be controlled.

Impact on treatment modifications and outcome

A small group of studies looked at both treatment modifications and outcomes.

The first study by Ghanem-Zoubi et al. (18) prospectively recruited patients with *S. aureus* BSI for a matched cohort to compare 149 patients who underwent [^{18}F]FDG-PET/CT with 149 who did not. [^{18}F]FDG-PET/CT found a relatively high number of foci initially not suspected which all required longer antibiotic regimens (e.g., bones) or surgical interventions (e.g., soft tissue abscess drainage). Thus, patients of the intervention group received antibiotics for longer periods (42 days versus 19 days), and 18% underwent focus controlling procedures as a direct consequence of [^{18}F]FDG-PET/CT findings. Consequently, the intervention group had significantly lower 90-day mortality (14%) compared with the controls (29%). Interestingly, differences in baseline characteristics were skewed toward potentially more severe disease in the intervention group, e.g., more long-term bacteremia and thus higher rates of high-risk *S. aureus* BSI, which should actually have skewed the mortality toward a more favorable outcome for the control group.

Berrevoets et al. (3) included consecutive patients in a retrospective cohort of in-patients with high-risk *S. aureus* BSI and an [^{18}F]FDG-PET/CT ($n = 99$) and compared it with a control group who did not undergo [^{18}F]FDG-PET/CT ($n = 49$). In the case group, metastatic infection was present in 73%, most without any diagnostic clues. Again, many foci were located in organs or tissue requiring prolonged antibiotics or intervention (e.g., bones, joints, and abscesses), and 104 treatment modifications were recorded in 74 patients (e.g., escalation/de-escalation of antibiotics or invasive interventions). The overall relapse rates were 2.2% (4/184), whereas

the 3-month mortality was 19% (35/184). However, comparing the two groups, *S. aureus*-related 3-month mortality was only 12% in the PET group compared with 33% in the no PET group. In a univariate analysis, the performance of an [^{18}F]FDG-PET/CT was one of the factors associated with improved survival.

The same group performed a study in a similar setup but looked at the impact on the outcome of de-escalation treatment regimens in a retrospective cohort of consecutive in-patients with complicated *S. aureus* BSI (19). A dreaded complication of *S. aureus* BSI is infective endocarditis, and according to guidelines, complicated *S. aureus* BSI requires prolonged antibiotics for 4–6 weeks. Some studies suggest a switch from an IV regimen to oral antibiotics after 2 weeks to shorten hospital stay, reduce patient inconvenience, and reduce costs. This study tested the safety of this approach in 106 patients with complicated *S. aureus* BSI without evidence of infective endocarditis or other endovascular foci on echocardiography and [^{18}F]FDG-PET/CT. They compared the switch strategy ($n = 60$) with continuous IV treatment ($n = 46$) and found no relapses in either group. Although mortality was lower in the switch group (6.6% vs. 13.3%), results were not statistically significant, but the duration of hospital stay was significantly shorter (17 days vs. 29 days) (19).

It is important to note that continuous or prolonged IV treatment was at the discretion of the treating physician, and the continuous IV treatment group included significantly more high-risk patients. Nonetheless, the IV-to-oral switch of antibiotic regimen is feasible and safe in complex, metastatic high-risk *S. aureus* BSI without signs of endovascular foci on echo and [^{18}F]FDG-PET/CT.

Conclusion/perspectives

[^{18}F]FDG-PET/CT has an overall clinical impact on up to half of the patients; more specifically, it leads to changes in treatment in 15–73% of patients, and as a result of these management changes, reduced relapse and mortality of 2–3-fold are observed (Table 2).

However, the literature is not without challenges; the studies presented here, although not systematically retrieved, probably comprise the bulk of the clinical studies on the subject and they are relatively small with 18–157 patients. Most are retrospective with only two prospective ones, and the patient populations and the microorganisms covered are highly heterogeneous. Thus, pooling the results and making overall conclusions may be difficult. For instance, two of these studies, albeit the two smallest ones, included ICU patients that are notoriously difficult with a multitude of pitfalls.

A number of knowledge gaps remain. For instance, the timing of [^{18}F]FDG-PET/CT — should it be performed upfront or only after a number of futile examinations? Cost issues may suggest the latter to reduce the number of scans, but some proportion of these patients end up in the PET scanner eventually, so some efforts should be put into defining when to use [^{18}F]FDG-PET/CT. Moreover, very little is known about the impact of the clinical courses themselves, for instance, the potential impact on diagnostic yield from long-term antibiotics, the duration of symptoms, underlying malignancies, etc.

[^{18}F]FDG-PET/CT may save futile exams but may also prompt additional unnecessary exams due to false positive findings. This may affect cost-effectiveness, but although some studies address some of these issues as secondary endpoints, the available data do not allow definite conclusions. More widespread implementation of novel technologies such as digital or whole-body PET scanners may alleviate some of the aforementioned shortcomings, e.g., improved image resolution, reduction of false positive findings, and reduced radiation dose, especially in children, but further studies are needed.

Nonetheless, the available literature leaves no doubt of the potential of [^{18}F]FDG-PET/CT in the diagnostic workup of BSI, at least in patients with high-risk complex BSI with risk of metastatic disease, and perhaps especially in *S. aureus* BSI. This was also the conclusion of two very recent systematic and focused reviews compiling much of the same literature (21, 22). [^{18}F]FDG-PET/CT reduced relapse rate and mortality due to the detection of additional foci that led to better-guided treatment and ultimately better source control.

TABLE 2 Main conclusions on [^{18}F]FDG-PET/CT in bloodstream infections.

Important patient populations	• Suspected complex blood stream infections • Patients at high risk of metastatic spread • Blood stream infections in ICU-patients
Potential impact on patient management, treatment strategy, and patient outcome	• Directing the diagnostic process towards more specific diagnostics • Modify treatment regimen o Guide to invasive treatment (e.g., abscess drainage) o Escalation or elongation of therapy (positive findings) o De-escalation of therapy (negative scans) o Switch from intravenous to oral regimens in limited disease (negative scans in complex bloodstream infections) • Decreased mortality when [^{18}F]FDG-PET/CT is performed • Negative scans may reduce the need for further workup

Author contributions

The author confirms being the sole contributor of this work and has approved it for publication.

Conflict of interest

The author declares that the research was conducted in the absence of any commercial or financial relationships that could be construed as a potential conflict of interest.

Publisher's note

References

1. Søgaard M, Nørgaard M, Pedersen L, Sørensen HT, Schønheyder HC. Blood culture status and mortality among patients with suspected community-acquired bacteremia: a population-based cohort study. *BMC Infect Dis*. (2011) 11:139. doi: 10.1186/1471-2334-11-139

2. Pijl JP, Londema M, Kwee TC, Nijsten MWN, Slart R, Dierckx R, et al. FDG-PET/CT in intensive care patients with bloodstream infection. *Crit Care*. (2021) 25:133. doi: 10.1186/s13054-021-03557-x

3. Berrevoets MAH, Kouijzer IJE, Aarntzen E, Janssen MJR, De Geus-Oei LF, Wertheim HFL, et al. (18)F-FDG PET/CT optimizes treatment in *Staphylococcus aureus* bacteremia and is associated with reduced mortality. *J Nucl Med*. (2017) 58:1504–10. doi: 10.2967/jnumed.117.191981

4. Berrevoets MAH, Kouijzer IJE, Slieker K, Aarntzen E, Kullberg BJ, Oever JT, et al. (18)F-FDG PET/CT-guided treatment duration in patients with high-risk *Staphylococcus aureus* bacteremia: a proof of principle. *J Nucl Med*. (2019) 60:998–1002. doi: 10.2967/jnumed.118.221929

5. Vos FJ, Bleeker-Rovers CP, Sturm PD, Krabbe PF, van Dijk AP, Cuijpers ML, et al. 18F-FDG PET/CT for detection of metastatic infection in gram-positive bacteremia. *J Nucl Med*. (2010) 51:1234–40. doi: 10.2967/jnumed.109.072371

6. Muñoz P, Cruz AF, Rodríguez-Créixems M, Bouza E. Gram-negative bloodstream infections. *Int J Antimicrob Agents*. (2008) 32:S10–4. doi: 10.1016/j.ijantimicag.2008.06.015

7. Todorovic Markovic M, Pedersen C, Gottfredsson M, Todorovic Mitic M, Gaini S. Focus of infection and microbiological etiology in community-acquired infections in hospitalized adult patients in the Faroe Islands. *BMC Infect Dis*. (2019) 19:16. doi: 10.1186/s12879-018-3650-3

8. Laupland KB, Church DL. Population-based epidemiology and microbiology of community-onset bloodstream infections. *Clin Microbiol Rev*. (2014) 27:647–64. doi: 10.1128/CMR.00002-14

9. Saginur R, Suh KN. *Staphylococcus aureus* bacteraemia of unknown primary source: where do we stand? *Int J Antimicrob Agents*. (2008) 32:S21–5. doi: 10.1016/j.ijantimicag.2008.06.008

10. del Rio A, Cervera C, Moreno A, Moreillon P, Miró JM. Patients at risk of complications of *Staphylococcus aureus* bloodstream infection. *Clin Infect Dis*. (2009) 48:S246–53. doi: 10.1086/598187

11. Rubinstein E. *Staphylococcus aureus* bacteraemia with known sources. *Int J Antimicrob Agents*. (2008) 32:S18–20. doi: 10.1016/j.ijantimicag.2008.06.006

12. Kluge S, Braune S, Nierhaus A, Wichmann D, Derlin T, Mester J, et al. Diagnostic value of positron emission tomography combined with computed tomography for evaluating patients with septic shock of unknown origin. *J Crit Care*. (2012) 27:316.e1–7.

13. Feld R. Bloodstream infections in cancer patients with febrile neutropenia. *Int J Antimicrob Agents*. (2008) 32:S30–3. doi: 10.1016/j.ijantimicag.2008.06.017

14. Brøndserud MB, Pedersen C, Rosenvinge FS, Hoilund-Carlsen PF, Hess S. Clinical value of FDG-PET/CT in bacteremia of unknown origin with catalase-negative gram-positive cocci or *Staphylococcus aureus*. *Eur J Nucl Med Mol Imaging*. (2019) 46:1351–8. doi: 10.1007/s00259-019-04289-5

15. van Leerdam EJ, Gompelman M, Tuinte RAM, Aarntzen E, Berrevoets MAH, Maat I, et al. Individualizing the use of [(18)F]FDG-PET/CT in patients with complicated *Staphylococcus aureus* bacteremia: experiences from a tertiary care center. *Infection*. (2022) 50:491–8. doi: 10.1007/s15010-021-01740-4

16. Tsai HY, Lee MH, Wan CH, Yang LY, Yen TC, Tseng JR. C-reactive protein levels can predict positive (18)F-FDG PET/CT findings that lead to management changes in patients with bacteremia. *J Microbiol Immunol Infect*. (2018) 51:839–46. doi: 10.1016/j.jmii.2018.08.003

17. Yildiz H, Reychler G, Rodriguez-Villalobos H, Orioli L, D'Abadie P, Vandeleene B, et al. Mortality in patients with high risk *Staphylococcus aureus* bacteremia undergoing or not PET-CT: a single center experience. *J Infect Chemother*. (2019) 25:880–885.

18. Ghanem-Zoubi N, Kagna O, Abu-Elhija J, Mustafa-Hellou M, Qasum M, Keidar Z, et al. Integration of FDG-PET/CT in the diagnostic workup for *Staphylococcus aureus* bacteremia: a prospective interventional matched-cohort study. *Clin Infect Dis*. (2021) 73:e3859–66. doi: 10.1093/cid/ciaa929

19. Kouijzer IJE, van Leerdam EJ, Gompelman M, Tuinte RAM, Aarntzen E, Berrevoets MAH, et al. Intravenous to oral switch in complicated *Staphylococcus aureus* bacteremia without endovascular infection: a retrospective single-center cohort study. *Clin Infect Dis*. (2021) 73:895–8. doi: 10.1093/cid/ciab156

20. Berrevoets MAH, Kouijzer IJE, Slieker K, Aarntzen E, Kullberg BJ, Ten Oever J, et al. F-FDG-PET/CT-guided treatment duration in patients with high-risk *Staphylococcus aureus* bacteremia: a proof of principle. *J Nucl Med*. (2019) 60:998–1002.

21. Buis DTP, Sieswerda E, Kouijzer IJE, Huynh WY, Burchell GL, Berrevoets MAH, et al. [18F]FDG-PET/CT in *Staphylococcus aureus* bacteremia: a systematic review. *BMC Infect Dis*. (2022) 22:282. doi: 10.1186/s12879-022-07273-x

22. Thottacherry E, Cortés-Penfield NW. Evidence of clinical impact supports a new petition for Medicare coverage of 2-[18F]Fluoro-2-Deoxy-D-glucose positron emission tomography/computed tomography in the evaluation of *Staphylococcus aureus* bacteremia: a focused literature review and call to action. *Clin Infect Dis*. (2022) 75:1457–61. doi: 10.1093/cid/ciac363

frontiers | Frontiers in Medicine

TYPE Original Research
PUBLISHED 26 April 2023
DOI 10.3389/fmed.2023.1141636

OPEN ACCESS

EDITED BY
Domenico Albano,
University of Brescia, Italy

REVIEWED BY
Francesco Dondi,
Università degli Studi di Brescia, Italy
Luigi Mansi,
Interuniversity Research Center for Sustainability (CIRPS), Italy

*CORRESPONDENCE
David Morland
✉ david.morland@reims.unicancer.fr

RECEIVED 10 January 2023
ACCEPTED 03 April 2023
PUBLISHED 26 April 2023

CITATION
Morland D, Chiappetta M, Falcoz P-E, Chenard M-P, Annunziata S, Boldrini L, Lococo F and Imperiale A (2023) 18F-FDG primary tumor uptake to improve N status prediction in cT1 non-metastatic non-small cell lung cancer: development and validation of a positron emission tomography model.
Front. Med. 10:1141636.
doi: 10.3389/fmed.2023.1141636

18F-FDG primary tumor uptake to improve N status prediction in cT1 non-metastatic non-small cell lung cancer: development and validation of a positron emission tomography model

David Morland[1,2,3]*, Marco Chiappetta[4,5], Pierre-Emmanuel Falcoz[6], Marie-Pierre Chenard[7], Salvatore Annunziata[3], Luca Boldrini[8], Filippo Lococo[4,5] and Alessio Imperiale[9,10,11]

[1]Médecine Nucléaire, Institut Godinot, Reims, France, [2]CReSTIC EA 3804 et Laboratoire de Biophysique, Université de Reims Champagne-Ardenne, Reims, France, [3]Unità di Medicina Nucleare, GSTeP Radiofarmacia, TracerGLab, Dipartimento di Radiologia, Radioterapia ed Ematologia, Fondazione Policlinico Universitario A. Gemelli IRCCS, Rome, Italy, [4]Università Cattolica del Sacro Cuore, Rome, Italy, [5]Chirurgia Toracica, Fondazione Policlinico Universitario A. Gemelli IRCCS, Rome, Italy, [6]Service de Chirurgie Thoracique, Hôpitaux Universitaires de Strasbourg, Strasbourg, France, [7]Service de Pathologie, Hôpitaux Universitaires de Strasbourg, Strasbourg, France, [8]Unità di Radioterapia, Radiomics, Dipartimento di Radiologia, Radioterapia ed Ematologia, Fondazione Policlinico Universitario A. Gemelli IRCCS, Rome, Italy, [9]Médecine Nucléaire, Institut de Cancérologie Strasbourg Europe (ICANS), Strasbourg, France, [10]Hôpitaux Universitaires de Strasbourg, Faculté de Médecine, Université de Strasbourg, Strasbourg, France, [11]DRHIM, IPHC, UMR7178, CNRS/Unistra, Strasbourg, France

Purpose: Occult lymph node involvement is a major issue in the management of non-small cell lung carcinoma (NSCLC), with an estimated prevalence of approximately 2.9–21.6% in 18F-FDG PET/CT series. The aim of the study is to construct a PET model to improve lymph node assessment.

Methods: Patients with a non-metastatic cT1 NSCLC were retrospectively included from two centers, one used to constitute the training set, the other for the validation set. The best multivariate model based on Akaike's information criterion was selected, considering age, sex, visual assessment of lymph node (cN0 status), lymph node SUVmax, primary tumor location, tumor size, and tumoral SUVmax (T_SUVmax). A threshold minimizing false pN0 prediction was chosen. This model was then applied to the validation set.

Results: In total, 162 patients were included (training set: 44, validation set: 118). A model combining cN0 status and T_SUVmax was selected (AUC 0.907, specificity at threshold: 88.2%). In the validation cohort, this model resulted in an AUC of 0.832 and a specificity of 92.3% versus 65.4% for visual interpretation alone (p=0.02). A total of two false N0 predictions were noted (1 pN1 and 1 pN2).

Conclusion: Primary tumor SUVmax improves N status prediction and could allow a better selection of patients who are candidates for minimally invasive approaches.

KEYWORDS

NSCLC, lymph nodes, positron emission tomography, FDG, model

1. Introduction

The prediction of lymph node involvement (LNI) is a major challenge in the management of non-small cell lung tumors (NSCLC), as illustrated in the eighth edition of the TNM classification (1). LNI is strongly correlated with overall survival and disease-free interval (2, 3). Regardless of T status, the 5-year survival rates decrease from 56% in pathologic (p) pN0 patients to 38% (pN1), 26% (pN2), and 6% in pN3 disease (4). 18F-Fluorodeoxyglucose (18F-FDG) positron emission tomography coupled with computed tomography (PET/CT) is considered the reference examination for staging NSCLC. However, the sensitivity of PET/CT for the prediction of LNI is insufficient to dispense with surgical and pathological confirmation. The prevalence of occult pN2 disease in patients with clinical stage I NSCLC is estimated to be 6.5% (5), ranging from 2.9 to 21.6% in patients with peripheral and central tumors, respectively (6, 7).

Improving LNI assessment would open interesting perspectives, especially in early-stage NSCLC. For resectable tumors, as thoracotomy is progressively supplanted by mini-invasive approaches, such as video-assisted thoracic surgery (8), it would help to solve the dilemma of lymphadenectomy extension (8) and secures the decision whether to perform postoperative chemotherapy. For unresectable tumors, it would allow better planning of radiotherapy and possible adjuvant treatments. Overall, some 18F-FDG PET/CT predictors of occult LNI have already been described: primary tumor localization as central and right superior lobe tumors are associated with a greater risk of occult N2 node (6); primary tumor size: the negative predictive value of 18F-FDG PET/CT was higher for tumors of less than 3 cm in diameter (9–11); primary tumor 18F-FDG uptake (11–13). The objective of this study is to build and validate a model to identify patients without LNI more accurately than the simple visual interpretation of 18F-FDG PET/CT. We will focus on patients suitable for mini-invasive surgery, namely T1 non-metastatic patients.

2. Materials and methods

2.1. Patients

Patients satisfying the following criteria were included in the study: histologically proven NSCLC; available baseline PET/CT data; clinical (c) T1 and clinical M0 status (maximum diameter of primary tumor of less than 3 cm, as measured on baseline PET/CT and no visible metastasis); available pathological results with pN status; delay between PET/CT and pathological results of less than 2 months. Exclusion criteria were as follows: benign lung disease; non-FDG-avid subtypes (lepidic adenocarcinoma, carcinoid tumors); neoadjuvant systemic therapy performed prior to PET/CT.

A total of two data sources were used as follows: a training database consisting of patients with lung cancer referred to Strasbourg University Hospital (Strasbourg, France) between July 2004 and September 2009 for preoperative PET/CT; a validation database consisting in patients referred to Policlinico Universitario A. Gemelli (Rome, Italy) between January 2018 and December 2021.

2.2. PET/CT acquisition and interpretation

After checking patients' blood glucose levels (<2 g/l), staging PET/CT was performed at least from the skull base to the proximal thigh using two different PET/CT machines and acquisition protocols.

For the training cohort, images were acquired 60 min after an intravenous administration of 5 mg of diazepam, 80 mg of phloroglucinol, and 5.5 MBq/kg of 18F-FDG. A Discovery ST system (GE Medical System, Milwaukee, United States) was used. CT (140 kV, 80 mAs) was acquired first, followed by a two-dimensional PET/CT acquisition (seven fields of view of 15 cm, 4 min/field). PET data were reconstructed using an Ordered Subset Expectation Maximization algorithm (OSEM 2 iterations, 15 subsets, 128 × 128 matrix, slice thickness: 3.27 mm). PET/CT was reviewed on-site by two nuclear medicine physicians, with 4 and 14 years of experience in nuclear medicine, on a Xeleris workstation (GE Medical System, Milwaukee, United States).

For the validation cohort, images were acquired 60 min after the administration of 3 MBq/kg of 18F-FDG. A Biograph mCT (Siemens Healthineers) PET/CT was used, using the following parameters: CT (120 kV, 50 mAs, slice thickness: 3 mm), PET (2.5 min/position, reconstruction with OSEM algorithm: two iterations, 21 subsets, voxel size: 3.2 mm × 3.2 mm × 5 mm). Again, images were interpreted by two experienced nuclear medicine physicians (5 and 12 years of experience) on a SyngoVia workstation (Siemens Healthineers).

2.3. Surgical staging

In all cases, lymph node dissection systematically included at least three mediastinal stations including station 7, as recommended in the study of (14). In the training cohort, furthermore, systematic lymph node dissection was performed.

2.4. Data collection

The following parameters were collected as follows: sex, date of birth, date of diagnosis, histology of the primary tumor, and pN status. Regarding PET/CT studies, the following characteristics were measured on the training set: upper right lobe location of the primary tumor (yes/no); central location of the primary (yes/no); cT status derived from the diameter of the primary measured on the CT part of the PET/CT; cN status based on visual interpretation; 18F-FDG uptake (SUVmax) of both primary and nodal stations, denoted as T_SUVmax and N_SUVmax, respectively. Only features identified as relevant in the model were measured on the validation set.

SUVmax was measured using a manually drawn encompassing region of interest (ROI). For N_SUVmax, if no LNI was identified, an ROI encompassing right and left inferior paratracheal groups (4R-4L) was drawn (see Figure 1). Discrepancies between the measurements were resolved by consensus.

The 8th TNM classification was used (1), and pathological results were updated if an earlier version was used.

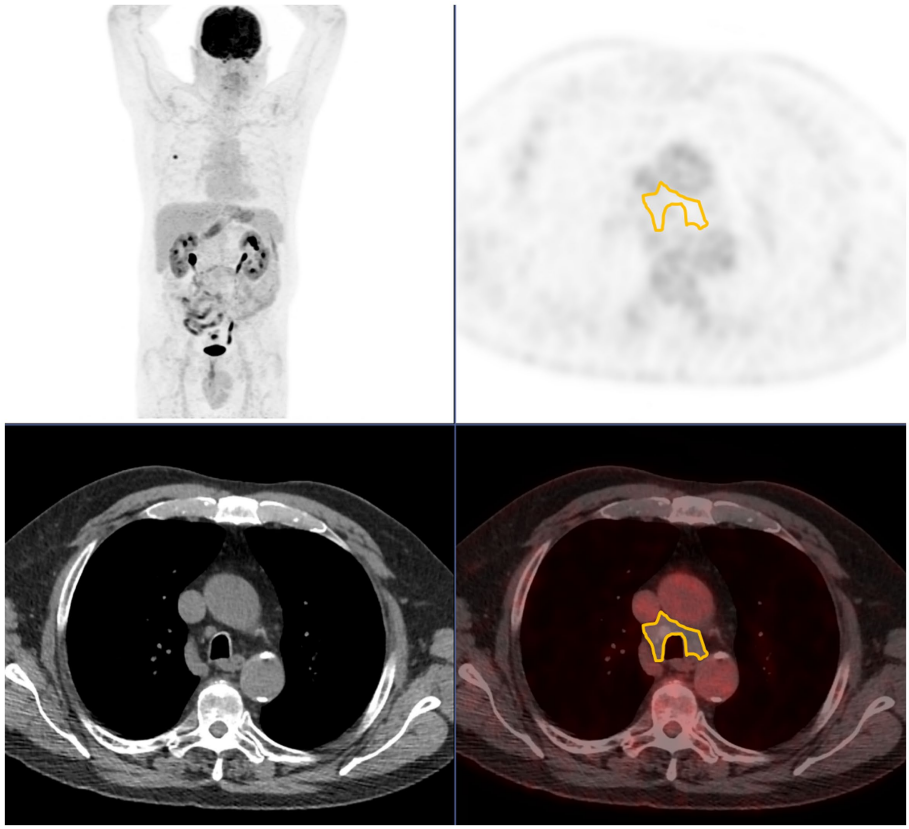

FIGURE 1
Region of interest used when no pathological lymph node uptake is seen, encompassing 4R and 4L station. From top to bottom and from left to right: maximum intensity projection; axial PET; axial CT; axial fused PET/CT.

2.5. Statistical analysis

Quantitative data were described as mean and standard deviation (SD) and qualitative data as number and percentage. Comparison between training and validation set was performed using Student's *t*-test, two proportion *Z*-test, or Fisher's test when appropriate. In the training set, logistic regression was used to derive odds ratios (ORs) and 95% confidence intervals (95%CIs) on both univariate and multivariate analyses. The best multivariate model to predict pN0 status was selected based on Akaike's Information Criterion. A receiver operating characteristic (ROC) curve was drawn to derive the area under the curve (AUC) and threshold. A threshold that favors specificity (least number of false positives, i.e., patients falsely predicted as pN0) while keeping sensitivity above 50% was chosen. False positives were reported, either when using the model or the visual interpretation alone and compared using a McNemar test.

In the validation set, an ROC curve using the identified optimal model was drawn to derive AUC. False positives, specificities, and positive predictive values were reported, either when using the model or the visual interpretation alone. The numbers of false positives were compared using a McNemar test based on a 2×2 contingency table (false positive vs. non-false positive, visual analysis vs. model). As SUV may be dependent on the machine used to acquire the PET/CT, the calculations were performed two times as follows: once without and once with a harmonization procedure. We used the ComBat algorithm (15) to perform this harmonization.

3. Results

3.1. Included patients

A total of 62 non-metastatic cT1 patients were identified in the training set. In total, 18 (29%) patients were excluded (10 benign findings, four lepidic adenocarcinomas, two neuroendocrine tumors, and two composite carcinomas with neuroendocrine component). In the end, 44 patients were included in the training set.

For the validation set, 118 cT1 cM0 patients with available PET/CT and pathological N status were identified, and eight patients with neuroendocrine tumors and two patients with missing data were excluded. A total of 108 patients were included.

Patients' characteristics are presented in Table 1. The validation set included significantly older patients with more female patients (52.8% vs. 25.0%), higher adenocarcinoma frequency (78.7% vs. 61.4%), and less LNI both on clinical and pathological assessments.

3.2. Model development

In univariate analysis, only N_SUVmax and cN0 (visual analysis) were significant predictors of pN0 status ($p < 0.001$). N_SUVmax OR was 0.10 (the higher the N_SUVmax, the lower the probability of pN0), and cN0 OR was 84.55 (increased probability of pN0 if cN0).

10.3389/fmed.2023.1141636

TABLE 1 Patients' characteristics.

	Training set	Validation set	Comparison
	(*n* =44)	(*n* =108)	
Age years (SD)	61.0 (8.4)	68.9 (9.2)	<0.001*
Sex number (%)			
Male	33 (75.0%)	57 (47.2%)	0.002*
Female	11 (25.0%)	51 (52.8%)	
Histological subtype number (%)			
Adenocarcinoma	27 (61.4%)	85 (78.7%)	
Epidermoid carcinoma	13 (29.5%)	22 (20.4%)	0.012*
Other	4 (9.1%)	1 (0.9%)	
Clinical T status number (%)			
cT1a	11 (25.0%)	20 (18.5%)	
cT1b	14 (31.8%)	52 (48.2%)	0.17
cT1c	19 (43.2%)	36 (33.3%)	
Primary tumor location number (%)			
Upper Right Lobe	7 (15.9%)	–	–
Centrally located	3 (6.8%)	–	–
PET/CT parameters			
cN0 number (%)	30 (68.2%)	100 (92.6%)	0.002*
T_SUVmax mean (SD)	7.6 (4.7)	6.9 (5.4)	0.444
N_SUVmax mean (SD)	3.1 (2.7)	–	–
Pathological N status number (%)			
pN0	27 (61.4%)	94 (87.0%)	
pN1	6 (13.6%)	8 (7.4%)	0.001*
pN2	11 (25.0%)	6 (5.6%)	
pN3	0 (0%)	0 (0%)	

SD, standard deviation. *$p < 0.05$.

T_SUVmax and T status even not significant, had a value of $p < 0.1$. Age, primary tumor location, and sex were not predictive of pN0 status (Table 2). The best model derived from those parameters associated T_SUVmax, even not significant, and cN0 binary status. The derived equation giving the probability P of being pN0 was as follows:

$$P = 1 / \left[1 + \exp\left(\begin{matrix} 1{,}383842 + 0{,}168884 \times \\ T\_SUVmax - 4{,}602946 \times cN0 \end{matrix} \right) \right]$$

The corresponding ROC curve (Figure 2) had an AUC of 0.907 [0.809–1.000]. The optimal threshold to maximize the specificity of the model was 90%, with N0 status being predicted when $P \geq 90\%$. Derived sensitivity and specificity were, respectively, 0.519 [0.340–0.692] and 0.882 [0.642–0.977].

The whole training population (Table 1, $n = 44$) comprised six pN1 patients (13.6%) and 11 pN2 patients (25.0%). The use of visual analysis alone predicted 30 N0 patients, resulting in four false positives: four pN1 (13.3%) and 0 pN2 (0.0%). When applying our model, 16 patients were predicted as N0, resulting in two pN1 (12.5%) false positives. The specificity of the visual analysis approach was 0.765, and the specificity of the model was 0.882 ($p = 0.480$, Table 3). A total of five patients (11.3%) were upstaged from cT1 to pT2 based on measurement uncertainty.

TABLE 2 Prediction of pN0 status in cT1M0 patients: univariate and multivariate analyses.

	Univariate analysis	Multivariate analysis
		(Best Model)
Upper right lobe location	1.23 [0.24–6.34] $p = 0.803$	–
Peripheral location	3.47 [0.29–41.53] $p = 0.309$	–
Age	1.03 [0.96–1.11] $p = 0.439$	–
T (1a, 1b, 1c)	0.46 [0.20–1.06] $p = 0.054$	–
Sex (F)	1.96 [0.44–8.77] $p = 0.363$	–
T_SUVmax	0.88 [0.77–1.01] $p = 0.065$	0.85 [0.67–1.07] $p = 0.139$
N_SUVmax	0.10 [0.02–0.62] $p < 0.001$	–
cN0	84.55 [8.56–834.61] $p < 0.001$	99.78 [8.49–1172.90] $p < 0.001$

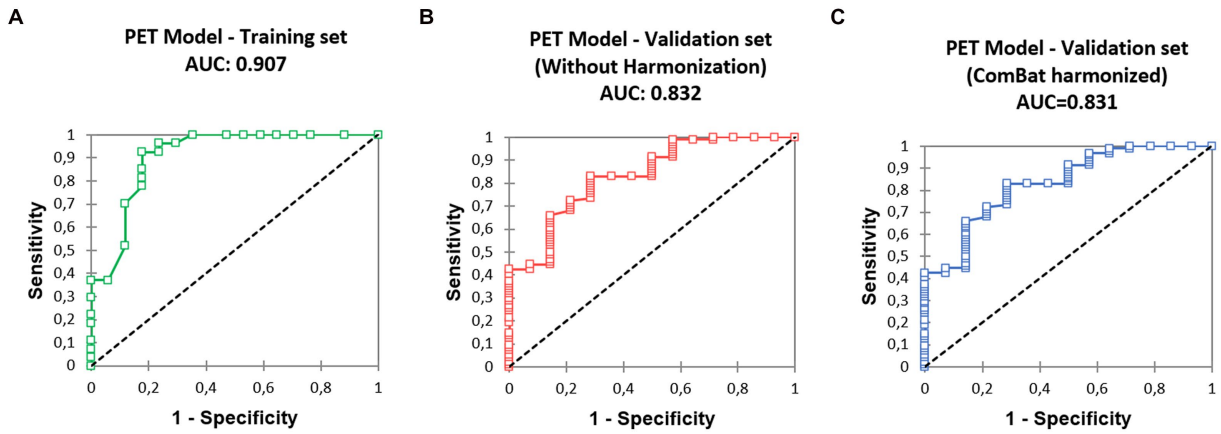

FIGURE 2
Receiver operating characteristic (ROC) curves derived from the predictive model, **(A)** training set, **(B)** validation set, without SUV harmonization, **(C)** validation set after SUV harmonization.

TABLE 3 Specificity and positive predictive value of visual analysis and model-based prediction.

	Training cohort			Validation cohort		
	Visual analysis	Model-based prediction	Comparison (false positive number)	Visual analysis	Model-based prediction	Comparison (false positive number)
Specificity	76.5%	88.2%	$p = 0.480$	65.4%	92.3% (92.3%)	$p = 0.023$*
False pN0 prediction rate						
Positive predictive value	86.7%	87.5%		91.0%	96.4% (95.7%)	($p = 0.023$*)
% of predicted N0 that are pN0						

Data using harmonized SUV are presented in parenthesis; *$p < 0.05$.

3.3. Model validation

3.3.1. Validation using native, unharmonized SUV data

The ROC curve (Figure 2) calculated on the validation cohort showed an AUC of 0.832 [0.721, 0.944]. The whole population ($n = 108$) comprised eight pN1 (7.4%) and six pN2 (5.6%). Using visual analysis only, 100 patients were predicted to be N0, resulting in nine false positives: four pN1 (4.0%) and five pN2 (5.0%). When using the predictive model, 56 patients were predicted as N0, with two false positive patients: one pN1 (1.8%) and one pN2 (1.8%). Specificities were 0.654 (visual analysis) and 0.923 (model), significantly different ($p = 0.023$, Table 3). In total, 18 (16.7%) patients classified as cT1 were not pT1 after surgery: 16 patients were pT2 (size difference < 5 mm between estimation and pathological measure); one was pT3 (unseen separate nodule adjacent to the main primary); and one was pT4 (due to adjacent organs invasion).

3.3.2. Validation using harmonized SUV data

The ComBat algorithm was used to determine corrected SUV (corSUV) corresponding to the SUV that would have been found if the patients in the validation cohort (Biograph mCT PET/CT—Siemens) had undergone the examination under the machine used in the training cohort (Discovery ST system—General Electrics).

The ROC curve (Figure 2) calculated on the validation cohort showed an AUC of 0.831 [0.720; 0.942]. When using the predictive model with corSUV, 46 patients instead of 56 were predicted as N0. All those 46 patients were considered as N0 using unharmonized SUV. The remaining discrepant 10 patients were all pN0. The number of false positives was thus unchanged.

4. Discussion

Occult lymph node involvement on 18F-FDG PET/CT is a central problem in the management of lung cancer, with an estimated average occult N2 rate for stage I tumors of 6.1% (16).

4.1. Positron emission tomography model

Successive studies have attempted to determine new parameters to decrease this proportion, mainly based on size, location, and uptake of the primary tumor. Our model retained only two parameters among these factors as follows: the visual interpretation of the lymph node status by the nuclear medicine physician (cN0 vs. cN1, cN2, or cN3) and the SUVmax of the primary tumor. In this study, we propose a simple algorithm to detect a subpopulation with a very low risk of lymph node involvement in two steps as follows:

1. Check the eligibility of the patient: measure the primary tumor (< 3 cm, corresponding to a cT1) and ensure the absence of metastasis.
2. Use the model: the model equation (eq. 1.), although complex, can be simplified and decomposed by noting that the condition $P \geq 0.9$ can only be met if a patient fulfills two conditions: being cN0 and having a T_SUVmax of less than 6.05 without harmonization procedure.

Using this algorithm, the proportion of occult LNI was significantly reduced: 3.6% (N1 or N2) and 1.8% (N2 only). The false positive rate, even lower when using the algorithm, was not significantly different on the training dataset in comparison to visual analysis, presumably due to the sample size of the training set. However, it reached significance in the validation set.

We considered only the clinical T-stage, which is the only one accessible preoperatively. This measure is, however, a source of uncertainty, as shown by the proportion of upstaging after surgery encountered in our two cohorts (between 10 and 20%). The majority of upstaging concerned cT1 tumors with a size close to 3 cm, the limit of the T2 stage.

The T_SUVmax threshold of 6.05 is not directly comparable to the one reported in other studies: we did not seek an optimal threshold but a threshold minimizing the number of occult lymph nodes. However, it is interesting to note that this threshold remains in the same range as those previously reported between 4 (13) and 7.5 (12). The study by Vansteenkiste et al. (17), although not directly concerning occult LNI, reported a better 2-year survival when the primary tumor had SUV lesser than 7 and tumor size lower than 3 cm. Like all SUV-based indices, the concern of inter-machine generalization is raised. However, our model showed similar good performances, with and without harmonization showing some robustness to the change of reconstruction protocol and machine. This problem could be more present with the new digital PET/CT, given their better technical characteristics in terms of resolution and sensitivity. Harmonization will, then, probably be systematically required.

4.2. Potential clinical implications

From a theoretical point of view, the model presented herein would allow a better selection of patients who are candidates for minimally invasive staging or more conservative intra-operative lymph node dissection with several practical implications: optimizing resources and reducing costs; avoiding complications and delay due to unnecessary procedures. Obviously, these results need to be confirmed in a prospective clinical cohort of patients.

4.3. Limitations

Several limitations need to be discussed. Apart from the limitations inherent in the retrospective nature of the study, our training cohort presents some notable differences from our validation cohort, mainly related to the period of patient recruitment (2004 to 2009 vs. 2018 to 2021). In particular, the proportion of women is increased in the validation cohort, consistent with the increased prevalence of lung cancer in this population; this increase probably explains the increased proportion of lung adenocarcinomas, which are more frequent in the female population. The age of the validation population was significantly higher with a delta of 7 years, probably due to a center effect, as was the proportion of cN0. Despite these differences, the good performance of the model is reassuring.

Several factors were not taken into account for the measure of N_SUV, particularly the background uptake level and the partial volume effect. Indeed, we tried to use a method of measurement as simple as possible to be applied in clinical routine. In addition for simplicity, we estimated lymph node uptake only by measuring the lymph node with the highest uptake not by measuring all the most frequently affected mediastinal lymph nodes.

5. Conclusion

A model associating the SUVmax of the primary tumor with the lymph node visual interpretation allows to reduce the number of occult adenopathy in early-stage NSCLC.

Data availability statement

The raw data supporting the conclusions of this article will be made available by the authors, without undue reservation.

Ethics statement

The studies involving human participants were reviewed and approved by Institutional Ethics Committee Fondazione Policlinico Universitario A. Gemelli IRCCS —Università Cattolica del Sacro Cuore (registration number: 0015316–03/05/2022). Written informed consent for participation was not required for this study in accordance with the national legislation and the institutional requirements.

Author Contributions

DM and AI: conceptualization and validation. DM: methodology, software, formal analysis, and writing – original draft preparation. DM, MC, and FL: data curation. DM, MC, P-EF, M-PC, SA, LB, FL, and AI: writing – review and editing. All authors have read and agreed to the published version of the manuscript.

Conflict of interest

The authors declare that the research was conducted in the absence of any commercial or financial relationships that could be construed as a potential conflict of interest.

Publisher's note

All claims expressed in this article are solely those of the authors and do not necessarily represent those of their affiliated organizations, or those of the publisher, the editors and the reviewers. Any product that may be evaluated in this article, or claim that may be made by its manufacturer, is not guaranteed or endorsed by the publisher.

References

1. Detterbeck FC, Boffa DJ, Kim AW, Tanoue LT. The eighth edition lung cancer stage classification. *Chest*. (2017) 151:193–203. doi: 10.1016/j.chest.2016.10.010

2. Ettinger DS, Kris MG. NCCN non-small cell lung cancer clinical practice guidelines. *J Natl Compr Cancer Netw*. (2004) 2, 3:S-9-13.

3. Pignon J-P, Tribodet H, Scagliotti GV, Douillard J-Y, Shepherd FA, Stephens RJ, et al. Lung adjuvant cisplatin evaluation: a pooled analysis by the lace collaborative group. *JCO*. (2008) 26:3552–9. doi: 10.1200/JCO.2007.13.9030

4. Osarogiagbon RU, Yu X. Mediastinal lymph node examination and survival in resected early-stage non–small-cell lung cancer in the surveillance, epidemiology, and end results database. *J Thorac Oncol*. (2012) 7:1798–806. doi: 10.1097/JTO.0b013e31827457db

5. Beyaz F, Verhoeven RLJ, Schuurbiers OCJ, Verhagen AFTM, van der Heijden EHFM. Occult lymph node metastases in clinical N0/N1 NSCLC; a single center in-depth analysis. *Lung Cancer*. (2020) 150:186–94. doi: 10.1016/j.lungcan.2020.10.022

6. Alsarraf N, Aziz R, Gately K, Lucey J, Wilson L, Mcgovern E, et al. Pattern and predictors of occult mediastinal lymph node involvement in non-small cell lung cancer patients with negative mediastinal uptake on positron emission tomography. *Eur J Cardiothorac Surg*. (2008) 33:104–9. doi: 10.1016/j.ejcts.2007.09.026

7. Lee PC, Port JL, Korst RJ, Liss Y, Meherally DN, Altorki NK. Risk factors for occult mediastinal metastases in clinical stage i non-small cell lung cancer. *Ann Thorac Surg*. (2007) 84:177–81. doi: 10.1016/j.athoracsur.2007.03.081

8. Aprile V, Ceccarelli I, Korasidis S, Mastromarino MG, Bacchin D, Sicolo E, et al. A narrative review on lymphadenectomy: from open to minimally invasive surgery. *Video-Assist Thorac Surg*. (2022) 7:6. doi: 10.21037/vats-21-33

9. Wang J, Welch K, Wang L, Kong F-M. Negative predictive value of positron emission tomography and computed tomography for stage T1-2N0 non–small-cell lung cancer: a meta-analysis. *Clin Lung Cancer*. (2012) 13:81–9. doi: 10.1016/j.cllc.2011.08.002

10. Gomez-Caro A, Boada M, Cabanas M, Sanchez M, Arguis P, Lomena F, et al. False-negative rate after positron emission tomography/computer tomography scan for mediastinal staging in ci stage non-small-cell lung cancer. *Eur J Cardiothorac Surg*. (2012) 42:93–100. doi: 10.1093/ejcts/ezr272

11. Kaseda K, Watanabe K, Asakura K, Kazama A, Ozawa Y. Identification of false-negative and false-positive diagnoses of lymph node metastases in non-small cell lung cancer patients staged by integrated 18F-fluorodeoxyglucose-positron emission tomography/computed tomography: a retrospective cohort study. *Thoracic Cancer*. (2016) 7:473–80. doi: 10.1111/1759-7714.12358

12. Su M, Li Y, Li F, Li L, Tian R. Risk factors for N2 metastasis in patients with non-small-cell lung cancer: multivariate analyses of 18F-FDG PET/CT data. *Nucl Med Commun*. (2014) 35:916–21. doi: 10.1097/MNM.0000000000000144

13. García B, de Castro A, Ferreirós Domínguez J, Delgado Bolton R, Fernández Pérez C, Cabeza Martínez B, et al. La PET-TC en la estadificación ganglionar prequirúrgica del carcinoma de pulmón de células no pequeñas: implicación de los falsos negativos y falsos positivos. *Radiologia*. (2017) 59:147–58. doi: 10.1016/j.rx.2016.12.001

14. Lardinois D, Deleyn P, Vanschil P, Porta R, Waller D, Passlick B, et al. ESTS Guidelines for Intraoperative lymph node staging in non-small cell lung cancer. *Eur J Cardiothorac Surg*. (2006) 30:787–92. doi: 10.1016/j.ejcts.2006.08.008

15. Orlhac F, Eertink JJ, Cottereau A-S, Zijlstra JM, Thieblemont C, Meignan M, et al. A guide to ComBat harmonization of imaging biomarkers in multicenter studies. *J Nucl Med*. (2022) 63:172–9. doi: 10.2967/jnumed.121.262464

16. Verhagen AFT, Bootsma GP, Tjan-Heijnen VCG, van der Wilt GJ, Cox AL, Brouwer MHJ, et al. FDG-PET in Staging Lung Cancer. *Lung Cancer*. (2004) 44:175–81. doi: 10.1016/j.lungcan.2003.11.007

17. Vansteenkiste JF, Stroobants SG, Dupont PJ, De Leyn PR, Verbeken EK, Deneffe GJ, et al. Prognostic importance of the standardized uptake value on ^{18}F-fluoro-2-deoxy-glucose–positron emission tomography scan in non–small-cell lung cancer: an analysis of 125 cases. *JCO*. (1999) 17:3201–6. doi: 10.1200/JCO.1999.17.10.3201

frontiers | Frontiers in Medicine

TYPE Original Research
PUBLISHED 27 April 2023
DOI 10.3389/fmed.2023.1148287

OPEN ACCESS

EDITED BY
Luka Lezaic,
University Medical Centre Ljubljana, Slovenia

REVIEWED BY
Murat Fani Bozkurt,
Hacettepe University, Türkiye
Soňa Balogová,
Comenius University, Slovakia

*CORRESPONDENCE
Alessio Imperiale
✉ a.imperiale@icans.eu

RECEIVED 19 January 2023
ACCEPTED 07 April 2023
PUBLISHED 27 April 2023

CITATION
Imperiale A, Bani J, Bottoni G, Latgé A, Heimburger C, Catrambone U, Vix M, Treglia G and Piccardo A (2023) Does ^{18}F-Fluorocholine PET/CT add value to positive parathyroid scintigraphy in the presurgical assessment of primary hyperparathyroidism? *Front. Med.* 10:1148287. doi: 10.3389/fmed.2023.1148287

Does ^{18}F-Fluorocholine PET/CT add value to positive parathyroid scintigraphy in the presurgical assessment of primary hyperparathyroidism?

Alessio Imperiale[1,2]*, Jacob Bani[1], Gianluca Bottoni[3], Adrien Latgé[1], Céline Heimburger[1,4], Ugo Catrambone[5], Michel Vix[6], Giorgio Treglia[7,8,9,10] and Arnoldo Piccardo[3]

[1]Nuclear Medicine and Molecular Imaging, Institut de Cancérologie de Strasbourg Europe (ICANS), Strasbourg University Hospitals, Strasbourg, France, [2]Molecular Imaging, DRHIM, Institut Pluridisciplinaire Hubert Curien (IPHC), UMR7178, CNRS, University of Strasbourg, Strasbourg, France, [3]Nuclear Medicine, Ente Ospedaliero "Ospedali Galliera", Genoa, Italy, [4]Nuclear Medicine, Hopital Civil de Haguenau, Haguenau, France, [5]General Surgery, Ente Ospedaliero "Ospedali Galliera", Genoa, Italy, [6]General, Digestive, and Endocrine Surgery, IRCAD-IHU, Strasbourg University Hospitals, Strasbourg, France, [7]Clinic for Nuclear Medicine, Imaging Institute of Southern Switzerland, Ente Ospedaliero Cantonale, Bellinzona, Switzerland, [8]Nuclear Medicine and Molecular Imaging, Lausanne University Hospital, Lausanne, Switzerland, [9]Faculty of Biology and Medicine, University of Lausanne, Lausanne, Switzerland, [10]Faculty of Biomedical Sciences, Università Della Svizzera Italiana, Lugano, Switzerland

Introduction: To investigate the value of presurgical ^{18}F-FCH PET/CT in detecting additional hyperfunctioning parathyroids despite a positive ^{99m}Tc-sestamibi parathyroid scintigraphy in patients with primary hyperparathyroidism (pHPT).

Methods: This is a retrospective study involving patients with pHPT, positive parathyroid scintigraphy performed before ^{18}F-FCH PET/CT, and parathyroid surgery achieved after PET/CT. Imaging procedures were performed according to the EANM practice guidelines. Images were qualitatively interpreted as positive or negative. The number of pathological findings, their topography, and ectopic location were recorded. Histopathology, Miami criterion, and biological follow-up were considered to ensure effective parathyroidectomy confirming the complete excision of all hyperfunctioning glands. The impact of ^{18}F-FCH PET/CT on therapeutic strategy was recorded.

Results: 64/632 scanned pHPT patients (10%) were included in the analysis. According to a per lesion-based analysis, sensitivity, specificity, positive predictive value, and negative predictive value of ^{99m}Tc-sestamibi scintigraphy were 82, 95, 87, and 93%, respectively. The same values for ^{18}F-FCH PET/CT were 93, 99, 99, and 97%, respectively. ^{18}F-FCH PET/CT showed a significantly higher global accuracy than ^{99m}Tc-sestamibi scintigraphy: 98% (CI: 95–99) vs. 91% (CI: 87–94%). Youden Index was 0.79 and 0.92 for ^{99m}Tc-sestamibi scintigraphy and ^{18}F-FCH PET/CT, respectively. Scintigraphy and PET/CT were discordant in 13/64 (20%) patients (49 glands). ^{18}F-FCH PET/CT identified nine pathologic parathyroids not detected by ^{99m}Tc-sestamibi scintigraphy in 8 patients (12.5%). Moreover, ^{18}F-FCH PET/CT allowed the reconsideration of false-positive scintigraphic diagnosis (scinti+/PET-) for 8 parathyroids in 7 patients (11%). The ^{18}F-FCH PET/CT influenced the surgical strategy in 7 cases (11% of the study population).

Conclusion: In a preoperative setting, ^{18}F-FCH PET/CT seems more accurate and useful than ^{99m}Tc-sestamibi scan in pHPT patients with positive scintigraphic results. Positive parathyroid scintigraphy could be not satisfactory before neck

surgery particularly in patients with multiglandular disease, suggesting a need to evolve the practice and define new preoperative imaging algorithms including ^{18}F-FCH PET/CT at the fore-front in pHPT patients.

KEYWORDS

hyperparathyroidism, parathyroid, PET, choline, scintigraphy, sestamibi, parathyroid adenoma

Introduction

Primary hyperparathyroidism (pHPT) is a common endocrine disease caused by excessive secretion of parathyroid hormone (PTH) from one or more hyperfunctioning parathyroid glands. In 80% of cases, pHPT is related to a solitary parathyroid adenoma. Moreover, the patient may harbor multiple-gland disease (MGD), with double adenomas or 4-gland hyperplasia in 15–20% of cases (1), and ectopic hyperfunctioning parathyroids in about 16% of cases (2).

A mini-invasive parathyroidectomy (MIP) is emerging as the standard of care in patients with pHPT, reducing the operative complications, time, and cost with cure rates comparable to those of surgery (3). After a decision was made to proceed with parathyroidectomy, the success of the minimally invasive surgical strategy depends on effective detection of the hyperfunctioning gland during the preoperative work-up (4, 5). Currently, neck ultrasound (US) and parathyroid scintigraphy with ^{99m}Tc-sestamibi are recommended as first-line imaging techniques. However, US diagnostic performances are influenced by the experience of the operator, and scintigraphy success largely depends on the adopted scintigraphic protocol (6, 7), and on patient underlying pathology. Indeed, the systematic review by Ruda et al. (8) alerts about the low sensitivity of ^{99m}Tc-sestamibi scintigraphy for the detection of multigland hyperplasia (44%) and double adenomas (29.9%).

In recent years, positron emission tomography/computed tomography/computed tomography (PET/CT) with ^{18}F-fluorocholine (^{18}F-FCH) has emerged as second-line imaging with high resolution, low radiation exposure, and shorter examination times in patients with previously negative or inconclusive ^{99m}Tc-sestamibi scintigraphy and/or ultrasound (9). A growing body of evidence suggests the high sensitivity of ^{18}F-FCH PET/CT in detecting hyperfunctioning parathyroids (sensitivity and detection rate up to 90 and 80%, respectively) in patients with pHPT (10), even in reoperated patients (11). Recently published parathyroid imaging guidelines suggest, when possible, ^{18}F-FCH PET/CT as a potential "alternative" first-line option in patients with pHPT (12). All these considerations emphasize the debate about the possible role of ^{18}F-FCH PET/CT as first-line nuclear medicine imaging method for preoperative localization of hyperfunctioning parathyroids in patients with pHPT (13). With a perspective to participate in the discussion, in the present study we analyzed whether and in what percentage of patients with pHPT scheduled for neck surgery, ^{18}F-FCH PET/CT detect additional hyperfunctioning parathyroids despite a positive ^{99m}Tc-sestamibi parathyroid scintigraphy. The impact of ^{18}F-FCH PET/CT results on therapeutic strategy has been also investigated.

Materials and methods

Patient population

This is a non-interventional retrospective study involving patients with HPT who underwent ^{18}F-FCH PET/CT for preoperative identification of hyperfunctioning parathyroid glands at the nuclear medicine unit of the *Strasbourg University Hospital*/Institut de Cancérologie de Strasbourg Europe (ICANS) of Strasbourg, France, and the Galliera Hospitals of Genoa, Italy. 632 patients were retrieved from own Institutional parathyroid ^{18}F-FCH PET/CT registry from March 2016 to March 2021. Only patients satisfying the following criteria were retrospectively included: (1) pHPT, (2) positive parathyroid scintigraphy performed before ^{18}F-FCH PET/CT, (3) parathyroid surgery achieved after ^{18}F-FCH PET/CT.

Clinical, imaging and biological data were extracted from hospital databases, clinician reports, and biomedical laboratories, including sex, age, previous parathyroid surgery, the results of diagnostic imaging performed before ^{18}F-FCH PET/CT [i.e., neck ultrasound (US)], patient genetic status, calcimimetic treatment, hypercalcemia-related symptoms, PTH, and calcium serum concentrations. Surgical procedures, perioperative and post-surgical follow-up PTH measurements, and pathological reports concerning the parathyroid surgery after ^{18}F-FCH PET/CT were collected.

In accordance with French Jarde Law, the *Ethical Committee of Strasbourg University Hospital and Faculty of Medicine* waives the requirement for informed consent for retrospective use of anonymized data obtained in the course of routine clinical care. The local Institutional Review Board *has confirmed that no ethical approval is required (CE-2022-100).*

Imaging procedures

All scintigraphic and PET/CT procedures were achieved according to the EANM practice guidelines for parathyroid imaging (12). Parathyroid scintigraphy was performed using single-tracer (^{99m}Tc-sestamibi) dual-phase technique, or dual-tracer subtraction technique (^{99m}Tc-sestamibi/^{123}I or ^{99m}Tc-sestamibi/^{99m}Tc-pertechnetate). Imaging protocol included neck and mediastinum anterior planar scan, followed by single photon emission tomography/computed tomography (SPECT/CT) acquisition. A low-dose CT scan was performed for anatomical correlation only. Concerning PET/CT, all examinations were performed by combined devices equipped with time-of-flight technology. Patients fasted for at least 6 h before the intravenous injection of about 2 MBq/kg of ^{18}F-FCH. PET acquisition from the mandible to the carina was acquired 60 min after ^{18}F-FCH administration in the supine position

with arms along the body and headrest. PET datasets were reconstructed iteratively by ordered subset expectation maximization (OSEM) algorithm, using no contrast-enhanced CT for attenuation correction.

Scintigraphic and PET/CT images were qualitatively interpreted as positive or negative. Focal non-physiological uptake corresponding to any cervical or thoracic abnormalities discriminable from thyroid tissue and positioned in typical parathyroid sites or in ectopic areas was considered positive. The number of pathological findings on ^{99m}Tc-sestamibi scintigraphy and ^{18}F-FCH PET/CT, their topography in reference to the midline and the thyroid gland, ectopic location, and embryologic origin of the parathyroid (superior vs. inferior gland) were recorded.

Gold standard

Histopathology after parathyroidectomy, associated with a decrease of more than 50% of perioperative PTH blood level (Miami criterion), AND/OR a 6-months biological follow-up were considered to ensure operative success confirming the complete excision of all hyperfunctioning parathyroid tissue (true positive results) (14). Intraoperative parathyroid hormone monitoring (IPM) was also used to preserve the normally functioning parathyroid glands during parathyroidectomy with resection of only the pathological. Normal glands (true negative results) were defined according to a combination of neck surgical exploration result, biological follow-up (PTH, serum calcium), and Miami ">50% intraoperative PTH drop" criterion.

^{18}F-FCH PET/CT was considered contributory to modifying the therapeutic strategy according to the following situations: (1) lateralize the side of mini-invasive parathyroidectomy (MIP): right vs. left, or left vs. right, (2) bilateral MIP converted in unilateral MIP, (3) unilateral MIP converted in bilateral MIP, and (4) MIP converted in cervicotomy eventually associated to mediastinoscopy.

Statistical analysis

Categorical variables were presented as numbers and percentages. Results for continuous data were expressed as mean ± standard deviation, or median and interquartile (IQ) range, as appropriate. Diagnostic performance of both ^{18}F-FCH PET/CT and ^{99m}Tc-sestamibi scintigraphy in detecting hyperfunctioning parathyroids were assessed on a per-lesion basis. Sensitivity (Se), specificity (Sp), positive predictive value (PPV), negative predictive value (NPV), and overall accuracy were assessed and presented with 95% confidence intervals (95% CI). Finally, the Youden Index, which is independent from the prevalence of the disease, was estimated as (Sp + Se)-1. A p value <0.05 were considered statistically significant. Statistical analysis has been provided using Graphpad Prism software (v.9.1.1, 2021).

Results

Patient population

In the study period, 64 among 632 scanned patients (10%) were addressed for preoperative ^{18}F-FCH PET/CT investigation after a positive ^{99m}Tc-sestamibi scintigraphy, and were included in the analysis. The median time interval between a positive ^{99m}Tc-sestamibi scintigraphy and ^{18}F-FCH PET/CT was 104 days (IQ range: 47–247). Patients' refusal immediate parathyroidectomy, or delayed surgery due to the COVID-19 pandemic, mainly explain why patients underwent ^{18}F-FCH PET/CT despite a positive ^{99m}Tc-sestamibi scintigraphy, and the delay between scintigraphy and PET/CT. In all cases, cross-disciplinary team stated about ^{18}F-FCH PET/CT indication. Medical treatment, if any, was not changed between the two examinations.

Population median age was 65 years (IQ: 58–70, range 29–85), with a female to male ratio of 3.6 (14:50). The preoperative median PTH and serum calcium levels were 116.3 ng/l (IQ range: 92.6–170.8) and 2.68 nmol/l (IQ range: 2.58–2.80), respectively. Five patients (8%) presented with recurrent/persistent pHPT, and the remaining 59 cases (92%) had no previous parathyroid surgery. Thus, a total of 248 glands (12 and 236, respectively) were considered for further analysis. Result from neck US was not available for 4 of 64 selected patients, including 1 case of primary diagnosis, 2 persistent pHPT, and 1 recurrent pHPT. US was positive in 36/60 patients (60%) and negative in the remaining 24 cases. No case of MGD was suspected by US. After ^{18}F-FCH PET/CT, 40 patients underwent MIP (63%), 23 exploratory cervicotomy (36%), and 1 thoracoscopy (1%), for a total of 72 excised pathologic parathyroid glands corresponding to 56 adenomas and 16 hyperplasia. Size and weight of pathologic parathyroid was available in 67 and 44 glands, and the median values were 12 mm (IQ: 10–20) and 0.4 g (IQ: 0.2–1.0), respectively. Five patients had MGD (8%). Median time interval between ^{18}F-FCH PET/CT and parathyroid surgery was 138 days (IQ range 63–271). Median biological follow-up after parathyroid surgery was 3 months (IQ range 1–12), and 53% of patients had at least 6 months post-surgical follow-up.

^{99m}Tc-sestamibi scintigraphy

Parathyroid scintigraphy was performed using ^{99m}Tc-sestamibi dual-phase technique in 5 patient (8%), and dual-tracer subtraction technique including ^{99m}Tc-sestamibi/^{123}I or ^{99m}Tc-sestamibi/^{99m}Tc-pertechnetate in 59 patients (92%). According to the inclusion criteria, parathyroid scintigraphy was positive in all patients, suggesting the presence of one or two hyperfunctioning parathyroids in 60 and 2 patients, respectively. According to a per lesion-based analysis, parathyroid scintigraphy was true-positive in 59 cases (24%), false-positive in 9 cases (4%), true-negative in 167 cases (68%), and false-negative in 13 cases (5%, 5 adenomas, 8 hyperplasia). Se, Sp, PPV, NPV, and global accuracy of ^{99m}Tc-sestamibi scintigraphy were 82, 95, 87, 93, and 91%, respectively. The Youden index was 0.79 (Table 1).

^{18}F-FCH PET/CT

^{18}F-FCH PET/CT was positive in 63 out of 64 included patients indicating the presence of one, two, or three hyperfunctioning parathyroids in 57, 5, and 1 patient, for a total of 70 pathological parathyroids. According to a per lesion-based analysis, ^{18}F-FCH PET/CT was true-positive in 67 cases (27%), false-positive in 3 cases (1%), true-negative in 175 cases (71%), and false-negative in 1 case. Se, Sp,

TABLE 1 Head-to-head comparison (per gland analysis) of diagnostic performances of ^{99m}Tc-sestamibi scintigraphy and ^{18}F-FCH PET/CT in the whole population of 64 patients with pHPT.

	TP	FP	TN	FN	Se (%)	Sp (%)	PPV (%)	NPV (%)	Global accuracy (%)	Youden index
^{99m}Tc-sestamibi scintigraphy	59	9	167	13	82 (71–90)	95 (91–98)	87 (77–93)	93 (89–95)	91 (87–94)	0.79
^{18}F-FCH PET/CT	67	1	175	5	93 (85–98)	99 (97–100)	99 (90–100)	97 (94–99)	98 (95–99)	0.92

TP, true-positive; FP, false-positive; TN, true-negative; FN, false-negative; Se, Sensitivity; Sp, specificity; PPV, positive predictive value; NPV, negative predictive value. In parentheses are reported the 95% CI values.

PPV, NPV, and global accuracy of ^{18}F-FCH PET/CT were 93, 99, 99, 97, and 98%, respectively. Although higher values of Se, Sp, PPV, NPV of ^{18}F-FCH PET/CT, no statistically significance was reached probably due to the limited number of analyzed glands. The Youden index was 0.92 (Table 1).

^{18}F-FCH PET/CT versus ^{99m}Tc-sestamibi scintigraphy

^{99m}Tc-sestamibi scintigraphy and ^{18}F-FCH PET/CT showed concordant results in 51/64 (80%) patients (199 glands). In a per lesion-based analysis, ^{99m}Tc-sestamibi scintigraphy and ^{18}F-FCH PET/CT were concordant positive in 51/199 glands (26%) and concordant negative in 148/199 glands (74%). The remaining 13/64 (20%) patients (49 glands) showed discordant imaging results: 7/49 glands were scinti-/PET+, and 5/49 glands were scinti+/PET- (Table 2). In patients with discordant results, median time interval between ^{99m}Tc-sestamibi scintigraphy and ^{18}F-FCH PET/CT was 161 days (IQ range 63–254). ^{99m}Tc-sestamibi scintigraphy was true-positive in 9 glands, false-positive in 8, true-negative in 21, and false-negative in 11. On the other hand, ^{18}F-FCH PET/CT was true-positive in 17 glands, false-positive in 2, true-negative in 27, and false-negative in 3. In the whole population, ^{18}F-FCH PET/CT showed a significantly higher global accuracy (98% (CI: 95–99) vs. 91% (CI: 87–94%), $p = 0.0001$) and superior Youden Index (0.79 vs. 0.92) than ^{99m}Tc-sestamibi scintigraphy.

^{18}F-FCH PET/CT identified nine pathologic parathyroids not detected by ^{99m}Tc-sestamibi scintigraphy in 8 out of 64 examined patients (12.5%) (Figure 1), allowing to detect four patients with MGD, and 1 ectopic gland. In all eight patients, parathyroid scintigraphy was performed according to the ^{99m}Tc-sestamibi/^{123}I subtraction protocol. Moreover, ^{18}F-FCH PET/CT allowed the reassessment of false-positive scintigraphic diagnosis (scinti+/PET-) for 8 parathyroids from 7/64 patients (11%). Only one hyperfunctioning gland in one patient was missed on ^{18}F-FCH PET/CT and correctly identified by ^{99m}Tc-sestamibi scintigraphy. Neither pathological features nor hormone secretion or the patient's clinical profile explained the discordant imaging results.

In two of the six patients with recurrent/persistent pHPT, ^{18}F-FCH PET/CT revealed three hyperfunctioning glands undetected by ^{99m}Tc-sestamibi scintigraphy and confirmed as glandular hyperplasia after surgical excision. One patient was MEN1. Both patients showed no biological abnormalities more than 6 months later. An additional case with recurrent pHPT showed a scinti+/PET- imaging pattern. This patient presented persistent disease after a second surgery and removal (hyperplasia) of the parathyroid indicated by scintigraphy.

Patient management

In the 13 patients with discordant imaging results, the change of patient management was discussed for each case with the clinical and surgical investigators involved in the decision-making process. Accordingly, the preoperative ^{18}F-FCH PET/CT was considered contributory to influence the surgical strategy in 7 patients (54%) (Table 2). In those cases, ^{18}F-FCH PET/CT allowed the change of the side of minimally invasive surgical approach (MIP) in 1 patient, the conversion of bilateral MIP in unilateral MIP in 2 patients (3), the conversion of unilateral MIP in bilateral MIP in 1 patient, and the conversion of MIP in cervicotomy/thoracotomy in 3 patients.

Discussion

The finding from our study confirms the diagnostic relevance of ^{18}F-FCH PET/CT in pHPT, emerging as an efficient imaging option for preoperative detection of hyperfunctioning parathyroids. If previous studies emphasized the usefulness of ^{18}F-FCH PET/CT in patients with negative or inconclusive ultrasound and/or ^{99m}Tc-sestamibi scintigraphy (9, 15–18), our results bring new and, in our opinion, important elements for discussion because they specifically concern selected patients with positive ^{99m}Tc-sestamibi scintigraphy. To our knowledge, no data are available about the potential benefit of ^{18}F-FCH PET/CT in terms of preoperative detection of additional hyperfunctioning parathyroids in this specific clinical scenario. Herein, we highlight the diagnostic and therapeutic impact of preoperative ^{18}F-FCH PET/CT allowing the identification of nine pathologic parathyroids in 12.5% of patients not previously detected by ^{99m}Tc-sestamibi scintigraphy, and confirmed after parathyroidectomy. Moreover, ^{18}F-FCH PET/CT influenced the surgical management of 7 patients, equivalent to 11% of the study population.

Surgical success requires an experienced surgeon and depends on the effective identification of the hyperfunctioning gland during the preoperative work-up (4, 5), especially in view of a conservative surgical strategy. MIP can necessitate conversion to bilateral surgery in about 20% of cases (19), mostly because of incorrect preoperative parathyroid localization and unrecognized MGD. Therefore, there is no real reason to discard the use of ^{18}F-FCH PET/CT as first-line imaging in order to reduce the need for repeat surgery, which is

TABLE 2 Characteristics and therapeutic management of 13 patients with discordant ^{99m}Tc-sestamibi scintigraphy and ^{18}F-FCH PET/CT findings.

Pt	Sex (M/F)	Age (y)	Genetic status	Cinacalcet (Y/N)	Serum PTH (ng/L)	Calcemia (mmol/L)	Parathyroid localization		Histology (from PET target)	Parathyroid		Surgical strategy before PET/CT	Surgical strategy after PET/CT	Modification of surgical strategy after PET/CT
							^{99m}Tc-sestamibi scintigraphy	^{18}F-FCH PET/CT		Height (mm)	Weight (g)			
1	F	65	/	N	232	3.4	LS, LI*	LS	Ad	20	1.0	Left MIP	Left MIP	No
2	M	63	/	Y	143	2.5	RS*	**LS**	Ad	15	na	Right MIP	Left MIP	Yes
3	F	58	/	N	148	2.5	RI	RI, **LI**	Hpl, Hpl	10, 10	1.0, 1.0	Unilateral MIP	bilateral MIP	Yes
4	F	62	/	N	243	2.9	LS	RI*, LS	Ad	10	1.0	Thyroidectomy for cancer suspicion	Thyroidectomy for cancer suspicion	No
5	M	79	/	Y	237	3.1	RI, LS*	RI	Ad	100	10.0	Thyroidectomy for goiter	Thyroidectomy for goiter	No
6	M	48	/	N	102	2.6	LS	not detected	na	na	na	Left MIP	No contributive result	No (*)
7	F	28	MEN1	N	133	2.7	LI	**LS**, **RI**, LI	Hpl, Hpl, Hpl	na	na	Left MIP	Cervicotomy	Yes
8	F	56	/	N	72	2.3	LS	LS, **ectopic (mediastinum)**	Hpl, Hpl	12, na	na, na	Left MIP	Cervico-thoracotomy	Yes
9	F	72	/	N	44	2.6	Intrathyroidal*	Intrathyroidal*, **LI**	Ad	10	0.4	Thyroidectomy for cancer suspicion	Thyroidectomy for cancer suspicion	No
10	M	68	/	N	174	2.9	RI*, LS*	**LI**	Ad	13	0.7	Bilateral MIP	Left MIP	Yes
11	F	68	/	N	199	2.6	RI, LI*	RI	Ad	10	0.1	Bilateral MIP	Right MIP	Yes
12	F	62	/	N	49	2.7	RI	RI, **LS**	Hpl, Hpl	10, 10	0.1, 0.1	Right MIP	Cervicotomy	Yes
13	F	46	/	N	70	2.6	RS*	**RI**	Ad	8	0.1	Right MIP	Right MIP	No

Pt, patient; LS, left superior; LI, left inferior; RS, right superior; RI, right inferior, *False positive results. In Bold are indicated the nine pathologic parathyroids identified by ^{18}F-FCH PET/CT and not detected by ^{99m}Tc-sestamibi scintigraphy, Ad, adenoma; Hpl, hyperplasia; MIP, mini-invasive parathyroidectomy, (*): the only case of persistent pHPT after surgery. Patients #7 and #12 are represented in Figures 1, 2.

10.3389/fmed.2023.1148287

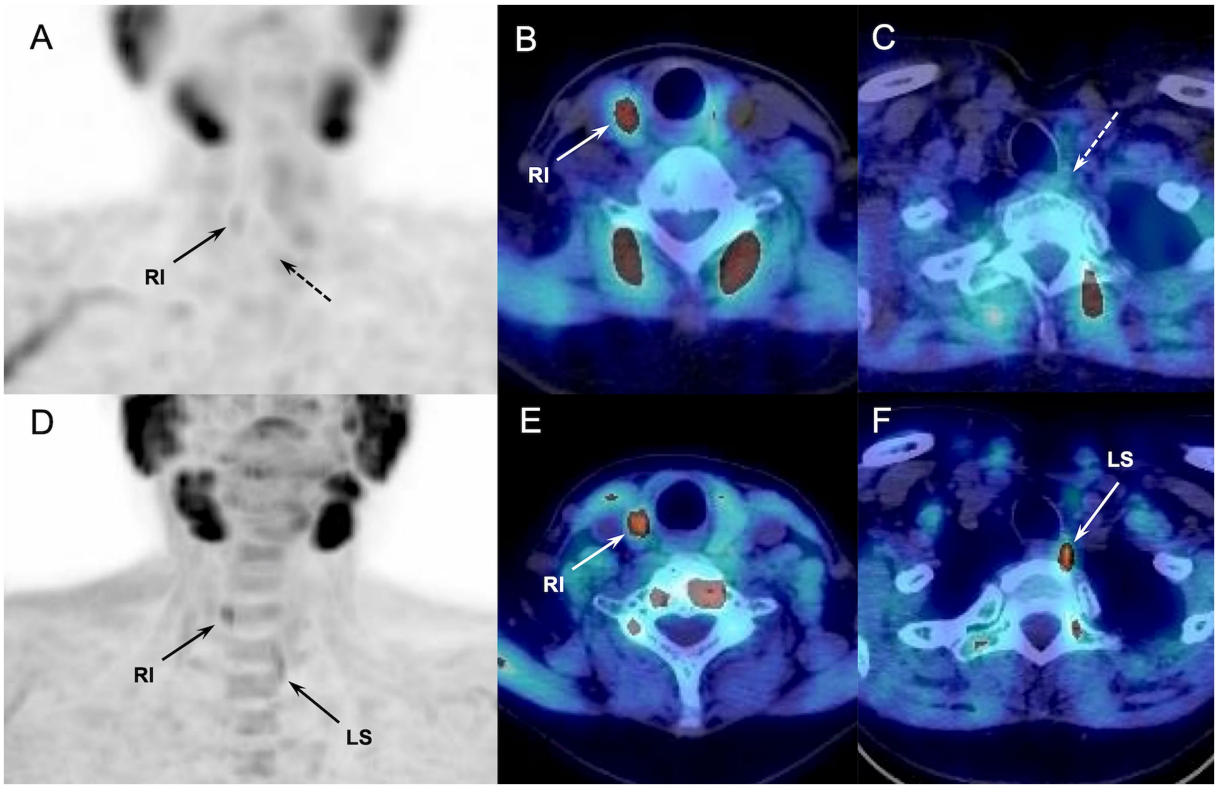

FIGURE 1
Discordant results of ^{99m}Tc-sestamibi parathyroid scintigraphy (upper panel, **A-C**) and ^{18}F-FCH PET/CT (lower panel, **D-F**) (anterior MIP, coronal and axial fusion images) performed in a 62-y-old MEN patient with sporadic pHPT at primary staging (patient#12, Table 2). ^{18}F-FCH PET/CT revealed a hyperfunctioning right inferior and left superior (in lower position) parathyroids (arrows), confirmed after surgery. ^{99m}Tc-sestamibi scintigraphy detected only the right inferior gland.

commonly expensive and with increased morbidity. After deciding to proceed with parathyroidectomy, the choice of the most appropriate diagnostic imaging modality to guide gland localization should rely on diagnostic performance. Of course, among the various techniques proposed for the detection and treatment of hyperfunctioning glands, the adopted method which must be available, safe, and inexpensive. ^{99m}Tc-sestamibi scintigraphy is the current investigation for presurgical detection of hyperfunctioning parathyroid glands in pHPT patients (20). However, its sensitivity is suboptimal and significantly lower in MGD compared with single-gland disease (21, 22). This data has some important consequences because the effectiveness of MIP relies on the success in identifying patients with MGD and ectopic glands that cannot be visualized with US. Thus, it is generally patients with hyperplasic glands, smaller and more difficult to detect, who may benefit most from the use of ^{18}F-FCH PET/CT. In this regard, pHPT patients with multiple endocrine neoplasia of type-1 (MEN1) represent critical clinical candidates for accurate parathyroid diagnostic imaging with potential therapeutic implications (Figure 2). In this setting only few data are available comparing the imaging findings of parathyroid US, ^{99m}Tc-sestamibi scintigraphy, and ^{18}F-FCH PET/CT. In a recent retrospective study including 22 MEN1 patients with pHPT, ^{18}F-FCH PET/CT provided more surgically relevant data regarding the number of pathologic parathyroid glands and their localization than ^{99m}Tc-sestamibi scintigraphy in 4/11 patients with initial surgery and in 1/4 patient who underwent second surgery (23). Additional large cohort studies are still necessary to confirm the usefulness of ^{18}F-FCH PET/CT in patients with hereditary disorders, such as MEN.

About 2–10% of pHPT patients develop persistent or recurrent disease after first surgery. In those cases, reoperation must be evaluated carefully due to a higher rate of complications than the initial surgery. Typical situations are the presence of unknown ectopic glands, unrecognized MGD, and a negative preoperative imaging workup. Hence, an upfront optimized imaging for the detection and precise localization of hyperfunctioning parathyroid glands remains crucial, as the first intervention is the best time to achieve patient cure. Despite the only limited data available regarding the role of ^{18}F-FCH PET/CT in the reoperative setting, ^{18}F-FCH PET/CT appears to be a valuable technique to accurately detect hyperfunctioning parathyroid tissue in patients with persistent/recurrent pHPT and is better than 4D-CT and ^{99m}Tc-sestamibi scintigraphy (11, 24). In our cohort, ^{18}F-FCH PET/CT revealed three hyperfunctioning parathyroid hyperplasia undetected by scintigraphy in two patients with recurrent pHPT. Both cases were cured after surgical excision of the hyperfunctioning parathyroid. Another patient with recurrent pHPT and scinti+/PET- imaging pattern showed persistent disease after the excision of a parathyroid hyperplasia.

A worldwide shortage of Molybdenum-99/Technetium-99 m has been recently experienced with major impact in clinical nuclear medicine practices, reducing the access to broadly

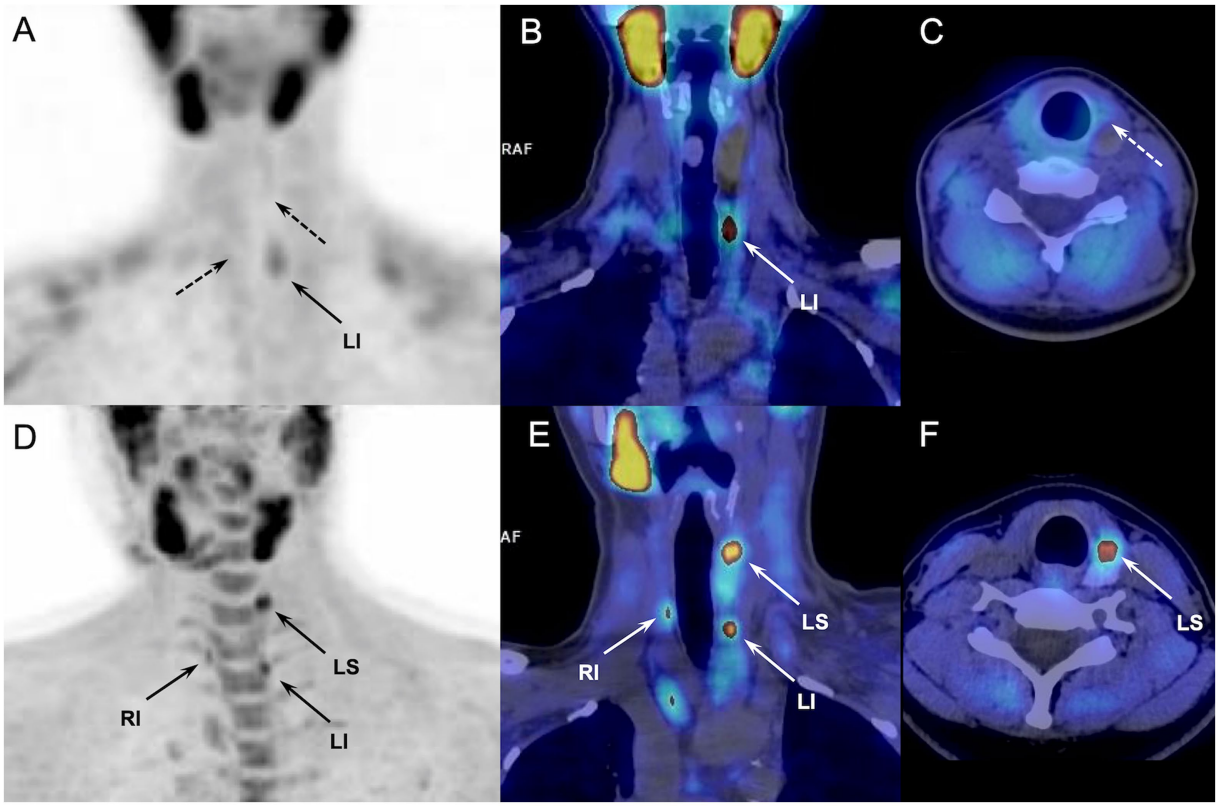

FIGURE 2
Discordant results of ^{99m}Tc-sestamibi parathyroid scintigraphy (upper panel, **A-C**) and ^{18}F-FCH PET/CT (lower panel, **D-F**) (anterior MIP, coronal and axial fusion images) performed in a 28-y-old MEN1 patient with previous history of superior right parathyroidectomy (patient#7, Table 2). ^{99m}Tc-sestamibi scan showed a pathological left inferior parathyroid (arrow). ^{18}F-FCH PET/CT confirmed scintigraphy findings and detected 2 more hyperfunctioning glands (arrows, inferior right and superior left) not revealed by scintigraphy, and afterwards confirmed by pathology after surgical excision.

performed imaging and diagnostic tests. In this context, ^{18}F-FCH PET/CT represents a viable first-line option, ensuring diagnostic and therapeutic continuity in patients with pHPT if ^{99m}Tc-sestamibi scintigraphy is not available. On the other hand, the higher costs, the reimbursement and licensing not always possible are potential drawbacks of ^{18}F-FCH PET/CT. However, there is currently a lack of data from large patient cohorts with cost-effectiveness evaluation comparing the combination of neck US and parathyroid scintigraphy with ^{18}F-FCH PET/CT as a first-line investigation, making it difficult for clinical diagnostic practices to evolve.

The risk of false positive results in patients with inflammatory lymph nodes and/or thyroid nodules is another major potential limitation of ^{18}F-FCH PET/CT. Although, its impact on sensitivity is still a matter of debate, the combined use of ^{18}F-FCH PET and 4D/CT in one stop-shop examination could potentially help in the differential diagnosis, lowering the incidence of false positive PET/CT results (25–28).

Our study suffers from several limitations that require precisions. First, the limited number of patients due to both the inclusion criteria (pre-PET positive scintigraphy) and the retrospective nature of the investigation. In addition, the long delay between a ^{99m}Tc-sestamibi-positive scintigraphy and ^{18}F-FCH PET/CT potentially could have affected the results. However, no major changes in biological parameters (PTH, calcemia) were observed during the time from scintigraphy to PET scan, reducing the potential risk of bias. Finally, 6-month follow-up was not achieved for all included patients. However, normal glands (true-negative results) were defined based on a combination of the results of surgical neck exploration, biological follow-up (PTH, serum calcium), and Miami's "$>$50% intraoperative PTH decline" criterion, which strength the analysis.

In conclusion, in a preoperative setting, ^{18}F-FCH PET/CT appears more accurate and useful than ^{99m}Tc-sestamibi scan even in patients with positive scintigraphic results, and may be preferred over ^{99m}Tc-sestamibi scan allowing the identification of patients with MGD. A positive parathyroid scintigraphy could not be adequate and sufficient before neck surgery in a not negligible percentage of patients with pHPT and related multiple hyperfunctioning parathyroids, suggesting the need to evolve the practice and define new preoperative imaging algorithms including ^{18}F-FCH PET/CT at the fore-front in pHPT patients.

Data availability statement

The original contributions presented in the study are included in the article/supplementary material, further inquiries can be directed to the corresponding author.

Ethics statement

The studies involving human participants were reviewed and approved by Ethical Committee of Strasbourg University Hospital and Faculty of Medicine (CE-2022-100). The patients/participants provided their written informed consent to participate in this study.

Author contributions

AI, JB, GT, and AP: conception or design of the work. AI, JB, GB, AL, CH, UC, MV, GT, and AP: acquisition, analysis, or interpretation of data for the work and drafting the work or revising it critically for important intellectual content. All authors have read and agreed to the submitted version of the manuscript.

Conflict of interest

The authors declare that the research was conducted in the absence of any commercial or financial relationships that could be construed as a potential conflict of interest.

Publisher's note

All claims expressed in this article are solely those of the authors and do not necessarily represent those of their affiliated organizations, or those of the publisher, the editors and the reviewers. Any product that may be evaluated in this article, or claim that may be made by its manufacturer, is not guaranteed or endorsed by the publisher.

References

1. Walker MD, Silverberg SJ. Primary hyperparathyroidism. *Nat Rev Endocrinol*. (2018) 14:115–25. doi: 10.1038/nrendo.2017.104

2. Roy M, Mazeh H, Chen H, Sippel RS. Incidence and localization of ectopic parathyroid adenomas in previously unexplored patients. *World J Surg*. (2013) 37:102–6. doi: 10.1007/s00268-012-1773-z

3. Bilezikian JP, Khan AA, Silverberg SJ, Fuleihan GE-H, Marcocci C, Minisola S, et al. Evaluation and Management of Primary Hyperparathyroidism: summary statement and guidelines from the fifth international workshop. International workshop on primary hyperparathyroidism. *J Bone Miner Res*. (2022) 19:2293:2314. doi: 10.1002/jbmr.4677

4. Zafereo M, Yu J, Angelos P, Brumund K, Chuang HH, Goldenberg D, et al. American head and neck society endocrine surgery section update on parathyroid imaging for surgical candidates with primary hyperparathyroidism. *Head Neck*. (2019) 41:2398–409. doi: 10.1002/hed.25781

5. Hindié E, Schwartz P, Avram AM, Imperiale A, Sebag F, Taïeb D. Primary hyperparathyroidism: defining the appropriate preoperative imaging algorithm. *J Nucl Med*. (2021) 62:3S–12S. doi: 10.2967/jnumed.120.245993

6. Schalin-Jäntti C, Ryhänen E, Heiskanen I, Seppänen M, Arola J, Schildt J, et al. Planar scintigraphy with 123 I/ 99m Tc-Sestamibi, 99m Tc-Sestamibi SPECT/CT, 11 C-methionine PET/CT, or selective venous sampling before reoperation of primary hyperparathyroidism? *J Nucl Med*. (2013) 54:739–47. doi: 10.2967/jnumed.112.109561

7. Treglia G, TrimboI P, Huellner M, Giovanella L. Imaging in primary hyperparathyroidism: focus on the evidence-based diagnostic performance of different methods. *Minerva Endocrinol*. (2018) 43:133–43. doi: 10.23736/S0391-1977.17.02685-2

8. Ruda JM, Hollenbeak CS, Stack BC Jr. A systematic review of the diagnosis and treatment of primary hyperparathyroidism from 1995 to 2003. *Otolaryngol Head Neck Surg*. (2005) 132:359–72. doi: 10.1016/j.otohns.2004.10.005

9. Quak E, Blanchard D, Houdu B, le Roux Y, Ciappuccini R, Lireux B, et al. F18-choline PET/CT guided surgery in primary hyperparathyroidism when ultrasound and MIBI SPECT/CT are negative or inconclusive: the APACH1 study. *Eur J Nucl Med Mol Imaging*. (2018) 45:658–66. doi: 10.1007/s00259-017-3911-1

10. Treglia G, Piccardo A, Imperiale A, Strobel K, Kaufmann PA, Prior JO, et al. Diagnostic performance of choline PET for detection of hyperfunctioning parathyroid glands in hyperparathyroidism: a systematic review and meta-analysis. *Eur J Nucl Med Mol Imaging*. (2019) 46:751–65. doi: 10.1007/s00259-018-4123-z

11. Latge A, Riehm S, Vix M, Bani J, Ignat M, Pretet V, et al. 18F-Fluorocholine PET and 4D-CT in patients with persistent and recurrent primary hyperparathyroidism. *Diagnostics*. (2021) 11:2384. doi: 10.3390/diagnostics11122384

12. Petranovic Ovčariček P, Giovanella L, Carrió I, Huellner MW, Luster M, Hindié E, et al. The EANM practice guidelines for parathyroid imaging. *Eur J Nucl Med Mol Imag*. (2021) 48:2801–22. doi: 10.1007/s00259-021-05334-y

13. Giovanella L, Bacigalupo L, Treglia G, Piccardo A. Will ^{18}F-fluorocholine PET/CT replace other methods of preoperative parathyroid imaging? *Endocrine*. (2021) 71:285–97. doi: 10.1007/s12020-020-02487-y

14. Khan ZF, Lew JI. Intraoperative parathyroid hormone monitoring in the surgical Management of Sporadic Primary Hyperparathyroidism. *Endocrinol Metab*. (2019) 34:327–39. doi: 10.3803/EnM.2019.34.4.327

15. Quak E, Lasne Cardon A, Ciappuccini R, Lasnon C, Bastit V, le Henaff V, et al. Upfront F18-choline PET/CT versus Tc99m-sestaMIBI SPECT/CT guided surgery in primary hyperparathyroidism: the randomized phase III diagnostic trial APACH2. *BMC Endocr Disord*. (2021) 21:3. doi: 10.1186/s12902-020-00667-5

16. Boudousq V, Guignard N, Gilly O, Chambert B, Mamou A, Moranne O, et al. Diagnostic performance of cervical ultrasound, 99mTc-Sestamibi scintigraphy, and contrast-enhanced 18F-Fluorocholine PET in primary hyperparathyroidism. *J Nucl Med*. (2022) 63:1081–6. doi: 10.2967/jnumed.121.261900

17. Graves CE, Hope TA, Kim J, Pampaloni MH, Kluijfhout W, Seib CD, et al. Superior sensitivity of 18F-fluorocholine: PET localization in primary hyperparathyroidism. *Surgery*. (2022) 171:47–54. doi: 10.1016/j.surg.2021.05.056

18. Hope TA, Graves CE, Calais J, Ehman EC, Johnson GB, Thompson D, et al. Accuracy of 18F-Fluorocholine PET for the detection of parathyroid adenomas: prospective single-center study. *J Nucl Med*. (2021) 62:1511–6. doi: 10.2967/jnumed.120.256735

19. Hughes DT, Miller BS, Park PB, Cohen MS, Doherty GM, Gauger PG. Factors in conversion from minimally invasive parathyroidectomy to bilateral parathyroid exploration for primary hyperparathyroidism. *Surgery*. (2013) 154:1428–35. doi: 10.1016/j.surg.2013.04.020

20. Treglia G, Sadeghi R, Schalin-Jäntti C, Caldarella C, Ceriani L, Giovanella L, et al. Detection rate of 99m Tc-MIBI single photon emission computed tomography (SPECT)/CT in preoperative planning for patients with primary hyperparathyroidism: a meta analysis. *Head Neck*. (2016) 38:E2159–72. doi: 10.1002/hed.24027

21. Medas F, Erdas E, Longheu A, Gordini L, Pisano G, Nicolosi A, et al. Retrospective evaluation of the pre- and postoperative factors influencing the sensitivity of localization studies in primary hyperparathyroidism. *Int J Surg*. (2016) 25:82–7. doi: 10.1016/j.ijsu.2015.11.045

22. Nichols KJ, Tomas MB, Tronco GG, Palestro CJ. Sestamibi parathyroid scintigraphy in multigland disease. *Nucl Med Commun*. (2012) 33:43–50. doi: 10.1097/MNM.0b013e32834bfeb1

23. Gauthé M, Dierick-Gallet A, Delbot T, Bricaire L, Bertherat J, North MO, et al. 18F-fluorocholine PET/CT in MEN1 patients with primary hyperparathyroidism. *World J Surg*. (2020) 44:3761–9. doi: 10.1007/s00268-020-05695-9

24. Amadou C, Bera G, Ezziane M, Chami L, Delbot T, Rouxel A, et al. 18F-Fluorocholine PET/CT and parathyroid 4D computed tomography for primary hyperparathyroidism: the challenge of Reoperative patients. *World J Surg*. (2019) 43:1232–42. doi: 10.1007/s00268-019-04910-6

25. Pretet V, Rotania M, Helali M, Ignat M, Vix M, Imperiale A. 18F-Fluorocholine PET and multiphase CT integrated in dual modality PET/4D-CT for preoperative evaluation of primary hyperparathyroidism. *J Clin Med*. (2020) 26:2005. doi: 10.3390/jcm9062005

26. Piccardo A, Bottoni G, Boccalatte LA, Camponovo C, Musumeci M, Bacigalupo L, et al. Head-to-head comparison among 18F-choline PET/CT, 4D contrast-enhanced CT, and 18F-choline PET/4D contrast-enhanced CT in the detection of hyperfunctioning parathyroid glands: a systematic review and meta-analysis. *Endocrine*. (2021) 74:404–12. doi: 10.1007/s12020-021-02798-8

27. Piccardo A, Trimboli P, Rutigliani M, Puntoni M, Foppiani L, Bacigalupo L, et al. Additional value of integrated ^{18}F-choline PET/4D contrast-enhanced CT in the localization of hyperfunctioning parathyroid glands and correlation with molecular profile. *Eur J Nucl Med Mol Imaging*. (2019) 46:766–75. doi: 10.1007/s00259-018-4147-4

28. Fiz F, Bottoni G, Massollo M, Trimboli P, Catrambone U, Bacigalupo L, et al. [18F] F-choline PET/CT and 4D-CT in the evaluation of primary hyperparathyroidism: rivals or allies? *Q J Nucl Med Mol Imaging*. (2023) In press.

frontiers | Frontiers in Medicine

TYPE Original Research
PUBLISHED 09 June 2023
DOI 10.3389/fmed.2023.1169970

OPEN ACCESS

EDITED BY
Giorgio Treglia,
Ente Ospedaliero Cantonale (EOC), Switzerland

REVIEWED BY
Joachim Nilsson,
Karolinska Institutet (KI), Sweden
Alessio Rizzo,
IRCCS Candiolo Cancer Institute, Italy
Majid Assadi,
Bushehr University of Medical Sciences, Iran

*CORRESPONDENCE
Martina Hinterleitner
martina.hinterleitner@med.uni-tuebingen.de

RECEIVED 20 February 2023
ACCEPTED 17 May 2023
PUBLISHED 09 June 2023

CITATION
Trautwein NF, Schwenck J, Jacoby J, Reischl G, Fiz F, Zender L, Dittmann H, Hinterleitner M and la Fougère C (2023) Long-term prognostic factors for PRRT in neuroendocrine tumors. *Front. Med.* 10:1169970. doi: 10.3389/fmed.2023.1169970

Long-term prognostic factors for PRRT in neuroendocrine tumors

Nils Florian Trautwein[1,2,3], Johannes Schwenck[1,2,4], Johann Jacoby[5], Gerald Reischl[2,4], Francesco Fiz[1,6], Lars Zender[3,4,7,8], Helmut Dittmann[1,3], Martina Hinterleitner[3,4,6]* and Christian la Fougère[1,3,4,8]

[1]Department of Nuclear Medicine and Clinical Molecular Imaging, University Hospital of Tübingen, Tübingen, Germany, [2]Werner Siemens Imaging Center, Department of Preclinical Imaging and Radiopharmacy, Eberhard Karls University, Tübingen, Germany, [3]ENETS Center of Excellence, University Hospital of Tübingen, Tübingen, Germany, [4]Cluster of Excellence iFIT (EXC 2180) "Image-Guided and Functionally Instructed Tumor Therapies", Eberhard Karls University, Tübingen, Germany, [5]Institute for Clinical Epidemiology and Applied Biometry, University Hospital of Tübingen, Tübingen, Germany, [6]Department of Nuclear Medicine, E.O. Ospedali Galliera, Genoa, Italy, [7]Department of Internal Medicine VIII, University Hospital of Tübingen, Tübingen, Germany, [8]German Cancer Consortium (DKTK), German Cancer Research Center (DKFZ) Partner Site Tübingen, Tübingen, Germany

Aim/introduction: Peptide receptor radionuclide therapy (PRRT) is an effective and well-tolerated treatment option for patients with neuroendocrine tumors (NETs) that prolongs progression-free survival (PFS). However, the limited overall survival (OS) rates in the prospective phase III study (NETTER1) highlighted the need to identify patient-specific long-term prognostic markers to avoid unnecessary side effects and enable better treatment stratification. Therefore, we retrospectively analyzed prognostic risk factors in NET patients treated with PRRT.

Methods: A total of 62 NET patients (G1: 33.9%, G2 62.9%, and G3 3.2%) with at least 2 cycles of PRRT with [^{177}Lu]Lu-HA-DOTATATE (mean 4 cycles) were analyzed. Of which, 53 patients had primary tumors in the gastroenteropancreatic (GEP) system, 6 had bronchopulmonary NET, and 3 had NET of unknown origin. [^{68}Ga]Ga-HA-DOTATATE PET/CT scans were performed before PRRT start and after the second treatment cycle. Different clinical laboratory parameters, as well as PET parameters, such as SUVmean, SUVmax, and PET-based molecular tumor volume (MTV), were collected, and their impact on the OS was investigated. Patient data with a mean follow-up of 62 months (range 20–105) were analyzed.

Results: According to interim PET/CT, 16 patients (25.8%) presented with partial response (PR), 38 (61.2%) with stable disease (SD), and 7 (11.3%) with progressive disease (PD). The 5-year OS was 61.8% for all patients, while bronchopulmonary NETs showed poorer OS than GEP-NETs. Multivariable Cox regression analysis showed that chromogranin A level and MTV together were highly significant predictors of therapeutic outcome (HR 2.67; 95% CI 1.41–4.91; $p = 0.002$). Treatment response was also influenced by the LDH level (HR 0.98; 95% CI 0.9–1.0; $p = 0.007$) and patient age (HR 1.15; 95% CI 1.08–1.23; $p < 0.001$). ROC analysis revealed baseline MTV > 112.5 ml [Sens. 91%; Spec. 50%; AUC 0.67 (95% CI 0.51–0.84, $p = 0.043$)] and chromogranin A >1,250.75 μg/l [Sens. 87%; Spec. 56%; AUC 0.73 (95% CI 0.57–0.88, $p = 0.009$)] as the best cutoff values for identifying patients with worse 5-year survival.

Conclusion: Our retrospective analysis defined MTV and chromogranin A in combination as significant prognostic factors for long-term OS. Furthermore, an interim PET/CT after two cycles has the potential in identifying non-responders who may benefit from a change in therapy at an early stage.

KEYWORDS

neuroendocrine tumor (NET), ^{177}Lu, DOTA-TATE, peptide receptor radionuclide therapy (PRRT), Ga-HA-DOTATATE, molecular tumor volume

Introduction

Neuroendocrine tumors (NETs) originate from the neuroendocrine system and can synthesize and secrete different neuro amines and peptides (1). Although still a fairly rare subtype of cancer, NETs have become more common over the past few decades (2, 3). Most NETs remain asymptomatic until they have spread. Therefore, more than 40% of NET patients have metastatic disease at the time of first diagnosis (4). For this reason, curative surgery is often no longer possible, and alternative treatments must be considered.

Somatostatin receptors (SSTR) are overexpressed by most well and moderately differentiated gastroenteropancreatic neuroendocrine tumors (GEP-NETs) by 80–100% (5) and are currently the most important target for treatment stratification. The interaction between the SSTR and somatostatin can lead to a profound treatment response, including the suppression of cell secretion and cell proliferation (6), and thus, the number of SSTR-targeting therapies for NETs has grown since the early 2000s. For GEP-NET G1 and G2, the prospective studies CLARINET and PROMID showed that antiproliferative somatostatin analog (SSA) therapies prolonged patients' progression-free survival compared to placebo (7, 8). Since the early 1990s, the combination of SSA coupled with a radioactive beta emitter (peptide receptor radionuclide therapy; PRRT) has been used as a treatment strategy for SSTR-positive NET (9), showing promising results, especially in patients suffering from GEP-NET (10). Moreover, the first multicenter prospective phase III clinical trial (NETTER1) revealed that patients treated with PRRT had a longer progression-free survival (PFS) when compared to high-dose SSA monotherapy. After 20 months of randomization, the rate of PFS was significantly higher in the PRRT group (65.2%) than in the control group (10.8%) (11). Recently, the long-term follow-up data were published, showing a difference of 11.7 months in median overall survival between the PRRT group (48 months) and controls (36.3 months), which did not achieve statistical significance (12). The current European Neuroendocrine Tumor Society (ENETS) guidelines recommend the use of PRRT as a second- to third-line therapy after progression under SSA in metastasized intestinal (midgut) NETs and as a third-line therapy in pancreatic NET with advanced locoregional disease (13). Data for PRRT in bronchopulmonary carcinoma are still rare. The comparatively low number of bronchopulmonary NETs that express enough somatostatin receptors to qualify as therapy candidates is an important issue (14). However, in a large retrospective study with over 100 patients and several smaller cohorts, PRRT was shown to be a well-tolerated treatment option for bronchopulmonary carcinoma (15, 16). These studies showed a PFS of 19–59 months; therefore, PRRT was included as a treatment option for bronchopulmonary carcinoma in the ESMO guidelines (17, 18).

Measuring sufficient SSTR expression by pre therapeutic PET or SPECT imaging is an important prerequisite for selecting patients for PRRT. Although adequate SSTR expression has been measured, insufficient response to PRRT can, however, occur at a rate that has been estimated between 15 and 30%; moreover, there are no established biomarkers for the prediction of long-term response and survival (19, 20).

Therefore, this retrospective analysis aimed to explore the prognostic value of different clinical parameters as biomarkers for long-term response to PRRT.

Materials and methods

Patients and PRRT

We screened our database for patients who received PRRT between February 2013 and February 2019 at the University Hospital of Tübingen. Only patients with tumor SSTR expression higher than the liver in a pre-therapeutic [^{68}Ga]Ga-HA-DOTATATE-PET/CT scan were treated (21). PRRT was performed according to the practical guidelines of the Joint International Atomic Energy Agency (IAEA), the European Association of Nuclear Medicine (EANM), and the Society of Nuclear Medicine and Molecular Imaging (SNMMI), in accordance with the Rotterdam Protocol (22).

Patients were treated for a median of four cycles, each including an intravenous administration of 7,180 ± 650 MBq [^{177}Lu]Lu-HA-DOTATATE per cycle which was accompanied by an amino acid solution for renal protection (23). Patients were treated with at least two and a maximum of nine cycles (Table 1). The median time between the two cycles was 14 weeks (range: 8–24 weeks). The goal was to administer four cycles of PRRT; in some patients, the number of cycles was not achieved due to individual circumstances. In the case of more than four cycles per patient, retreatments were performed. In 18 patients, salvage PRRT was carried out during the follow-up period. In five patients, the administered activity was reduced because of impaired renal function or other relevant secondary diseases. SSA therapy was maintained during PRRT; however, a time interval of at least 4 weeks between the last SSA administration and PRRT was ensured. No other oncological treatments were performed in addition to SSA therapy, but supportive therapies, such as antidiarrheal medications or antibiotics, were administered to patients according to their individual needs.

[^{177}Lu]Lu-HA-DOTATATE was prepared according to good manufacturing practice and the German Medicinal Products Act (AMG § 13 2b). Interim [^{68}Ga]Ga-HA-DOTATATE-PET/CT scans were performed after two cycles of PRRT. Blood counts and creatinine were monitored on the day of [^{177}Lu]Lu-HA-DOTATATE therapy injection. Side effects were monitored according to the Common Terminology Criteria for Adverse Events (CTCAE v5.0) (24).

PET/CT image acquisition

A baseline [^{68}Ga]Ga-HA-DOTATATE-PET/CT scan was performed, on average, a median of 7 (range: 0–17) weeks before PRRT. A median of 11 (range: 6–32) weeks after the second cycle, but before the administration of the third cycle, a PET scan was conducted for imaging. All scans were conducted on a state-of-the-art PET/CT scanner (Biograph mCT, Siemens Healthineers) 45 min p.i. after i.v. injection of 2 MBq kg/BW [^{68}Ga]Ga-HA-DOTATATE (25). Additionally, a diagnostic CT scan including

10.3389/fmed.2023.1169970

TABLE 1 Patients' characteristics.

Number of patients	62
Age, median (range) in years	64 (27–80)
Gender, *n* (%)	
Male	36 (58%)
Female	26 (42%)
Prior therapies, *n* (%)	
Surgery	49 (79%)
Somatostatin analog	44 (71%)
Systemic therapies	6 (10%)
PRRT	9 (15%)
Local therapies (SIRT, RFA, and TACE)	4 (6%)
Primary tumor site, *n* (%) and grading, *n* (%)	
Gastroenteropancreatic	53 (85%)
G1	20 (38%)
G2	31 (58%)
G3	2 (4%)
Bronchopulmonary	6 (10%)
G1	0 (0%)
G2	6 (100%)
G3	0 (0%)
Cancer of unknown primary	3 (5%)
G1	1 (33%)
G2	2 (67%)
G3	0 (0%)
Cycles of PRRT, *n* (%)	
2	7 (11%)
3	10 (16%)
4	31 (50%)
>4	14 (22%)

SIRT, selective internal radiation therapy; RFA, radiofrequency ablation; TACE, trans-arterial chemoembolization; G, grading.

contrast enhancement in arterial and portal venous phase (120 ml of Ultravist 370b®, Bayer Healthcare Pharmaceuticals; flow rate 2.5 ml/s) was performed. In patients with contraindications to contrast agents, a diagnostic CT scan without a contrast medium was performed. Data were corrected for attenuation as well as scattered and reconstructed with OSEM3D including time of flight and point spread functions (2 iterations, 21 subsets, and Gaussian filter 2 mm).

PET/CT image interpretation

The [^{68}Ga]Ga-HA-DOTATATE PET-based assessment of the SSTR molecular tumor volume (MTV) was performed by semi-automatic volumetric segmentation of non-physiologic tracer uptake using the software tool Affinity Hybrid Viewer (Hermes Medical Solution, Sweden).

Pathologic SSTR expression was defined as standardized uptake values (SUV), which were higher than the 1.5-fold mean SUV of the liver plus two times the standard deviation (SD).

$$MTV = SUV_{tumor} > 1.5 \times SUVmean_{liver} + 2 \times SD_{liver} \quad (1)$$

SUVmean, SUVmax, and SD of the liver were determined by a 5 ml spherical volume of interest (VOI) in the left liver lobe. A 3 ml spherical VOI in the fifth lumbar vertebrae was used to assess the SUV parameters of the bones, whereas a 5 ml spherical VOI was used to measure the SUV characteristics of the spleen. First, the "single click segmentation" tool was used to mark all regions with an SUV value higher than the reference SUV. Furthermore, several volumes of interest (VOIs) were formed. Then, the semi-automatically segmented areas were selected and reviewed by a trained physician, who excluded physiological SSTR-expressing areas (e.g., the kidney and pituitary gland) and non-disease-related lesions (Supplementary Figure 1).

SUVmax and MTV-based SUVmean of the largest metastatic tumor lesion were evaluated. The SUV was calculated based on body weight.

Early therapy response was estimated by the relative change in MTV after the first two PRRT cycles. As described by Ohlendorf et al., partial response (PR) was defined as a reduction in MTV of more than 73% and progressive disease (PD) as an increase in MTV of more than 63%, whereas stable disease (SD) was defined between the two upper values (26). PR and SD were considered as responders, a non-responder was defined by PD. For one patient, a PET/CT after the second PRRT cycle was not available. Furthermore, response to treatment after two cycles of PRRT was assessed using CT or MR images according to RECIST 1.1 (27).

Statistical analysis

For the whole statistical analysis, patient data with a follow-up for a maximum of 8 years were analyzed. The SUV parameters of responders and non-responders were not normally distributed and were therefore compared with Mann–Whitney *U*-test. With the use of univariable and multivariable Cox regression, the prognostic value of different variables was assessed. Due to the skewed distribution of the γ-GT, the MTV, and the chromogranin A in our cohort, the values were log-transformed. The MTV is an image morphological biomarker, and chromogranin A is a blood-based biomarker for the tumor burden of the patients. For the predictors, MTV and chromogranin A alone, the assumption of proportional hazards is not plausible. To solve this problem and due to the strong correlation between MTV and chromogranin A, these two factors were combined. For this purpose, the values were first z-standardized and then averaged. The assumption of constant hazards ratio (HR) was examined using the derived Schoenfeld residuals.

To identify optimal cutoff values for 5 years OS, a receiver operating characteristic (ROC) analysis was performed. The OS was determined as time in months from the baseline PET/CT to death from any cause. The OS was evaluated using the Kaplan–Meier

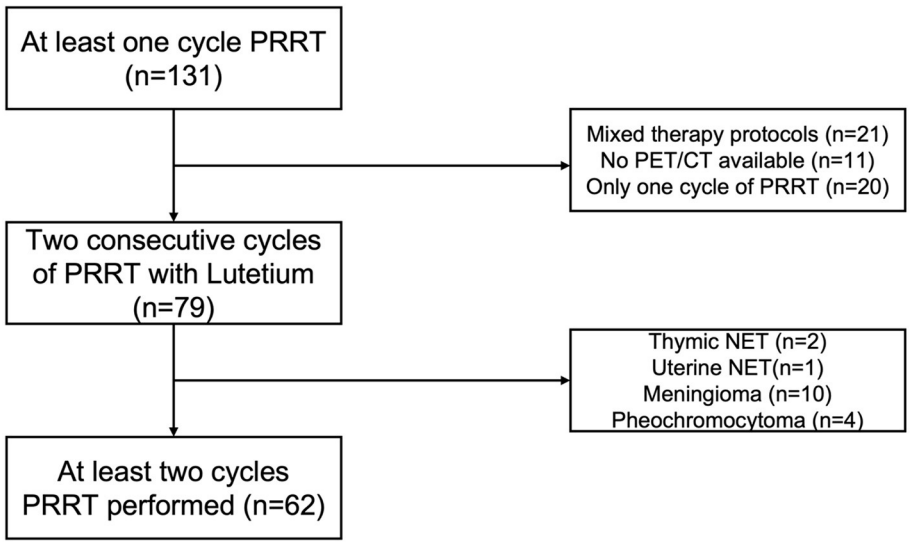

FIGURE 1
Patient selection algorithm.

technique. Two distinct groups were compared using a log-rank test. The statistical analysis was performed using GraphPad Prism 9.4 and R version 4.1.1.

The institutional ethics committee of our institution approved this retrospective analysis (Decision 530/220BO). Due to the retrospective nature of this study, the requirement to obtain informed consent was waived.

Results

Patients

Between February 2013 and February 2019, 131 patients were treated with PRRT in our department. First, we excluded all patients with only one cycle of PRRT ($n = 20$), mixed protocols including [^{90}Y] Yttrium ($n = 21$), or no available baseline PET/CT ($n = 11$). Then, patients were selected according to their histological classifications, excluding meningiomas ($n = 10$), pheochromocytomas ($n = 4$), thymic ($n = 1$), or uterine ($n = 1$) NETs (Figure 1). The remaining 62 patients had a histologically confirmed gastroenteropancreatic, bronchopulmonary, or CUP-NET and were treated with a median of four cycles (range 2–9), but at least with two consecutive cycles of [^{177}Lu]Lu-HA-DOTATATE. The mean of the administered cumulative activity of all cycles per patient was 29,665 MBq (range: 11,503–59,446 MBq). The median time between the two cycles was 14 weeks (range: 8–24 weeks). The median follow-up time was 62 months (range 33–104 months). To assess whether the longer treatment interval might have an impact on our data, an additional analysis was performed in which patients with a longer interval than the mean and two standard deviations between two treatment cycles were excluded (Supplementary Figure 1).

Patients' characteristics are summarized in Table 1. In total, 21 patients (33.9%) suffered from WHO grade 1 (G1) NET, 39 from grade 2 (G2) NET (62.9%), and 2 (3.2%) from grade 3 (G3) NET. The majority of the patients ($n = 53$) were diagnosed with gastroenteropancreatic (GEP)-NET (85.4%), six had bronchopulmonary NET (9.7%), and three had CUP-NET (4.8%). One CUP-NET patient probably had a GEP-NET histologically. For the others, no inference of the primary region could be obtained by histology. Baseline and interim PET parameters are presented in Tables 2, 3. Treatment-related adverse events according to CTCAE v5.0 are displayed in Table 4. One patient developed a myelodysplastic syndrome (MDS) during the follow-up period.

Clinical imaging and response assessment

According to the clinical follow-up PET/CT scan after the second PRRT cycle, 16 out of 62 patients (25.8%) presented with a PR, while an SD was observed in 38 patients (61.2%). Seven patients (11.3%) suffered from PD and were defined as non-responders. Non-responders displayed a significantly worse OS than responders (Figure 2). Baseline SUV values from responders and non-responders did not differ significantly ($p > 0.05$). Furthermore, the response to PRRT after two cycles were assessed according to RECIST 1.1. In total, 44 patients showed an SD, 11 patients showed a PR, and 6 patients suffered from a PD (Table 5). No CR was achieved in any patient. For one patient, a PET/CT after the second PRRT cycle was not available.

Prognostic factors for overall survival

The 5-year OS was 61.8% for all patients, while bronchopulmonary NETs (5-year OS 50%) showed a poorer OS than GEP-NETs (5-year OS 69.5%) (Figure 3). In the univariable Cox regression, a combination of MTV, derived from

10.3389/fmed.2023.1169970

TABLE 2 PET parameters of the baseline PET scan.

PET parameters	All ($n = 62$) Mean (SD)	PR ($n = 16$) Mean (SD)	SD ($n = 38$) Mean (SD)	PD ($n = 7$) Mean (SD)
SUV_{mean} liver	4.41 (1.14)	4.30 (1.23)	4.58 (1.18)	4.10 (0.53)
SUV_{max} liver	6.28 (1.53)	6.03 (1.61)	6.62 (1.60)	5.81 (0.62)
SUV_{mean} spleen	14.57 (5.13)	14.21 (4.15)	14.92 (5.64)	14.22 (5.72)
SUV_{max} spleen	17.86 (6.22)	17.20 (4.90)	18.25 (6.91)	17.91 (6.88)
SUV_{mean} bone	0.97 (0.39)	1.01 (0.40)	0.94 (0.41)	0.93 (0.36)
SUV_{max} bone	1.82 (1.12)	2.00 (1.56)	1.69 (0.68)	1.74 (0.69)
SUV_{mean} tumor	12.21 (3.97)	12.52 (4.99)	12.51 (3.26)	10.21 (1.92)
SUV_{max} tumor	25.87 (14.14)	28.61 (18.06)	25.67 (10.71)	17.98 (7.38)
MTV in ml	121.5 (238.1)	69.54 (35.26)	168.1 (125.7)	114.6 (182.9)

SUV values did not differ significantly ($p > 0.05$).

TABLE 3 PET parameters of the interim PET scan after two cycles of PRRT.

PET parameters	All ($n = 62$) Mean (SD)	PR ($n = 16$) Mean (SD)	SD ($n = 38$) Mean (SD)	PD ($n = 7$) Mean (SD)
SUV_{mean} liver	4.92 (1.30)	4.92 (1.16)	5.06 (1.41)	4.31 (1.28)
SUV_{max} liver	6.94 (1.89)	6.64 (1.41)	7.37 (2.19)	6.23 (1.92)
SUV_{mean} spleen	15.87 (5.46)	15.21 (4.37)	17.09 (6.19)	13.90 (5.19)
SUV_{max} spleen	19.59 (6.53)	18.42 (4.95)	21.07 (7.46)	17.95 (6.61)
SUV_{mean} bone	0.93 (0.27)	0.88 (0.22)	0.99 (0.31)	0.84 (0.23)
SUV_{max} bone	1.72 (0.55)	1.66 (0.60)	1.77 (0.52)	1.71 (0.54)
SUV_{mean} tumor	13.10 (4.18)	12.83 (4.18)	13.93 (4.29)	10.53 (2.86)
SUV_{max} tumor	26.48 (13.22)	24.49 (14.70)	30.25 (12.44)	17.12 (3.28)
MTV in ml	112.3 (250.1)	23.36 (33.95)	157.1 (306.9)	227.9 (335.3)

SUV values did not differ significantly ($p > 0.05$).

TABLE 4 Adverse Events according to CTCAE v5.0.

Events	Grade 1	Grade 2	Grade 3	Grade 4
Anemia	7	0	0	0
Platelets	17	1	1	0
White blood cells	6	1	1	0

CTCAE, Common terminology criteria for adverse events.

the baseline [^{68}Ga]Ga-HA-DOTATATE PET, and chromogranin A ($p < 0.001$) were risk factors and correlated with a significantly lower probability of survival. The γ-GT parameter alone was indicative of a lower overall survival ($p = 0.038$). In addition, the age ($p < 0.001$) was highly relevant to OS. In contrast, grading was not significantly relevant to OS ($p = 0.412$) in the univariable Cox regression (Table 6).

In the multivariable Cox regression analysis, the combination of MTV and chromogranin A (HR 2.67; 95% CI 1.41–4.91; $p = 0.002$) was confirmed as a highly significant independent prognostic factor. In addition, LDH (HR 0.98; 95% CI 0.98–1.0; $p = 0.007$) and age (HR 1.15; 95% CI 1.08–1.23; $p < 0.001$) showed a significant impact on OS (Table 7). However, the re-analysis had only a minor effect on our result, so the changes were minimal (Supplementary Tables 1, 2). The highest impact was found in the covariate MTV/chromogranin A in our multivariable Cox regression for OS, which tended to be more significant after the exclusion of the four outliers.

A ROC analysis was performed to analyze the 5-year survival rates and revealed the best cutoff value for the baseline MTV of >112.5 ml [sensitivity 91%; specificity 50%; AUC; 0.67 (95% CI 0.51–0.84, $p = 0.043$)] to identify patients with a worse 5-year survival rate. The best cutoff value for the baseline chromogranin A level was 1,250.75 µg/l [sensitivity 87%; specificity 56%; AUC 0.73 (95% CI 0.57–0.88, $p = 0.0092$)] to identify patients with a worse 5-year survival rate (Figure 4).

Discussion

Following EMA approval in 2017, PRRT has emerged as a frequently used therapy for GEP-NETs G1 and G2.

NETTER1 was the first prospective phase 3 trial to demonstrate the benefit of PRRT. However, the authors of NETTER1 did not provide any information on prognostic factors. As stratification of treatment is of utmost interest, especially when very expensive therapies are used, we attempted to identify further prognostic markers.

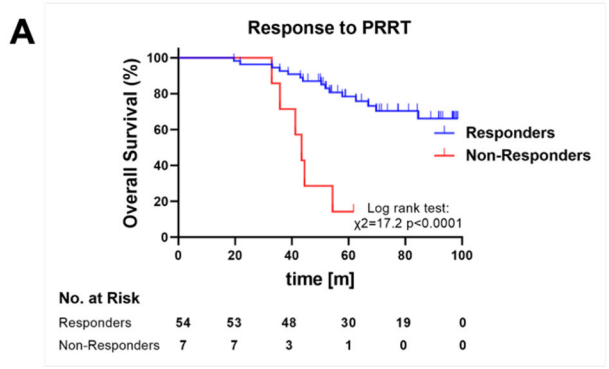

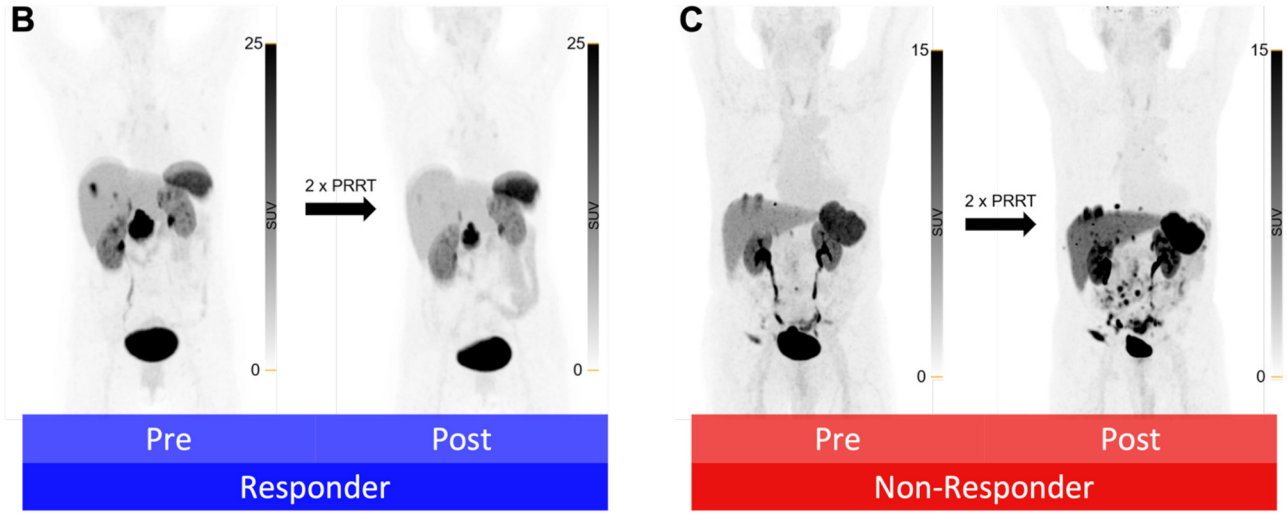

FIGURE 2
(A) Kaplan–Meier curves for overall survival separated by responders (blue) to PRRT after two cycles and non-responders (red) after two cycles. m, months. Exemplary the maximum intensity projection (MIP) of a PET from a responder **(B)** and a non-responder **(C)** pre and post two cycles of PRRT.

TABLE 5 Treatment response to two cycles of PRRT, according to RECIST 1.1 and MTV-based.

RECIST 1.1	CR	PR	SD	PD
Patients *n*, (%)	0 (0)	11 (18)	44 (72)	6 (10)
MTV-based				
Patients *n*, (%)		16 (26)	38 (62)	7 (12)

In our study, we retrospectively evaluated prognostic factors prior to PRRT for the long-term outcome; the combination of MTV and chromogranin A was identified as a crucial surrogate marker for OS. In fact, MTV and chromogranin A represent the imaging-based and laboratory estimates of tumor burden, respectively. LDH was used since this marker is known to be a prognostic factor for different tumors (28). As 75% of NET patients are affected by liver metastases, γ-GT is a good biomarker for the effects of liver damage, and we selected and were able to confirm γ-GT as an additional indicator of treatment outcome in univariable Cox regression. In addition, our findings demonstrated that age plays a crucial role in terms of overall survival. Since the OS in NET was shown to be approximately 9 years (29), the long duration of the disease must be included in analyses of NET cohorts. However, out of all factors, the combination of MTV and chromogranin A showed the highest HR for OS.

At present, only two studies with more than 40 patients showed that the long-term survival of NET patients treated with PRRT was dependent on MTV. However, both studies did not report the potential confounding impact of age on OS in their analyses (30, 31). One study could not assess long-term prognostic markers due to a limited follow-up time of 31 months (30). Differences were found with regard to the cutoff values of MTV, which may be explained by the longer follow-up, the larger cohort, and the different segmentation methodologies in our study. Therefore, our patient cohort is one of the largest with a long follow-up period in the currently available literature, which demonstrates the impact of MTV on OS, and thus is the first study that evidenced MTV to be a risk factor independent of patients' age.

Since younger patients are known to recover faster and better from invasive interventions, such as surgery or other local therapies, and due to the known prolonged survival rates of NET patients, one might speculate that lowering the MTV prior to PRRT could improve the OS (32–34).

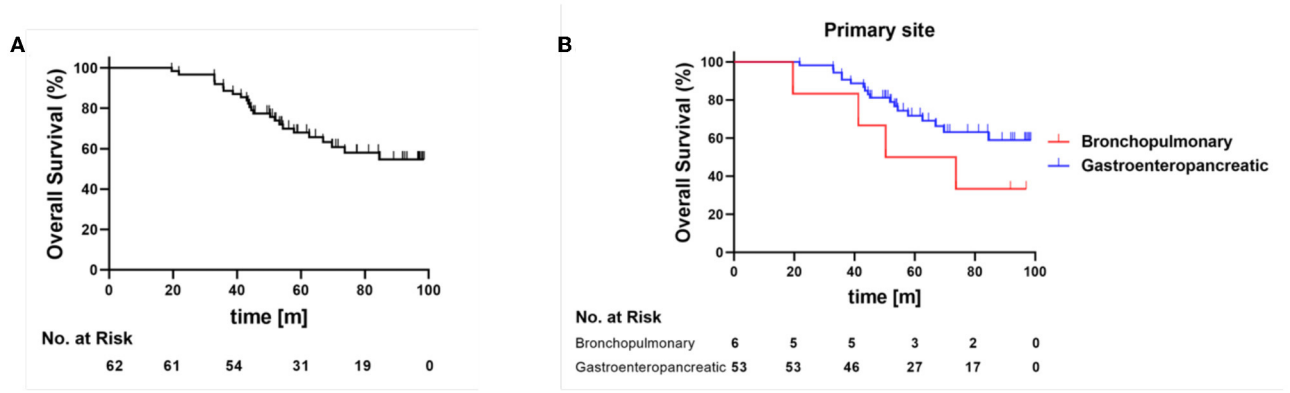

FIGURE 3
Overall survival for all patients **(A)** and in dependence of primary side **(B)**, Bronchopulmonary NET red line, gastroenteropancreatic NET blue line, m, months.

TABLE 6 Univariable Cox regression for OS.

Variable	Coefficient (Odds)	95% CI	*p*
MTV/chromogranin A	2.67	1.60–4.43	**<0.001**
γ-GT.log	1.41	1.02–1.95	**0.038**
LDH	1.00	0.99–1.01	0.615
Age	1.13	1.07–1.20	**<0.001**
Gender	0.78	0.34–1.76	0.549
Grading	1.45	0.60–3.50	0.412

Both MTV and/chromogranin A can be considered to represent the tumor burden. MTV, molecular tumor volume; γ-GT, gamma-glutamyl transferase; LDH, lactate dehydrogenase. Correlation of clinical factors on overall survival. Bold values are statistically significant.

TABLE 7 Multivariable Cox regression for OS.

Covariate	Coefficient (Odds)	95% CI	*p*
MTV/chromogranin A	2.67	1.46–4.91	**0.002**
γ-GT.log	0.97	0.60–1.55	0.890
LDH	0.99	0.98–1.00	**0.007**
Age	1.15	1.08–1.23	**<0.001**
Gender	0.75	0.28–1.99	0.560
Grading	1.26	0.46–3.47	0.653

Both MTV and/chromogranin A can be considered to represent the tumor burden. MTV, molecular tumor volume; γ-GT, gamma-glutamyl transferase; LDH, lactate dehydrogenase. Correlation of clinical factors on overall survival. Bold values are statistically significant.

We also analyzed the change of the MTV after 2 cycles in comparison to the baseline PET/CT as described above. Non-responders to PRRT showed significantly worse overall survival. Therefore, in clinical practice, a PET/CT should be performed for therapy evaluation in patients after two treatment cycles, as non-responders may benefit from therapy adjustment.

Of course, these therapeutic adaptations have to be discussed in an interdisciplinary manner in consideration of all alternative treatment approaches.

In the NETTER-1 study, no statistically significant difference in the ultimate overall survival rate was shown between the PRRT arm and the control group, which might have been caused by a crossover of patients with PD in the SSA group (12).

Therefore, the results of the NETTER-1 study, including the limited OS, the low response rate of 15% together with a PFS of under 1 year, highlight the urgent need for prognostic factors and treatment monitoring measures to identify those patients for whom a change in treatment has to be considered.

The NETTER-1 study reported a 5-year OS rate of 35%, whereas, in our cohort, the 5-year OS rate was approximately 65%. These differences are most likely because not all patients in our cohort had previously a progression under SSA therapy. Patients with a high tumor burden or severe clinical complaints were sometimes directly treated with a combination of SSA therapy and PRRT.

NETTER-1 showed very similar rates of adverse events related to hematological disorders, reported to be approximately 3–4% grade 3/4 toxicities, as in our cohort. Moreover, in the prospective phase III study, as in our retrospective analysis, 1–2% developed MDS during the follow-up period.

Limitations

A limitation of our study is the relatively small cohort size in a single center and the retrospective approach, as well as the fact that in the follow-up period, not all information about further therapies has been provided. The effectiveness of PRRT may be impacted by various primary tumor sites and different gradings. Moreover, due to the retrospective design and the patients' comorbidities, the clinical protocol is not uniform. Since many patients were treated prior to 2017, an 8-week therapy interval was not scheduled, which is common today. Furthermore, a different number of therapy cycles were performed in the patients. In addition, different SSTR targeting tracers, such as [^{18}F]-SiFAlin-TATE, are available yet, which might show significantly different imaging properties from [^{68}Ga]Ga-DOTA-TOC (35) or [^{68}Ga]Ga-DOTA-TATE. In this respect, the cutoff values reported in this study cannot be

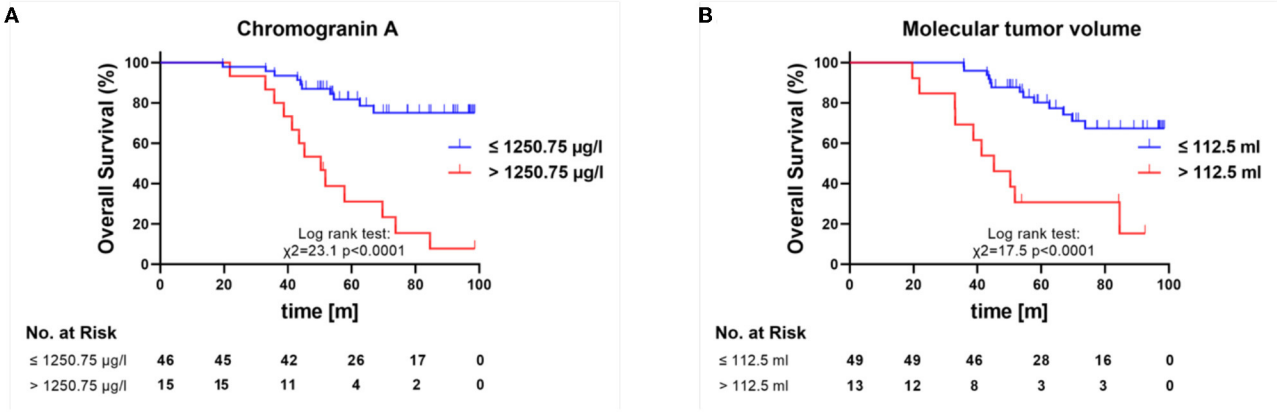

FIGURE 4
Kaplan–Meier overall survival curves for patients with high and low chromogranin A **(A)** and MTV **(B)** as based on ROC. m, months.

used as an absolute reference, but our results indicate that the determination of other parameters, such as MTV, should also be used for therapy stratification in patients with NET.

Conclusion

The limited long-term survival rates of the NETTER-1 study demonstrate the urgent need to find prognostic and follow-up markers. Our study demonstrated that a reference tissue-based MTV in combination with chromogranin A significantly affects long-term survival. Furthermore, the γ-GT showed a significant impact on OS in the univariable Cox regression. An interim PET/CT after two cycles can assist in identifying non-responders who might benefit from therapeutic adjustments. Further studies with larger sample sizes may be needed to better identify the optimal therapeutic sequence after progression to PRRT.

Data availability statement

The raw data supporting the conclusions of this article will be made available by the authors, without undue reservation.

Ethics statement

The study was approved by the IRB (Ethics Committee of the Faculty of Medicine of the Eberhard Karls University Tuebingen) of the University Hospital Tuebingen, and was conducted in accordance with the Declaration of Helsinki (Reference No. 530/220BO). The patients/participants provided their written informed consent to participate in this study.

Author contributions

NT, HD, LZ, MH, and CF conceived and designed the study. NT, JS, JJ, GR, FF, HD, LZ, MH, and CF conducted the patient data, as well as the medical evaluation and analysis. NT, JS, JJ, GR, HD, and CF analyzed the data. NT prepared the figures. NT, JS, and CF wrote the first draft of the manuscript. LZ, HD, and MH contributed to the data interpretation and manuscript editing. All authors critically reviewed, read, and approved the final manuscript. All authors have read and agreed to the published version of the manuscript.

Funding

This study was supported by the Deutsche Forschungsgemeinschaft (DFG, German Research Foundation, Germany's Excellence Strategy-EXC2180-390900677) and the Werner Siemens Foundation.

Conflict of interest

The authors declare that the research was conducted in the absence of any commercial or financial relationships that could be construed as a potential conflict of interest.

Publisher's note

All claims expressed in this article are solely those of the authors and do not necessarily represent those of their affiliated organizations, or those of the publisher, the editors and the reviewers. Any product that may be evaluated in this article, or claim that may be made by its manufacturer, is not guaranteed or endorsed by the publisher.

Supplementary material

The Supplementary Material for this article can be found online at: https://www.frontiersin.org/articles/10.3389/fmed.2023.1169970/full#supplementary-material

References

1. Cives M, Strosberg J. An update on gastroenteropancreatic neuroendocrine tumors. *Oncology (Williston Park).* (2014) 28:749–56, 758.

2. Hallet J, Law CH, Cukier M, Saskin R, Liu N, Singh S. Exploring the rising incidence of neuroendocrine tumors: a population-based analysis of epidemiology, metastatic presentation, and outcomes. *Cancer.* (2015) 121:589–97. doi: 10.1002/cncr.29099

3. Modlin IM, Lye KD, Kidd M. A 5-decade analysis of 13,715 carcinoid tumors. *Cancer.* (2003) 97:934–59. doi: 10.1002/cncr.11105

4. Yao JC, Hassan M, Phan A, Dagohoy C, Leary C, Mares JE, et al. One hundred years after "carcinoid": epidemiology of and prognostic factors for neuroendocrine tumors in 35,825 cases in the United States. *J Clin Oncol.* (2008) 26:3063–72. doi: 10.1200/JCO.2007.15.4377

5. Reubi JC. Somatostatin and other Peptide receptors as tools for tumor diagnosis and treatment. *Neuroendocrinology.* (2004) 80 Suppl 1:51–6. doi: 10.1159/000080742

6. Patel YC, Srikant CB. Somatostatin receptors. *Trends Endocrinol Metab.* (1997) 8:398–405. doi: 10.1016/S1043-2760(97)00168-9

7. Caplin ME, Pavel M, Cwikla JB, Phan AT, Raderer M, Sedlackova E, et al. Lanreotide in metastatic enteropancreatic neuroendocrine tumors. *N Engl J Med.* (2014) 371:224–33. doi: 10.1056/NEJMoa1316158

8. Rinke A, Muller HH, Schade-Brittinger C, Klose KJ, Barth P, Wied M, et al. Placebo-controlled, double-blind, prospective, randomized study on the effect of octreotide LAR in the control of tumor growth in patients with metastatic neuroendocrine midgut tumors: a report from the PROMID Study Group. *J Clin Oncol.* (2009) 27:4656–63. doi: 10.1200/JCO.2009.22.8510

9. Krenning EP, Kooij PP, Bakker WH, Breeman WA, Postema PT, Kwekkeboom DJ, et al. Radiotherapy with a radiolabeled somatostatin analogue, [111In-DTPA-D-Phe1]-octreotide. A case history. *Ann N Y Acad Sci.* (1994) 733:496–506. doi: 10.1111/j.1749-6632.1994.tb17300.x

10. Kwekkeboom DJ, Teunissen JJ, Bakker WH, Kooij PP, de Herder WW, Feelders RA, et al. Radiolabeled somatostatin analog [177Lu-DOTA0,Tyr3]octreotate in patients with endocrine gastroenteropancreatic tumors. *J Clin Oncol.* (2005) 23:2754–62. doi: 10.1200/JCO.2005.08.066

11. Strosberg J, El-Haddad G, Wolin E, Hendifar A, Yao J, Chasen B, et al. Phase 3 Trial of (177)Lu-dotatate for midgut neuroendocrine tumors. *N Engl J Med.* (2017) 376:125–35. doi: 10.1056/NEJMoa1607427

12. Strosberg JR, Caplin ME, Kunz PL, Ruszniewski PB, Bodei L, Hendifar A, et al. (177)Lu-Dotatate plus long-acting octreotide versus highdose long-acting octreotide in patients with midgut neuroendocrine tumours (NETTER-1): final overall survival and long-term safety results from an open-label, randomised, controlled, phase 3 trial. *Lancet Oncol.* (2021) 22:1752–63. doi: 10.1016/S1470-2045(21)00572-6

13. Pavel M, O'Toole D, Costa F, Capdevila J, Gross D, Kianmanesh R, et al. ENETS consensus guidelines update for the management of distant metastatic disease of intestinal, pancreatic, bronchial neuroendocrine neoplasms (NEN) and NEN of unknown primary site. *Neuroendocrinology.* (2016) 103:172–85. doi: 10.1159/000443167

14. Robelin P, Hadoux J, Forestier J, Planchard D, Hervieu V, Berdelou A, et al. Characterization, prognosis, and treatment of patients with metastatic lung carcinoid tumors. *J Thorac Oncol.* (2019) 14:993–1002. doi: 10.1016/j.jtho.2019.02.002

15. Mariniello A, Bodei L, Tinelli C, Baio SM, Gilardi L, Colandrea M, et al. Long-term results of PRRT in advanced bronchopulmonary carcinoid. *Eur J Nucl Med Mol Imag.* (2016) 43:441–52. doi: 10.1007/s00259-015-3190-7

16. Mirvis E, Toumpanakis C, Mandair D, Gnanasegaran G, Caplin M, Navalkissoor S. Efficacy and tolerability of peptide receptor radionuclide therapy (PRRT) in advanced metastatic bronchial neuroendocrine tumours (NETs). *Lung Cancer.* (2020) 150:70–5. doi: 10.1016/j.lungcan.2020.10.005

17. Ianniello A, Sansovini M, Severi S, Nicolini S, Grana CM, Massri K, et al. Peptide receptor radionuclide therapy with (177)Lu-DOTATATE in advanced bronchial carcinoids: prognostic role of thyroid transcription factor 1 and (18)F-FDG PET. *Eur J Nucl Med Mol Imag.* (2016) 43:1040–6. doi: 10.1007/s00259-015-3262-8

18. Baudin E, Caplin M, Garcia-Carbonero R, Fazio N, Ferolla P, Filosso PL, et al. Lung and thymic carcinoids: ESMO Clinical Practice Guidelines for diagnosis, treatment and follow-up(⋆). *Ann Oncol.* (2021) 32:439–51. doi: 10.1016/j.annonc.2021.01.003

19. Bodei L, Cremonesi M, Grana CM, Fazio N, Iodice S, Baio SM, et al. Peptide receptor radionuclide therapy with (1)(7)(7)Lu-DOTATATE: the IEO phase I-II study. *Eur J Nucl Med Mol Imaging.* (2011) 38:2125–35. doi: 10.1007/s00259-011-1902-1

20. Zwirtz K, Hardt J, Acker G, Baur ADJ, Pavel M, Huang K, et al. Comparison of Choi, RECIST and Somatostatin Receptor PET/CT Based Criteria for the Evaluation of Response and Response Prediction to PRRT. *Pharmaceutics.* (2022) 14:1278. doi: 10.3390/pharmaceutics14061278

21. Siebinga H, de Wit-van der Veen BJ, Beijnen JH, Dorlo TPC, Huitema ADR, Hendrikx J. A physiologically based pharmacokinetic model for [(68)Ga]Ga-(HA-)DOTATATE to predict whole-body distribution and tumor sink effects in GEP-NET patients. *EJNMMI Res.* (2023) 13:8. doi: 10.1186/s13550-023-00958-7

22. Bodei L, Mueller-Brand J, Baum RP, Pavel ME, Horsch D, O'Dorisio MS, et al. The joint IAEA, EANM, and SNMMI practical guidance on peptide receptor radionuclide therapy (PRRNT) in neuroendocrine tumours. *Eur J Nucl Med Mol Imaging.* (2013) 40:800–16. doi: 10.1007/s00259-012-2330-6

23. Veerman C, Siebinga H, de Vries-Huizing DMV, Tesselaar MET, Hendrikx J, Stokkel MPM, et al. The effect of long-acting somatostatin analogues on the uptake of [(177)Lu]Lu-HA-DOTATATE. *Eur J Nucl Med Mol Imaging.* (2023). doi: 10.1007/s00259-022-06094-z

24. Health UDo, Services H. *Common Terminology Criteria for Adverse Events.* Version 5.0. Published November 27, 2017. (2020).

25. Jakoby BW, Bercier Y, Conti M, Casey ME, Bendriem B, Townsend DW. Physical and clinical performance of the mCT time-of-flight PET/CT scanner. *Phys Med Biol.* (2011) 56:2375–89. doi: 10.1088/0031-9155/56/8/004

26. Ohlendorf F, Werner RA, Henkenberens C, Ross TL, Christiansen H, Bengel FM, et al. Predictive and prognostic impact of blood-based inflammatory biomarkers in patients with gastroenteropancreatic neuroendocrine tumors commencing peptide receptor radionuclide therapy. *Diagnostics.* (2021) 11:504. doi: 10.3390/diagnostics11030504

27. Eisenhauer EA, Therasse P, Bogaerts J, Schwartz LH, Sargent D, Ford R, et al. New response evaluation criteria in solid tumours: revised RECIST guideline (version 1.1). *Eur J Cancer.* (2009) 45:228–47. doi: 10.1016/j.ejca.2008.10.026

28. Jurisic V, Radenkovic S, Konjevic G. The actual role of LDH as tumor marker, biochemical and clinical aspects. *Adv Exp Med Biol.* (2015) 867:115–24. doi: 10.1007/978-94-017-7215-0_8

29. Dasari A, Shen C, Halperin D, Zhao B, Zhou S, Xu Y, et al. Trends in the incidence, prevalence, and survival outcomes in patients with neuroendocrine tumors in the United States. *JAMA Oncol.* (2017) 3:1335–42. doi: 10.1001/jamaoncol.2017.0589

30. Durmo R, Filice A, Fioroni F, Cervati V, Finocchiaro D, Coruzzi C, et al. Predictive and prognostic role of pre-therapy and interim 68Ga-DOTATOC PET/CT parameters in metastatic advanced neuroendocrine tumor patients treated with PRRT. *Cancers.* (2022) 14:592. doi: 10.3390/cancers14030592

31. Pauwels E, Van Binnebeek S, Vandecaveye V, Baete K, Vanbilloen H, Koole M, et al. Inflammation-Based Index and (68)Ga-DOTATOC PET-Derived uptake and volumetric parameters predict outcome in neuroendocrine tumor patients treated with (90)Y-DOTATOC. *J Nucl Med.* (2020) 61:1014–20. doi: 10.2967/jnumed.119.236935

32. Lin HS, Watts JN, Peel NM, Hubbard RE. Frailty and post-operative outcomes in older surgical patients: a systematic review. *BMC Geriatr.* (2016) 16:157. doi: 10.1186/s12877-016-0329-8

33. Brinson Z, Tang VL, Finlayson E. Postoperative functional outcomes in older adults. *Curr Surg Rep.* (2016) 4:21. doi: 10.1007/s40137-016-0140-7

34. Yau T, Yao TJ, Chan P, Epstein RJ, Ng KK, Chok SH, et al. The outcomes of elderly patients with hepatocellular carcinoma treated with transarterial chemoembolization. *Cancer.* (2009) 115:5507–15. doi: 10.1002/cncr.24636

35. Ilhan H, Lindner S, Todica A, Cyran CC, Tiling R, Auernhammer CJ, et al. Biodistribution and first clinical results of (18)F-SiFAlin-TATE PET: a novel (18)F-labeled somatostatin analog for imaging of neuroendocrine tumors. *Eur J Nucl Med Mol Imaging.* (2020) 47:870–80. doi: 10.1007/s00259-019-04501-6

frontiers | Frontiers in Medicine

TYPE Original Research
PUBLISHED 28 June 2023
DOI 10.3389/fmed.2023.1169451

OPEN ACCESS

EDITED BY
Giorgio Treglia,
Ente Ospedaliero Cantonale (EOC), Switzerland

REVIEWED BY
Harun Ilhan,
LMU Munich University Hospital, Germany
Priyank Yadav,
Sanjay Gandhi Post Graduate Institute of Medical Sciences (SGPGI), India

*CORRESPONDENCE
Matthias Weissinger
✉ MatthiasWeissinger@med.uni-tuebingen.de

RECEIVED 19 February 2023
ACCEPTED 30 May 2023
PUBLISHED 28 June 2023

CITATION
Weissinger M, Seyfried KC, Ursprung S, Castaneda-Vega S, Seith F, von Beschwitz S, Vogel J, Ghibes P, Nikolaou K, la Fougère C and Dittmann H (2023) Non-invasive estimation of split renal function from routine ^{68}Ga-SSR-PET/CT scans.
Front. Med. 10:1169451.
doi: 10.3389/fmed.2023.1169451

Non-invasive estimation of split renal function from routine ^{68}Ga-SSR-PET/CT scans

Matthias Weissinger[1,2]*, Kyra Celine Seyfried[2], Stephan Ursprung[1], Salvador Castaneda-Vega[2,3], Ferdinand Seith[1], Sebastian von Beschwitz[2], Jonas Vogel[1,2], Patrick Ghibes[1], Konstantin Nikolaou[1,4,5], Christian la Fougère[2,4,5] and Helmut Dittmann[2]

[1]Department of Diagnostic and Interventional Radiology, University Hospital Tuebingen, Tuebingen, Germany, [2]Department of Nuclear Medicine and Clinical Molecular Imaging, University Hospital Tuebingen, Tuebingen, Germany, [3]Department of Preclinical Imaging and Radiopharmacy, Werner Siemens Imaging Center, Eberhard Karls University Tuebingen, Tuebingen, Germany, [4]iFIT-Cluster of Excellence, Eberhard Karls University Tuebingen, Tuebingen, Germany, [5]German Cancer Consortium (DKTK), Partner Site Tuebingen, Tuebingen, Germany

Objective: Patients with impaired kidney function are at elevated risk for nephrotoxicity and hematotoxicity from peptide receptor radionuclide therapy (PPRT) for advanced neuroendocrine tumors. Somatostatin receptor (SSR)-PET/CT imaging is the method of choice to identify sufficient SSR expression as a prerequisite for PRRT. Therefore, our study aimed to explore whether split renal function could be evaluated using imaging data from routine SSR-PET/CT prior to PRRT.

Methods: In total, 25 consecutive patients who underwent SSR-PET/CT (Siemens Biograph mCT®) before PRRT between June 2019 and December 2020 were enrolled in this retrospective study. PET acquisition in the caudocranial direction started at 20 ± 0.5 min after an i.v. injection of 173 ± 20 MBq [^{68}Ga]Ga-ha DOTATATE, and the kidneys were scanned at 32 ± 0.5 min p.i. The renal parenchyma was segmented semi-automatically using an SUV-based isocontour (SUV between 5 and 15). Multiple parameters including SUVmean of renal parenchyma and blood pool, as well as parenchyma volume, were extracted, and accumulation index (**ACI**: renal parenchyma volume/SUVmean) and total kidney accumulation (**TKA**: SUVmean x renal parenchyma volume) were calculated. All data were correlated with the reference standard tubular extraction rate (TER-MAG) from [^{99m}Tc]Tc-MAG3 scintigraphy and glomerular filtration rate ($GFR_{CDK-EPI}$).

Results: SUVmean of the parenchymal tracer retention showed a negative correlation with TER_{MAG} (r: −0.519, $p < 0.001$) and $GFR_{CDK-EPI}$ (r: −0.555, $p < 0.001$) at 32 min p.i. The herein-introduced ACI revealed a significant correlation ($p < 0.05$) with the total tubular function (r: 0.482), glomerular renal function (r: 0.461), split renal function (r: 0.916), and absolute single-sided renal function (r: 0.549). The mean difference between the split renal function determined by renal scintigraphy and ACI was 1.8 ± 4.2 % points.

Conclusion: This pilot study indicates that static [^{68}Ga]Ga-ha DOTATATE PET-scans at 32 min p.i. may be used to estimate both split renal function and absolute renal function using the herein proposed "Accumulation Index" (ACI).

KEYWORDS

accumulation index, DOTATATE, NET (neuro-endocrinal tumors), PRRT (peptide receptor radionuclide therapy), split renal function, SSR PET/CT, single-sided renal function, total kidney accumulation

1. Introduction

Peptide receptor radionuclide therapy (PRRT) with the lutetium 177-labeled sandostatin analog (^{177}Lu)-oxodotreotide (e.g., Lutathera®) is a well-tolerated and approved second-line therapy for the treatment of advanced midgut neuroendocrine tumors (1, 2). PRRT is administered in combination with nephroprotective amino acids in multiple cycles usually 6–12 weeks apart (1, 2).

The kidneys are exposed to a high radiation dose in PRRT. The theranostic somatostatin analog is predominantly glomerular filtrated and actively reabsorbed in the proximal renal tubules by the endocytic megalin receptor (3, 4). This results in a high radiation dose to the renal cortex (3). Based on the traditional dose limit established for external beam irradiation and ^{177}Lu and ^{90}Y PRRT dosimetry, the absorbed dose of kidneys should be restricted to 23–40 Gy (depending on risk factors) (5), which is often exceeded when multiple cycles of PRRT are applied in routine clinical practice (1, 2, 6). Early PRRT using 90-Yttrium-labeled somatostatin analogs reported severe nephrotoxicity grade 3/4 in approximately 3% of all patients (7, 8). PRRT with (^{177}Lu)-oxodotreotide has shown to be considerably less nephrotoxic (7). However, up to 25% of all patients treated with ^{177}Lu PRRT develop a mild renal toxicity grade 1/2, which was persistent in about half of the patients (1, 7, 9). Nephrotoxicity was not only associated with previous 90-Yttrium PRRTs and the number of PRRT cycles but also with hypertension and other nephrotoxic risk factors (7).

Notably, preexisting poor renal function has been identified as a risk factor for deteriorated kidney function after PRRT (7, 8, 10, 11). Reduced renal function results in higher radiation doses to the kidneys and increases the risk of hematotoxicity (10). Thus, it can be assumed that unilateral renal insufficiency will result in disproportionate ipsilateral radiation damage during PRRT. Unilateral renal dysfunction that is partially compensated by the contralateral kidney remains undetected in laboratory testing and can be diagnosed, at present, only by imaging techniques. Renal scintigraphy is the gold standard for determining split renal function (12). Renal scintigraphy with ^{99m}Technetium-mercaptoacetyltriglycine (MAG3) was introduced in 1984 and became the method of choice for the precise determination of the split renal function, tubular function, and renal plasma flow, and defines the gold standard in most clinical trials (12, 13). However, renal function scintigraphy is an additional examination for the patient, associated with additional time spent in the hospital and cost.

An interesting approach to avoid additional time-consuming or potentially harmful tests is the integration of split renal function estimation into other routine imaging procedures. For instance, Geist et al. described a method to determine side-separated glomerular filtration rate (GFR) and renal plasma flow using a short dynamic FDG PET/MRI imaging protocol (14). These short dynamic sequences can be acquired within the setting of a clinical PET scan without the need for additional tracer, contrast media, or radiation exposure and might save the patient an extra hospital appointment.

Integrating renal function tests into the PET workflow is clinically very attractive, especially for patients requiring periodic PET/CT follow-up and regular renal function monitoring due to potentially nephrotoxic therapy such as PRRT.

Therefore, this study aimed to determine split renal function using data from routine static somatostatin receptor (SSR)-PET/CT with the predominately glomerular filtrated [^{68}Ga]Ga-ha DOTATATE tracer and to correlate results with renal scintigraphy and serum GFR as reference standards.

2. Materials and methods

This retrospective study enrolled patients with predominantly non-resectable and/or metastasized neuroendocrine tumors who underwent [^{68}Ga]Ga-ha DOTATATE PET/CT and [^{99m}Tc]Tc-mercaptoacetyltriglycine (MAG3) renal scintigraphy before PRRT between June 2019 and December 2020. Patients with a history of potentially nephrotoxic chemotherapy or PRRT within 5 years before PET/CT were excluded from the analysis. All patients agreed to the anonymized data analysis and provided written informed consent to the scientific analysis of pseudonymized medical data collected at our University Hospital. The institutional review board approved the retrospective data analyses (registry No. 386/2021BO2). One patient underwent an additional dynamic PET acquisition for tracer kinetic measurements within a review board approved prospective dynamic PET/CT imaging trial (registry No. 863/2019BO1, DRKS 00021217).

2.1. [^{68}Ga]Ga-ha DOTATATE PET/CT

Whole-body [^{68}Ga]Ga-ha DOTATATE PET/CT comprising skull to mid-thigh was performed on a Biograph mCT® scanner, (Siemens Healthineers) with continuous-bed-motion technique (Siemens FlowMotion®). PET acquisition started 20 ± 0.5 min after an i.v. injection of 173 ± 20 MBq ^{68}Ga-ha-DOTATATE in caudocranial direction. No diuretics were administered. The kidneys were imaged by PET 32 ± 0.5 min p.i. Weight and size for mean standardized uptake value (SUVmean) calculation were measured for each patient immediately before the PET/CT examination. Patients were asked to drink 1,000 ml of oral contrast media solution (1,000 ml of mannitol 2.5%) starting 1 h before tracer application. Patients were positioned on the PET/CT bed on a vacuum mattress and asked to breathe as shallowly and evenly as possible and were asked not to move. The PET/CT examination started with a contrast-enhanced diagnostic multi-slice CT (80–120 ml Ultravist 370® i.v., arterial and portal-venous phase) except for contraindications. PET imaging data were reconstructed by applying an iterative OSEM 3D algorithm (256*256 matrix) with a 4 mm Gaussian filter.

2.2. Renal scintigraphy

All patients were asked to drink at least 10 ml of mineral water/kg body weight 30 min before scintigraphy. Each individual underwent dynamic renal scintigraphy starting with a bolus injection of 100 ± 6 MBq [^{99m}Tc]Tc-MAG3 on a SPECT or SPECT/CT camera. Camera heads were in H-mode, and the acquisition was done in a dorsal view. Regions of interest (ROI) were placed in the renal parenchyma including the renal pelvic

caliceal system (RPCS) and aorta by technicians with more than 5 years of experience in renal scintigraphy and adjusted in case of motion artifacts. Calculation of split renal function was obtained by the activity increase over 60 s starting 45–60 s p.i. The tubular extraction rate of [^{99m}Tc]Tc-MAG3 was quantified using Bubeck's method (15) from single blood samples 20 and 30 min p.i. Side-separated TER-MAG was calculated by multiplying the split renal function with TER. All estimates were validated by a nuclear medicine specialist.

2.3. Glomerular function rate calculation

The glomerular function rate was calculated from serum creatinine levels using the clinically established CKD-EPI formula (16). Serum creatinine was measured on the day of renal scintigraphy, as well as a maximum of 2 weeks before PET/CT examination.

2.4. Semiquantitative PET/CT measurements and renal parenchyma segmentation

Segmentation of renal parenchyma and RPCS in PET/CT images was performed with a HERMES SMART® Workstation v2.13.0.37 (HERMES MEDICAL SOLUTIONS) by a PhD student (K.S.) and validated by an expert in hybrid imaging (M.W). SUVmean of the renal parenchyma and the parenchymal volume were quantified for each kidney by the following methods.

First, a freehand volume of interest (VOI) was placed over the kidney excluding the renal pelvis in the fused PET/CT images. Overlaps with other organs, such as the liver or adrenal glands, were strictly avoided. Second, an isocontour was applied to the VOI. The volume of [^{68}Ga]Ga-ha DOTATATE avid renal parenchyma was segmented semi-automatically using a lower threshold of SUV = 5.0, which has shown the best visual fit to the anatomy, and an upper threshold of SUV = 15 was used to exclude radioactive urine extracted in the RPCS. In addition, the following indexes were calculated.

Total Kidney Accumulation:

$$\mathbf{TKA}_{5-15} = \mathrm{SUVmean}_{5-15\ \mathrm{isocontour}} \times [68\mathrm{Ga}]\mathrm{Ga} - \text{ha DOTATATE avid renal parenchyma}$$

Total Kidney Accumulation with blood pool correction:

$${}_{\mathrm{bpc}}\mathbf{TKA}_{5-15} = (\mathrm{SUVmean}_{5-15\ \mathrm{isocontour}} - \mathrm{SUVmean\ blood\ pool}) \times [^{68}\mathrm{Ga}]\mathrm{Ga} - \text{ha DOTATATE avid renal parenchyma}$$

Accumulation Index:

$$\mathbf{ACI}_{5-15} = \frac{[68\mathrm{Ga}]\mathrm{Ga} - \text{ha DOTATATE avid renal parenchyma}}{\mathrm{SUVmean}\ (5-15\ \mathrm{isocontour})}$$

For the left kidney, split renal function is expressed as a percentage.

$$\textbf{Split renal function} = \frac{\textit{left kidney}}{\textit{left} + \textit{right kidney}} \times 100$$

The activity concentration of [^{68}Ga]Ga-ha DOTATATE in the blood pool was measured semiquantitatively per SUVmean within a cylindric VOI placed in the descending aorta with a volume of ≥5 ml.

2.5. Tumor segmentation

Freehand 3D VOI was plotted around the tumor areas by an expert in hybrid imaging (M.W.) using Hermes Affinity v.3.0.5 (Hermes Medical Solutions). The tumor segmentation was PET based using an isocontour with an individual threshold defined over the SUVmax of the adjacent healthy tissue. A tissue density of 1 g/ml was assumed for the calculation of the fraction of the injected dose. The following parameters were obtained:

Metabolic Volume:

$$\mathbf{MTV} = \mathrm{SUVmean} \times \text{VOI of segmented tumor}$$

Fraction of the injected dose:

$$\%\mathbf{ID} = \frac{\mathrm{MTV}}{\text{body weight} \times \mathrm{SUV\ 1}}$$

2.6. Statistical analysis

Renal scintigraphy is defined as the gold standard for absolute and side-separated tubular renal function. Statistical analysis was performed using SPSS Statistics v.28.0 (IBM Inc.) and Excel® 2019 v.1808 software (Microsoft).

Significance testing was performed for interval-scaled data using the Students' *t*-test. A *p*-value of <0.05 was considered statistically significant. A Pearson's correlation coefficient of $r > 0.7$ was defined as strong, 0.7–0.3 as moderate, and <0.3 as a weak linear correlation.

3. Results

3.1. Patients' characteristics

In total, 25 patients met the inclusion criteria. All patients suffered from metastatic tumors, with predominantly neuroendocrine differentiation (details in Table 1) and underwent SSR-PET/CT for the evaluation of PRRT. Gender was balanced with 13 male and 12 female patients. The average patient age on the day of the PET/CT examination was 64.4 ± 15.6 years (range: 21–81 years) with average patient size and weight of 166.4 ± 19 cm and 69.3 ± 20.3 kg. Male patients were non-significantly older, larger, and heavier than female patients at the timepoint

TABLE 1 Detailed listing of the participants' underlying disease and prior therapies.

Patient ID	Sex	Age in years	Primary Tumor	Tumor Stage	Proliferation index Ki 67	Prior Therapy	GFR ml/min/1.73m²	MTV/%ID
1	Male	74	Ileum NET	T3, N1, M0	<10%	Surgery	66	161/0.2%
2	Female	67	Ileum NET	Tx, Nx, M1	17.8%	Surgery, SSA, PRRT	78	1,371/1.8%
3	Male	72	Atypical pulmonary carcinoid	T4, Nx, M1	20%	SSA	64	3,077/3.4%
4	Female	78	Parotid Gland NET	Tx, Nx, M1	20%	Surgery, RT	40	104/0.1%
5	Female	54	Pancreas NET	T4, Nx, M1	3–5%	SSA	95	1,815/2.6%
6	Female	68	CUP NET	Tx, N1, M1	15%	SSA	100	1,899/27.2%
7	Male	68	Ileum NET	T3, N1, M1	5%	Surgery, SSA	54	1,121/1.4%
8	Female	63	Duodenum NET	Tx, Nx, M1	2–5%	None	77	246/0.5%
9	Male	71	Pancreas NET	Tx, Nx, M1	5%	SSA	67	1,686/20.8%
10	Female	79	Pancreas NET	T3, N1, M1	5%	Surgery	69	732/2.1%
11	Male	24	Pancreas NET	Tx, Nx, M1	20%	SSA	98	1,041/1.6%
12	Female	51	Pancreas NET	Tx, Nx, M1	40%	None	89	14,002/24.4%
13	Male	79	CUP NET	Tx, N1, M1	<1%	SSA	83	12,448/18.6%
14	Male	60	Ileum NET	T3, N1, M1	<2%	Surgery, SSA	100	8/0.1 %
15	Female	65	Ileum NET	Tx, N1, M1	-	Surgery, PRRT, SSA	68	342/0.6%
16	Male	70	Ileum NET	T4, N1, M1	<2%	Surgery, SSA	95	8,574/10.2%
17	Male	79	Ileum NET	T3, N1, M1	3%	Surgery, SSA	85	809/1.0%
18	Male	61	Oncocytic thyroid carcinoma	T3, N0, M1	-	Surgery, RT, RIT	70	2,475/2.2%
19	Female	55	Ileum NET	T3, N1, M1	5–7 %	Surgery, SSA	59	873/1.1%
20	Male	81	Pancreas NET	Tx, Nx, Mx	5–10%	SSA	85	1,691/2.8%
21	Male	51	Pancreas NET	Tx, Nx, M1	25–30%	None	109	17,228/25.5%
22	Female	65	CUP NET	Tx, Nx, M1	5%	Surgery	66	1,836/2.9%
23	Male	78	Ileum NET	Tx, N1, M1	<1%	Surgery, SSR, CT	59	2,764/4.6%
24	Female	21	Pancreas NET	T3, N1, M1	5 %	Surgery, CT	139	550/0.9%
25	Female	77	CUP NET	Tx, Nx, M1	25%	Surgery	70	280/0.5%

CT, Chemotherapy; NET, Neuroendocrine Tumor; PRRT, Peptide Receptor Radionuclide Therapy; RIT, Radioiodine Therapy RT, Radiotherapy; SSA, Somatostatin Analog therapy.

of PET/CT ($p = 0.290$–0.558). The mean GFR was 79.4 ± 20.9 ml/min/1.73 m². In total, 4 out of the 25 patients presented with moderately impaired kidney function and chronic kidney disease (CKD) stage 3 (3a: $n = 3$, 3b: $n = 1$), and 14 out of the 25 patients had mild impaired kidney function, CKD Stage 2. The average time between renal scintigraphy and PET/CT was 15.9 ± 40.6 days and was similar between genders in the two-sided t-test ($p = 0.162$).

3.2. Tracer kinetics

As a proof of concept, [^{68}Ga]Ga-ha DOTATATE kinetics in the renal parenchyma was measured using a dynamic PET acquisition in one patient without renal function impairment during oncological staging. [^{68}Ga]Ga-ha DOTATATE concentration reached its peak in the renal parenchyma 180 s after bolus injection followed by an exponential decrease until the end of the examination 43 min p.i., as shown in Figure 1.

3.3. Total renal function

TER-MAG revealed a strong correlation with $GFR_{CDK-EPI}$ (r: 0.756, $p < 0.001$). The calculated accumulation index (ACI) showed a moderate correlation with TER-MAG (r: 0.482, $p = 0.015$,

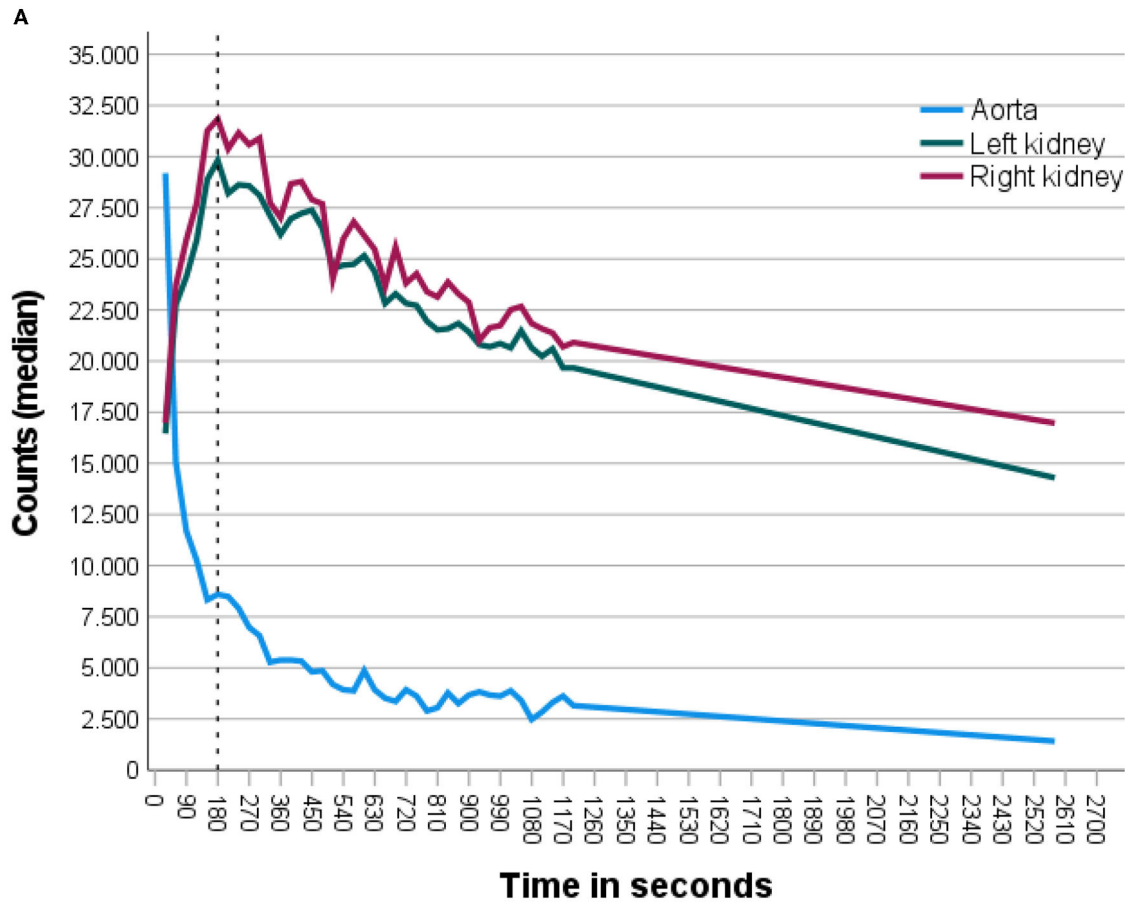

FIGURE 1
Dynamic SSR-PET acquisition of a patient with an initial diagnosis of NET with normal renal function and without previous nephrotoxic therapies was analyzed. **(A)** Time–activity curve was plotted from dynamic [^{68}Ga]Ga-ha DOTATATE PET 0–20 min (30 s frames) after i.v. tracer injection followed by static acquisition at 43 min for the left (green) and right (purple) kidney. [^{68}Ga]Ga-ha DOTATATE concentration reached its peak in the renal parenchyma 180 s after tracer injection followed by a continuous decrease until the end of the examination 43 min p.i. Blood pool activity measured in the abdominal aorta presents with a rapid exponential decrease. **(B)** PET images of [^{68}Ga]Ga-ha DOTATATE tracer distribution at different time points p.i. with plotted isocontours of semiautomatic parenchyma segmentation. Renal parenchyma demarcates clearly from the background and adjacent organs at all time points. The isocontour used for renal parenchymal volumetry removes background (SUV <5) and excreted urine in the pelvicocaliceal system (SUV >15).

Figure 1) and $GFR_{CDK-EPI}$ (0.461, $p = 0.020$) as shown in Figure 2.

Furthermore, the magnitude of SUVmean of the segmented renal parenchyma was moderately and negatively correlated with TER-MAG (r: −0.519, $p < 0.001$) and $GFR_{CDK-EPI}$ (r: −0.555, $p < 0.001$) as shown in Figure 3.

SUVmean of the blood pool at 32 ± 0.5 min p.i. correlated negatively and moderately with TER-MAG

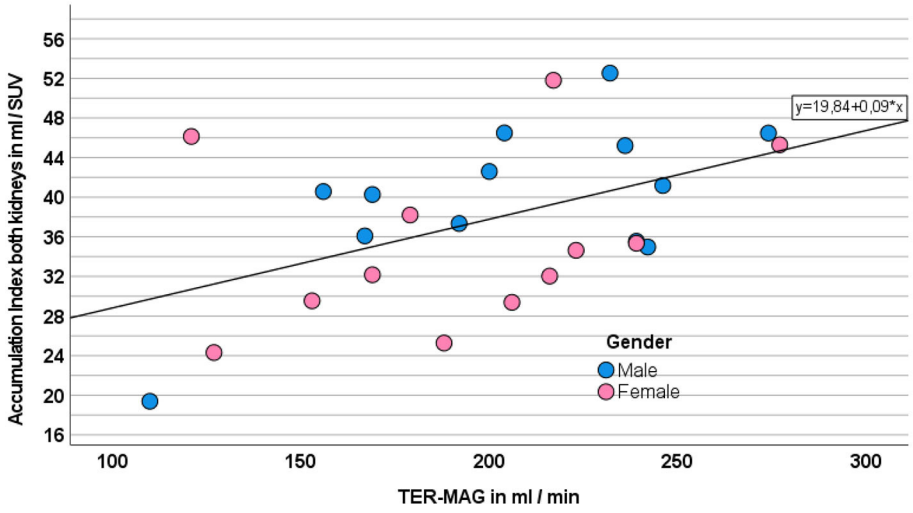

FIGURE 2
Correlation between ACI as the sum of both kidneys and TER-MAG. Gender is displayed in different colors.

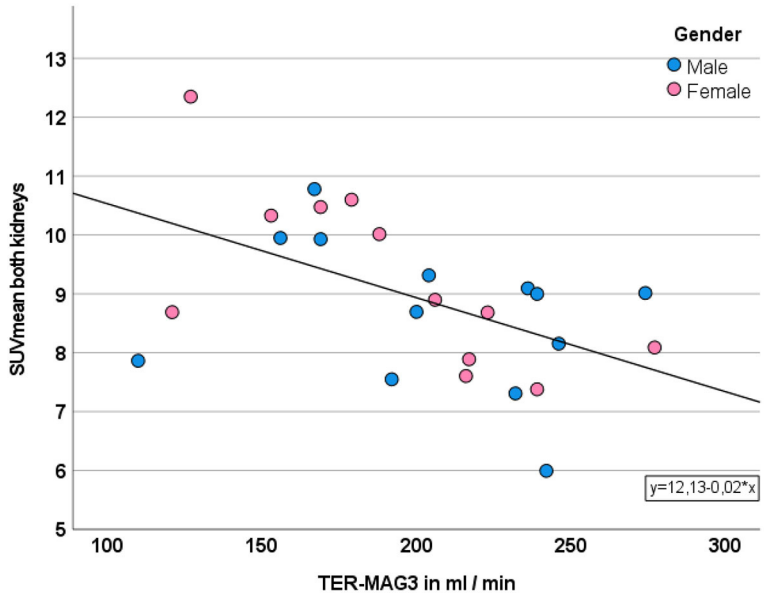

FIGURE 3
Correlation between SUVmean and TER. Gender is displayed in different colors.

(r: −0.590 p = 0.002) and $GFR_{CDK-EPI}$ (r = −0.438, $p = 0.028$).

In contrast, total kidney accumulation (TKA_{5-15}) as well as the volume of [^{68}Ga]Ga-ha DOTATATE avid renal parenchyma showed no significant correlation with TER-MAG (p = 0.241 and p = 0.601) or $GFR_{CDK-EPI}$ (p = 0.135 and $p = 0.713$).

3.4. PET-based assessment of split renal function

Split renal function as estimated using ACI attained the highest correlation with renal scintigraphy, with a very strong correlation of $r = 0.916$ ($p < 0.001$). The mean difference between the split renal function determined by renal scintigraphy and ACI was 1.8 ± 4.2 %

points. In 96% of patients ($n = 24/25$), the deviation between split renal function determined by ACI and renal scintigraphy was <10 % points. There was one outlier (patient ID 12) with a difference of 14 % points as illustrated in Figures 4, 5.

Further estimation of split renal function with SUVmean (r: −0.740, $p < 0.001$), total kidney accumulation (TKA_{5-15}) (r: 0.623, $p < 0.001$), or the volume of the [^{68}Ga]Ga-ha DOTATATE avid parenchymal volume (r: 0.905, $p < 0.001$) resulted in moderate to strong correlations with the gold standard renal scintigraphy. Blood pool corrected TKI_{bpc} did not improve correlation with renal scintigraphy (r: 0.479, $p = 0.015$).

3.5. PET-based assessment of absolute single-sided renal function

3.5.1. Accumulation index

The accumulation index correlated significantly with the absolute single-sided TER-MAG (r: 0.549, $p < 0.001$, $n = 50$) and the side-separated $GFR_{CDK-EPI}$ values (0.549, $p < 0.001$ $n = 50$). In particular, a hydronephrosis grade IV kidney with severe parenchymal atrophy was identified as non-functional despite the presence of residual parenchyma (patient ID 12, kidney ID: 23 R, TKI 5 ml, TER-MAG 0 ml/min) as shown in Figure 6.

3.5.2. SUVmean

SUVmean measurements of the renal parenchyma correlated negatively but only moderately with side-separated TER-MAG (r: −0.330, $p = 0.019$) and $GFR_{CDK-EPI}$ (r: −0.337, $p = 0.017$) as shown in Figure 7. The non-functional, shrunken kidney in one patient had no relevant uptake, resulting in an extreme value that negatively affected the correlation as shown in the scatterplot Figure 7.

3.5.3. Total Kidney Accumulation and parenchyma volume

TKA_{5-15} trended toward a non-significant, negative correlation with TER-MAG (r: −0.243, $p = 0.241$) and $GFR_{CKD-EPI}$ (r: −0.308 $p = 0.135$).

The volume of the [^{68}Ga]Ga-ha DOTATATE avid renal parenchymal showed a borderline insignificant correlation with TER-MAG and $GFR_{CDK-EPI}$ (r: 0.272 and r: 0.272, $p = 0.056$).

Table 2 summarizes different correlations.

3.6. Tumor sink effect

The average MTV was 4,376 ± 6,215 ml x SUV. The mean %ID was 6.3 ± 9.0% with a range of 0.1–27.2%. The MTV showed a moderate, negative correlation with the blood pool SUVmean (r: −0.433, $p = 0.031$). The %ID correlated weakly negatively with the SUVmean of renal parenchyma (r: −0.403, $p = 0.046$) and moderately negatively with SUVmean blood pool (r: −0.416, $p = 0.038$). No correlation was observed between MTV or %ID and renal function parameters (ACI, GFR, and TER-MAG 3).

4. Discussion

To our knowledge, this is the first study that demonstrates that split renal function, as well as absolute renal function, can be estimated from routine static oncologic SSR-PET/CT with a ^{68}Ga-labeled DOTA-conjugated peptide.

The data of this pilot study indicate that the amount of [^{68}Ga]Ga-ha DOTATATE accumulating in the renal parenchyma correlates with the renal tubular and glomerular function and consequently with the split renal function. This might be of high clinical relevance, as patients with inferior renal function reveal a significantly higher renal absorbed dose and higher grade of hematological toxicity during treatment with ^{177}Lu-DOTATATE (10).

Renal uptake of DOTA-conjugated peptides is reported to be predominantly caused by renal reabsorption in the proximal tubules, especially the megalin receptors (3, 17). A biochemical explanation might be an increased DOTATATE reabsorption in the megalin receptor or higher megalin transporter density, although the exact mechanism is still unclear (3). In addition, slower blood pool clearance could increase tracer bioavailability and thus renal DOTATATE retention (3, 10). This hypothesis is based on the ^{68}Ga-DOTA-conjugated peptide kinetics with an early peak at about 5 min in the renal parenchymal and an early glomeruli washout as well as blood pool clearance in patients with unrestricted renal function (3, 18, 19). Of particular note, somatostatin receptors have been shown to have no significant effect on renal DOTATATE uptake (3).

Previous attempts of SSR-PET-based renal function estimation might have failed due to the later acquisition time of 60–120 min p.i. and an incomplete parenchyma segmentation (20, 21). According to the literature data, the parenchymal activity remains relatively constant at a low level after 30 min p.i., owing to tubular reabsorption (3, 17, 18).

As another possible confounding factor for the SSR-PET-based assessment of renal function, tumor sequestration of somatostatin analogs has to be discussed, which is the main cause of the tumor sink effect (22). This effect was also evident in our cohort with a decrease in tracer concentration in the renal parenchyma and the blood pool in patients with high tumor masses. However, this did not significantly affect the accuracy of renal function determination by ACI.

The SUVmean of the segmented renal parenchyma correlated with the gold standard renal scintigraphy for both split function and absolute renal function. However, the SUVmean-based measurements of absolute split function revealed an outlier, which was attributed to grade IV hydronephrosis with severe atrophy and only little residual parenchyma. In this particular case, residual renal parenchyma was within the range of healthy renal tissue with an SUV of 6 and higher than blood pool or muscle tissue. This semiquantitatively estimated tracer uptake may be due to the smallest amounts of residual functional renal parenchyma (parenchyma volume 3 ml), which can be underestimated in scintigraphy due to the partial volume effect. Beyond that, a tracer fixation to the damaged renal tubule independent of the renal function might be considered.

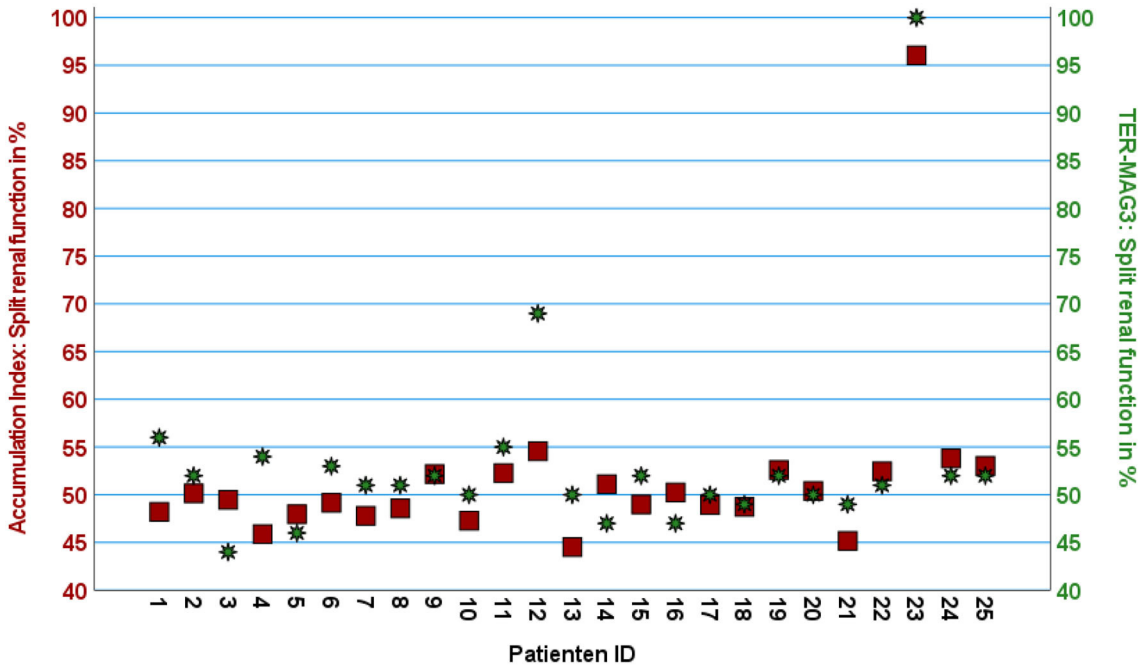

FIGURE 4
Scatter plot with two Z-axes displaying split renal function calculated using ACI on the left axis (red squares) and TER-MAG on the right axis (green stars) given for each patient in percent of the left kidney.

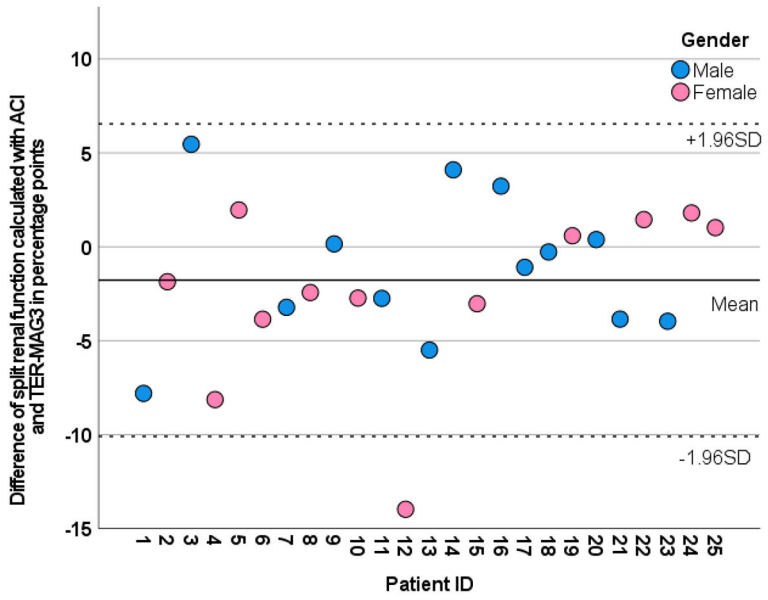

FIGURE 5
Modified Bland–Altman plot illustrating the deviation between the split renal function of the left kidney calculated by ACI (dots) from the reverence method MAG3 scintigraphy (0-line) for each patient. Gender is color coded. The mean value and ±1.96 SD are plotted as a line and dotted line.

Regardless of the underlying effect, a major risk of the SUV method is to overestimate the partial function of a small kidney, by neglecting kidney volume and thus the total renal corpuscular volume (total number of glomeruli x mean renal corpuscular volume) (23).

An approach to solving this issue is to implement the volume of SSR-avid renal parenchymal, which correlated significantly with split renal function. The volume of SSR-avid renal parenchymal seems to be a significant indicator in addition to SUV as a higher number of functioning nephrons can be assumed

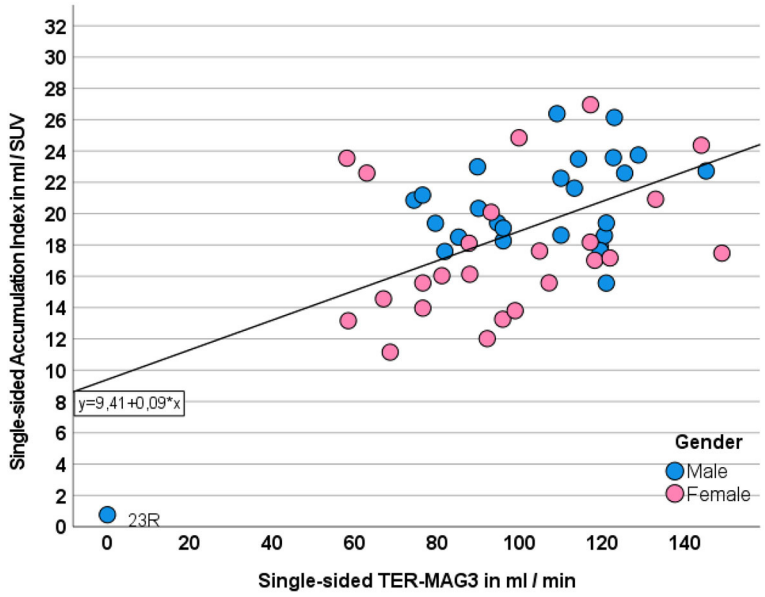

FIGURE 6
Correlation between single-sided ACI and TER-MAG. Gender is displayed in different colors.

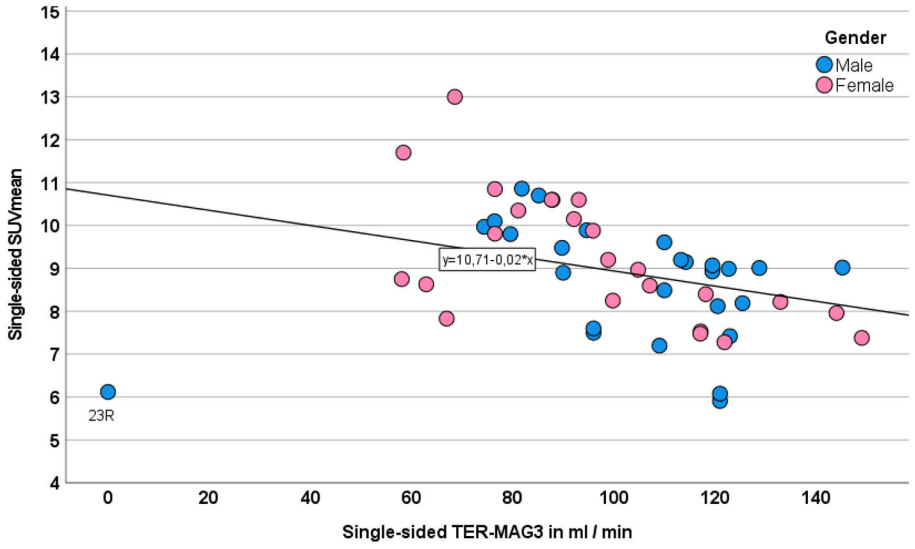

FIGURE 7
Correlation between single-sided SUVmean and TER-MAG. Gender is displayed in different colors.

in a larger parenchyma volume, thus increasing the filtration rate. Furthermore, the pharmacokinetic data indicate that the DOTATATE concentration of ∼30 min p.i. is predominantly attributed to the residual activity in the proximal tubules, and only a relatively small part of the parenchymal activity should be attributed to the tubular reabsorption at this early time point (3, 17, 18).

Based on the negative correlation of the parenchymal SUV and the presumed positive correlation of the tracer filtering renal parenchymal volume with TER, the simple isocontour-based ACI_{5-15} was defined by dividing the parenchyma volume by the SUV.

This ACI represented a highly significant predictor of split renal function and single-sided absolute function. A case of the non-functional kidney was identified due to the small volume of tracer-avid parenchyma.

From a clinical point of view, the ACI achieved the highest correlation with renal scintigraphy as the reference standard with an acceptable deviation of <5 % points. However, in one patient, the deviation of split renal function calculated with ACI (left 55:

TABLE 2 Correlation between SSR-PET-based renal function estimation and reference TER-MAG3 scintigraphy.

	Accumulation index (ACI)	SUVmean	Total kidney accumulation (TKA_{5-15})	[^{68}Ga]Ga-ha DOTATATE avid renal parenchymal volume
Single-sided renal function				
Split renal scintigraphy (MAG3)	**0.916****	**0.740****	**0.623****	**0.905****
Absolute single-sided renal function (Bubeck's method)	**0.549****	**−0.330***	0.056	0.272
Absolute renal function				
Tubular extraction rate (MAG3)	**0.482***	**0.519****	0.243	0.110
GFR	**0.461***	**−0.555****	−0.308	0.272

*$p < 0.05$, **$p < 0.01$.
Significant results are highlighted in bold.

right 45%) and MAG3 scintigraphy (left 69%: right 31%) was more than 10 % points before PRRT. Though the unbalanced split renal function was confirmed in the 2-month follow-up scintigraphy (after the first PRRT cycle), the partial function of the dominant kidney later declined under second–fourth PRRT cycles to 50:50%. Furthermore, TER-MAG declined from 216 ml/min/1.73 m² to 165 ml/min/1.73 m² (lower limit of the norm: 192 ml/min/1.73 m²). In addition to variances in the measurement method itself, differences in the measured structure can lead to different results. Minor glomerular damages may remain occult in the tubular excretion of MAG3 tracers, whereas glomerular-filtered tracers like [^{68}Ga]Ga-ha DOTATATE may be more sensitive.

In recent years, great efforts have been made to estimate the split renal function without radiation exposure. A processing method is functional MRI (24, 25). Apart from the time and financial expense of an additional examination, gadolinium-based contrast media must still be used for accurate quantification (26). Unfortunately, the risk for side effects of gadolinium-based contrast agents, such as nephrogenic systemic fibrosis (NSF), increases with decreasing renal function; however, these are the individuals who require renal function measurements the most (27). In addition, older adults, in particular, may not qualify for MRI due to claustrophobia, ferromagnetic material, or pacemakers. Here, the integration of split renal function estimation into follow-up examinations seems to be more appropriate.

4.1. Limitations

First, renal scintigraphy as the standard of reference has some limitations. In particular, the [^{99m}Tc]Tc-MAG3 tracer used for renal scintigraphy is tubularly extracted, whereas SSR-targeting peptide tracers are mainly subject to glomerular filtration and partially reabsorbed in the proximal tubule via the Megalin receptor (3, 17). Furthermore, owing to the lower spatial resolution and two-dimensional imaging, planar scintigraphy tends to systematically underestimate small parenchymal volumes. However, renal scintigraphy provides an accurate and robust assessment of side-separated renal function and remains the gold standard in the majority of clinical trials.

One alternative to [^{99m}Tc]Tc-MAG3 undergoing predominantly tubular excretion would be the use of [^{99m}Tc]Tc -diethylenetriaminepetaacetic acid [^{99m}Tc]Tc-DTPA) which is subject to glomerular filtration. [^{99m}Tc]Tc-DTPA or ^{68}Ga-labeled EDTA would potentially have been more comparable with the complex filtration of the [^{68}Ga]Ga-ha DOTATATE tracer but is not routinely used for renal function monitoring (4).

Furthermore, owing to the retrospective study design, the period between PET and scintigraphy was not predefined and was 16 days on average. Additionally, the calculation of GFR may show uncertainties and is dependent on the hydration status at the time of blood sampling, which remains unknown in this retrospective study (14).

However, as TER-MAG and GFR are highly correlated in determining overall renal function, TER-MAG may be used as a sufficient surrogate marker for the estimation of glomerular filtration rate.

Optimization of the ACI with the weighting of the individual factors and implementation of the blood pool as a tracer clearance indicator should be performed on a larger patient population to establish a more accurate SSR-PET-based renal function assessment.

5. Conclusion

The data from this pilot study indicate that absolute single-sided renal function can be estimated using SSR-PET with DOTA-conjugated peptide tracers such as [68 Ga]Ga-ha DOTATATE acquired prior to PRRT. It was shown that the remaining parenchymal tracer uptake and blood pool activity at about 30 min p.i. correlate negatively with the tubular extraction rate and glomerular filtration rate. The proposed "**Ac**cumulation **I**ndex" revealed a highly significant correlation with the absolute TER-MAG and GFR as well as split renal function and absolute single-sided renal function. Further validation of these results in a larger cohort is needed.

Data availability statement

The raw data supporting the conclusions of this article will be made available by the authors, upon request, subject to national data protection regulation.

Ethics statement

The studies involving human participants were reviewed and approved by Ethik-Kommission an der Medizinischen Fakultät der Eberhard-Karls-Universität und am Universitätsklinikum Tübingen. The patients/participants provided their written informed consent to participate in this study.

Author contributions

MW: visualization, writing—original draft, data curation, investigation, formal analysis, conceptualization, and methodology. KS: data curation and investigation. SU: visualization. SC-V: software and formal analysis. SB: methodology. JV, MW, and PG: validation. KN and CF: funding acquisition and resources. CF, HD, FS, and SU: writing—review and editing. HD: project administration, supervision, conceptualization, and methodology. KS: writing—original draft, formal analysis, and methodology. All authors contributed to the article and approved the submitted version.

Funding

This study was funded by the Deutsche Forschungsgemeinschaft (DFG, German Research Foundation) under Germany's Excellence Strategy (EXC 2180-390900677).

Acknowledgments

The authors would like to thank PET/CT technicians J. Deuble, S. Georgoulis, H. Heners, M. Pflumm, and S. Schnell for their great efforts and highly accurate PET/CT scan acquisition. We acknowledge support from the Open Access Publishing Fund of the University of Tübingen.

Conflict of interest

The authors declare that the research was conducted in the absence of any commercial or financial relationships that could be construed as a potential conflict of interest.

Publisher's note

All claims expressed in this article are solely those of the authors and do not necessarily represent those of their affiliated organizations, or those of the publisher, the editors and the reviewers. Any product that may be evaluated in this article, or claim that may be made by its manufacturer, is not guaranteed or endorsed by the publisher.

References

1. Pavel M, Oberg K, Falconi M, Krenning EP, Sundin A, Perren A, et al. Gastroenteropancreatic neuroendocrine neoplasms: ESMO clinical practice guidelines for diagnosis, treatment and follow-up. *Ann Oncol.* (2020) 31:844–60. doi: 10.1016/j.annonc.2020.03.304

2. Shah MH, Goldner WS, Benson AB, Bergsland E, Blaszkowsky LS, Brock P, et al. Neuroendocrine and adrenal tumors, version 2.2021, NCCN clinical practice guidelines in oncology. *J Natl Compr Canc Netw.* (2021) 19:839–68. doi: 10.6004/jnccn.2021.0032

3. Melis M, Krenning EP, Bernard BF, Barone R, Visser TJ, de Jong M. Localisation and mechanism of renal retention of radiolabelled somatostatin analogues. *Eur J Nucl Med Mol Imaging.* (2005) 32:1136–43. doi: 10.1007/s00259-005-1793-0

4. Erbas B, Tuncel M. Renal Function Assessment During Peptide Receptor Radionuclide Therapy. *Semin Nucl Med.* (2016) 46:462–78. doi: 10.1053/j.semnuclmed.2016.04.006

5. Bodei L, Cremonesi M, Ferrari M, Pacifici M, Grana CM, Bartolomei M, et al. Long-term evaluation of renal toxicity after peptide receptor radionuclide therapy with 90Y-DOTATOC and 177Lu-DOTATATE: the role of associated risk factors. *Eur J Nucl Med Mol Imaging.* (2008) 35:1847–56. doi: 10.1007/s00259-008-0914-y

6. Emami B, Lyman J, Brown A, Coia L, Goitein M, Munzenrider JE, et al. Tolerance of normal tissue to therapeutic irradiation. *Int J Radiat Oncol Biol Phys.* (1991) 21:109–22. doi: 10.1016/0360-3016(91)90171-Y

7. Bodei L, Kidd M, Paganelli G, Grana CM, Drozdov I, Cremonesi M, et al. Long-term tolerability of PRRT in 807 patients with neuroendocrine tumours: the value and limitations of clinical factors. *Eur J Nucl Med Mol Imaging.* (2015) 42:5–19. doi: 10.1007/s00259-014-2893-5

8. Imhof A, Brunner P, Marincek N, Briel M, Schindler C, Rasch H, et al. Response, survival, and long-term toxicity after therapy with the radiolabeled somatostatin analogue [90Y-DOTA]-TOC in metastasized neuroendocrine cancers. *J Clin Oncol.* (2011) 29:2416–23. doi: 10.1200/JCO.2010.33.7873

9. Sabet A, Ezziddin K, Pape UF, Reichman K, Haslerud T, Ahmadzadehfar H, et al. Accurate assessment of long-term nephrotoxicity after peptide receptor radionuclide therapy with (177)Lu-octreotate. *Eur J Nucl Med Mol Imaging.* (2014) 41:505–10. doi: 10.1007/s00259-013-2601-x

10. Svensson J, Berg G, Wangberg B, Larsson M, Forssell-Aronsson E, Bernhardt P. Renal function affects absorbed dose to the kidneys and haematological toxicity during (1)(7)(7)Lu-DOTATATE treatment. *Eur J Nucl Med Mol Imaging.* (2015) 42:947–55. doi: 10.1007/s00259-015-3001-1

11. Kwekkeboom DJ, de Herder WW, Kam BL, van Eijck CH, van Essen M, Kooij PP, et al. Treatment with the radiolabeled somatostatin analog [177 Lu-DOTA 0, Tyr3]octreotate: toxicity, efficacy, and survival. *J Clin Oncol.* (2008) 26:2124–30. doi: 10.1200/JCO.2007.15.2553

12. Itoh K. 99mTc-MAG3: review of pharmacokinetics, clinical application to renal diseases and quantification of renal function. *Ann Nucl Med.* (2001) 15:179–90. doi: 10.1007/BF02987829

13. Fritzberg AR, Kasina S, Eshima D, Johnson DL. Synthesis and biological evaluation of technetium-99m MAG3 as a hippuran replacement. *J Nucl Med.* (1986) 27:111–6.

14. Geist BK, Baltzer P, Fueger B, Hamboeck M, Nakuz T, Papp L, et al. Assessing the kidney function parameters glomerular filtration rate and effective renal plasma flow with dynamic FDG-PET/MRI in healthy subjects. *EJNMMI Res.* (2018) 8:37. doi: 10.1186/s13550-018-0389-1

15. Bubeck B, Brandau W, Eisenhut M, Weidenhammer K, Georgi P. The tubular extraction rate (Ter) of Tc-99m-Mag3—A new quantitative parameter of renal-function. *Nuc Compact-European-American Communications in Nuc Med.* (1987) 18:260.

16. Levey AS, Stevens LA, Schmid CH, Zhang YL, Castro AF. 3rd, Feldman HI, et al. A new equation to estimate glomerular filtration rate. *Ann Intern Med.* (2009) 150:604–12. doi: 10.7326/0003-4819-150-9-200905050-00006

17. de Jong M, Barone R, Krenning E, Bernard B, Melis M, Visser T, et al. Megalin is essential for renal proximal tubule reabsorption of (111)In-DTPA-octreotide. *J Nucl Med.* (2005) 46:1696–700.

18. Hofmann M, Maecke H, Borner R, Weckesser E, Schoffski P, Oei L, et al. Biokinetics and imaging with the somatostatin receptor PET radioligand (68)Ga-DOTATOC: preliminary data. *Eur J Nucl Med.* (2001) 28:1751–7. doi: 10.1007/s002590100639

19. Hartmann H, Freudenberg R, Oehme L, Zophel K, Schottelius M, Wester HJ, et al. Dosimetric measurements of (68)Ga-high affinity DOTATATE: twins in spirit - part III. *Nuklearmedizin.* (2014) 53:211–6. doi: 10.3413/Nukmed-0667-14-05

20. Guhne F, Heinzig A, Seifert P, Drescher R, Freesmeyer M. The dependence of renal (68)Ga[Ga]-DOTATOC uptake on kidney function and its relevance for peptide receptor radionuclide therapy with (177)Lu[Lu]-DOTATOC. *Diagnostics*. (2021) 11:1216. doi: 10.3390/diagnostics11071216

21. Kaewput C, Vinjamuri S. Comparison of renal uptake of 68Ga-DOTANOC PET/CT and estimated glomerular filtration rate before and after peptide receptor radionuclide therapy in patients with metastatic neuroendocrine tumours. *Nucl Med Commun.* (2016) 37:1325–32. doi: 10.1097/MNM.0000000000000591

22. Beauregard JM, Hofman MS, Kong G, Hicks RJ. The tumour sink effect on the biodistribution of 68Ga-DOTA-octreotate: implications for peptide receptor radionuclide therapy. *Eur J Nucl Med Mol Imaging.* (2012) 39:50–6. doi: 10.1007/s00259-011-1937-3

23. Hoy WE, Douglas-Denton RN, Hughson MD, Cass A, Johnson K, Bertram JF. A stereological study of glomerular number and volume: preliminary findings in a multiracial study of kidneys at autopsy. *Kidney Int Suppl.* (2003) 83:S31–7. doi: 10.1046/j.1523-1755.63.s83.8.x

24. Zhou JY, Wang YC, Zeng CH, Ju SH. Renal Functional MRI and Its Application. *J Magn Reson Imaging.* (2018) 48:863–81. doi: 10.1002/jmri.26180

25. Barker AJ, Berthusen A, Vigers T, Schafer M, Browne LP, Bjornstad P. Estimation of glomerular filtration rate in a pediatric population using non-contrast kidney phase contrast magnetic resonance imaging. *Pediatr Nephrol (*. (2022). doi: 10.1007/s00467-022-05832-7

26. Boss A, Martirosian P, Fuchs J, Obermayer F, Tsiflikas I, Schick F, et al. Dynamic MR urography in children with uropathic disease with a combined 2D and 3D acquisition protocol–comparison with MAG3 scintigraphy. *Br J Radiol.* (2014) 87:20140426. doi: 10.1259/bjr.20140426

27. Wagner B, Drel V, Gorin Y. Pathophysiology of gadolinium-associated systemic fibrosis. *Am J Physiol Renal Physiol.* (2016) 311:F1–F11. doi: 10.1152/ajprenal.00166.2016

Frontiers in Medicine

Translating medical research and innovation into improved patient care

A multidisciplinary journal which advances our medical knowledge. It supports the translation of scientific advances into new therapies and diagnostic tools that will improve patient care.

Discover the latest Research Topics

See more →

Frontiers

Avenue du Tribunal-Fédéral 34
1005 Lausanne, Switzerland
frontiersin.org

Contact us

+41 (0)21 510 17 00
frontiersin.org/about/contact